



UNIVERSITAT^{DE}
BARCELONA

Single molecule electrochemical studies of photosynthetic complexes

Manuel López Ortiz



Aquesta tesi doctoral està subjecta a la llicència **Reconeixement 4.0. Espanya de Creative Commons.**

Esta tesis doctoral está sujeta a la licencia **Reconocimiento 4.0. España de Creative Commons.**

This doctoral thesis is licensed under the **Creative Commons Attribution 4.0. Spain License.**



UNIVERSITAT DE
BARCELONA

UNIVERSITAT DE BARCELONA

FACULTAT DE FARMÀCIA I CIÈNCIES DE L'ALIMENTACIÓ

SINGLE MOLECULE ELECTROCHEMICAL STUDIES OF PHOTOSYNTHETIC
COMPLEXES

MANUEL LÓPEZ ORTIZ 2023

UNIVERSITAT DE BARCELONA

FACULTAT DE FARMÀCIA I CIÈNCIES DE L'ALIMENTACIÓ

DOCTORAT EN BIOTECNOLOGIA

SINGLE MOLECULE ELECTROCHEMICAL STUDIES OF PHOTOSYNTHETIC
COMPLEXES

Memòria presentada per Manuel López Ortiz per optar al títol de doctor per la
universitat de Barcelona

Co-director, Pau Gorostiza Langa

Co-directora, Marina Inés Giannotti

Doctorand, Manuel López Ortiz

Tutora, Josefa Badía Palacín

Realizat a l'Institut de Bioenginyeria de Catalunya



UNIVERSITAT DE
BARCELONA

MANUEL LÓPEZ ORTIZ 2023

Contents

1	Introduction	1
1	Outline.....	1
2	Model system introduction	2
2.1	Photosynthesis outlook.....	2
2.2	Photosynthetic light reactions	3
2.3	Photosystem I: a ferredoxin-plastocyanin oxido-reductase powered by light.....	4
2.4	Plastocyanin: soluble electron carrier between cytochrome <i>b₆f</i> and PSI.....	7
2.5	Interprotein electron transfer between PSI and Pc	8
2.6	Light harvesting in PSI-LHCI.....	10
3	Experimental methods	13
3.1	Introduction to nanoprobe techniques.....	13
3.2	Atomic force microscopy and spectroscopy.....	14
3.3	Scanning Tunnelling Microscopy.....	17
3.4	Electrochemical Measurements.....	25
3.5	Introduction to 2d-electron spectroscopy	32
3.6	Protein immobilization bioengineering	34
3.7	Sample irradiation with LED sources	36
4	Theory.....	37
4.1	Introduction to quantum mechanics and the Fermi Golden Rule	37
4.2	ET Theory	38
4.3	Light absorption	47
5	Literature experimental results on ET and PSI.....	51
5.1	Bulk techniques for ET.....	51
5.2	ECSTM experiments	53
5.3	PSI based bio-hybrid devices.....	56
2	Objectives	57

3	Distance and Potential Dependence of Charge Transport Through the Reaction Center of Individual Photosynthetic complexes	59
1	Abstract	60
2	Introduction	60
3	Results and discussion	63
4	Conclusions	71
5	Acknowledgements	72
6	Bibliography	72
7	Supporting information	78
4	The protein matrix of plastocyanin supports long-distance charge transport with photosystem I and the copper ion regulates its spatial span and conductance	95
1	Abstract	96
2	Introduction	96
3	Results and Discussion.....	100
	3.1 Current-distance spectroscopy: spatial span of the charge exchange.	100
	3.2 Blinking: formation of spontaneous PSI/Pc junctions.....	103
4	Discussion	106
5	Conclusions	109
6	Methods	110
7	Bibliography.....	114
8	supporting information.....	120
5	Light- and redox-dependent force spectroscopy reveals that the interaction between plastocyanin and plant photosystem I is favored when one partner is ready for electron transfer	130
1	Abstract	131
2	Introduction	131
3	Results and Discussion.....	134
	3.1 The interaction between PSI and Pc is independent of the redox state of P700 when Pc is reduced.	135
	3.2 Reduced PSI in the dark displays a weaker interaction with oxidized Pc.....	137
	3.3 Mg ²⁺ ions decrease the frequency of PSI-Pc binding.....	140
4	Conclusions	143
5	Methods	143
6	Associated content	146
7	References.....	146
8	Supporting information	152

6	Photoelectrochemical two-dimensional electronic spectroscopy (PEC2DES) of photosystem I to study charge separation dynamics in photosynthesis	156
1	Abstract	157
2	Introduction	157
3	Experiment	159
	3.1 Photo electrochemical current readout of PSI-LHCI samples.....	159
	3.2 Phase modulation and 2DES parameters	160
4	Results.....	161
	4.1 Photo-electrochemical and AFM characterization of Au-pIQAcys-PSI-LHCI samples	161
	4.2 PEC2DES results	163
	4.3 Global analysis of PEC2DES data	165
5	Discussion	166
6	Conclusions	169
7	Acknowledgments.....	170
8	References.....	170
9	supporting information.....	178
7	Fast photochronoamperometry of photosynthetic complexes for biosensors and electron transport studies	182
1	Abstract	182
2	Introduction	183
	2.1 Sample Characterization: AFM and Spectral Dependence.	185
3	results and disscussion	186
	3.1 Proof of Concept: Power Dependence and Sensing.....	186
	3.2 Chopped Light Voltammetry: Transient Photocurrent.....	188
	3.3 Fast Chronoamperometry: Empirical Characterization with Double Exponential Function.....	189
	3.4 Kinetic Model: Describe Mediator and PSI Cofactors Concentration.	189
	3.5 Considerations for Sensor Design and Optimization.	192
4	Conclusions	193
5	Acknowledgements.....	193
6	Bibliography	194
7	Supplementary Information	198
8	Summary of the obtained results	200
9	Discussion	206
10	Conclusions	213
11	Bibliography	216

Chapter 1

Introduction

1 Outline

The experimental results we present deal with **interprotein electron transfer (ET)**. Throughout this manuscript, plant **photosystem I (PSI)**, has been used as model system to study ET between cognate redox proteins at the single complex level, making use of **nanoprobe** and non-linear spectroscopy techniques.

Chapter 1 is an introduction providing the context for the biological **model system**, the **experimental methods** that we exploit, the **theory underlying ET** and a revision of **literature experimental results** relevant for discussion. Introduction chapter is followed by the **objectives** that will be pursued throughout the manuscript.

As a basis for further experiments, in **chapter 3**, we have developed a method to unidirectionally **bind PSI to gold electrodes**. This system has allowed us to evaluate its characteristic **charge exchange distance** and its dependence with electrodes potential.

In chapter 4, the **charge exchange distance and the conductance of the complex that PSI forms with Plastocyanin (Pc)**, a cognate protein in the photosynthetic electron transport chain is characterized. In this work, we dissect the contributions of Pc structure and of its redox cofactor to charge exchange.

The same model system is studied in **chapter 5**, estimating the **binding probability of the PSI-Pc transient complex** and how the redox state of the partners modulates their association.

Additionally, we have expanded the tools developed for studying ET in PSI to different fields. **In chapter 6**, we present a novel **non-linear electron spectroscopy technique based on photocurrent detection** (photo-electrochemical current two-dimensional

electronic spectroscopy, PEC2DES) in collaboration with the institute of photonic sciences (ICFO) and the chemistry department of Padova University. On the other hand, **in chapter 7**, we show how photocurrent readout can be exploited to detect analytes in a **PSI based herbicide biosensor**.

Finally, chapters 8,9 and 10 provides a **summary of the obtained results, a comparative discussion and the conclusions** obtained from the results exposed throughout the dissertation.

2 Model system introduction

2.1 Photosynthesis outlook

Life has been described as an autopoietic machine “*a network of processes [...] which through their interactions and transformations regenerate and realize the network of processes (relations) that produce them*”.¹ In 1943, the seminal lectures of E. Schrödinger *What is Life?* identified in the self-assembling process of life, evolving from order to disorder, a decrease of the free energy of the self-replicating system. The major source of this free energy is the Sun, which provides an entropy flux to the earth² of $6 \cdot 10^{14} JK^{-1}s^{-1}$. As life managed to harvest and exploit sunlight, photosynthesis has powered practically all the life on earth with an estimated global power output of 130 TW.³ Two widespread examples evidence the huge impact of photosynthesis on a planetary scale: i) The green colour of the earth crust, which is due to the absorption of the chlorophyll pigments in photosynthetic complexes and ii) the presence of oxygen in the atmosphere, that was triggered by the great oxygenation event in the Palaeozoic era due to the evolution of photosynthetic organisms 3.4 billion years ago. In plants, algae and cyanobacteria, oxygenic photosynthesis takes place in two stages: in light dependent reactions (figure 1), photonic excitation catalyses water oxidation ($2 H_2O \rightarrow 4 H^+ + 4 e^- + O_2$) and powers the photosynthetic electron transport chain. This chain shuttles electrons reducing NADP to NADPH and simultaneously generates a proton gradient exploited for ATP synthesis. In light independent reactions, NADPH and ATP are used to fix CO_2 into sugars in the Calvin cycle. In this manuscript I will focus on charge transport within the light dependent reactions, specifically, the charge exchange between Pc and PSI. Photon absorption and subsequent excitation energy transfer (EET) and charge separation (CS) processes promoting PSI photo-oxidation are presented in section 2.6. A further discussion on light independent reactions is out of the scope of this work. In plants and algae, photosynthesis takes place in the chloroplast, a separated organelle with specific DNA and ribosomes evolved from cyanobacteria in an endosymbiotic event similar to mitochondria engulfment.⁴ Chloroplasts contain stacks of thylakoids membrane

compartments that embeds the protein complexes of the photosynthetic electron transport chain (figure 1.1).

2.2 Photosynthetic light reactions

Photosynthetic light reactions are initiated by photon absorption in photosystem II (PSII). Photo-excited chlorophylls, embedded in the protein complex or in the accessory light harvesting antennas, funnel excitation to the reaction centre by EET. Charge separation takes place in the photo-excited chlorophyll special pair P680*, that transfer electrons to an accessory plastoquinone via a pheophytin cofactor. P680⁺ hole is transferred sequentially to the oxygen-evolving complex that catalyse water splitting. Plastoquinone electron carrier diffuses throughout the thylakoid membrane shuttling electrons from PSII to cytochrome *b₆f* proton pump. Cytochrome *b₆f* couples plastoquinone oxidation to the translocation of protons from the stromal to the luminal side of the thylakoid membrane. At the same time, cytochrome *b₆f* reduces Pc, which shuttles electrons between cytochrome *b₆f* and PSI.

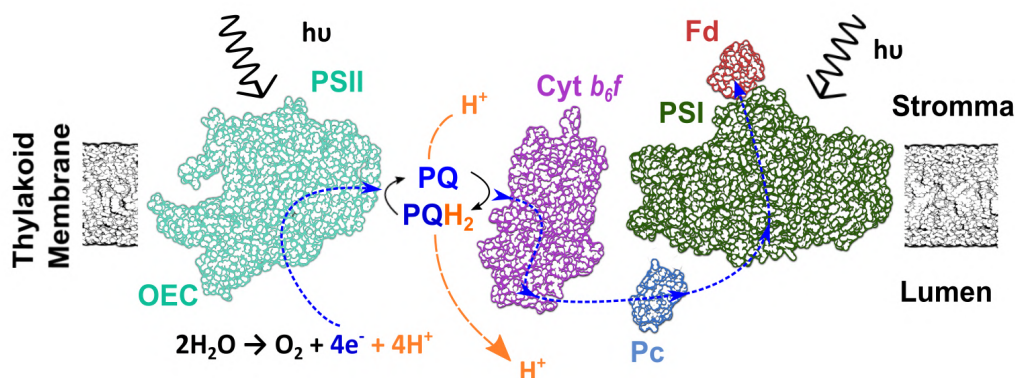


Figure 1.1: Light dependent reactions in photosynthesis. The protein complexes that we have employed in this work for interprotein charge exchange are photosystem I (PSI), in green, and plastocyanin (Pc), in blue. Pc shuttles electrons from cytochrome *b₆f* (purple) to PSI, diffusing in the thylakoid inner medium (lumen). PSI transports electrons from the photo-oxidable cofactor (P700 chlorophyll special pair) located in the luminal surface to Ferredoxin (Fd, red) that binds PSI in the outer side (stroma) of the thylakoid membrane. Please note that this figure is a cartoon representation (not to scale) of an idealized and simplified thylakoid membrane. PSII (aquamarine) and PSI are not evenly distributed in the thylakoid membrane, and they can be separated by hundreds of nm.

In this dissertation I focus on the ET between PSI and Pc. PSI complex is a light-driven oxido-reductase, that is, PSI employs light excitation to transport electrons throughout the thylakoid membrane from Pc to ferredoxin (Fd), PSI-redox partner in the stromal

side. Fd eventually reduces Ferredoxin-NADP⁺ reductase, an enzyme catalysing NADP⁺ reduction to NADPH. Simultaneously, ATP synthase makes use of the intermembrane proton gradient produced by cytochrome *b₆f* to synthesize ATP from ADP and inorganic phosphate. Fd can also reduce cytochrome *b₆f* instead of Ferredoxin-NADP⁺ reductase increasing the proton gradient across the thylakoid membrane (circular electron flow). We have presented the electron transport chain reactions as a sequential process to ease explanation, however we shall picture photosynthetic light reactions taking place simultaneously, as photons don't excite PSII and PSI sequentially. In addition, photosynthetic organisms need to adapt to fluctuating light conditions that may produce charge imbalance throughout the transport chain. Changes in the photon absorption by PSI and PSII accessory light-harvesting complexes,⁵ their relative distance and the circular electron flow⁶ are strategies of photo-protection from excessive irradiation.⁷ In the following sections, a detailed description of the PSI protein complex (section 2.3), Pc (section 2.4) and the charge exchange between Pc and PSI (section 2.5) will be provided.

2.3 Photosystem I: a ferredoxin-plastocyanin oxido-reductase powered by light

PSI forms a trimer in cyanobacteria while in plants and red and green algae PSI is found in monomeric form. PSI monomer is made up of two moieties, the light-harvesting antenna (LHCI) and the core complex, PSI reaction center.⁸ Throughout the thesis, the experiments are carried out with PSI-LHCI complexes, however for simplicity we address them as PSI. Only in chapter 6, dealing with the spectroscopic features of the photosynthetic complex, the full name is employed. The light harvesting complex II, LHCII, associated to PSII, can bind to PSI-LHCI under fluctuating illumination conditions to balance light harvesting.⁹

PSI exhibits an ellipsoidal cylinder shape with a major and minor axis diameter of 15 and 10.5 nm, respectively, and 4 nm in height.¹⁰ The supercomplex, with a mass of ~530 kDa, contains 18 subunits (figure 1.2a, 1.2b). The PsaA/PsaB heterodimer is the heart of PSI complex, as it harbours 80 out of the 100 chlorophylls found in the reaction centre. Among these chlorophylls, the PsaA/PsaB heterodimer harbours the P700 chlorophyll special pair as well as the cofactors constituting the electron transport chain shown in figure 1.2c. In the electron transport chain, electrons are rapidly transferred from the photo-oxidized primary electron donor, P700, to the terminal electron acceptor, the iron sulfur cluster F_B, that donates electrons to Fd. The electron transport chain is formed by: the chlorophyll special pair (P700), two additional chlorophyll pairs (A₀), a pair of phylloquinones (A₁) and three iron sulphur clusters (F_X), (F_A) and (F_B). It has been shown that both PsaA and PsaB participate in charge separation and ET¹¹ with an uneven branching ratio favouring PsaA.¹² The PsaC subunit harbours the two terminal cofactors of the electron transport chain, the pair of iron sulphur clusters, F_A and final electron

donor F_B . PsaC forms, with PsaD and PsaE, a protruding domain in the stromal side of the membrane that constitutes the binding site for Fd. In eukaryotic organisms, positively charged residues in the N-terminal domain of the transmembrane PsaF sub-unit extends beyond the luminal surface. N-terminal PsaF electrostatic interactions with Pc¹³ and PsaA and PsaB hydrophobic interactions¹⁴ are critical to the charge exchange process with Pc and will be discussed in more detail section 2.5.

The time scales of the cascade of events triggering PSI photo-oxidoreductase function span over several orders of magnitude, from photon absorption (10^{-15} s), EET (10^{-13} to 10^{-12} s), CS (10^{-12} s),¹⁵ discussed in section 2.6, to intra-protein ET (10^{-11} - 10^{-7} s) and inter-protein ET (10^{-6} to 10^{-3}). In particular, interprotein ET rates between P700⁺/Pc range between 10^{-6} - 10^{-3} s while ET times of 10^{-4} s are reported for F_B^- /Fd.¹⁶ Therefore, intra-protein ET, as well as interprotein ET are faster than the P700⁺/ F_B^- recombination, that has a lifetime $t_{1/2}$ of ~ 50 ms.¹⁷ The research presented in this manuscript focuses on the two extreme time scales. Ultra-fast time scale (10^{-15} to 10^{-13} s) concerning photon absorption and the onset of EET, is studied by two-dimensional electronic spectroscopy (*chapter 6*). In the slow extreme, we study PSI-Pc inter-protein charge exchange exhibiting two time scales, one associated with ET within the PSI-Pc transient complex (10^{-6} to 10^{-5} s) and a slower phase (10^{-4} to 10^{-3} s) attributed to complex binding, unbinding and rearrangement. The ET phase will be addressed in chapter 4 while the binding contribution will be treated separately in chapter 5.

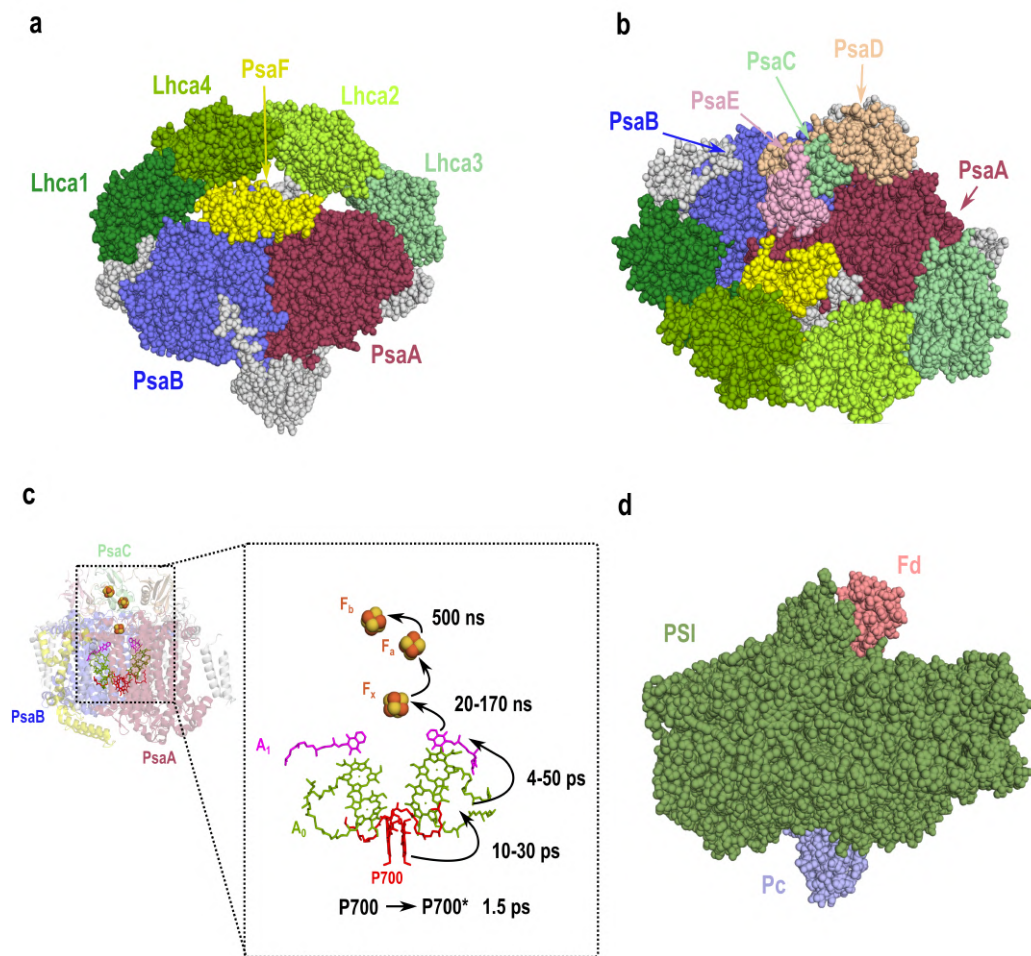


Figure 1.2: PSI-LHCI structure (PDB 4XK8) bottom view showing the core units PsaA (red), PsaB (blue) and PsaF (yellow) in the luminal side. Light harvesting sub-units, Lhca1-4 are coloured in green. (b) Top view showing the stromal side subunits: PsaC (green), PsaD (orange) and PsaE (pink). (c) Reaction center sub-units (PsaA, PsaB and PsaC) harbouring the cofactors constituting the electron transport chain and their associated ET. Cofactors in the electron transport chain: P700 chlorophyll special pair (red), A_0 double chlorophyll pair (green), A_1 phylloquinone pair (magenta) and F_X , F_A and F_B iron sulphur clusters (orange Fe, yellow S). (d) Crystallographic structure of the trimer complex formed by PSI (green), Pc (blue) and Fd (red), PDB 6ZOO.

2.4 Plastocyanin: soluble electron carrier between cytochrome b_6f and PSI

Plastocyanin is a type-I blue copper globular protein of 10.4 kDa. It exhibits a β -barrel structure conformed by eight β strands and a small α -helix. It fulfils its electron carrier function between cytochrome b_6f and PSI by changing the oxidation state of its Cu(I)/Cu(II) cofactor. This metallic centre is located in the northern pole of the protein near the binding site for PSI and cytochrome b_6f . It is coordinated by two histidines, one methionine, and one cysteine in a tetrahedral geometry (see figure 3).¹⁸

In early photosynthetic bacteria, the role of reducing reaction centre was fulfilled by the heme protein cytochrome c_6 (cyt c_6) in figure 3. In some cyanobacteria and algae, bioavailability of metal ions determines the expression of Pc or cyt c_6 , while higher plants only express Pc. Interestingly, both proteins have converged to serve the same function though their structure and origin are distinct (see figure 3).¹⁹ However, Pc exhibits a precise molecular recognition with PsaF sub-unit providing finely a tuned dissociation mechanism controlled redox state which is not present in cyt c_6 .^{19,20}

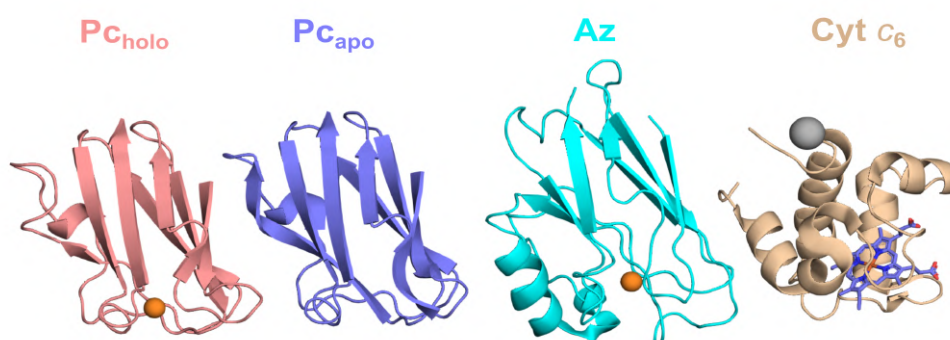


Figure 1.3: Comparison of crystallographic structure for Pcholo_{holo} (1PLC) in red, Pcapo (2PCY) in dark blue, Az (1AZU) in cyan and Cyt c6 (4KMG) in brown. In Pcholo and Az, the Cu atom is shown in orange. In Cyt c6, the heme group is coloured in purple and the gray sphere represents a Na⁺ ion.

Pc forms, together with azurin (Az), a family of globular blue-copper proteins shuttling electrons in plants and bacteria respectively.²¹ Pc and Az exhibit two opposing β -sheets encapsulating a highly similar Cu binding in one pole of the structure (figure 3).²² Az has been a model system to study redox-protein ET due to its small size, stability and surface exposed cysteine facilitating electrode binding.²³

In chapter 4, I will pay special attention to the role of the Cu metal centre in the interprotein ET with PSI, contrasting experimental results of Pc lacking the Cu atom

(apo-plastocyanin, Pc_{apo}) with the regular form (holo-plastocyanin, Pc_{holo}). This will allow us to tell apart the contribution to ET of the redox centre and the protein structure, which is similar in Pc_{apo} ²⁴ and Pc_{holo} (figure 3).²⁵

2.5 Interprotein electron transfer between PSI and Pc

To transfer electrons between cytochrome b_{6f} and PSI, Pc undergoes a redox cycle modifying the oxidation state of its Cu centre, reduced by cyt b_{6f} ($Cu^{2+} + e^- \rightarrow Cu^+$) and oxidized by PSI ($Cu^+ \rightarrow e^- + Cu^{2+}$). In both cases, Pc forms a transient complex with the respective partner subject to a trade-off between low binding affinity (with binding constants in the range 10^2 - 10^6 M^{-1}) enabling rapid turn-over, and close distance configuration between the redox centres (< 14 Å) that is required for rapid ET.²⁶⁻²⁸ In PSI-Pc and cyt b_{6f} -Pc, long-range electrostatic interactions orient the formation of an encounter complex²⁶ while hydrophobic interactions optimize the orientation of both partners, as it has been described for other proteins.²⁹ In addition, due to the distant localization of PSI and cyt b_{6f} in the thylakoid membrane, to shuttle charge between the membrane bound complexes, Pc has to diffuse long distances (> 100 nm) in the crowded thylakoid lumen.³⁰⁻³²

Using the transferred cross-saturation method based on NMR, the interacting residues of labelled Pc with PSI were identified to be Gly10, Gly11, Leu12, His37, Leu62, Asn64, Ala65, His87, Gln88, Gly89, Ala90, and Gly91 in Pc sequence (shown in dark blue in figure 4).³³ These residues form a continuous hydrophobic patch surrounding Cu ion, however, evidences of salt bridges formation were not found.³³ This reinforces the transient nature of the PSI-Pc complex enabling high turn-over rates. PSI-Pc hydrophobic interactions are also remarkable in the cryo-EM structure of plant PSI-Pc complex.^{34,35}

Previous to the release of the PSI-Pc complex structure, mutagenesis studies had already identified PSI residues critical for ET, making use of time resolved spectroscopy. In this technique, light flashes photo-oxidise P700 triggering PSI-Pc ET. The population of $P700^+$ state is then tracked by monitoring the absorption of $P700^{14,28,36-38}$ or photovoltage³⁹⁻⁴¹ changes. Time evolution of these signals provides information on the $P700^+$ reduction kinetics by Pc. The evolution of $P700^+$ population exhibits a bi-phasic exponential decay with a fast phase (μs time scale) associated with the ET of pre-formed complexes and a slower phase (ms time scale) associated with the transient complex formation stage.^{14,28,36-38}

Analysis of the relative amplitude of these two phases allowed to identify three groups of residues critical for the ET process:^{14,28,36-38} i) PsaA Trp625 and PsaB Trp658 (shown in red in figure 4), a pair of tryptophan residues located below P700 special pair. They facilitate the hydrophobic interaction with Pc, thus their substitution affects the slow binding phase and the amplitude of the fast ET phase of pre-formed complexes prior to

flash.^{8,14,38} The results presented in chapter 3, suggest that they might play an additional role facilitating ET with P700. ii) PsaF lysines Lys93, 96, 100, and 101 (figure 4, yellow) participate in PSI-Pc lateral binding and notably in the release of the oxidized Pc after ET.^{13,35} On the other hand, mutations affecting these lysines do not affect the ET of the pre-formed complex.¹³ iii) PsaB Glu613 (magenta) affects the orientation of the soluble part of the N-terminal domain of PsaF containing the aforementioned lysines and thus affecting PSI-Pc binding. The ET rates of mutant PsaB Glu-613- Lys are comparable to PSI complexes lacking the PsaF subunit.⁴²

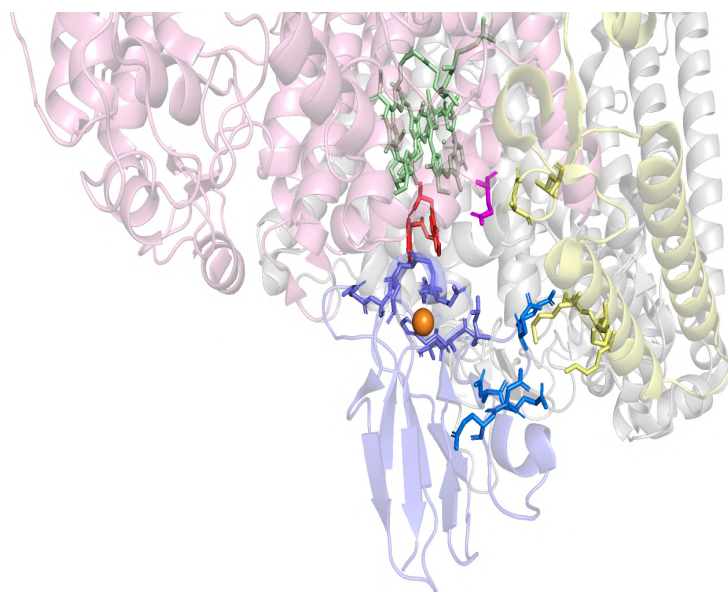


Figure 1.4: PSI-Pc complex structure with Pc (blue) and PSI sub-units PsaA (pink) and PsaB (white) and PsaF (yellow). Redox cofactors, P700 (green) and Cu atom in Pc (orange) are highlighted as well as residues with a reported role on PSI-Pc ET: PsaA Trp625 PsaB and Trp658 (red), PsaB Glu613 (pink) and PsaF lysines Lys93, Lys96, Lys100, Lys101 (yellow). Pc Residues interacting with PsaA and PsaB are shown in purple and those interacting with PsaF lysines are shown in blue. Adapted from panel 1 in chapter 4.

Transient absorption measurements were also exploited to evaluate the effect of Pc oxidation state on ET kinetics, revealing that the dissociation constant of oxidized plastocyanin is six times larger than its reduced counterpart.³⁶ While these measurements of PSI-Pc charge exchange are performed *in vitro*,^{14,28,36–38} the changes P700 absorbance have also been tracked in *Chlamydomonas reinhardtii* mutant cells.⁴² PSI-Pc charge exchange revealed that PsaA Trp-651-Ser mutation that reduced five-fold the binding affinity of PSI-Pc *in vitro*, did not affect the charge exchanged measured under physiological conditions. However, PsaB Glu-613-Lys mutants, affecting the release of oxidized Pc significantly slows down the overall charge exchange rate *in vivo*.⁴²

2.6 Light harvesting in PSI-LHCI

Pigments in PSI-LHCI

Chromophores absorb light thanks to their molecular dipoles which have transition energies in the visible spectra (see section 4.3). Photosynthetic chromophores are mainly the different forms of chlorophylls and carotenoids. The exact number of identified chlorophyll pigments is around 160, and it differs in the different available structures from 155⁴³ to 177.⁴⁴ In the crystallographic structure of PSI-LHCI shown in figure 5, there have been identified 155 chlorophylls (143 chlorophylls a and 12 chlorophylls b) and 35 carotenoids (26 β -carotenes, 5 luteins, and 4 violaxanthins). Thus, in PSI-LHCI, light harvesting is carried out mainly by chlorophyll a, chlorophyll b and in a minor extent by carotenoid pigments, that also play photoprotection role. Chlorophylls are composed by a porphyrin ring coordinating a Mg^{2+} atom and a side phytyl chain. The porphyrin is a tetrapyrrole macrocycle which cyclic geometry facilitates electronic states delocalization. In chlorophylls, ground and excited states are formed by a linear combination of the extended π orbitals in the cycle.⁴⁵

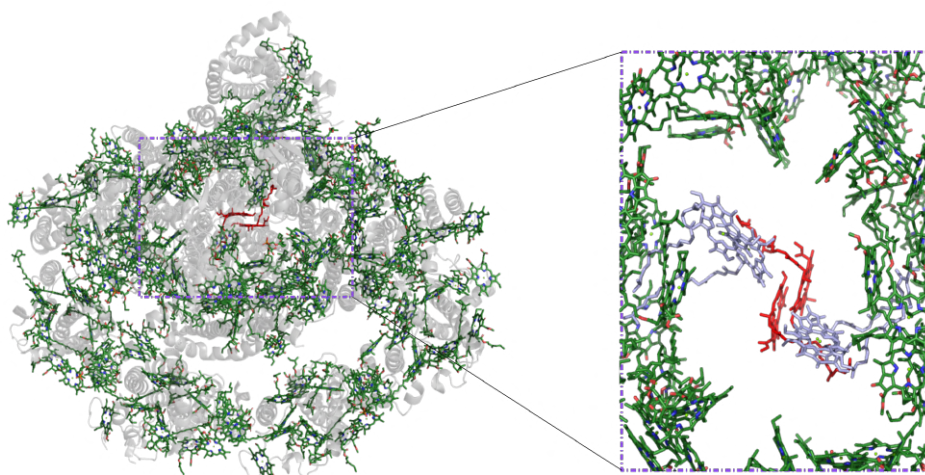


Figure 1.5: Crystallographic structure of PSI-LHCI (PDB 4XK8) highlighting photosynthetic pigments in green. Chlorophyll special pair P700 is shown in red. The concentric arrangement around P700 promotes EET to the RC. Inset shows a closer view of the RC. The orientation of bulk chlorophylls (dark green), P700 (red) and A₀ chlorophylls (light blue), facilitates EET, CS and ET respectively.

It is remarkable that chlorophyll pigments in PSI can perform distinct functions making use of the same building block,⁴⁵ such as light absorption, EET, CS, and ET. These diverse functionalities are achieved by PSI chlorophylls modifying their relative position and orientation. Within all the chlorophylls in the complex, only the P700 special pair (red in

figure 5) promotes CS and subsequent ET to the electron transport chain. Following CS, A_0 , another chlorophyll pair dimer (blue in figure 1.5) is the primary electron acceptor in the electron transport chain. This architecture with numerous antennas and a single CS site strongly affects the light harvesting efficiency and the spectroscopic features of PSI-LHCI.

Under standard sunlight irradiation, approximately one photon reaches a PSI-LHCI complex every ms exciting a chlorophyll pigment within the complex.⁷ What happens once the chlorophyll, or several chlorophylls, are in an excited state? How are the excitations in the chlorophylls transferred throughout the complex? How are they transduced into separated charges in the reaction centre? In the following, we will briefly introduce the different excitation decay pathways in photosynthetic pigments: fluorescence, energy transfer, charge separation and thermal dissipation via coupling with the vibrational modes.

Fluorescence, energy transfer and charge separation in PSI-LHCI

The fastest process (100's fs timescale) following excitation of the chromophores is the internal conversion from higher excited states to the first excited state. This energy relaxation process is non-radiative and is coupled with the vibrational modes leading to thermal dissipation. From the first excited state, excitation energy is transferred to the neighbouring chlorophylls.⁴⁶ Vibrational modes (phonons), similarly to electronic states, are experimentally observed as absorption bands in the electromagnetic spectrum matching their energies, that lie, in the case of nuclear vibrations, in the infra-red region. In chlorophyll a, coupling of the electronic (optical) and vibrational modes is evidenced by the appearance of an absorption band at $\sim 750 \text{ cm}^{-1}$ under illumination (see chapter 5).^{47,48}

Chlorophylls in the excited can decay to the ground state by emission of a photon. The emission spectrum of chlorophyll is redshifted with respect to the absorption spectrum, meaning that part of the energy has been dissipated. PSI-LHCI super complex harbours a chlorophyll concentration around 0.5 M.¹⁵ While the excitation life-time of dilute chlorophyll samples is $\sim 6 \text{ ns}$, at 0.5 M concentration closely packed chlorophylls with random orientations quench the excited state reducing its lifetime to 100 ps.⁴⁹ In PSI-LHCI, chlorophylls are precisely spaced and oriented to avoid concentration quenching, to enhance chlorophyll cross section and to promote multichromophoric excited states allowing efficient EET to the RC.⁵⁰ In particular, embedded in PSI-LHCI complexes, chlorophyll's fluorescence decays with a lifetime of $\sim 2 \text{ ns}$,⁴⁶ which suggests that additional deexcitation pathways are contributing. Pigments transfer excitation energy to nearby resonant pigments (that is absorbing at a similar wavelength) by means of Förster resonance energy transfer (FRET).⁵¹ FRET is a non-radiative process that depends on pigments dipole-dipole interaction, that decays with 6th power of

inter-pigment distance. In addition, FRET rate depends on the fluorescence/absorption overlap between emitter/acceptor chromophores, the fluorescence quantum yield of the emitter and their relative orientation.⁵¹ If two or more pigments are located below 1.5 nm as it occurs in photosynthetic complexes, excitations delocalize among the pigments, giving rise to an excitonic state that facilitates the energy transfer.⁵² EET is responsible for the efficient energy transfer within antenna subunits (~0.1-1 ps timescale), inter-subunits transfer (~10-100 ps timescale) and eventually to transfer to P700 in the RC.^{15,46,50} Bulk-antenna chlorophylls absorption is centred at 685 nm, while chlorophyll special pair absorbs at 700 nm, thus in the RC vicinity, energy is funnelled to P700. However, in the antenna pigments of plants and algae chlorophylls that absorb below 700 nm are found. These redshifted chlorophylls, named red forms, must transfer excitonic energy up-hill which increases the EET time.⁵³

The overall trapping time, that is, the time required to transfer excitation to P700 and for CS is ~20 ps for the bulk pigments in the RC, while it increases above 60 ps for large PSI-LHCI complexes.⁴⁶ As excitations must be trapped before they decay by fluorescence, the photoconversion efficiency or quantum yield of the light harvesting process is defined as $1 - \tau_{CS} / \tau_{Fluo}$. For PSI-LHCI units with a trapping time ~ 60 ps and fluorescence lifetime of 2 ns, the quantum yield is near unit, that is, practically all absorbed photons are transferred to the RC. The photo-conversion efficiency is preserved because the forward ET steps rates that follows CS outcompete the recombination rates.¹⁶ The photo-oxidized P700⁺ state, also known as closed state, efficiently quenches the excitations reaching the RC by a non-physiological process that doesn't lead to charge separation.⁵⁴ This implies that in spectroscopic experiments, the excitation rate must be lower than the rate of P700⁺ reduction to open state.

The above described EET processes in photosynthetic complexes are studied by means of pump-probe spectroscopy, that employs short (< 100 fs) laser pulses to excite (pump pulse) the chromophores in the complex. Following excitation, absorption or fluorescence spectra is recorded (probe pulse) after a precisely controlled time delay τ , ranging from 100's fs to ns timescale.⁴⁵ Upon excitation, differences in the absorption spectra with respect to non-previously irradiated samples exhibit wavelength-dependent dynamics. These differences in the spectra and their associated kinetics are due to: i) the depletion of the ground state by the pump pulse (photobleaching), ii) stimulated emission of the excited states, and iii) absorption of the excited states. In pump probe experiments, the CS is indirectly measured as a decrease in the absorption at ~700 nm associated to the chlorophyll special pair P700.

Alternatively, direct evidence of the population of CS states in the sample effectively leading to interprotein ET can be measured probing the concentration changes of PSI redox partners (natural or artificial) upon illumination. In an electrochemical set-up (see section 3.4), concentration changes of redox species give rise to a photo-electrochemical

currents associated to the population of $P700^+/F_b^-$ state. Photo-electrochemical current spectroscopy allows to determine whether absorption bands lead to charge separation. This is particularly useful to probe novel artificial photosynthetic complexes based on the self-assembly of molecular catalyst,⁵⁵ protein maquettes,^{56,57} addition of artificial dyes to light harvesting complexes,^{58,59} or the assembly chimeras formed by plant and bacterial light harvesting complexes⁶⁰ extending their absorption band. In the latter, the photocurrent action spectra were recorded to compute the external quantum efficiency (number of charges per incident photon).⁶⁰

3 Experimental methods

In the following sections, relevant features of two nanoprobe techniques, key for the experiments developed throughout this manuscript are presented, **electrochemical scanning tunnel microscopy and spectroscopy (EC-STM, EC-TS)**, employed in chapters 3,4, and **atomic force microscopy (AFM)**, in all experimental chapters and **single molecule force spectroscopy (AFM-SMFS)** used in chapter 5. We will also briefly introduce potentiostat assisted measurements, **cyclic voltammetry** (used in chapters 3,4,7) and **fast chrono-amperometry photocurrent measurements** employed in chapters 6 and 5. In addition, we will present the bioengineering techniques that we exploit to **immobilize PSI and Pc** in gold substrates allowing bulk, single protein and single protein pair experiments. Eventually, we will provide an introduction for non-expert readers to ease interpretation of two-dimensional electronic spectroscopy (2DES) maps issued from photo-electrochemical current **PEC2DES measurements** in chapter 6.

3.1 Introduction to nanoprobe techniques

Imaging nanometric objects like proteins with visible light is unfeasible due to the diffraction-limited resolution of visible light (400-700 nm). Photons with shorter wavelengths, used in X-ray diffraction of protein crystals, or electrons used in Cryo-electron microscopy,⁶¹ have revolutionized our understanding of protein structure, with over 200.000 (and counting) available structures in the protein data bank. Diffraction of protein crystals or electron density maps of nitrogen frozen protein samples provide a valuable snapshot of the protein architecture, however *in vitro* experiments measuring protein functionality (i.e. enzymatic activity, binding to other proteins or compounds, charge exchange) are not accessible with X-ray and are very limited in cryo-electron microscopy. Protein activity is characterized with bulk techniques as protein electrochemistry (see section 5.1.2), confocal fluorescence spectroscopy,⁶²⁻⁶⁴ Raman,^{65,66} FTIR⁶⁷ averaging protein behaviour over a large ensemble. Combining the

best of two worlds, nanoprobe techniques are able to measure protein functionality and interact with proteins at the single (or few) protein level.

Scanning probe techniques, invented by Binnig and Rohrer in 1981,⁶⁸ allow to image nanometric size objects overcoming the limitation of diffraction limit. They operate finely positioning a probe that measures a physical scalar magnitude. Scanning the probe over the raster area, the values measured by the probe at each pixel are translated into an image. This versatile concept is behind a family of experimental set-ups probing different magnitudes: electrochemical current (ECSM), voltage (SVM), near electromagnetic field (SNOM), tunnel current (STM) and force (AFM). Atomic force microscopy (AFM) based techniques are as diverse as the nature of the force to be probed: chemical force (CFM), electrostatic force (EFM), magnetic force (MFM), kelvin probe (KPGM). In addition to the enhanced resolution w.r.t. optical techniques, nano-probe techniques allow to perturb and interact with samples at the single molecule level. In particular, we exploit nano-positioning capabilities of nano-probe techniques to force the interaction of the PSI-Pc cognate pair controlling their relative orientation, distance and redox state. This will allow us to characterize the charge exchange and the binding of PSI-Pc at the single protein pair level.

3.2 Atomic force microscopy and spectroscopy

In atomic force microscopy, the probed magnitude is the force felt by a sharp tip located at the end of a flexible cantilever. In elastic regime, the cantilever deflection is proportional to the force exerted on the tip (Hooke's Law). Thus, knowing the cantilever spring constant, the force at the probe tip can be monitored tracking the position of a laser beam reflecting on the cantilever back surface. The beam deflection is monitored by photodiode array, that transduces, via a differential amplifier, the relative incident beam power into a voltage signal that is proportional to the force.⁶⁹

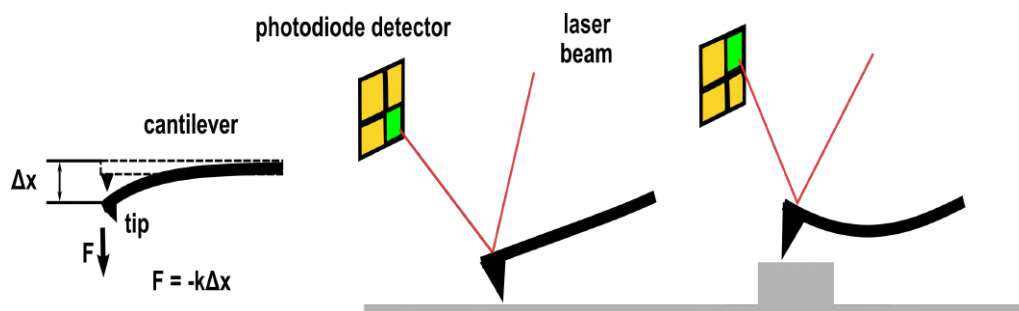


Figure 1.6: Scheme of AFM working principle. Force on the tip (F) deflects the flexible cantilever yielding a linear deformation (Δx). Cantilever deflection is tracked with a laser beam pointing at the cantilever back surface that reflects the incident beam to a photodiode detector. The cantilever deflection proportional to the force between the sample and the tip (due to irregularities in the sample morphology or tip substrate adhesion or repulsion events) is transduced in the photodiode detector.

As in other scanning probe techniques, the cantilever is controlled by a piezo-electric material allowing nanometric positioning of the probe. Via an electronic feedback-loop between the piezo signal controlling the z-axis position (perpendicular to sample plane) and the detected force, the latter is kept constant to a set value. This feedback control allows to safely scan produce a raster the sample scanning the cantilever in x-y directions to produce topographic images. Through this manuscript, AFM scans have been used to characterize the tethering of PSI complexes to gold electrodes (chapters 3,6 and 7). Imaging parameters and probes employed are specified in the supplementary information of the respective chapters.

In force spectroscopy mode, the forces exerted on the AFM tip are monitored as the cantilever is approached to the substrate up to reaching a set-force.^{69,70} After reaching this force, the probe is retracted, recording approach and retreat force vs. distance curves. In the absence of adhesion or indentation, approach and retreat curves exhibit a similar profile, with a negligible force prior to contact and a force proportional to distance upon contact due to elastic deformation of the cantilever (blue curve in figure 7). When probe and substrate are functionalized with complementary molecules, complex formation is evidenced by force spectroscopy retraction curves as the adhesive forces pulls the tip (stage 4 in figure 7). Complex unbinding (rupture) produces a sudden decrease of the adhesion force (stage 4 to 5 in figure 7).

To distinguish specific PSI/Pc binding from unspecific probe substrate binding events, Pc is grafted to the AFM tip via a flexible polymer linker (polyethylene glycol, $n = 27$ with a length ~ 8 nm). This allows to discard most of unspecific binding events. In addition, the linker confers further degrees of freedom with respect to direct functionalization of the probe, increasing binding probability.⁷⁰

The experimental observable of the PSI/Pc that we obtain from SMFS experiment is the binding probability, computed as the ratio of curves displaying specific binding events over the total number of curves. In curves displaying unbinding events, the unbinding force and the rupture distance are obtained.

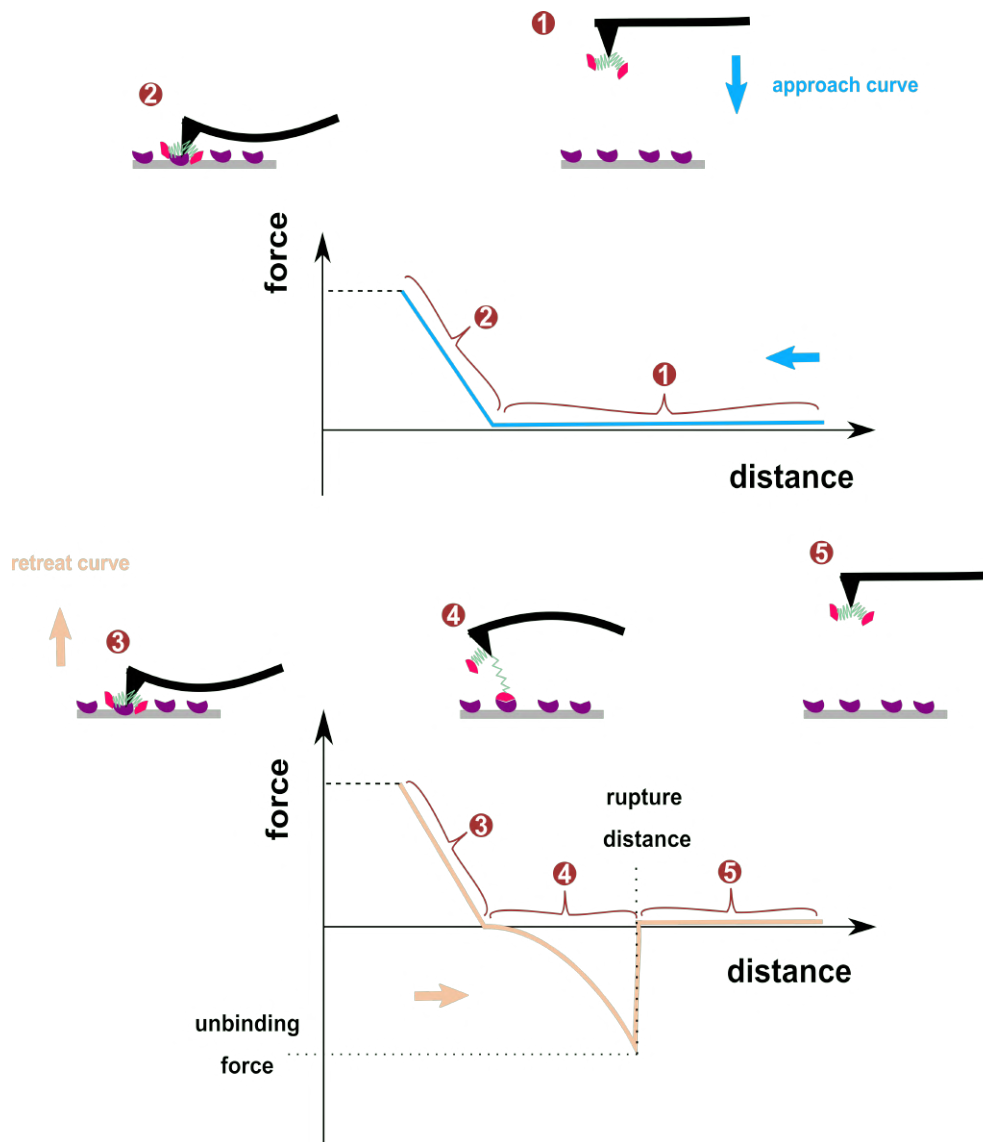


Figure 1.7: Diagram representing the SMFS experiment. In the approach curve (blue) no force is detected (1) until the probe reaches the rigid substrate resulting in a linear deflection of the cantilever (2) up to the set-point force. If there is no adhesion between the probe and the substrate a similar force-distance trace is expected for the retreat curve. If an adhesion event takes place, a negative force due to probe pulling is observed. An abrupt jump in the force back to zero is observed upon rupture. Specific binding events are expected at rupture distances around the linker molecule length.

3.3 Scanning Tunnelling Microscopy

In STM, the probed physical magnitude is the electric current resulting from the flow of tunnelling electrons between an electrode pair separated a few nm. The tunnel effect is a quantum process in which electrons, due to their wave-like nature, can overcome a potential barrier “passing through” it, that is, tunnelling through it. Tunnelling probability depends on the overlap of the initial and the final state electron wavefunctions with the potential barrier. This means that the typical length of this process is intimately related to the spatial span of the electron wavefunction along the electrode pair gap. In the initial and final states, the electron occupies the highest energy states of the band structure of the electrodes (Fermi level). With respect to the potential barrier, it is set by the vacuum, electrolyte, organic molecule or, in our case, protein filling the gap between the electrodes.⁷¹

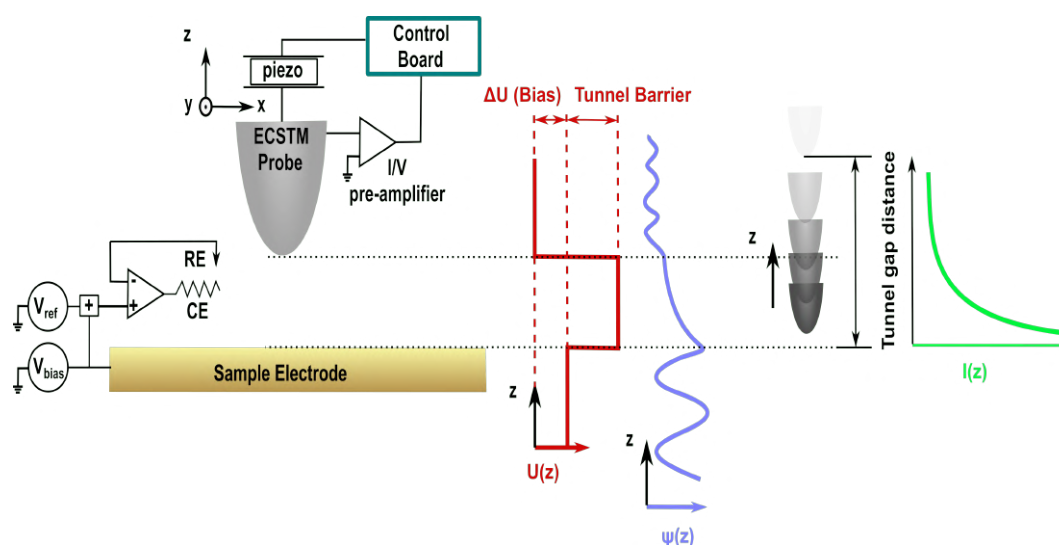


Figure 1.8: Scheme depicting the working principle of ECSTM. The sample electrode is held at U_{Sample} potential with respect to the reference electrode (RE) by the potentiostat control loop. To this potential, an additional potential U_{Bias} with respect to the probe electrode (set to ground) is added. The probe electrode current is transduced to a voltage signal by a pre-amplifier placed in proximity of the probe to minimize noise. Transduced signal is sent to the control board where a proportional-differential-integrative control system regulates the probe position. This feedback system controls position sending a high voltage signal to the piezo-electric tube in the microscope scanner that moves the probe with sub-nanometric precision. In the left side, the fermi energy of the probe and sample electrodes and their difference (U_{Bias}) is depicted in red. In purple, a simplified model for the electron wave function associated to the red potential is depicted (see theory section 4.2.2 for more details). The resulting current (green trace), decays exponentially as the amplitude of the electron wave function decays.

The energy difference between electrodes, U_{Bias} , drives the tunnel current. If the electrodes were isoenergetic, electrons would tunnel through the potential barrier,

however the tunnelling probability would be symmetric resulting in a null current. The bias potential is defined as $U_{Bias} = U_{Probe} - U_{Sample}$ and its sign sets the electron flow direction and thus the current sign. For instance, for $U_{Probe} > U_{Sample}$ electrons flow from the sample to the probe electrode and the resulting tunnelling current is negative. To describe tunnel current, a first approximation is to model the potential barrier between sample and probe electrodes as a square potential. Solving Schrödinger equation for this potential (red curve in figure 8), results in exponentially decaying wavefunction in the gap (purple curve in figure 8). Accordingly, the tunnel current decays exponentially with the gap distance $I \propto e^{-\beta z}$ (green curve in figure 8) with a decaying constant β with inverse length units, usually expressed in \AA^{-1} or nm^{-1} . ECSTM current modelling is further discussed in the theory section. From an experimental point of view, we must keep in mind two concepts: current decays exponentially with distance and the distance decay constant β is related to the potential barrier between the electrodes.

A partial-derivative-integrative feedback loop controls the piezo-electric transducer signal setting z axis position (perpendicular to the electrode plane) at a distance such that the current equals a set-point value (figure 9). As x,y axis position is scanned, the control signal that is sent to the z-piezo to keep the tunnel current constant is mapped into an color-scale image. The apparent height represents a convolution of the sample topography and its conductivity (figure 9). In addition, the resolution of the resulting scan depends also on the probe geometry that convolutes the apparent height features with its shape (see figure 9). To achieve reproducible sharp probes and enhance resolution, an electrochemical etching probe preparation procedure was developed in the group.⁷² Sample electrode roughness is also critical, therefore mono-crystal electrodes in which the bulk material preserves the crystallographic unit cell orientation are employed. Throughout the manuscript, all STM experiments have been performed with gold monocrystals with [111] orientation (Au[111]).

To mimic physiological conditions, proteins are immersed in an electrolytic buffer solution. Applying voltages to electrodes inside an electrolyte solution give rise to electrochemical (faradaic) currents that mask the tunnel current. In addition, current flow through the sample electrode might alter its surface potential, losing control on the effective bias potential. Therefore, to work in aqueous solution, the STM set up needs to incorporate a bi-potentiostat that fixes probe and sample potential. In electrochemical STM (ECTSM), the potential is controlled with respect to the reference electrode (the working principles of potentiostat are provided in section 3.4). The reference electrode allows to set a common ground for electrons energy in the electrodes and their electrochemical potential, making a bridge between solid state electrode Fermi energy and molecular orbitals redox potential. In addition to the reference electrode, ECSTM electrochemical cell counts with a counter or auxiliary electrode to allow the current flow through the sample electrode without altering reference electrode potential. As

potential is applied, faradaic currents appear on the sample electrode due to the charge flow between sample and counter electrode. If faradaic currents flow through the probe electrode, they mask tunnel currents which are several orders of magnitude smaller. To prevent (or at least minimize) faradaic currents, probes are coated with an insulating material: electrophoretic paint,⁷² cataphoretic paint,⁷³ epoxy,⁷⁴ nail varnish,⁷⁵ or the thermo-retractile apiezon wax.⁷⁶ Probe coating defects result in faradaic or leakage currents. Large leakage currents make ECSTM experiments unviable, in which case, the probe is discarded. However, small defects might lead to leakage currents that are in the same order of magnitude of tunnelling currents resulting in a possible source of artifacts.

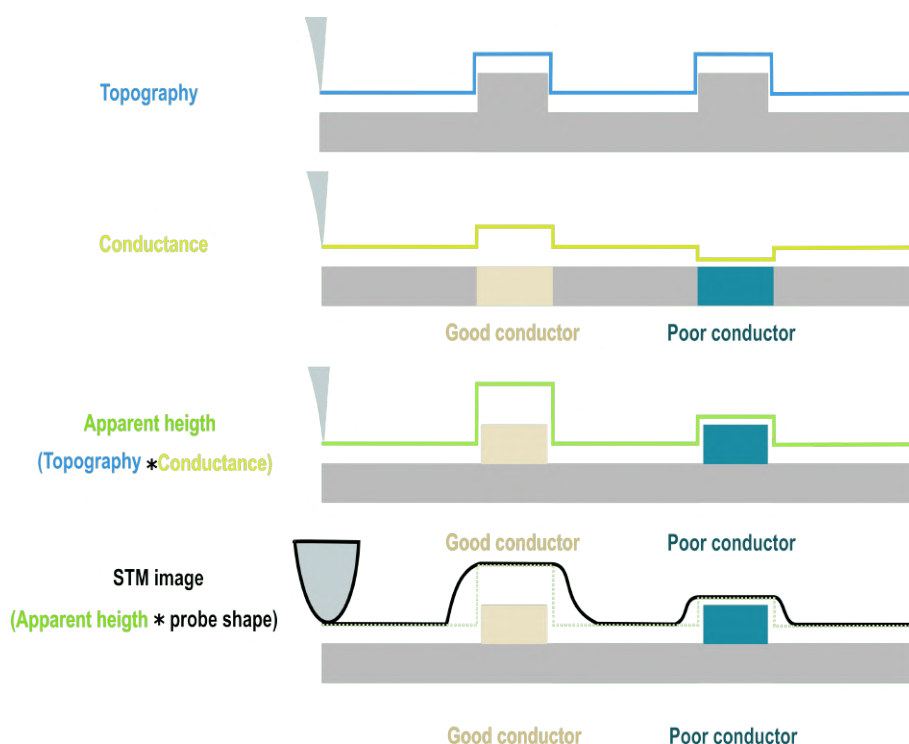


Figure 1.9: Scheme of STM imaging mode. The feedback mechanism control the piezo-electric transducer voltage to set probe position at a tunnelling distance yielding the set-point current. Irregularities in the sample morphology are translated into the piezo-electric signal to keep current at the set-point level. For instance, a bump in the electrode surface leads to probe retraction. For an ideal flat sample with inhomogeneous conductivity regions, the probe is approached in a decreased conductivity region and retracted in an enhanced conductivity region. The apparent height is thus a convolution of the sample morphology and conductivity. In addition, the sample apparent height is convoluted by the probe shape.

ECSTM allows scanning single proteins absorbed on planar electrodes in buffer solution (see section 5.2, literature experimental results). Reported lateral sizes of Az,⁷⁷ Pc,⁷⁸ ferredoxine,⁷⁹ to cite some, are in agreement with the size predicted by crystallographic structures.⁸⁰ ECSTM measured apparent heights are, however, about tenfold lower than

the crystallographic size, due to the smaller conductance (with respect to electrode) of the proteins.⁸⁰ Interestingly, the apparent height of such redox proteins is modulated by the electrode potential as a result of protein conductance gating.^{77,81} ECSTM scans of redox proteins reveal an enhanced apparent height as the electrode Fermi energy aligns with the potential of the redox centres in the protein (see sections 4.2.7 and 5.2.2). To ease protein size characterization and thus increase the number of analysed complexes (up to $N \sim 300$), we automated a 2D-fit routine (described in the supplementary information in chapter 3) that we apply to the ECSTM apparent height maps.

The tunnel current can also be exploited in spectroscopic mode. In absence of feedback control, the applied voltage (current-voltage spectroscopy) or the distance (current-distance spectroscopy) between the electrodes is ramped to record characteristic $I(v)$ or $I(z)$ curves, respectively.⁸² Also lacking feedback control, time traces of tunnel current between the electrodes can be recorded. If the electrodes are functionalized with molecules, they might form transitory junctions giving rise to conductance bursts and/or jumps, giving rise to telegraphic noise features (“blinking” mode).⁸³ A variation of these methods, somehow combining both techniques, is the “break-junction” method,⁸⁴ in which the probe is brought to contact with the sample electrode and then retracted. As it is retracted, the adsorption of molecules between the two electrodes (the tunnelling junction) is favoured resulting in current *plateaux* revealing the conductance of a protein junction. In this work, we have not employed break-junction methodology for PSI-Pc experiments to avoid damaging the probe functionalized with Pc. In the following sections we discuss technical aspects of the ECSTM based techniques that we have employed with PSI and PSI-Pc systems, namely current-distance spectroscopy and blinking.

STM Current-distance spectroscopy

A schematic representation of an $I(z)$ curve is shown in figure 10. Departing from the set-point current, the ECSTM probe is retracted in the direction perpendicular to the electrode plane. The $I(z)$ curves show a two-range exponential decay, with lower β values (β_1) at close probe-sample distance and a long-distance regime with higher β values (β_2). This two-regime decay has been reported in electrodes functionalized with protein⁸⁵ and DNA⁸⁶ and was identified with double layer charge screening regions in experiments with different salt concentrations.⁸⁷ It has been suggested that the lower β values found at short range are due to the lowering of the effective tunnel barrier height by the double layer.⁸⁸ To avoid this potential artifact and to avoid protein squeezing,⁸⁰ in the experiments reported in chapters 3-4, we work at a low set-point current (300 pA for $U_{\text{Bias}} = 100$ mV, that is a set-point conductance of $0.3 G\omega$) and thus minimize double layer effects.

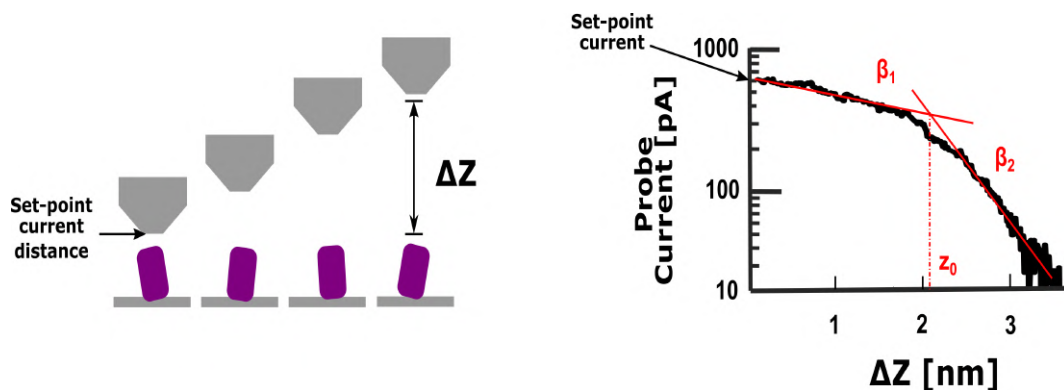


Figure 1.10: Scheme depicting current-distance spectroscopy. The STM probe is retracted from the set-point current distance for a defined distance in the direction perpendicular to the electrode plane (Z) in absence of positioning feedback control. After that, the probe is approached back to the sample electrode the same distance and the feedback control is re-established. In this manuscript we focus only on retraction curves. Current-distance curves follow a two-regime exponential decay. The first regime, spanning from the set-point current to the regime change cross-point (z_0), is fit with an exponential function with a decay constant β_1 . This regime is associated to the electric double layer formed in the vicinity of the sample electrode. The second regime, fit with an exponential decay constant β_2 extends until the tunnel signal is masked by faradaic current due to probe insulation defects.

Leakages currents have to be minimized to avoid affecting the measured β values. In our experiments, leakage currents is always monitored and probes with leakages above a threshold set at ~ 8 pA are discarded. To estimate leakage currents, we measure the offset current of the probe in a distant location from the sample electrode ($z > 1 \mu\text{m}$) and subtract the background noise and electronic noise at the experimental conditions. To do so, the current offset of a thoroughly insulated probe is used to define the noise level. The cyclic voltammogram of such probe is completely flat, in contrast to a poorly insulated probe that exhibits capacitive load currents as the voltage is swept (figure 11). Interestingly, poorly insulated Au probes coated with Pc proteins exhibit a cyclic voltammogram similar to bulk measurements in Au electrodes functionalized with Pc. While these defective probes are not suitable for imaging or spectroscopic experiments, they validate Pc functionalization protocol on Au probes (see section 3.6. for more details).

To define the leakage threshold level in 8 pA, we have represented $1/\beta$ vs the leakage currents of $I(z)$ curves recorded with $N=30$ different probes. For leakage values below ~ 8 pA, the typical charge exchange distance $1/\beta$ is not related to the leakage values (Pearson correlation coefficient $r = 0.15$). However, for probes with coating defects yielding leakage current > 8 pA, $1/\beta$ and leakage current are correlated (Pearson correlation coefficient $r = 0.91$). I consider the 8 pA criteria for discarding probes to be sufficient to avoid experimental artifacts.

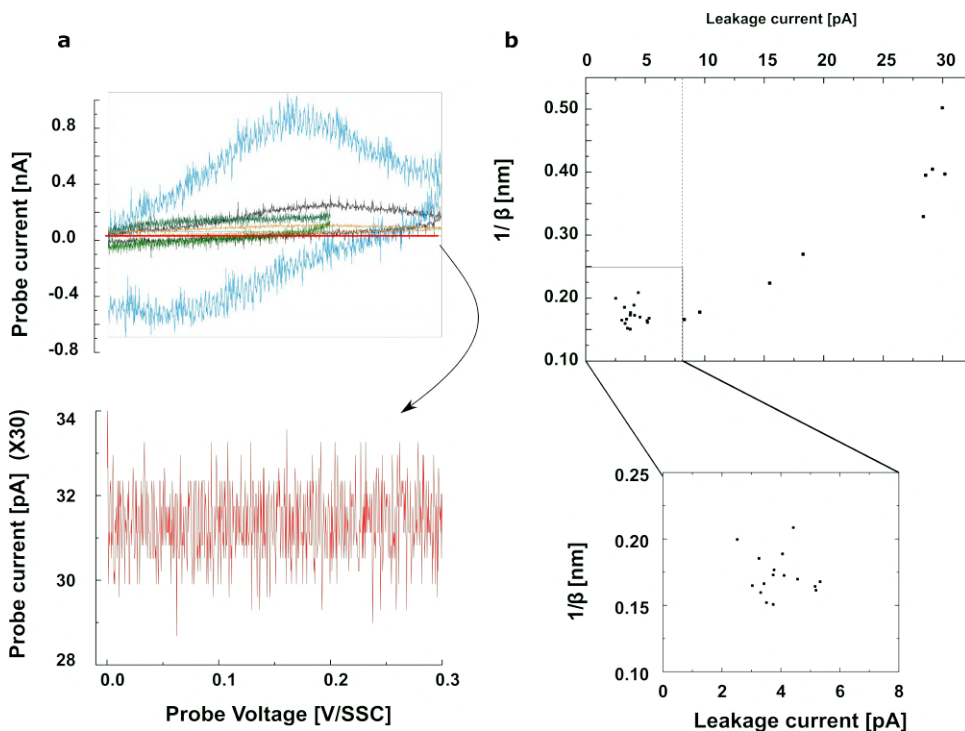


Figure 1.11: (a) Cyclic voltammetry performed with different probes immersed in the ECSTM electrochemical cell with working buffer (PBS 50 mM pH 7.4). The blue trace is recorded with a probe functionalized Pc-SH mutants displaying oxidation/reduction peaks. The leak-current of this probe prevents its use for tunnel spectroscopy measurements. The current of the different traces (black, green, yellow and red) are associated with the quality of the probe insulation. The inset shows a flat cyclic voltammogram of a perfectly insulated probe (red trace). (b) Leakage/ β correlation is obtained plotting the average β value for a set of 1000 $I(z)$ curves recorded for $N=30$ probes with different insulation and thus leakage current level. Below 8 pA no correlation is observed between the leakage current and the current decay constant β

To analyse large datasets ($N \sim 10^4$), an automated double exponential fit routine for $I(z)$ curves has been implemented (see supplementary information in chapter 3). In chapters 2-3, we report β value for the distant regime, however the close-distance regime and the cross-point between regimes is also provided in their respective supplementary information sections.

In the experiments presented in this manuscript, we have characterized the tunnel decay constant β of the charge exchange process mediated by the proteins bound to the sample, probe or both electrodes. I note that, despite being closely related and noted with the same symbol (β), the tunnel current decay constant determined experimentally is not equivalent to the distance decay constant that is present in protein electron transfer formalism (see section 4.2) related to the electronic coupling between donor and acceptor molecular orbitals of the proteins.

STM Blinking experiments

In blinking experiments, the evolution of the tunnel current between the probe and sample electrodes is recorded as the probe is freed from positioning control. Probe drifts due to mechanical instabilities (see below) and thermal drifts produce shifts in the electrodes gap. The range of these fluctuations is delimited by the physical contact of the electrodes (or the saturation of the tunnel current pre-amplifier) and on the other extreme by the detection limit of the tunnel current due to the pre-amplifier noise and the leakage currents. If the probe is properly fixed to the instrument head, and the ambient vibrations are damped, the probe can remain within the tunnelling range from a fraction of a second up to several minutes. For instance, in the blinking experiments of PSI-Pc samples shown in chapter 4, the current was recorded for 3 s with a time step of 10 μ s. If the gap between probe and sample is transiently occupied by a molecule, the conductance of the gap will be modified resulting in a sudden increase of the current (see figure 12). The random and transient nature of the junction result in a telegraphic noise like signal that switches between two or more levels. Telegraphic noise signals are also observed in the conductance of ionic channels,⁸⁹ or in transistors where defects produce local states where charges are trapped.⁹⁰ Mathematically, these systems are described as a Markovian process because the probability of remaining in a state is independent of the previous state. This implies that the probability of finding the system in a given state, in this case the high conductance state that we associate with the formation of the PSI/Pc complex, decays exponentially with the blink duration. The typical blink duration provides information about the PSI/Pc binding kinetics.



Figure 1.12: Scheme of the blinking experiment. In spontaneous formation of protein tunnelling junctions, the protein functionalized in the probe, sample or both electrodes contacts the two electrodes simultaneously. This results in a sudden increase of the current, which for a fixed bias voltage, is proportional to the conductivity. The current results in a telegraphic noise like signal, with current “blinks” associated to the junction formation. In this experiment two magnitudes are measured, the amplitude of the blink and its duration.

As the probe positioning feed-back control is not operating in the blinking experiment, the set-up is extremely sensitive to mechanical and acoustic perturbations. To minimize such effects, we designed and built an anti-vibratory system (Figure 14) composed by a heavy mass (~ 950 kg) that is hanged by three low elastic constant springs (~ 1.7 kN \cdot m $^{-1}$).

The resulting mechanical system has a resonance frequency of ~ 0.3 Hz (blue trace in figure 13) and efficiently damps the laboratory resonant frequencies (black trace) of 11 Hz and 110 Hz by two orders of magnitude. In addition, the electrochemical cell is placed in an air-tight container inside a thick rubber enclosure to minimize acoustic noise.

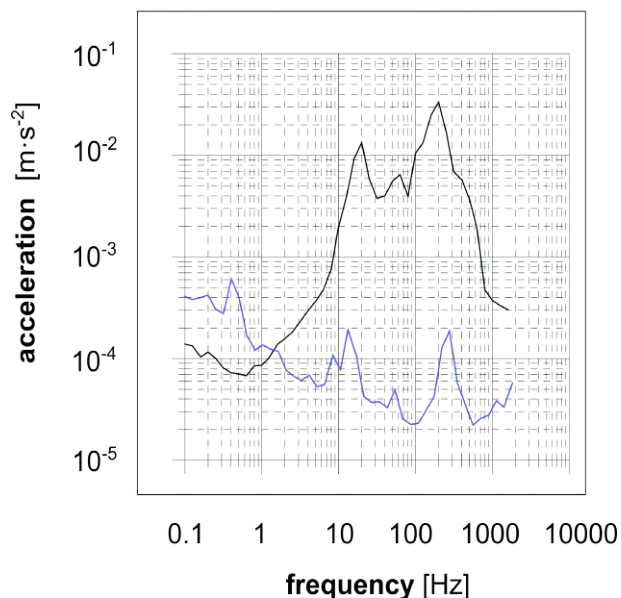


Figure 1.13: Vibration analysis comparing the building floor (black trace) with the passive mechanical anti-vibratory system (blue trace). Measurements were carried out by the applied geophysics service of Universitat Politècnica de Catalunya.

Additional details of ECSTM experiments

The experimental ECSTM set-up employed in chapters 3-4 is constituted by a PicoStat ECSTM head and a bi-potentiostat (Molecular Imaging), controlled by a Dulcinea electronic board (Nanotec). Tunnel current pre-amplifier located in close proximity of the probe holder in the piezo-electric head is set to an amplification of $10 \text{ V}\cdot\text{nA}^{-1}$ for current decay spectroscopy and $1 \text{ V}\cdot\text{nA}^{-1}$ for imaging and blinking experiments. The instrument interface is supported by WSxM software.⁹¹ In addition to WSxM, the tunnel current is monitored with a TI board, and a custom LabVIEW software used to record blinking events.

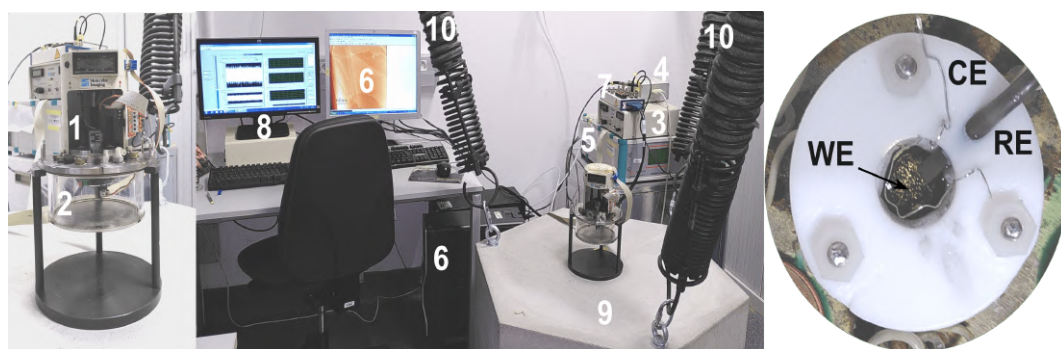


Figure 1.14: Molecular Imaging head holding ECSTM scanner (Agilent Technologies) with a pre-amplifier of $10 \text{ V}\cdot\text{nA}^{-1}$, (2) air-tight container for electrochemical cell, (3) Picostat bi-potentiostat (Molecular Imaging), (4) electronic board/potentiostat interface (Nanotec), (5) Dulcinea control unit electronics board (Nanotec), (6) PC with integrated electronic board for Dulcinea electronics commanded by WsXM software (Nanotec), (7) acquisition card for external current monitoring, (8) LabVIEW program current monitoring and blinking data recordings, (9) mass and (10) springs for the passive anti-vibratory system, (11) rubber enclosure for acoustic vibrations damping. Inset: Electrochemical cell with sample electrode (SE) Au[111] monocrystal, counter electrode (CE) Pt wire and reference electrode (RE) silver/silver chloride (SSC) miniaturized low-leakage reference electrode (World Precision Instruments).

3.4 Electrochemical Measurements

A potentiostat is an electronic device that allows setting the electrochemical potential of an electrode immersed in an electrolyte solution with respect to a reference electrode. By applying the set potential, current flows through the electrode is established. The potentiostat allows to measure this current flow as a fixed potential is applied (Chronoamperometry) or as the applied potential is swept (linear and cyclic voltammetry).⁹² All electrochemical measurements shown in this manuscript have been performed with an Autolab PGSTAT302N potentiostat (Metrohm).

The applied potential brings the electrode/electrolyte interface out of equilibrium allowing to catalyze redox reactions with molecules present in the electrolyte or tethered to the electrode. The resulting currents are directly related to the ET process with the electrode. In addition, capacitive currents due to the formation of the double-layer in the interface, the diffusion process in the case of dissolved molecules and the absorption of ions in the electrode, also contribute to the measured current. For the currents associated with ET processes, positive currents are due to an electron flow from the electrode to the species in the electrolyte, while negative currents arise when electrons are injected into the electrode.

In our work, bulk electrochemical measurements are performed in a three-electrode electrochemical cell adapted to the ECSTM. This configuration allows to directly transfer samples evaluated by bulk electrochemistry to the ECSTM set-up. For example, in

chapter 3, PSI activity was verified evaluating the bulk photo-current output of the PSI complexes bound to the Au[111] electrode, afterwards, the same PSI-Au sample electrode was characterized in ECSTM. The electrochemical set-up is composed by:

- i) Working or sample electrode. The potentiostat controls the electrochemical potential at this electrode, which is functionalized with protein samples, PSI or Pc (see protein immobilization, section 3.6). All electrochemical measurements in this manuscript are performed on Au[111] electrodes unless otherwise stated. The electrode active area is delimited by an o-ring exposing a surface of 0.12 cm^2 .
- ii) Reference electrode is a silver wire coated with a silver chloride layer immersed in KCl solution 1 M, separated from the electrolyte solution by a low-leakage frit. A very high input impedance in the potentiostat prevent current flow through the reference electrode making the electrochemical potential at the reference electrode constant (+235 mV w.r.t standard hydrogen electrode). We make use of a miniaturized ultra-low leakage electrode (world precision instruments) adapted to the geometry of the STM set-up.
- iii) Counter or auxiliary electrode, a Pt-Ir coil that “closes” the electrochemical “circuit” allowing the current flow. For instance, if oxidation is taking place at the working electrode, reduction takes place at the counter electrode satisfying the charge balance. In the counter electrode, a potential is applied such that the potential drop between the working electrode and the reference electrode matches the set potential.

The three-electrode system is contained in a teflon (polytetrafluoroethylene) vessel of 200 μl volume that is cleaned in piranha solution ($\sim 30/70 \%$ vol $\text{H}_2\text{O}_2/\text{H}_2\text{SO}_4$) before each use (caution! piranha solution must be handle with care).

In chapters 6 and 7, disposable screen-printed electrodes (Autr10 - Metrohm/Dropsens) are employed. The working electrode is made of a thin ($< 100 \text{ nm}$) gold sputtered layer, making it transparent to visible light. The counter (carbon) and pseudo-reference (silver) electrodes are integrated in the same chip. This configuration is highly versatile, facilitating the integration of the electrochemical set-up into the 2-dimensional electronic spectroscopy set-up. Electrode transparency allows irradiation of the samples from the bottom, that is, light hits PSI samples before passing through the electrolyte making the readout less sensitive to electrolyte absorption. In addition, their disposable nature facilitates sample preparation and enhances reproducibility. I have designed a custom electrochemical cell and a cell-holder for screen-printed electrodes to facilitate the combination of spectroscopic and electrochemical set-ups (chapter 6). In the following sections, I describe the electrochemical techniques used in this manuscript to study the electrochemical response and the photocatalytic activity of Pc and PSI.

Cyclic Voltammetry

In cyclic voltammetry, the sample potential is swept between two values (vertex potentials) for several cycles. Current flowing through the electrode is recorded and plotted versus the applied potential, resulting in a cyclic voltammogram (see figure 15). Characteristic peaks in the current are associated with redox reactions, which ET kinetics depend on the electrode potential. Reduction of the solvent or absorbed molecules is associated with positive current peaks. As the electrode supplies electrons for the reduction reaction (that is, it works as a cathode) the electron flow is negative, and thus the current is positive. Complementarily, oxidation of the solvent or absorbed species yields a negative current peak. The mid-point between reduction and oxidation peaks represents the formal potential of the interrogated redox species. At this potential the reduction and oxidation reactions take place at an equal rate. An example of cyclic voltammetry adapted from results in chapter 7 is shown in Figure 15.

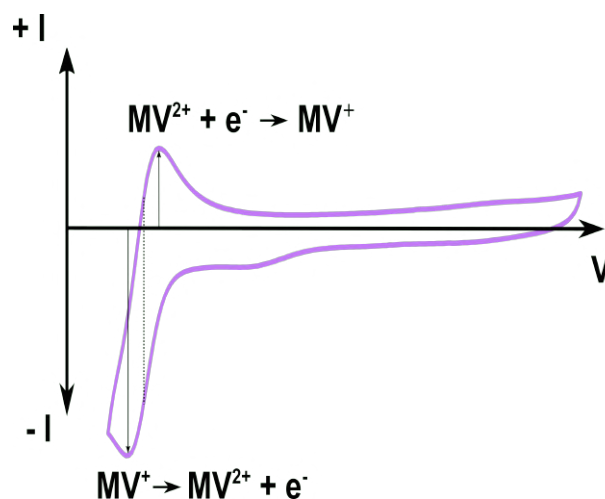


Figure 1.15: Typical CV exhibiting oxidation/reduction peaks. For this example, the redox mediator methyl viologen (MV^{+}/MV^{2+}) is employed (125 mM) in N_2 purged PBS buffer (pH 7.4 50 mM) to eliminate dissolved O_2 . Redox mediator reduction $MV^{2+} + e^{-} \rightarrow MV^{+}$ yields a positive peak. Negative peak is associated with redox mediator oxidation $MV^{+} \rightarrow MV^{2+} + e^{-}$. The redox mid-point is indicated with a dashed line between the redox peaks marked with black arrows.

Fast photo-chronoamperometry

In chrono-amperometric measurements, the current flow through the sample electrode is recorded at a constant working electrode potential. Following the application of the potential, a current transient is observed while the ions forming the double layer and the redox reactions with the electrode reach a new stationary state imposed by the set potential. After this transitory regime, the current is constant.⁹² We make use of chrono-amperometry to study the photo-catalytic activity of PSI complexes bound to

gold electrodes. Upon irradiation, PSI complexes are brought to a long-lived charge separated state with $P700^+$ oxidized and F_B^- reduced. Charge exchange with these PSI redox cofactors results in a photo-electrochemical current or simply photocurrent. An example of such recorded photocurrent is shown in Figure 16. Photocurrent is due to the PSI photo-catalytic activity, because the photocurrent action spectrum is proportional to the PSI absorption spectrum as we demonstrate in chapters 6 and 7 (we refer to these chapters for further details).

The photocurrent response of the PSI bound electrode depends on: i) The amount of PSI complexes in the sample, conditioned by the method used to bind to the electrode. An estimation of the number of PSI complexes on the electrode based on AFM characterization is provided in chapter 6. ii) The light power supplied to the sample, that is, the rate of photons striking PSI complexes. iii) The reactivity and concentration redox mediators used to scavenge charges from PSI redox cofactors. Redox mediators are compounds with electrochemical activity that are dissolved in the electrolyte solution and can mediate the charge exchange between PSI redox cofactors and the electrode, undergoing reversible redox reactions. Redox mediators are further discussed in section 3.4.3.

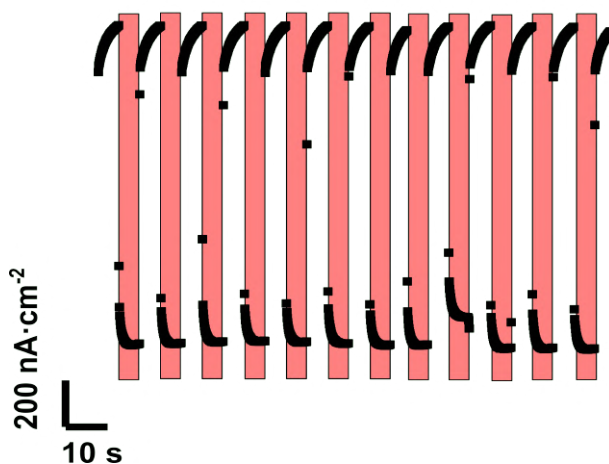


Figure 1.16: Photo-current response of PSI samples bound to Au electrodes. Typical photo-chrono amperometry recorded at -100 mV/SSC. Keeping the sample electrode voltage constant, the electrode is irradiated with 690 nm light (see sample irradiation section 3.7 for details) in 4 s on/off cycles (red/white shaded area).

Photocurrent measurements optimization for photo-electrochemical current two-dimensional spectroscopy (PEC2DES) have been technically challenging as they require a fast electrochemical response ($< \text{ms}$) and thus a high sampling rate (~ 100 kHz), and at the same time sufficient signal-to-noise ratio allowing to detect second

order (non-linear) features of the signal. However, the sensitivity and the bandwidth of a potentiostat are related. To optimize the bottlenecks and trade-offs of the technique we must understand potentiostat operation requirements:

- i) Current must not flow through the reference electrode. This is achieved by a voltage follower circuit based on high input impedance operational amplifier. This allows to read the reference electrode potential with a negligible current flow through it.
- ii) The potentiostat must furnish a potential to the counter electrode such that the potential drop between the working and reference electrodes equals the set potential. This is achieved by the control amplifier that has as inputs the output of the voltage follower and the set potential. The output of the control amplifier drives the voltage at the counter electrode. The control amplifier has a bandwidth of 100 kHz, that is, the minimal time step that can be recorded in these electrochemical experiments is 10 μ s.
- iii) The output current must be converted into a voltage signal in a current follower circuit. The current/voltage conversion follows the Ohm law $V=RI$. For example, to keep the signal in the voltage range, a resistor of $10^9 \Omega$ is used for following currents in the nA range. However, the bandwidth of the current follower decreases with the sensing resistance (R_{range} in Figure 17). For instance, the bandwidth of the PGSTAT302N for a current range of 1 μ A (the appropriate current range for the typical current that we obtain) is 10 kHz. To equal the controller amplifier bandwidth of 100 kHz, we should work in the 10 μ A current range, however this diminishes a tenfold the voltage output of the current follower impoverishing the signal to noise ratio. If the current was smaller than the μ A range, measurements in kHz repetition rate would not be possible.

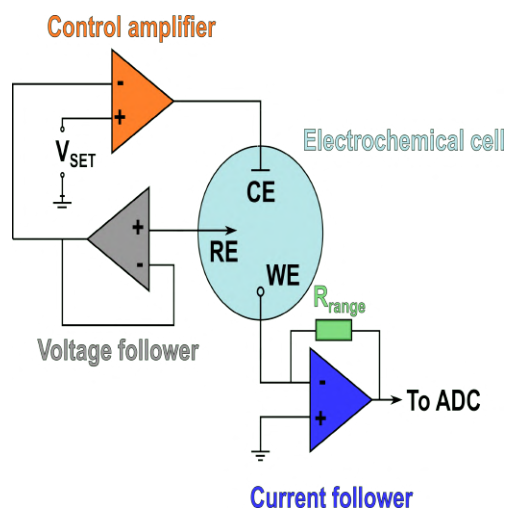


Figure 1.17: Potentiostat basic scheme. The electrochemical cell, represented in light blue, is formed by the counter electrode (CE), reference electrode (RE) and sample or working electrode (WE). The output current is converted to voltage signal by the voltage follower circuit (blue). The current range and associated bandwidth is set by the R_{range} resistor (green). The voltage in the reference electrode is read by the voltage follower amplifier (gray). This counts with a very high input impedance to prevent the current flow through the reference electrode. The control amplifier (orange) sets a driving voltage to the counter electrode such that the voltage drop between the reference and working electrode equals the set potential. For relatively high current ranges ($> 10 \mu\text{A}$) the instrument bandwidth is limited by the control amplifier system.

Redox mediators

In experiments with PSI functionalized electrodes, in order to generate current, the photo-generated charges must be transferred to the electrodes. It has been proposed that for PSI complexes bound to the electrode, nearby cofactors can directly transfer charge to the electrode.⁹³ Different PSI functionalization methods place P700 or F_B redox centres in the vicinity of the electrode surface. Soluble redox mediators indirectly transfer the photo-generated charges to the electrode increasing the photocurrent. First of all, unless the electrolyte solution is purged, dissolved O_2 is present in the electrolyte. Though O_2 is not a reversible redox mediator, it can uptake high-energy electrons from reduced F_B^- cluster forming reactive oxygen species (ROS).^{94,95} In absence of additional redox mediators, PSI samples in aerobic conditions exhibit low photocurrents ($\sim 10 \text{ nA}\cdot\text{cm}^{-2}$, see supplementary information in chapter 3). Addition of redox mediators increases in two orders of magnitude the photocurrent output (see figure 16 and figure 1 in chapter 6).

Two redox mediators have been employed throughout this manuscript, methyl viologen (MV), employed chapters 3, 6 and 7, and osmium bipyridine dichloride (osbipy), employed in chapters 6 and 6. MV is *N,N*-dimethyl-4,4-bipyridinium dichloride, an organic heterocyclic molecule of formula $[(\text{C}_6\text{H}_7\text{N})_2]\text{Cl}_2$. It is known as paraquat for

its use as herbicide, inhibiting the photosynthetic electron transport chain.⁹⁶ Paraquat accepts highly reducing electrons from F_B^- , transferring charge to O_2 ⁹⁷ and enhancing the formation of hazardous ROS species. In an electrochemical cell under anaerobic conditions, MV^+ can be re-oxidized by the electrode when a sufficiently negative potential (~ 900 mV/SSC) is applied. The redox reactions and the associated kinetics underlying photocurrent signal in a system formed by PSI and MV in absence of O_2 are discussed in chapter 7.

Reduction of photo-oxidized $P700^+$ is facilitated by Osbipy, as $P700^+$ redox potential is slightly below that of Osbipy.⁹⁸ While the use of Osbipy as a soluble redox mediator for PSI photocurrent enhancement has been reported only once⁹⁹ to our knowledge, the use of Osbipy crosslinked to redox polymers is extensive.^{95,98,100–102}

As it will be discussed in more detail in chapter 7, the electrode potential defines the ET rate of the electrochemical reactions in the electrode interface. These rates are directly responsible for the current. In addition, an electrochemical depletion of the redox mediators decreases the photocurrent as there are no reduced/oxidized species ready to donate/accept electrons to PSI redox cofactors. In Figure 18, we show how the photocurrent (red shaded bars) is modulated by the sample electrode potential. As well, extreme electrode potentials might compromise the stability of PSI complexes and/or PSI binding layer. To this end, the sample stability and photocurrent output has been evaluated to define a “safe” electrochemical window in chapter 3.

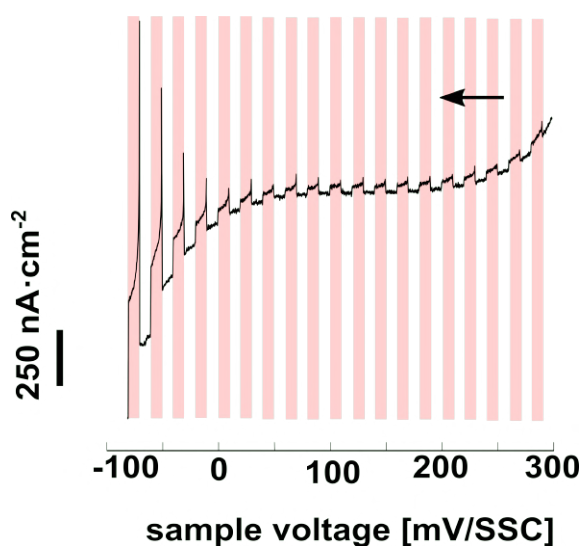


Figure 1.18: Example of chopped-light linear voltammetry. The voltage of the PSI-functionalized Au electrode is swept (from positive to negative potentials as it is indicated with the black arrow) while the sample is irradiated intermittently (red shaded areas). The magnitude of the photocurrent depends on the sample electrode potential (see chapter 7).

3.5 Introduction to 2d-electron spectroscopy

The development of the PEC2DES technique was carried out under the frame of a collaboration with the Molecular Nanophotonics group at ICFO (*Instituto de Ciencias Fotónicas*) and the Multidimensional and Ultrafast Spectroscopy group in the chemistry department of Padova University. Our contribution to the collaboration is based on the photo electrochemical current sensing and the preparation of oriented PSI-LHCI films on transparent gold electrodes. Thus, basic concepts of non-linear spectroscopy¹⁰³ are presented here to help non-expert readers to better follow the PEC2DES results presented in chapter5, however a deeper description of the method^{104,105} and the underlying¹⁰⁶ are out of the scope of this dissertation.

The goal of electronic spectroscopy in this work is to measure the response of a multi-chromophore system that has been brought to an excited state. The excitation dynamics of the system is probed modifying the time delay (t_2 in figure 19a) between excitation and detection pulses. This goal is also achieved by pump-probe spectroscopy, however pump-probe spectroscopy time resolution is limited because the time span of the carrier envelope and the frequency of the pulse band are inversely proportional, resulting in a frequency/time resolution trade-off.¹⁰³ This drawback is circumvented using a Fourier transform methodology,¹⁰⁷ in which the excitation pulse is split in two pulses delayed by the inverse of the desired excitation frequency $t_1=2/\omega_1$ (figure 19a). Measuring the response of the system for a grid of excitation-detection pairs yields excitation/detection (2DES) maps (figure 19b). As we interpret 2DES maps we might have in mind that along the diagonal the excitation and detection frequencies are equal, while signal features off-diagonal indicate excitation energy transfer (figure 19b). To study the excitation dynamics, several 2DES maps are recorded increasing the delay t_2 between excitation and detection (figure 19c). Global analysis of 2DES along t_2 fits the signal evolution for all ω_1 , and ω_2 simultaneously.¹⁰⁸ A global analysis retrieves the main kinetics components of the signal, which can be real and associated to the signal decay or complex and are thus associated to signal oscillations (figure 19d). These components are associated to the excitation detection frequencies to build decay associated spectra (CAS) maps for the former, and coherence associated spectra (CAS) for the latter (figure 19e).

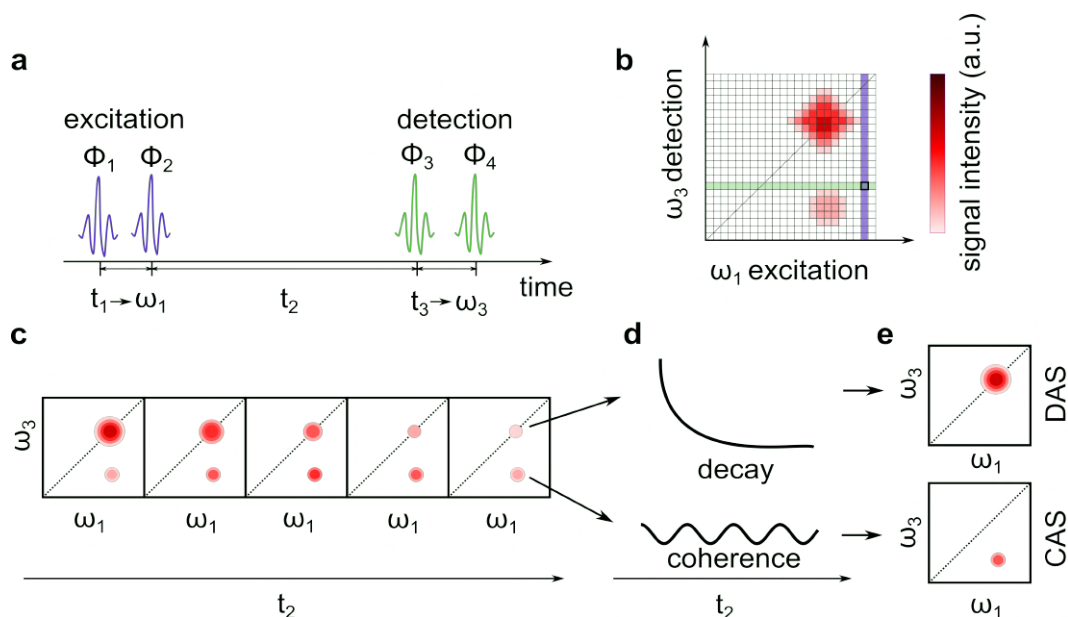


Figure 1.19: (a) Excitation pulse pair (blue) and detection pulse pair (green) are delayed by time t_2 . Within a pulse pair, the pulse delay t_1 or t_3 defines the respective excitation ω_1 or detection ω_3 frequencies respectively. The associated phases ϕ_1 and ϕ_3 are modulated periodically to retrieve the different components of the non-linear signal. (b) Excitation-detection 2DES map. The 2DES is built mapping a grid of excitation-detection pairs. An example point corresponding to excitation and detection pulses in figure 19a is shown. (c) Several 2DES maps recorded for increasing t_2 delays. (d) Real components of the kinetic fit correspond to excitation decays while imaginary components are due to oscillations (coherences). (e) The relative amplitude of the decays and coherences are mapped into the excitation-detection axis. For each decay or coherence component a DAS or CAS map is built respectively.

Up to now, we have not specified the nature of the response of the system. The common set-up in 2DES spectroscopy¹⁰³ is to interrogate the excited sample with a non-collinear (that is with a different incidence angle w.r.t to the probe pulses) and spectrally wide probe pulse. The spectra resulting from the interaction of the pump-excited sample with the probe pulse provides information about the 3rd order polarization of the chromophores in the sample. In more simple terms, the optical response of the system after interacting with 3 pulses is measured. In the case of multiple excitations, the phase of the incident radiation (that depends on its incidence angle and its time phase) can result in addition or subtraction of the interactions. The excitation pathways are associated with distinct linear combination of the pulse phases, thus controlling the phase of the incident pulses, or direction of detection, the different non-linear components of the response (rephasing, non-rephasing signals) are separated. In non-collinear set-ups, the components of the non-linear signal corresponding to different interaction pathways have distinct spatial directions. In the approach we have followed to develop PEC2DES, the sample is excited and probed by two collinear pulse pairs yielding a fully collinear 4-pulse configuration.

To obtain the non-linear components of the response, the phases $1-4$ are modulated periodically which separates the different components in the frequency domain and are thus obtained by Fourier filtering.¹⁰⁴ In our approach, the 4th order polarization is then probed by a process proportional to the population states (incoherent observables), namely fluorescence¹⁰⁹ or photocurrent.^{110,111} This approach simplifies the experimental set-up and allows the integration of several detection methods. An additional advantage of photocurrent is background-free detection.

In simple terms, in 3-pulse configuration the sample is probed “optically”, while the 4-pulse configuration allows to measure the response of the signal with photocurrent or fluorescence. 4-pulse configuration is technically simpler to implement and more robust with respect to other experimental 2DES approaches and is inherently background free.¹¹¹ In addition, photocurrent detection allows to separate the contributions of excitations leading to CS.

3.6 Protein immobilization bioengineering

Electrochemical characterization of redox proteins can be carried out with adsorbed or freely diffusing proteins. However, single molecule characterization with nanoprobe techniques requires proteins to be robustly adsorbed on the electrodes. To study the ET of PSI, Pc and PSI/Pc in bulk and at single protein level, we have followed a common absorption strategy for PSI throughout most of the manuscript (chapters 2-5). Pc has also been directly adsorbed on ECSTM metallic probes and working electrodes (chapter 4) and on AFM tips via a flexible polymer linker (chapter 5). Protein orientation,^{112,113} protein-electrode distance⁸¹ and protein-electrode electronic coupling^{114,115} have a significant impact on the effective charge exchange rate with the electrode.¹¹⁶

All the experiments reported in this manuscript have been performed on gold substrates. Gold and carbon are the most broadly employed material for bioelectrochemistry.¹¹⁷ We have chosen gold due to the low surface roughness of monocrystalline gold electrodes suitable for STM measurements and due to the surface chemistry that facilitates protein immobilization. Gold-sulphur chemistry has been extensively exploited for the formation of thiolates self-assembled monolayers¹¹⁷⁻¹¹⁹ used as protein linkers. Gold-sulphur bond is also established with a free cysteine amino-acid.^{120,121} Relatively low occurrence of surface cysteine allows immobilization with a well-defined orientation in proteins with the exposed cysteines¹²² as it is the case of Azurin.^{77,123} Cysteine residues can also be introduced in mutant proteins allowing to design the protein adsorption site and engineer ET pathways with the electrode.^{122,124} We have employed this strategy to functionalize Au electrodes with the PSI-binding peptide (chapters 3-6) and the Pc-SH mutants (chapters 4 and 5).

PSI immobilization techniques

During the last two decades, great progress has been made interfacing PSI monolayers with Au,^{125–130} semiconductors,^{131,132} graphene electrodes,¹³³ and fullerene particles.^{130,134} The use of thiolates self-assembled monolayers (SAM) for PSI immobilization is extensively reviewed^{135,136} comparing different chain lengths and terminal groups. In early STM experiments¹²⁷ and measurements on conducting-AFM,¹¹² the current rectifying behaviour of PSI monolayers was analysed to infer PSI orientation. The heterogeneous but still biased orientation of PSI molecules was explained by SAM-PSI electrostatic interactions. SAM's of bacterial cytochrome *c* have also been employed to immobilize PSI, to enhance electron transfer and PSI adhesion¹²⁸ and stability.¹³⁷ Finally, high surface loads and photocurrents have been achieved in PSI multilayers¹³⁸ trapped in redox hydrogels.^{95,98,100–102} However, while the multilayer approach significantly increases the photocurrent output, it is not suitable for single protein nanoprobe characterization.

To achieve unidirectional orientation of PSI monolayers, different strategies are adopted: i) Langmuir-Blodgett technique has been exploited to deposit oriented PSI monolayers on gold electrodes.¹³⁹ ii) Enhanced electrode-protein adhesion is achieved with mutant proteins including cysteines binding with gold¹²⁵ and carbon nanotubes.¹⁴⁰ iii) Small peptide chains have been produced to bind PSI with its partner Fd that was in turn bound to ITO.¹⁴¹ iv) Use of a linker peptide, binding to PSI and to electrodes. Following the latter strategy, Gordiichuck et al. developed through phage display screening technique, a library of peptides that allow binding PSI's stromal side to ITO electrodes.¹²⁶ The ability of the peptides to orient PSI was tested studying their rectifying behaviour of via Conductive-AFM. This peptide, identified as IQA, targets cyano-bacterial PSI extracted from *Synechococcus Elongatus*. To functionalize ITO electrodes with the generated peptide, the authors added an extra phosphorylated serine to one of the ends of the peptide.

Due to the high structural homology between the subunit present in the stromal side of the PSI of cyanobacteria and plants (see supplementary information in chapter 3) we infer that the IQA peptide also binds to plant PSI. Based on the publications by Jordan et al.¹⁴² and by Quin et al.⁴³ on the structure of PSI from *Cyanobacterium Synechococcus Elongatus* and from *Arabidopsis Thaliana*, respectively, we performed a structure-based sequence alignment of the PSI subunit exposed toward the stromal side. We compared the structural homology, sequence identity, and sequence similarity between PSI stromal side regions from cyanobacteria and plant PSI. The structural alignment was performed using the PROMALS3D and ESPript 3.0 server, to depict a similarity sequence coloring scheme.^{143,144} The calculation of the identity and similarity percentages was performed using the Sequence Manipulation Suite server (SMS).¹⁴⁵ The alignments performed for each pair of the subunits studied are shown in the supplementary information of chapter 3.

We only considered the PSI subunits A, B, C, D and E because these subunits are the ones that are mostly exposed to the solvent in the stromal side of both cyanobacteria PSI and plant PSI.¹⁴⁶ Based on the high structural homology and sequence similarity between stromal side regions in cyanobacteria and plant PSI, we concluded that IQA peptide would also be able to preferentially orient the plant PSI from *Arabidopsis thaliana*, exposing the luminal side to the solution.

In all the experiments with PSI presented in this manuscript (with the exception of chapter 7) we make use of a modified version of the IQA linker peptide. To the original binding sequence of 12 amino acids, we replaced the end phosphorylated serine with a Cysteine to allow binding to Au electrodes, pIQAcys (sequence IQAGKTEHLAPDC).

Plastocyanin immobilization

To bind Pc to gold surfaces (Au[111] electrodes, STM probes) and to AFM probes, we make use of cysteine mutants, Pc-SH, modified and characterized by *Andolfi et al.*⁷⁸ who kindly shared the modified Pc-SH with us. Pc-SH contains three additional residues (Thr-Cys-Gly) in the C-terminal introduced by a mutagenic primer. Although there is no crystallographic characterization of the Pc-SH mutant, we hypothesize that the inclusion of the three additional amino acids in the C-terminal does not modify the protein structure with respect to the wild type. This view is supported by previous nanoprobe characterization^{78,147} of this protein mutant and the redox activity that we measure (chapter 4), proving the functionality and thus the correct folding of the mutants. To simplify nomenclature, Pc-SH mutant employed throughout all experiments in the manuscript is referred as Pc. Pc_{apo} and Pc_{holo} are used to specify the absence or presence of the Cu redox centre in the protein. The cysteine modified Pc mutant was purified in a Cu-free form (Pc_{apo}), to avoid the oxidation reaction between surface-exposed cysteine residue of the Pc mutant and Cu²⁺. With the same aim, Pc_{apo} was first bound to the Au electrodes, STM or AFM probes and afterwards apo Pc-SH was exposed to fresh Cu²⁺ (CuSO₄ 50 mM solution) to bind Cu²⁺ in the apo Pc-SH structure. While Pc_{apo} does not exhibit reduction nor oxidation features in cyclic voltammetry, upon Cu²⁺ incorporation, Pc_{holo} exhibit redox activity (chapter 4).

3.7 Sample irradiation with LED sources

To study the photocurrent output of biohybrid PSI electrodes, it is key to irradiate the samples with a stable high power light source to provide a sufficient photon flux, that is, photons should be in excess. In this work, in all photocurrent and force spectroscopy experiments(except for the photocurrent spectroscopy experiments) irradiation has been performed with a high-power LED source with a central wavelength of 690 nm (SMB1N 690 Roithner Lasertechnik). A constant current of 600 mA is fed by a femtobuck LED

driver (Sparkfun electronics). We control illumination cycles with a signal generator operating on the LED driver. This allows us to produce short “flashes” as well as steady illumination cycles (from $\sim 10 \mu\text{s}$ up to minute scale). Short flashes are employed to characterise photocurrent signals exploited in chapter 6, while automated chopped light cyclic voltammetry and the use a lock-in excitation/detection strategy enhancing sensitivity is presented in chapter 7. To prevent overheating, the LED chip is mounted on a heat dissipator board, and it is furnished with a taped lens to focalize the light source (Roithner Lasertechnik), yielding an optical power output of $60 \text{ mW}\cdot\text{cm}^{-2}$ in the plane of the electrode.

4 Theory

In this section we present the basis of ET, studied in chapters 3 and 4, and provide a brief introduction to photosynthetic pigments light absorption for the light-harvesting study of chapter 6. In both cases a mathematical rigorous description is out of the scope of this work and can be found in manuals^{26,45,148,149} and publications^{150,151} that I have followed for the introductory sections 4.1 and 4.2. To describe ET and light absorption we must deal with the electrons in the outer shell of the atoms, that will be represented by quantum mechanical electronic states. ET and light absorption processes are thus represented by transitions between these states.

4.1 Introduction to quantum mechanics and the Fermi Golden Rule

The following formalism is valid for weakly interacting molecules where the intermolecular distance is large compared to the size of the atoms. For these weak interactions, initial $|i\rangle$ and final $|f\rangle$ states can be described in the same electronic basis, which is decoupled from nuclear motions (Born-Oppenheimer approximation). That is, we can separate the electronic and nuclear contributions as different products.

In quantum mechanics, to describe states evolution, states are represented in the basis of the operator propagating the time evolution of the system, the Hamiltonian, H . As we indicated, $|i\rangle$ and $|f\rangle$ are non-interacting states, therefore they are represented in the basis of a non-interacting Hamiltonian, H_0 that propagates the time evolution of the non-interacting system. However, if states $|i\rangle$ and $|f\rangle$ are described in a non-interacting basis, the system will remain in its initial state and the transition will not take place. Thus, to describe the transition, a term accounting for the weak interaction must be included. This weak interaction H' , is described as a perturbation of the non-interacting basis H_0 . Their addition yields the complete system time evolution operator $H_{Total}=H_0 + H'$. The latter term, H' couples the initial and the final states mixing the non-interacting states. As we will see, ET and light absorption differ on the nature of the perturbation.

The Fermi Golden rule (equation 1.1) provides the transition rate between weakly interacting states coupled by a perturbation H' . The transition rate is given by the product of the probability (density of states) of finding the system in a degenerate state $\rho(E_i=E_f)$, that is, with $|i\rangle$ and $|f\rangle$ having the same energy and the transmission probability between degenerate states, given by the square of the matrix element $|\langle i|H'|f\rangle|^2$.

$$\Gamma_{i \rightarrow f} = \frac{2\pi}{\hbar} |\langle f|H'|i\rangle|^2 \rho(E_i = E_f) \quad (1.1)$$

4.2 ET Theory

In ET, electrons are exchanged between electron donor and acceptor molecules or proteins. We will estimate ET rate as the transition rate between an initial state where the donor is reduced, the acceptor oxidized, and a final state with oxidized donor and reduced acceptor. Initial ($A^+ + D^-$) and final electronic states ($A^- + D^+$) are represented by charge localized diabatic states ($|i\rangle$ and $|f\rangle$, respectively). We can picture these states as totally independent (non-interacting) molecular orbitals where the electron occupies donor and acceptor species respectively, that is before and after ET. The weak interaction (H') represents how the electrostatic potential of the donor nuclei, is “slightly affected” by the electrostatic potential built up by the acceptor nuclei. Fluctuations in the nuclear coordinates (N) shaping the electronic states might take the $|i\rangle$ and $|f\rangle$ states to similar energy levels (degeneracy) allowing the transition. Thus, degeneracy condition is met if $N(E_i) = N(E_f)$. On the other hand, we need to estimate the transmission probability between degenerate states. This term, called electronic coupling, accounts for the electronic contribution to ET and is computed as the overlap of the perturbation with the initial and final electronic states $|H_{if}|^2 = |\langle i|H'|f\rangle|^2$.

Therefore, applying Fermi golden rule to ET, the rate k_{ET} is given by equation (1.2):

$$k_{ET} = \frac{2\pi}{\hbar} |H_{if}|^2 P(N(E_i) = N(E_f)) \quad (1.2)$$

Nuclear contribution

To compute the probability of degeneracy $P(N(E_i) = N(E_f))$, Marcus theory of ET describes the fluctuations of the nuclei classically. Following an Arrhenius-like expression, degeneracy probability is exponential with the activation free energy ΔG^{++} . Activation free energy ΔG^{++} is the free energy difference between the nuclear configurations compatible with the initial state and the configurations in degenerate state. To estimate this increment, free energy curves are built taking the energy gap (ΔE , the energy difference between $|i\rangle$ and $|f\rangle$ states) as reaction coordinate. ΔE values are

assumed to be normally distributed, which is justified by the large number of weakly interacting particles (linear response approximation). By definition, the Gibbs free energy, $\Delta G = -k_B T \ln(\Delta E)$ of a normally distributed energy gap is a parabola. Therefore, $|i\rangle$ and $|f\rangle$ free energy curves (with ΔE as reaction coordinate) are parabolas displaced by the difference of free energy at equilibrium (ΔG^0) of $|i\rangle$ and $|f\rangle$. Under the linear response approximation, the curvature of the free energy parabolas is the variance of the ΔE distribution. This curvature/variance is called reorganization energy, λ , and it is interpreted as the difference in energy of nuclear coordinates necessary to “re-organize” them from the initial equilibrium state $|i\rangle$ to the final equilibrium state $|f\rangle$ parabolas. We can thus obtain the activation energy ΔG^{++} from ΔG^0 and λ .

The nuclear contribution to ET is then encoded in two terms. The first is ΔG^0 and it can be obtained evaluating the energy difference of the donor and acceptor separately, that is the difference of the ionization energy of the donor molecule and the electron affinity of the acceptor. The second term is λ , and it accounts for the impact of ET in the nuclei motions surrounding the transferred electron. Lower rates are expected for ET with higher re-organization energy, as it is the case of solvent exposed cofactors where solvent molecule re-organization slow down the ET rate. Using ΔG^0 and λ to compute the activation energy ΔG^{++} , the expression for ET rate, k_{ET} , is known as the Marcus equation (equation 1.3).

$$k_{ET} = \frac{2\pi}{\hbar} |H_{if}|^2 \frac{1}{\sqrt{4\pi\lambda k_B T}} e^{-\frac{(\lambda + \Delta G^0)^2}{4\pi\lambda k_B T}} \quad (1.3)$$

Electronic Contribution

The electronic contribution to the ET rate is given by the square of the electronic coupling of the initial and final states by the perturbation term of the weak interaction, $H_{if} = |\langle i | H' | f \rangle|^2$.

H_{if} models how the perturbation couples the initial to the final state. Loosely speaking, it models how the perturbation “puts together initial and final states”, that is the tunnelling probability from $|i\rangle$ to $|f\rangle$. The electronic coupling, is the matrix element of the perturbation with initial and final states, that is, the overlap of the non-interacting molecular orbitals with the interaction. H_{if} depends strongly on the D-A distance and on their relative orientation. This is due to the spatial distribution of the electronic states around D and A atoms and also to the decay of the perturbation with distance. For increasing D-A distance, H_{if} the electronic coupling, and thus k_{ET} , decreases exponentially. Relevant to the present work, it is important to remark that aromatic amino acids, notably tyrosine and tryptophan, where charges are highly delocalized, facilitate ET spreading the spatial span of $|i\rangle$ or $|f\rangle$ and thus increasing the H_{if} term.

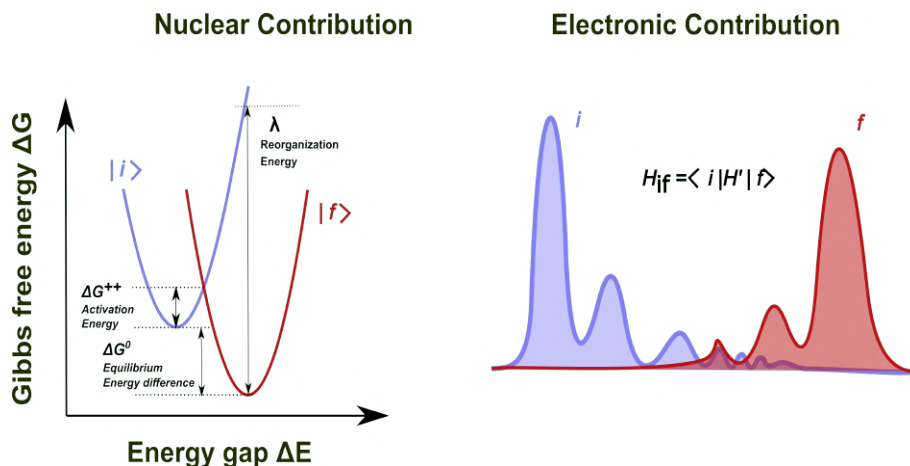


Figure 1.20: Nuclear and electronic contributions to electron ET. Nuclear contribution (left-side) is an Arrhenius-like term with an activation energy $\Delta G^{\ddagger\ddagger}$. Initial (purple curve) and final states (red curve) Gibbs free energy curves plotted vs the energy gap ΔE are represented by parabolas. Marcus theory approximation allows to compute $\Delta G^{\ddagger\ddagger}$ via the reorganization energy (λ) and the equilibrium free energy ΔG^0 , represented in the diagram. In the right side, a cartoon-like representation of the wave functions for the initial and final state (purple and red respectively) and their overlap.

One of the main experimental outcomes presented in this dissertation is the distance decay constant of the tunnel current between a couple of electrodes decorated with PSI or PSI-Pc partners. To ease the interpretation of the results, well-established and recent theories and empirical models to compute H_{if} are outlined. We will briefly present simplified models for the perturbation interaction that allows to compute H_{if} and accurately predict the exponential decay with distance observed for K_{ET} .

The first approach proposed to estimate electronic coupling was to simplify the tunnel barrier separating $|i\rangle$ and $|f\rangle$ states.¹⁵² The complex potential barrier established by the protein structure and the surrounding electrolyte medium is replaced by a square potential barrier with height U . Solving Schrodinger equation in one dimension (along the barrier distance, r) for such potential yields an exponential decay of the electron wavefunction within the barrier that depends on the potential height U , the electron effective mass m_{eff} and the Planck constant \hbar (figure 21).

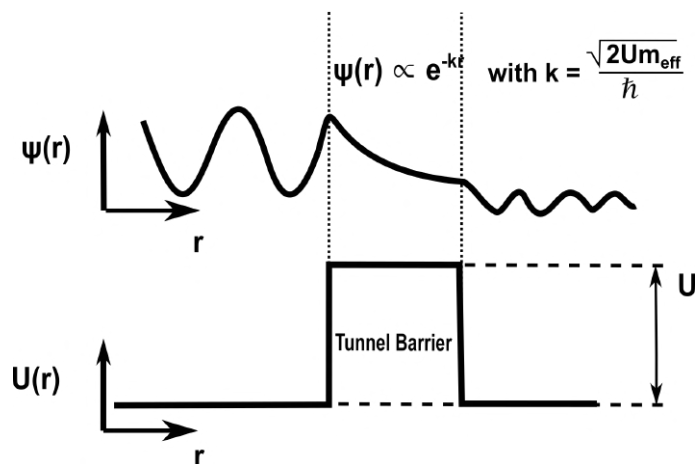


Figure 1.21: Wave function $\Psi(r)$ solving Schrödinger equation for the one-dimensional square potential $U(r)$. The wave function takes the form of free propagating waves $\Psi(r) \propto e^{ikr}$ in the regions where the energy of the system is higher than the potential barrier. In this simplified view, these regions correspond to the electrode or the redox cofactors. In the tunnelling gap, where the energy of the system is lower than the potential barrier, the wave function is described by a decaying exponential function $\Phi(r) \propto e^{-kr}$.

This iconic example of the one-dimensional square barrier problem in the wave function representation shown in figure 21, is translated into the Dirac representation of states and operators by equation (1.4). If we associate the potential barrier with the perturbation, the electronic coupling term for this model is:

$$|H_{if}|^2 \propto e^{-\beta r} \quad \text{with} \quad \beta = \frac{\sqrt{2m_e U}}{\hbar} \quad (1.4)$$

A first approximation of the barrier height estimates the potential barrier U as the difference in ionization potential between redox cofactors ($\sim 5\text{eV}$) and protein structure ($\sim 7\text{-}9\text{ eV}$). With a barrier of $\sim 2\text{ eV}$, equation (3) predicts a β value¹⁵³ of 14 nm^{-1} while experimental determination of β yields values^{23, 154} that range between $\sim 8\text{-}15\text{ nm}^{-1}$. To transfer electrons efficiently to the catalytic sites, electron transport sites k_{ET} must be below the typical bond-breaking millisecond time scale in catalytic sites.¹⁵⁵ This requirement constraining the edge-to-edge¹⁵⁶ distance between redox cofactors to $< 1.5\text{-}2\text{ nm}$,²³ and is fulfilled by most of the redox cofactors in ET proteins.¹⁵⁵ According to *Dutton et al.*,¹⁵⁵ mutations in the amino acid sequence surrounding redox cofactors are not determinant in the K_{ET} , provided that sequence modifications do not alter the free energy ΔG^0 and the re-organization energy λ . In this view, ET is efficient (not rate limiting) and robust (mutation tolerant) thanks to the protein structure playing the role of scaffold for the redox cofactors.

Empirical models

We present the packing density model¹⁵⁷ and the tunnelling pathway model,¹⁵⁸ two empirical models that map the square barrier model into the atoms of available protein structures. Both models are equivalent from a formal perspective.¹⁵⁹ The packing density model computes K_{ET} simplifying Marcus equation (equation 1) substituting numerical constants (ΔG^0 and λ are expressed in eV) and assuming room temperature (equation 1.5). The electronic coupling term in the packing density model, depends exponentially with D-A distance (R expressed in Å) and on the packing fraction of the medium ρ (ranging from 0 to 1). ρ is estimated computing the ratio of the volume occupied by intervening atoms (taking their van der Waals radius) over the volume between redox cofactors. Despite its simplicity, this model accurately reproduces K_{ET} of numerous redox ET proteins^{23, 155, 160} and it drives the design of the novo artificial ET proteins.¹⁶¹

$$\log_{10}(k_{ET}) = 13.0 - (1.2 - 0.8\rho)(R - 3.6) - 3.1(\Delta G + \lambda)^2/\lambda \quad (1.5)$$

In the tunnelling pathways method, all the possible chains of neighbour atoms connecting D and A, that is, the tunnelling pathways, are computed and weighted by their distance and type of bond (hydrogen, covalent or through space). This results in a bundle of possible pathways allowing to highlight atoms in pathways maximizing H_{if} . In the bacterial analogue of PSI-Pc, reaction centre- cytochrome c_2 , tunnelling pathways were calculated for a sequence of molecular dynamics snapshots of increasing donor-acceptor distance, from the bound complex configuration (0.14 nm) to the encounter complex configuration (2.2 nm).¹⁶² The encounter complex¹⁶³ is an ensemble of configurations of the solvated protein cognates, driven by non-specific long-range electrostatic interactions that facilitate the recognition of the partners and the formation of the complex. Five results from this¹⁵² work are relevant for the discussion of our results of PSI-Pc in chapter 4: i) water molecules are responsible for efficient inter-protein K_{ET} of the encounter complex. ii) The average ET rate is tenfold higher than the rate estimated with the average relative position of the structures. This is due to the exponential dependence of K_{ET} with distance and to the large fluctuations in the encounter complex configuration. That is, K_{ET} is dominated by infrequent but ET-favorable conformations brought by fluctuations. iii) K_{ET} for the bound complex is ~100 larger than for the encounter complex. iv) β estimated from the coupling decrease computed with the pathways method is ~11 nm⁻¹.

In addition to the above empirical models, we outline some theoretical models of protein ET that despite the drastic simplification that they imply, allow to grasp basic features and valuable proportionality relationships between to estimate k_{ET} .^{150, 164, 165}

Super-exchange Model

Super-exchange mechanism models electron tunnelling between initial and final states mediated by bridge states formed by un-occupied molecular orbitals. The energy gap between the initial/final states and the bridge states is assumed to be large, therefore electrons do not populate the bridge state (off-resonant tunnelling). However, the presence of these states lowers the effective potential tunnelling barrier increasing the coupling term H_{if} . Super-exchange mechanism predicts an exponential decay of k_{ET} with distance, where β values are lowered due to bridge states. As we explained above, H_{if} accounts for the electronic transmission probability while nuclear fluctuations bring the system to a degenerate state (Marcus equation) introducing the temperature dependence:

$$k_{ET} \propto \frac{1}{\sqrt{T}} e^{\frac{-1}{k_B T}} \quad (1.6)$$

Flickering resonance

In contrast to the super-exchange mechanism, the flickering resonance model¹⁶⁶ assumes that bridge states energy lies near initial and final states. Bridge states are then transiently occupied without energy relaxation. The concept of nuclear fluctuations bringing initial and final states to degeneracy (that is to a similar energy level) is generalized for a chain of N bridge states which are all transiently aligned with initial and final states. Under this view, the electronic coupling H_{if} decays linearly with N , the number of bridge states, and subsequently with the distance for a bridge chain of increasing length. However, the resonance probability, which is distance independent in tunnelling and super-exchange mechanisms, decays exponentially with N . The temperature dependence of the flickering resonance is similar to the super-exchange mechanism.

Hopping/Multi-step tunnelling

In a chain of redox cofactors with similar energy levels, a sequence of single tunnelling steps can take place. As we have stated above, in each tunnelling step, the transfer probability decreases exponentially with the cofactors distance, however k_{ET} for the whole ET cascade decreases linearly with the number of cofactors. This linear dependence with distance makes the hopping mechanism a suitable candidate to model the electron transfer for long (> 2 nm) ET in membrane proteins of photosynthetic and respiratory electron transport chains. In particular, the hopping mechanism is attributed to long-range ET of multi-heme cytochromes¹⁶⁷ responsible for extracellular electron transfer.¹⁶⁸ Conductance measurements in *Shewanella Oneidensis* bacterial nanowires¹⁶⁹ and cells¹⁷⁰ are compatible with multi-step incoherent hopping mechanism allowing to transfer charge up to millimetre scale.

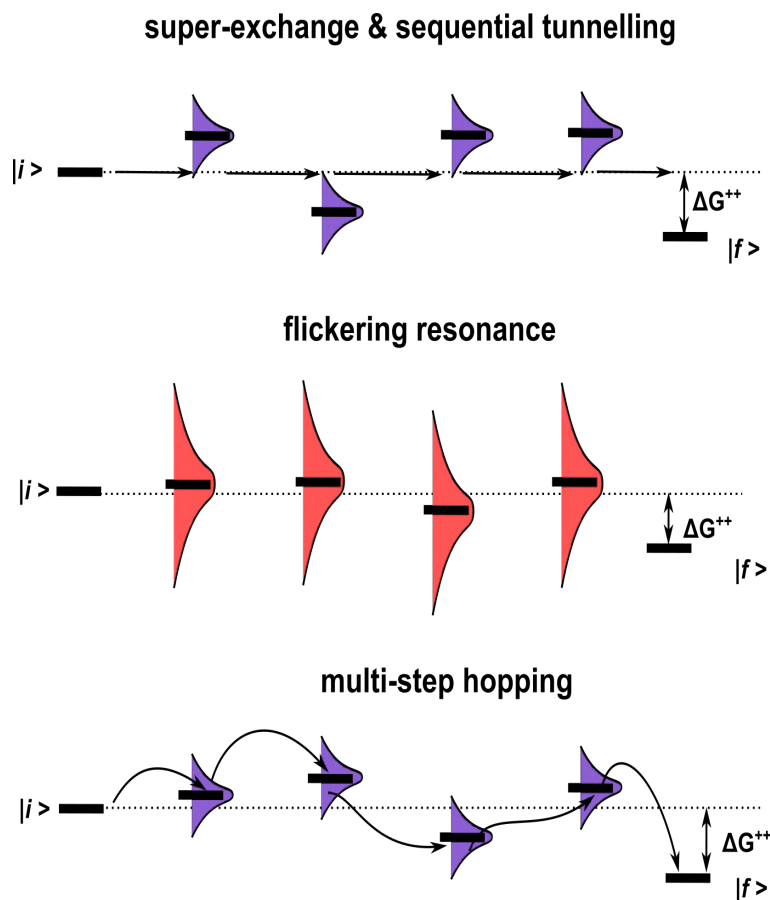


Figure 1.22: Cartoon-like representation of different ET models, adapted from.¹⁶⁴ In the super-exchange mechanism, the ET takes place directly between the initial and final states (indicated by black thick lines). The electron does not reside in the bridge levels (off-resonant tunnelling), indicated by black lines and purple shades. On the other hand, in flickering resonance, thermal fluctuations (red shades) bring intermediate bridge states to resonance. In multi-step hopping (bottom diagram), a series of tunnel events take place between the bridge states. In each step there is a partial relaxation of the electron's energy.

While in the flickering mechanism all intermediate redox cofactors have to be aligned, the hopping mechanism pictures a sequence of independent tunnelling steps in which the energy levels of the cofactors are aligned by pairs. The electron energy is relaxed (electronic and nuclear modes couple) in each step, allowing nuclear fluctuations to align the incoming electron (in a degenerate state with the previous donor cofactor) with the energy level of the following cofactor of the chain. This requisite for relaxation imposes a limit the electron mobility in organic materials.¹⁷¹ According to *Pirbadian* and *El-Naggar*,¹⁶⁹ this translates into a maximum value for $k_{ET} < k_{relaxation} \sim 10^{11} \text{ s}^{-1}$. Spectroscopic measurements of k_{ET} between the redox cofactors in PSI with typical transfer time above 10 ps (10^{11} s^{-1})¹⁷² are consistent with an incoherent hopping

mechanism. Regarding temperature, in the hopping mechanism the proportionality is modified to $k_{ET} \propto \exp(-1/k_B T)$.

Electron transfer (ET) and electron transport (ETp) configuration, theoretical considerations

We have outlined the ET mechanism between two redox centres defining the initial and final electronic states. This ET process can be tracked provided that the redox states of the donor/acceptor moieties exhibit distinct spectroscopic features. However, in the experimental approach we follow, proteins are squeezed between electrodes under electrochemical control. The charge exchange between electrodes mediated by proteins is called electron transport (ETp)¹⁶⁴ and presents some fundamental differences with respect to the ET transfer formalism between redox states. In the ECSTM configuration, the polypeptide structure is squeezed between the probe and sample electrodes, which provide an electron source and drain. Therefore, initial/final, donor/acceptor states are no longer defined by the molecular orbital of the ET cofactors, but they are set by the Fermi level of the electrodes, represented by the blue bands in the diagram in figure 23. In addition, the charge exchange is promoted by the bias potential applied between the electrodes (U_{Bias}) overriding the driving force set by the free energy difference between initial and final states.

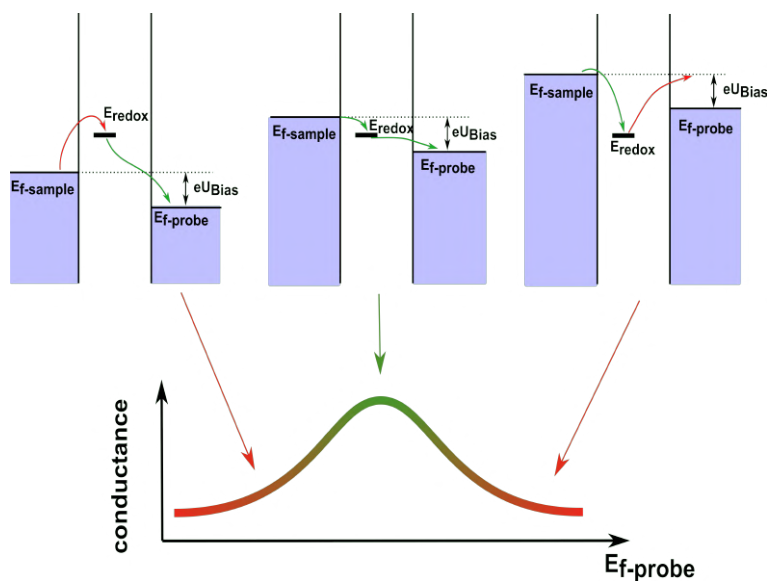


Figure 1.23: Diagram representing electrode Fermi level (purple bars) with the molecular orbital (E_{redox}) mediating the charge exchange. Barrier-less transfer is indicated with green arrows while up-hill transitions are marked in red. As the sample voltage is swept for a constant bias, E_{redox} falls above (left), in between (centre) or below (right) sample/probe Fermi levels. This results in a conductance gating effect.

In ETp configuration, the electronic coupling between the initial and final states is replaced by the electronic coupling between sample and probe electrodes. Electrodes coupling is thus mediated by the bridge states of the protein trapped in the tunnelling junction. The electronic coupling between protein and electrodes is determined by the molecular orbitals in the protein/electrode interface and by the electrode Fermi level and thus modulating the conductance of the whole junction.¹⁷³ As the sample (or probe) potential is swept for a constant U_{Bias} , the alignment of the protein molecular orbitals results in a conductance gating effect that translates in conductance gating.⁸¹ A diagram depicting Fermi-redox level alignment is shown in figure 23.

The ET models outlined in the previous section can be adapted to ETp configuration. For example, in ETp super-exchange, the mechanism does not require thermal activation to tunnel because the driving force is provided by the electrode bias potential, and it is thus temperature independent. In the super-exchange view of ETp, the charge exchange process is limited by the electronic transmission factor defined by the electronic coupling. However, a series of tunnelling steps, as the case of hopping mechanism, does require thermal energy to overcome intermediate barriers. Flickering resonance model is also temperature dependent in both ET and ETp configuration because the resonance condition of the bridge states required in this model is brought by thermal fluctuations.

“Direct” calculation of H_{if} in ETp configuration

The models presented above simplify the ET problem, providing a coarse grain approximation of the electronic structure of redox cofactors. However, we may wonder whether it is possible to compute the electron density of all the atoms in the protein, providing a direct estimation of the electronic coupling. For proteins, direct calculation of H_{if} employing high-level *ab initio* methods is computationally very demanding due to the large number of atoms involved and the small value for H_{if} (10^{-1} - 10^{-4} meV) which has been, until very recently, below convergence criteria and numerical noise of electronic structure computations.¹⁵⁰ However, recent advances have allowed first-principle calculation of the electronic structure of peptides¹¹⁵ and proteins^{2, 174, 175} in metal-protein-metal junctions. A detailed discussion on the computation¹⁵⁰ is out of the scope of this manuscript. Nevertheless, we highlight calculation results to support the discussion of chapters 3 and 4. Simulating a multi-heme cytochrome trapped in a tunnelling junction between two gold electrodes, the contribution of the protein highest band states was evaluated. These states, associated with the Fe ions in the heme groups, contribute poorly to the current, despite being very close in energy to the electrodes Fermi level, because they are highly localized around the heme clusters and therefore the resulting electronic coupling with the electrode is low.¹⁷⁶ In transistor-like configuration, the globular blue-copper protein Az_{apo} (similar to Pc) lacking the Cu centre, exhibits a conductance comparable to the Az_{holo} while it does not show a conductance gating

effect.¹⁷⁷ In addition, the similarity between the transmission values of Az with different metal centres (Co, Ni, Cu, Zn and apo form) suggest that, under the perspective of a fully coherent mechanism, the metal centres play a minor role.¹⁷⁸ Regarding the role of water molecules, in simulations of Az tunnelling junctions, water molecules induce a conductance increment as they increase the electronic coupling between the protein and the electrode.¹⁷⁵

Models not based on the Fermi golden rule

Temperature independent models in ETp are limited in theory by the spatial span of the electronic coupling of the electrodes to short distances (< 2nm). Longer ETp distances are described by temperature dependent models (flickering resonance and hopping mechanism). However, experiments have revealed temperature independent in long-range ETp (> 2 nm).^{179–183} To overcome this discrepancy, two non-perturbative models have been recently introduced.¹⁸⁴ These models don't treat the interaction as a perturbation and thus don't use the Fermi golden rule to compute the transfer rate.

The first model is based on voltage induced coherent transport.¹⁸⁴ In this approach, the bridge molecular orbitals are coupled to the electric potential driving the charge exchange. This coupling between bridge states and the electric potential delocalizes the bridge states and increases the electronic coupling of the initial and final states. This model, can, in principle, be applied to both ET and ETp, that is, the electric potential driving the charge exchange can be either the free energy difference between redox cofactors in the ET configuration or the electric potential imposed by the electrodes in the ETp configuration. However, temperature independent long range charge exchange has only been observed in ETp experiments.

The second model has been recently introduced to describe the temperature independent long-range ETp between electrodes.¹⁸⁵ It explicitly considers the electron reorganization of the molecule due to the reorientation of dipoles under the applied electric field. The authors provide an intuitive analogy comparing long range ETp with the conduction on a one-dimensional wire in which electron-electron interactions result in an effective long-range flow (despite the individual electron flow through the wire being relatively slow).

4.3 Light absorption

What are the mechanisms underlying light absorption in photosynthetic complexes? Light-matter interactions are described by quantum mechanics that pictures light absorption as the result of transition towards a higher excited state. The absorbed wavelength matches the energy of the transition, for instance, molecular vibrational modes absorb in the infrared region while the transition of electronic states are associated

to visible and UV radiation.⁴⁵ To estimate the transition rate, we recall Fermi's golden rule cited in the previous section describing ET. In this case, the perturbation H' allowing the transition from the ground to the excited state is precisely the electromagnetic radiation. Electromagnetic wave description is simplified by a spatially homogeneous oscillating electric field $E(t)$, that is, we neglect the contribution of the magnetic field, and we assume that molecule size (a few Å) is significantly smaller than the wavelength (100's nm λ for visible light).

$$E(r,t) \simeq E_0(t)(e^{-i\omega t + ikr} + e^{i\omega t - ikr}) \quad (1.7)$$

Under these approximations, the perturbation term H' promoting the transition is given by the product of electric field $E(t)$ and the dipole operator, defined as the product of position operator with the charges (equation 1.8). Translating into more simple terms, to compute the probability of photon absorption, we have to estimate the potential energy of the perturbation produced by the radiation. From elementary physics, we recall that the potential of a point charge in an electric field is simply the product of the electric field with the charge distance. In the case of a dipole produced by a charge distribution, the potential energy is the product of the dipole with the electric field. In quantum mechanics jargon, the distance observable is associated to the action of the position operator over the system's state, and so does the dipole moment that is associated to the dipole operator:

$$H(t) = -E(t)\mu \quad \text{where} \quad \mu = er \quad (1.8)$$

The transition takes place as the energy of the perturbation ($\hbar\omega$ for the electromagnetic radiation) matches the energy difference between the states for a frequency ω_0 , that is $\hbar\omega_0 = E_f - E_i$. This energy conservation principle explains why pigments absorb at a given frequency. The transition rate is given by equation 1.9. Here the E_0 is the amplitude of the electric field at frequency ω_0 , and $\rho(\omega_0)$ is the density of radiation modes at frequency ω_0 .

$$\Gamma_{i \rightarrow f} = \frac{2\pi}{\hbar} E_0^2 |\langle f | \mu | i \rangle|^2 \rho(\omega_0) \quad (1.9)$$

The transition dipole, defined as the matrix element of the dipole operator, $\langle i | \mu | f \rangle$ is analogous to the electronic term coupling in ET, that we introduced before as the matrix element of the perturbation, approximated by a square potential barrier. The spatial span of the matrix element of the dipole operator is larger than the matrix element of a potential barrier. This explains the longer range of excited states interactions with respect to ET. Excitations in photosynthetic complexes are shared between several pigments, giving rise to collective ensemble energy levels, named Frenkel excitons.⁵²

The states $|i\rangle$ and $|f\rangle$ are pure states, however the state of real samples, are described by an statistical ensemble of pure states. This ensemble is represented by the density matrix ρ that is constructed with the probability P_k of finding the system on a pure state ψ_k .

$$\rho = \sum_k P_k |\psi_k\rangle \langle \psi_k| \quad (1.10)$$

The diagonal elements of the density matrix ρ_{nn} which are highlighted in figure 1.24, represent the population of the states. In PEC2DES the electrochemical signal is proportional to the transition of excited states, $|e\rangle \langle e|$ and $|f\rangle \langle f|$, to the ground state.

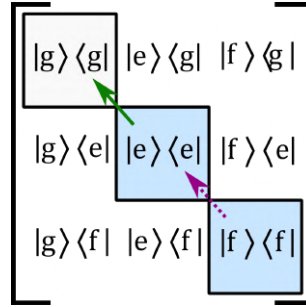


Figure 1.24: Density matrix for the three level system formed by the ground state $|g\rangle$, the first excited state $|e\rangle$ and the doubly excited state $|f\rangle$. The blue shaded diagonal elements $|e\rangle \langle e|$ and $|f\rangle \langle f|$ are proportional to the population of excited states, while the population of the ground state is proportional to $|g\rangle \langle g|$. PEC2DES measures the population of excited states leading to charge separation which is proportional to the $|e\rangle \langle e|$ to $|g\rangle \langle g|$ transition indicated with a green arrow. Dashed purple arrow represents doubly excited states relaxation.

The perturbations that represent the interactions with light pulses are better described in the interaction picture (sub-index I). This representation makes use of the time evolution operator, $U_0(t, t_0)$ that describes the free evolving system between t_0 and t in the non-interacting basis H_0 .

$$H_I' = e^{\frac{i}{\hbar}H_0(t-t_0)} H'(t) e^{-\frac{i}{\hbar}H_0(t-t_0)} = U_0(t, t_0) H(t) U_0^\dagger(t, t_0) \quad (1.11)$$

After n interactions (in our case the four laser pulses) the time evolution of the density matrix is ρ^n described by equation 1.12.

$$\rho^{(n)}(t) = \left(-\frac{i}{\hbar}\right)^n \int_{-\infty}^t d\tau_n \cdots \int_{-\infty}^{\tau_n} d\tau_{n-1} \int_{-\infty}^{\tau_{n-1}} d\tau_1 E(\tau_n) E(\tau_{n-1}) \cdots E(\tau_1) \quad (1.12)$$

$$U_0(t, t_0) \cdot [\mu_I(\tau_n), [\mu_I(\tau_{n-1}), \dots [\mu_I(\tau_1), \rho(-\infty)] \dots]] \cdot U_0^\dagger(t, t_0)$$

The photo-electrochemical signal S is proportional to the population of excited state $|e\rangle$ that decays to ground state via CS given by equation 1.13.

$$S \propto \langle e | \rho^n(t) | e \rangle \quad (1.13)$$

To simplify the operations in the density matrix computation, the different terms issued from equation 1.12 are represented as double sided Feynman diagrams (figure 1.25). The diagrams picture the action of the dipole operator as arrows acting on the initial density matrix $\rho(-\infty)$ represented by the ket $|g\rangle$ (on the left of the diagram) and the bra $\langle g|$ on the right. The action of the dipole operator modifies the state of kets and bras (remember that the dipole operator was the perturbation coupling the non-interacting states). In particular, arrows pointing towards the diagram correspond to an excitation while arrows pointing away correspond to de-excitations. The direction of the arrow is given by the sign of the phase of electric field with the term $e^{-i\omega t + ikr}$ pointing to right and the term $e^{i\omega t - ikr}$ pointing to the left. Time evolution is represented from bottom to top in the vertical axis, and is propagated by the time evolution operator $U_0(t_{n+1}, t_n)$ that dictates the evolution of the system between the interactions with the laser pulses.

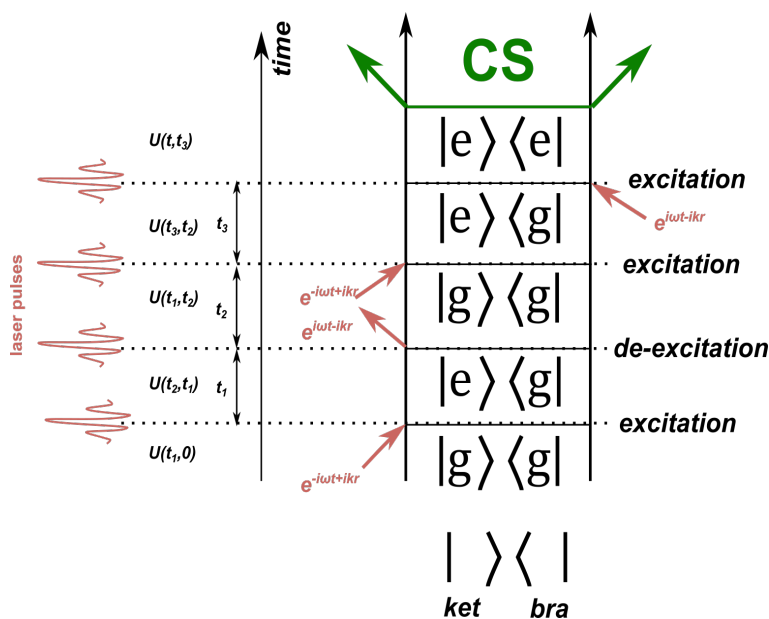


Figure 1.25: Example of a 4-pulses Feynman diagram.

The Feynman diagrams for standard 2DES experiments measuring third order polarization are different from the 4-pulses diagrams found in action spectroscopy (fluorescence, photocurrent, photoelectrons and photoions).[?] These differences and

their implications in PEC2DES will be further discussed in chapter 6. In particular, the Feynman diagrams relevant for the discussion of PECDES results, ground state bleaching (GSB), stimulated emission (SE), excited state absorption I and II (ESA I and ESA II) are shown in figure 1.26.

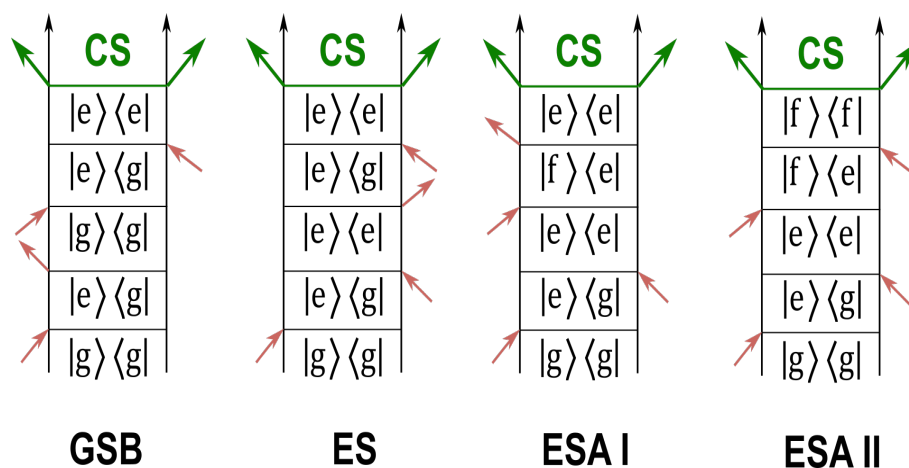


Figure 1.26: 4-pulses Feynman diagrams present in PEC2DES experiment, from left to right: ground state bleaching (GSB), stimulated emission (SE), excited state absorption I and II (ESA I and ESA II).

5 Literature experimental results on ET and PSI

In the following, we review experimental results of protein and interprotein ET^{2, 186, 187} and ETp,¹⁸⁸ organizing literature references by techniques. We highlight single molecule ECSTM experiments to provide a reference frame for the results that we will present throughout chapters 3 and 4.

5.1 Bulk techniques for ET

Spectroscopic methods for ET

The ET kinetics of photosynthetic complexes have been largely studied by transient absorption experiments.^{16, 54, 189} Absorption is recorded after irradiation with short light flashes triggering a single-turnover catalytic cycle. ET rates are estimated tracking the time course of the distinct absorbance and fluorescence bands associated to the redox cofactors of the photosynthetic electron transport chains in PSI.^{16, 17, 54, 189} The same strategy has been applied to study interprotein ET^{14, 28, 36–38} with Pc as it was outlined for PSI/Pc ET in the section 2.5.

Spectroscopic methods to study protein ET were extended to non-photoactive proteins by *Winkler* and *Gray*^{2,154,190–193} introducing Ruthenium prosthetic groups. Making use of laser flash-quench methods triggering ET, they report K_{ET} rates ranging from 10^3 to 10^9 s⁻¹. Placing prosthetic groups at different positions in the polypeptide chain, they were able to estimate a β of 11 nm⁻¹.¹⁵⁴

Protein Film Voltammetry

In experimental section 3.4, we presented the cyclic voltammetry methodology allowing to identify the redox potential of species in the electrolyte solution. Following protein immobilization techniques (section 3.6), protein films can be adsorbed on electrode surfaces allowing direct interfacial electron transfer between the adsorbed proteins and the electrode.¹⁹⁴ The ET between redox proteins and the electrode can be thus characterized performing protein film voltammetry (PFV).¹⁹⁵ In PFV, the background signal due to capacitive currents is subtracted. If adsorbed proteins don't transfer the electron any further (because they lack reacting substrate or because they lack catalytic activity, as it is the case of electron carrier proteins like Pc) the resulting current (after background subtraction) is directly proportional to the electron transfer rate, the scan rate and the effective number of adsorbed proteins.¹⁹⁶ PFV has been employed to characterize the redox properties of the membrane proteins from the respiratory chain¹⁹⁷ and photosynthetic complexes.¹¹⁷

Regarding the number of proteins on the electrode, it is usually in the pM·cm⁻² range, that is, a very small amount of protein is required for protein film electrochemistry compared to bulk spectroscopic techniques.¹⁹⁶

Protein film voltammetry, and in a larger extent, protein film electrochemistry can be exploited to characterize the enzymatic activity of proteins catalysing reactions such as CO₂ reduction,¹⁹⁸ hydrogenase activity,¹⁹⁹ and iron-sulfur enzymes.²⁰⁰ In addition, the enzymatic activity of proteins adsorbed to electrodes have been characterized at micro and nanoscopic scale.²⁰¹

ETp in protein monolayers

Early protein ETp experiments studied protein monolayers of bovine serum albumin, bacterial rhodopsin and Az deposited on SiO_x electrodes and contacted with a Hg drop or Au pads.²⁰² In this study, charge transporting proteins, Az and bacterial rhodopsin, showed higher conductance than bovine serum albumin, which conductance is still higher than simple saturated organic molecules. This study of protein conductance in solid-state-like configuration revealed the distinct nature of ET and ETp, and paved the way for the study of protein monolayer in ETp configuration.¹⁶⁴ A critical aspect of the protein monolayer conductance is the number of proteins effectively participating in

the junction and their contact resistance, which depends on contact geometry, electrode roughness and functionalization method.¹⁸² To address this issue, a cross-laboratory study was carried out revealing a wide dispersion in junction conductance depending on the contact geometry.¹⁸² Remarkably, all ETp experiments exhibited temperature independent ETp.¹⁸² Temperature independent ETp is a puzzling observation¹⁸⁰ reported in different protein systems below 160-200 K¹⁷⁹ and proved down to 4K in Az junctions.¹⁸¹ The lack of a thermal activation barrier is a signature of the tunnelling mechanism, however, protein junctions with lengths beyond 2 nm exceed the accessible tunnelling range.¹⁸⁰ For instance, temperature independent (down to 80 K) electronic conduction was observed in multi-heme c-type cytochromes²⁰³ in a tunnelling junction of ~ 5 nm. Temperature independent ETp is consistent with inelastic electron tunnelling spectra recorded in Az junctions that support the off-resonant tunnelling mechanism.¹⁸³

5.2 ECSTM experiments

ECSTM based techniques are employed to study single molecules²⁰⁴ and proteins,^{173,186,187} to characterize: the size and apparent height in scanning mode, the conductance and rectifying behaviour of the molecules in the junction in current-voltage spectroscopy, the charge exchange distance and the distance decay constant β in current-distance spectroscopy, and the formation of tunnelling junctions and their associated conductivity in blinking and tapping modes (see section 3.3).

5.2.1 Protein size

The lateral size of proteins adsorbed on electrodes has been reported for azurin⁷⁷ plastocyanin⁷⁸ ferredoxin⁷⁹ [Fe-Fe] hydrogenase,²⁰⁵ cytochromes OmcA and MtrC from *Shewanella Oneidensis*,²⁰⁶ and human sulfite oxidase,²⁰⁷ matching approximatively in all cases the crystallographic size. According to *Alliata et al.*⁸⁰ to accurately measure the protein lateral size in ECSTM, protein squeezing with the scanning probe must be avoided, otherwise the lateral size is overestimated. Based on protein apparent height and current distance measurements, they estimate that conductance set-points of 4 G Ω and 4 M Ω yield gap distances of 6.2 and 3 nm, respectively.⁸⁰ In ECSTM scans, proteins appear as uniform globular objects. To our knowledge, results of *López-Maritnez* applying differential conducting imaging are the only reported sub-protein heterogeneous features.²⁰⁸ In adsorbed Az proteins, differential conducting imaging revealed the signature of the Cu redox centre surrounded by the protein matrix.²⁰⁸

Apparent Height

All reported apparent height measurements of proteins in ECSTM scans are smaller than their associated crystallographic size.^{77-80,205,207} This is due to their lower conductance

with respect to the metal electrode on the scan “background” (see section 3.3). Repeating scans over the same region for different sample and/or probe potentials reveals through apparent height the conductance gating of the electrode/protein/electrode tunnelling junction. As we explained in the theory section 4.2, conductance gating is due to the alignment of the protein molecular orbitals participating in ET with the Fermi energy of the electrodes. Apparent height gating has been observed in Az,^{77,81} cytochrome *b*₅₆₂,²⁰⁹ and nitrite reductase.¹⁹⁴ Sigmoidal dependence with the electrode potential has been observed in human sulfite oxidase.²⁰⁷ At the single molecule level, the apparent height is a signature of the redox activity of the proteins as it is shown by constant apparent height found in redox inactive Zn-Az.²¹⁰

Current-voltage spectroscopy

Early current-voltage measurements of proteins with STM were carried out without potentiostatic control in ambient atmosphere, with photosynthetic reaction centres¹²⁷ and Pc-SH mutants.¹⁴⁷ In N₂ atmosphere, cytochromes OmcA and MtrC from *Shewanella Oneidensis*²⁰⁶ were studied. Under electrochemical control, current-voltage characteristics of Az absorbed on gold electrodes allowed to estimate its transition voltage, with a value of 0.4 V.²¹¹ In the recent years, the research group lead by Stuart Lindsay in Arizona state University has extensively exploited ECSTM current-voltage spectroscopy of proteins absorbed to probe and sample electrodes, providing valuable insights of ETp process.^{84,86,212–221} Protein conductance in the nanosiemens range (1 nS ~ 1.3·10⁻⁵ G₀ quantum conductance) were measured for protein junctions exceeding 2 nm and were determined to be dominated by contact resistance.²²⁰ Contacting different engineered sites of the protein²¹⁶ and making use of repeating monomer units,²¹⁸ they have precisely characterized the ETp distance dependence. Proteins support long-range ETp with a moderate distance decay compared to the steep exponential decay of canonical molecular wires that they outperform for long distances (> 6 nm).²¹⁸ In ETp protein junctions, current-voltage spectroscopy has revealed a conductance gating in several non-redox proteins²¹⁹ which suggests that the polypeptide matrix supports a ubiquitous charge exchange mechanism for proteins in ETp configuration.²¹²

Current-distance spectroscopy

Current-distance spectroscopy gives access to the decay constant β of the protein mediated charge exchange between the probe and sample electrodes. This characteristic value was employed to identify matching DNA bases immobilized in the sample and probe electrodes.⁸⁶ In another current-distance spectroscopy study, probes functionalized with tetraheme cytochrome from metal-reducing bacterium, *Shewanella Oneisensis*, increased the tunnelling distance with hematite (Fe₂O₃) substrates.⁸⁵

In Az protein, it was observed that the β value is modulated by the electrode potential, with β values of 3 nm^{-1} and 4.5 nm^{-1} in resonant and non-resonant conditions respectively.⁸⁷ This gating effect is related to the redox activity of Az, since no β -gating effect is observed in redox inactive Zn-Az. In these works,^{85,87} the effect of the ionic strength and the electrical double layer on the close-distance quasi-linear regime was discussed, for Az⁸⁵ in Au[111] electrodes and tetraheme cytochrome on hematite substrates.⁸⁵ The starting point of this dissertation are the experiments carried out on the current-distance spectroscopy of PSI complexes.²²² Current-distance spectroscopy at different potentials reveals electrochemically gated long range charge exchange near, with current extending farther under hole injection conditions.²²²

Current-distance spectroscopy was extended to the study of interprotein charge exchange between redox cognate partners of the mitochondrial respiratory chain, the human mitochondrial complex III (CIII), simplified by the cytochrome *bc*₁, and cytochrome *c* (Cc), functionalizing probe and sample electrodes respectively. In this protein-protein configuration, β modulation with electrode potential is also observed. Remarkably long-distance electron transfer is measured as both electrodes match the redox level of the respective proteins, with current-distances traces spanning for $> 10 \text{ nm}$, with associated $\beta < 1 \text{ nm}^{-1}$. Molecular dynamics simulations revealed an ion depletion zone between the cognate partners that establishes a Guoy-Chapman conduit that prevents screening of the electric potential between the interacting redox centres. This local cation depletion is associated with a lysine ring around the redox centres that accumulates anions and drain cations from the interacting hydrophobic patch.²²³ Recently, it was shown that the screening capability of the lysine ring is lost upon phosphorylation, which suggests that the observed long-range charge exchange can be physiologically regulated.²²⁴

A variant of current-distance spectroscopy is the tapping or break-junction method, in which the probe is brought into contact with the sample electrode and then retracted to facilitate molecule trapping.⁸⁴ While this method has been widely used for organic molecules,²²⁵ it has been less employed in protein junctions.²¹¹ The current signal (and thus the conductance, for a fixed bias) exhibits plateaus as the probe is retracted from the sample, indicating the formation of a junction. Conductance histograms reveal a peak associated to the protein junction conductance. This conductance also exhibits a gating effect in Az, that vanishes for redox inactive Zn-Az.²¹¹

Blinking

To prevent protein squeezing, the formation of protein junctions can be studied with blinking technique. The formation of spontaneous protein junctions is associated with sudden current increases resulting in a telegraphic noise signal (see experimental methods section 3.3). The associated conductance increase also displays a gating effect in accordance with the apparent height, current-voltage and current-distance spectroscopies,

and bulk measurements.⁸³ It has been shown that single point mutations in Az can modulate the lifetime of the junction and notably the charge transport regime.¹²⁴ In polymerase enzymes, the blinking signal has been used to evaluate its activity. In particular, polymerase $\phi 29$ was linked between probe and sample electrodes. Open and closed conformations were identified in the blinking signal allowing to monitor the enzymatic activity.²¹⁹ Highly stable tunnelling junctions suitable for blinking experiments have been recently developed.²¹⁴ This robust configuration allows to resolve distinct conductance channels of proteins ETp which are gated by the bias potential.²¹⁴

5.3 PSI based bio-hybrid devices

Eventually, we provide an applied perspective complementary to the basic research scope of chapters 3-6 highlighting several PSI-based biohybrid devices. With the same aim, in chapter 7 in we present our results with a proof-of-concept of a PSI based herbicide biosensor.

Thanks to the high quantum yield of PSI, and to the energy difference between the redox potential of the electron donor and acceptor cofactors, PSI-complexes are promising candidates for bio-hybrid photovoltaic devices^{136,226} and biofuel photocatalysts.²²⁷ Improvements in PSI functionalization strategies,⁹³ and the ET to the electrodes with soluble and polymer conjugated redox mediators (see section 3.4.3), have increased the photocurrent output²²⁶ from few $\text{nA}\cdot\text{cm}^{-2}$ up to $\text{mA}\cdot\text{cm}^{-2}$. In order to assess the limitations and bottlenecks of PSI-biohybrid photovoltaics, time resolved spectrochemical experiments have been performed leading to the conclusion that the ET limits the efficiency of the device.²²⁸ One of the major drawbacks of PSI-based photovoltaic devices is their limited stability.²²⁹ *Zhao et al.* showed that illuminating PSI-bioelectrodes produces partially reactive oxygen species that compromises the stability of the protein complexes.⁹⁵ therefore the operational lifetime of the devices was shown to be extended under anaerobic conditions.⁹⁸ Recently, storage stability of years and operation lifetimes over a month were achieved with bacterial RC based bioelectrodes stabilizing the ET pathways between protein and electrode.¹³⁷ Another strategy increasing the effective lifetime of the device was based on renewal of the photosynthetic complexes on the electrode in self-regenerating devices.²³⁰

Other applications of photosynthetic reactions centres are diverse, such as biodegradable photoelectrochemical cells,²³¹ charge storage,²³² UV detectors,²³¹ and touch sensors.²³³ Regarding herbicide biosensors, the photocurrent inhibition of bacterial RC has been employed to detect the concentration of quinone site inhibitors.²³⁴

Chapter 2

Objectives

The core of this dissertation deals with **interprotein electron transfer (ET)**, that is canonically described by diffusion, binding, and actual charge exchange stages. We pursue **the objective to separate the contribution of binding and charge exchange from the overall ET process** between PSI and Pc.

In general terms, as the underlying mechanisms of interprotein ET and ETp are poorly understood, we seek to:

General objective 1

To elucidate the mechanism of charge exchange between PSI and Pc in individual complexes.

To do so, we make use of the nanoprobe-based techniques AFM and ECSTM, allowing to control the relative position of the proteins, and sample preparation techniques allowing to control the composition, relative orientation, and redox state of the proteins involved in ET. To meet this goal, we set the following specific objectives:

Specific objectives

- 1.1 Develop experimental tools allowing robust unidirectional immobilization of both Pc and PSI onto electrodes and AFM and ECSTM probes.
- 1.2 Characterize protein binding to gold electrodes, protein stability and functionality under experimental conditions and determine the working electrochemical window.
- 1.3 Study the ET dependence with distance of PSI, Pc and PSI-Pc complex.
- 1.4 Measure the conductance of individual PSI-Pc complexes.
- 1.5 Distinguish the contributions of the Pc Cu redox centre and of the Pc protein structure to charge exchange with PSI.

General objective 2

To measure the influence of the proteins' redox state on their binding.

Specific objectives

2.1 Establish strategies for orthogonal control of the PSI and Pc redox state.

Making use of these tools we aim to:

2.2 Measure the binding frequency and the unbinding force of the PSI-Pc complex by means of SMFS.

General objective 3

To characterize, model, and exploit the transient photocurrent output of PSI biohybrid electrodes.

Specific objectives

3.1 Proof the viability of a PSI-based herbicide biosensor.

3.2 Proof the viability of photo-electrochemical current 2d-electronic spectroscopy (PEC2DES) by (1) integrating a PSI photo-electrochemical current detection set-up with a collinear phase-modulated 4-pulse 2d-spectroscopy excitation scheme, and (2) optimizing the electrochemical photo-current output of PSI-bound electrodes to yield photo-current transient signals with amplitude $> \mu A$ and in ms timescale .

Chapter 3

Distance and Potential Dependence of Charge Transport Through the Reaction Center of Individual Photosynthetic complexes

Distance and Potential Dependence of Charge Transport Through the Reaction Center of Individual Photosynthetic complexes

Manuel López-Ortiz,^{† 1,2} Ricardo A. Zamora,^{† 1,2}, Marina Inés Giannotti,^{1,2,3} Chen Hu,⁴ Roberta Croce,⁴ and Pau Gorostiza^{1,2,5*}

1. Institute for Bioengineering of Catalonia (IBEC), The Barcelona Institute of Science and Technology, Baldori Reixac 10-12, Barcelona 08028

2. Network Biomedical Research Center on Bioengineering, Biomaterials and Nanomedicine (CIBER-BBN), Madrid 28029

3. Department of Materials Science and Physical Chemistry, University of Barcelona, Martí i Franquès 1-11, Barcelona 08028

4. Biophysics of Photosynthesis. Dep. Physics and Astronomy, Faculty of Sciences, Vrije Universiteit Amsterdam, De Boelelaan 1081, 1081 HV Amsterdam

5. Catalan Institution for Research and Advanced Studies (ICREA), Barcelona 08010

** E-mail: pau@icrea.cat*

† These authors contributed equally to this work.

1 Abstract

Charge separation and transport through the reaction center of photosystem I (PSI) is an essential part of the photosynthetic electron transport chain. We have developed a strategy to immobilize and orient PSI complexes on gold electrodes allowing to probe the electron acceptor side of the complex, the chlorophyll special pair P700. Electrochemical scanning tunneling microscopy (ECSTM) imaging and current-distance spectroscopy of single protein complex shows a lateral size in agreement with its known dimensions, and a PSI apparent height that depends on the probe potential revealing a gating effect in protein conductance. In current-distance spectroscopy, we observe that the distance-decay constant of the current between PSI and the ECSTM probe depends on the sample and probe electrode potentials. The longest charge exchange distance (lowest distance-decay constant β) is observed at sample potential 0 mV/SSC (SSC: reference electrode silver/silver chloride) and probe potential 400 mV/SSC. These potentials correspond to hole injection into an electronic state that is available in the absence of illumination. We propose that a pair of tryptophan residues located at the interface between P700 and the solution and known to support the hydrophobic recognition of PSI redox partner plastocyanin, may have an additional role as hole exchange mediator in charge transport through PSI.

2 Introduction

Electron Transfer (ET) is a charge exchange process driven by the difference in redox potential between donor and acceptor species. In biology, ET is an essential component of the electron transport chains involved in cellular respiration and photosynthesis. ET in the photosystem I (PSI) complex has been extensively studied both for basic¹ and applied purposes.² PSI is a thylakoid membrane complex³ that transfers electrons from Plastocyanin in the luminal side to Ferredoxin in the stromal side upon light exposure. This is an energetically uphill process powered by the excitonic energy harvested by the pigments found in the reaction center and in the light harvesting complex (LHCI) associated to PSI. The combination of efficient excitonic energy transfer⁴ and fast ET (10^{-8} - 10^{-7} s)⁵ results in a quantum yield near unit for the PSI electron transport chain. This efficiency figure of merit is often used to highlight the potential of PSI in biohybrid solar energy harvesting.^{2,6,7} Upon illumination, PSI complexes are brought to a long-lived state formed by a pair of spatially and energetically distant redox cofactors: the photo-oxidized chlorophyll special pair P700+ (270 mV with respect to reference electrode silver/silver chloride, SSC)⁸ in the luminal side is an electron acceptor located 5 nm away from the terminal electron donor, the reduced iron sulfur cluster Fb- in the stromal side (Figure 1). Thus, for illuminated PSI complexes in physiological conditions, electrons flow from P700 to Fb.

Monitoring the ET of individual redox proteins allows singling out their contribution to the ensemble current and has been enabled by in situ scanning probe techniques along with methods to specifically connect proteins to planar conductive electrodes.⁹ Electrochemical scanning tunneling microscopy (ECSTM) studies of several metalloproteins^{9–15} have revealed a current enhancement or gating effect (see below) as the Fermi levels of the sample and probe electrodes align with the redox energy level of the protein. Alternative to ET, an electron transport (ETp) charge exchange mechanism has been proposed for protein junctions where the macromolecule contacts both electrodes. While ET is driven by redox potential, in ETp the charge exchange is driven by the potential drop between the electrodes.¹⁶ Although the physiological relevance of ETp through protein junctions is less studied than that of ET, understanding protein ETp is key to engineer protein-based electronic devices^{16,17} as ETp has been shown^{16,18–20} to be a ubiquitous charge conduction mechanism through the protein matrix of redox and non-redox proteins.²¹ In particular, ETp through PSI complexes in the dark, evidenced by the current rectifying behavior of oriented PSI monolayers^{22,23} is favored in the stroma-to-lumen direction (from Fb to P700) following the PSI natural dipole.²⁴ That is, in the dark the preferred sense of ETp in PSI is opposite to the physiological one. As a first step to link ET and ETp in PSI, we have chosen to study the behavior of PSI under dark conditions (non-redox active state) and we have applied potentials to favor currents in the sense of PSI ETp.

We evaluate the charge exchange between PSI's P700 side and ECSTM probe by estimating the current-distance decay constant $\beta \text{ nm}^{-1}$ of the process. In ET formalism, β is proportional to the electronic coupling between donor and acceptor molecular orbitals. Experimentally, the distance decay constant β of the ET between a prosthetic ruthenium atom and the copper center in Ru-modified Azurin (Az) mutants^{25,26} yields 11 nm^{-1} . For Az functionalized in gold electrodes with alkanethiol of different lengths,²⁷ a value of $\beta = 1.03 \pm 0.02 \text{ nm}^{-1}$ per CH_2 is found. In an ECSTM setup β can be directly evaluated from current-distance plots.²⁸ In this case, β accounts for the distance decay resulting from all charge exchange processes between the protein-functionalized sample and probe electrodes. For instance, the β value for bare gold electrodes in physiological medium is 10 nm^{-1} . In gold electrodes functionalized with Az proteins,²⁸ β is 4 nm^{-1} and similar β values have been obtained for DNA base pairs²⁹ and redox proteins.^{30,31} Moreover, β is modulated by the electrode potential and it is lowest (i.e. the spatial span of the current is longest) for electrode potentials matching the redox level of the protein^{28,30,31} or redox-active organic compound.³² Our previous results with PSI complexes³⁰ suggest that long distance charge transport is electrochemically gated.³⁰ In that work we used thiolated self-assembled monolayers (SAM) exposing a negatively charged surface, which have been largely employed for PSI immobilization.³³ The present study aims to determine the distance and potential dependence of ET/ETp through the P700 reaction

center of PSI and thus requires better defined protein orientation, and higher recognition specificity.

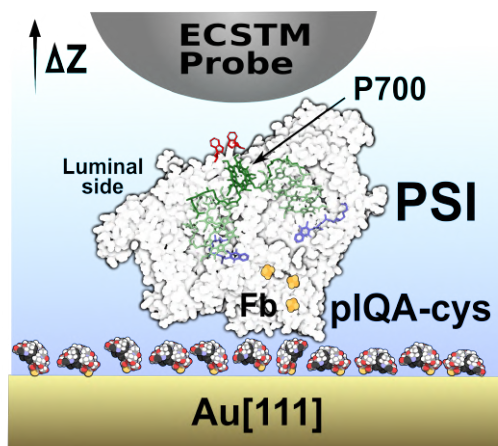


Figure 3.1: Scheme of the molecular arrangement set up in this work to attach and orient PSI complexes on Au[111] atomically flat electrodes. Peptides recognizing PSI stromal side with a C-terminal cysteine residue (pIQA-cys peptide) were attached to the gold surface in order to bind plant PSI complexes. This functionalization exposes the P700 site (luminal side) to the solution, enabling reproducible bulk photoelectrochemical measurements as well as single molecule measurements like scanning probe microscopy and spectroscopy. An electrochemical scanning tunneling microscopy (ECSTM) probe electrode is depicted on top of the PSI complex (reference and auxiliary electrodes are not shown for simplicity). The electrochemical potential and position (z) of the probe can be accurately controlled during charge exchange with the P700 site.

A preferential yet heterogeneous orientation of PSI molecules is obtained with SAM-PSI electrostatic interactions.³³ PSI orientation can be inferred from the current-rectifying behavior of SAM-PSI monolayers evaluated with STM³⁴ and C-AFM.³⁵ Specific binding and orientation of cyanobacterial PSI complexes to ITO electrodes has been achieved with a synthetic peptide (pIQA)²³ that binds to the stromal side of cyanobacterial PSI from *Thermosynechococcus elongatus*. PSI orientation was evaluated from the current-rectifying behavior of the PSI-pIQA-ITO monolayer. To investigate the charge exchange process with the P700 site in PSI, here we have designed a pIQA derivative to bind and orient plant PSI complexes on atomically flat gold electrodes. We reasoned that the pIQA structure would be recognized by the plant PSI based on the sequence similarity between the PSI stromal side regions from cyanobacterial PSI and plant PSI (see Supporting Information and Supplementary Figures S1-S4). We modified the pIQA peptide for Au substrate attachment by introducing a cysteine (pIQA-cys).²³ The resulting PSI-pIQA-cys-Au functionalization yields robust macroscopic photocurrents in a wide potential window and enables reproducible high-resolution microscopy and spectroscopy of individual PSI complexes. In these conditions, the charge exchange between the P700

site exposed to the solution and the ECSTM probe reveals long distance dependence (low β) and electrochemical gating. The results are in agreement with hole injection into PSI and reveal the presence of a low-energy state in the absence of illumination.

3 Results and discussion

AFM of PSI-pIQA-cys-Au electrodes (Figure 2a-c) shows the presence of a homogeneous and partial electrode surface coverage of 6 nm thickness, which is in agreement with previously reported PSI assemblies on gold^{36,37} (see Supplementary Information and Supplementary Figure S5). The lateral size of PSI single particles was not determined due to limited AFM probe resolution. Single complex resolution is achieved in ECSTM image (Figure 2d-e). For each complex, long and short axes in the horizontal plane were fit with a 2D-gaussian model (Supplementary Figure S6). Size distribution for N=334 particles yields 6.5 ± 0.1 nm and 10.7 ± 0.3 nm for short and long axes respectively. Protein lateral sizes, taken as full width at half maximum, are 60% and 70% smaller than available crystallographic structure of PSI-LHCI structure,³⁸ with an approximate size of 10.5 nm and 15 nm, respectively.

The topography (apparent height) of PSI-pIQA-cys-Au samples observed by ECTSM (Figure 3a) is tenfold lower than that observed by AFM (Figures 2ab). This result agrees with previous reports about PSI complexes on alkanethiol-functionalized gold substrates.³⁰ Since ECSTM is operated in constant current feedback mode, the apparent height is due both to the topography and to the conductance of the sample. ECSTM apparent heights lower than the known structural dimensions have been observed for several proteins deposited on metal substrates.^{27,39-43} These results confirm that protein conductance is larger than that of the surrounding electrolytic medium, both in metalloproteins⁴⁴⁻⁴⁶ and interestingly in non-redox active proteins.^{18,19} In addition, we observe that the apparent height of PSI complexes by ECSTM depends on the probe potential UP (Figure 3a). This effect allows using ECSTM imaging at different electrochemical potentials to study their conductance and charge transport properties. Several works showed a similar dependence in the small globular protein azurin,^{12,13} and more recently in a 100 kDa oxidoreductase complex.⁴⁷ This gated conductance resonance is attributed to the alignment of the Fermi levels of the ECSTM sample and probe electrodes with the redox energy (molecular orbital) of the molecule under study.

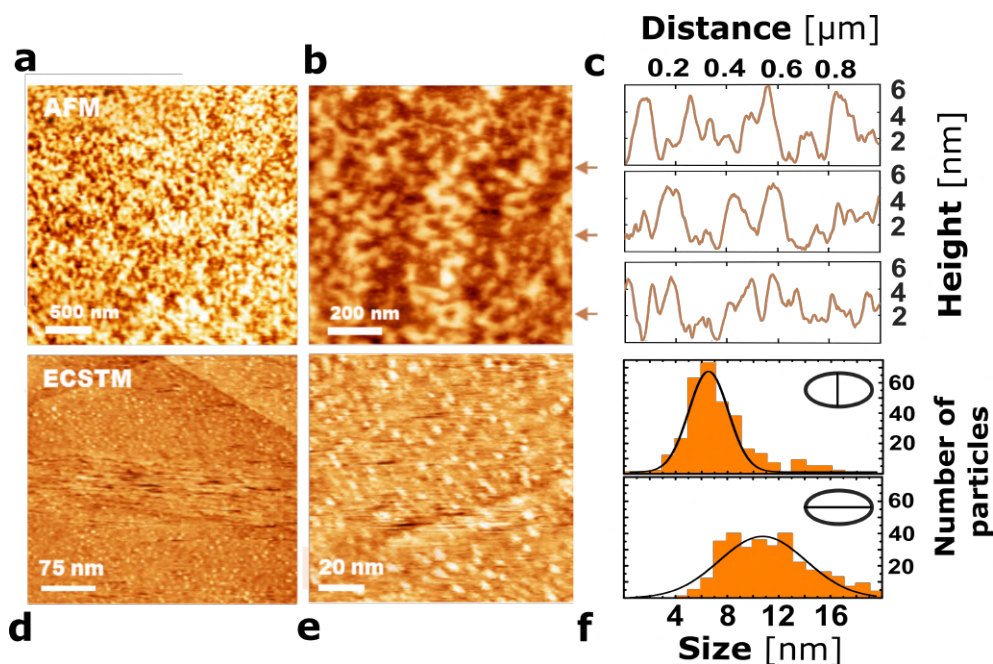


Figure 3.2: Structural characterization of of PSI-pIQa-cys-Au films attached to atomically flat Au[111] electrodes. AFM image of PSI-pIQa-cys-Au, a) scan size $3 \times 3 \mu\text{m}$ and b) $1 \times 1 \mu\text{m}$. The vertical (z) color scale is set to 8 nm amplitude. c) Example AFM height profiles at the positions indicated with arrows in panel (b). ECSTM images of the same sample, d) $350 \times 350 \text{ nm}$ and e) $150 \times 150 \text{ nm}$. The vertical (z) color scales correspond to 1.4 and 1.1 nm, respectively. The set point tunnel current is 0.2 nA and the bias is 300 mV ($U_{\text{sample}} = 0 \text{ mV/SSC}$, $U_{\text{probe}} = 300 \text{ mV/SSC}$). f) Distribution of ECSTMparticle size, short axis (top), and long axis (bottom).

To define a working electrochemical window, chopped light cyclic voltammetry (CV) experiments (Supplementary Figures S7, S8 and S9) were performed. Soluble redox mediators methyl viologen ($125 \mu\text{M}$) and osmium bipyridine dichloride ($10 \mu\text{M}$) were added to the buffer solution to enhance photocurrents and facilitate the characterization.³⁷ Illuminating PSI complexes at $U_{\text{sample}} = -100 \text{ mV/SSC}$ produces photocurrents with $1 \mu\text{A}\cdot\text{cm}^{-2}$ transient and $200 \text{ nA}\cdot\text{cm}^{-2}$ steady components (Figure 3b and Supplementary Figure S8) while no photocurrents are observed in the absence of PSI (Supplementary Figure S7). Photocurrents depend on the applied sample potential and can only be measured below 100 mV/SSC. Potential excursions within the range -200 mV/SSC to 300 mV/SSC do not alter the magnitude of photocurrents, but they are reduced after applying potentials outside this "safe" electrochemical window (Supplementary Figures S8-S9). The photocurrent loss (Figure 3c) was estimated comparing photocurrents measured in a reference potential region between -100 mV/SSC and -25 mV/SSC (indicated by red traces in Figure 3b) before and after applying a test potential during 5 min (Supplementary Figure S8-S9). For potentials $U_{\text{sample}} < -200 \text{ mV/SSC}$, cathodic currents increase significantly due to the presence of O_2 in the electrochemical cell.⁴⁸⁻⁵⁰

After applying $U_{sample} = -400$ mV/SSC for 5 min (Supplementary Figure S8), the voltammogram is broadened indicating a decrease of the electrode capacity revealing a partial depletion of absorbed molecules while a decrease in photocurrent amplitude is also observed. Photocurrent degradation has been attributed to the formation of ROS in aerobic systems where O_2 acts as terminal electron acceptor.^{48,49} Similar irreversible decrease of photocurrent and electrode capacity is observed for positive potentials ($U_{sample} > 300$ mV/SSC) that could be associated to the desorption of molecules absorbed on the electrode. The appearance of an anodic peak at 500 mV/SSC (Supplementary Figure S8) in PSI-pIQA-cys samples that is not present in pIQA-cys samples and the stability pIQA-cys samples (red traces in Supplementary Figure S7) suggest that the decrease in photocurrent observed in Figure 3c could be attributed to PSI desorption.

Reversible and stable photocurrent measurements in the electrochemical window between -200 mV/SSC $< U_{sample} < +300$ mV/SSC indicate the presence of functional (photo-active) PSI complexes in the electrode. We took these values to set the sample potential boundaries to study single PSI spectroscopy with ECSTM in the dark. Thus, in Figures 2 and 3 the microscopic and bulk photocurrent characterization of PSI-pIQA-cys functionalized gold electrodes show: (i) functionalization of PSI complexes on gold electrodes modified with a cysteine peptide, (ii) conductance gating in the PSI apparent height measured by ECSTM, as reported for other proteins and complexes, (iii) bulk photocurrent measurements demonstrate that PSI complexes remain (photo)active upon attachment to the electrode, and (iv) a safe working electrochemical window is identified where PSI activity is retained. Finally, the activity of PSI-pIQA-cys-Au samples was tested with photo-chrono-amperometry, in the absence of redox mediators, before current decay spectroscopy experiments, acquiring photocurrents of $10 \text{ nA}\cdot\text{cm}^{-2}$ at $U_{sample} = -100$ mV/SSC (Supplementary Figure S10) while no photocurrents were observed in the absence of PSI complexes. These results set the stage for reproducible ECSTM current distance decay experiments in the next section.

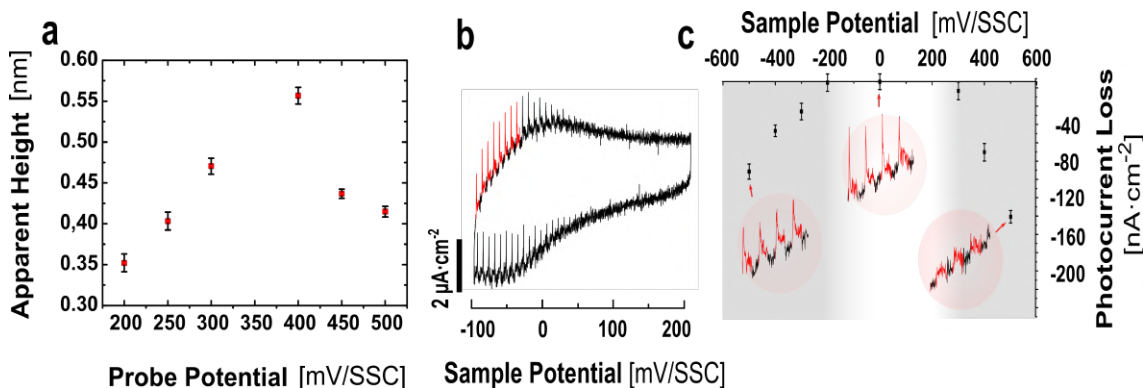


Figure 3.3: Dependence of PSI-pIQa-cys-Au microscopy and photocurrent recordings on the electrochemical potential: a) Apparent height of PSI complexes measured from ECSTM image profiles at different probe potentials UP (constant bias potential $U_{bias} = U_{probe} - U_{sample} = 300$ mV/SSC). A maximum PSI height is observed at $U_{probe} = 400$ mV/SSC indicating a conductance resonance as observed for redox proteins and complexes. b) Bulk photoelectrochemical current measured in a PSI-pIQa-cys-Au sample during cyclic voltammetry at 80 mV·s⁻¹ rate while switching on and off the 690 nm illumination every 125 ms (red and black traces, respectively). Photoresponses are observed at $U_{sample} < 100$ mV/SSC. c) An electrochemical potential window of PSI stability between 200 and +300 mV/SSC is identified where photocurrent loss is below 10% (white band and example photocurrent recording at the center, red traces corresponding to 690 nm illumination). Applying potentials outside this window diminishes photoresponses (indicated by grey bands and example photocurrent traces).

We used ECSTM to evaluate the distance decay constant of currents in PSI-pIQa-cys-Au samples at fixed locations. The charge exchange process between sample and probe electrodes was measured in dark conditions to prevent photo-oxidation of the P700 site²⁸ (i.e. in the absence of redox activity of PSI). ECSTM spectroscopy recordings were performed as previously described.²⁸ Briefly, we departed from a set-point current of 300 pA and switched off the feedback control loop prior to retracting the probe electrode (a Pt-Ir sharp tip) away from the sample electrode (an Au monocrystal, see Supplementary Information) at a constant rate, while measuring the probe current. Current-distance spectra were recorded under bi-potentiostatic control of probe and sample. We set 11 pairs of potentials for the sample ($U_{sample} = -100, 0, 100, 200$ mV/SSC) and probe ($U_{probe} = 200, 300, 400$ mV/SSC) which yield applied bias ranging from +100 mV to +500 mV ($U_{bias} = U_{probe} - U_{sample}$). The positive sign in bias potential was chosen to follow the favored sense of ETP for PSI in dark from stroma to lumen.^{22,23} Logarithmic current plots (Figure 4a) for PSI-pIQa-cys-Au (blue) show longer charge exchange distance with respect to pIQa-cys-Au controls (black). While most control traces are well described by a single exponential decay model, PSI data shows a double exponential behavior (Supplementary Figure S11). Double exponential traces exhibit a short distance regime with $z < 0.2$ nm (Supplementary Figure S12) and a second regime spanning from 0.2 nm to 1.0 - 2.5 nm depending on the applied probe potential. Beyond 2.5 nm the probe current is masked by faradaic currents (~ 25 pA) due to probe insulation defects. Double

exponential behavior has already been reported for DNA molecules²⁹ and proteins^{30,31} and has been attributed to the surface charge screening.²⁸

In the absence of PSI, the distribution of β values is centered around 7 nm^{-1} and is independent of potential. In contrast, the β for PSI-pIQA-cys-Au depends both on the sample and probe potentials. At sample potentials above 100 mV/SSC , β is around $4\text{-}5 \text{ nm}^{-1}$, similar to previously reported values for Az²⁸ and PSI complexes.³⁰ However, at sample potentials equal or below 0 mV/SSC and probe potential 400 mV/SSC we obtained β values below 2 nm^{-1} , which cannot be accounted for by a tunneling mechanism and are reminiscent of the long-distance currents observed for cytochromes.³¹

The effect of sample and probe potentials on β distributions (see Supplementary Figure S13) is shown respectively in Figures 5a and 5b. We remark that β values below 4 nm^{-1} are only found for $U_{\text{sample}} < 100 \text{ mV/SSC}$ irrespective of the applied probe potential. Thus, applying a sample potential $U_{\text{sample}} < 100 \text{ mV/SSC}$ is a necessary condition for enhanced charge exchange distance in the dark. Interestingly, bulk photoelectrochemical currents are only observed below this potential (Figure 3b). Fulfilled this condition ($U_{\text{sample}} < 100 \text{ mV/SSC}$), β decreases as the probe potential is increased (Figure 5b). The lowest β values (longest charge exchange distances) are found at $U_{\text{P}} = 400 \text{ mV/SSC}$ and bias potentials $U_{\text{bias}} = 500 \text{ mV}$ ($U_{\text{s}} = 0 \text{ mV/SSC}$) and $U_{\text{bias}} = 400 \text{ mV}$ ($U_{\text{s}} = 0 \text{ mV/SSC}$). These results suggest that farthest-reaching currents are due to the probe potential (Fermi energy position around -5.0 eV versus the vacuum level) irrespectively of the applied bias (driving force). The β values as a function of sample and probe electrodes are summarized in Figure 6.

It has been reported that β values in redox proteins^{28,30,31} and organic compounds³² depend on the electrode potentials. In PSI-pIQA-cys-Au, β values depend on the probe rather than on the sample potential (provided that -100 mV/SSC). We argue that the electric potential at the luminal side of PSI complexes is set by the probe electrode facing the P700 side while the sample potential is screened by pIQA-cys peptide and the 5 nm thick PSI protein matrix. In this sense, the probe electrode can be likened to a PSI redox partner under potentiostatic control.

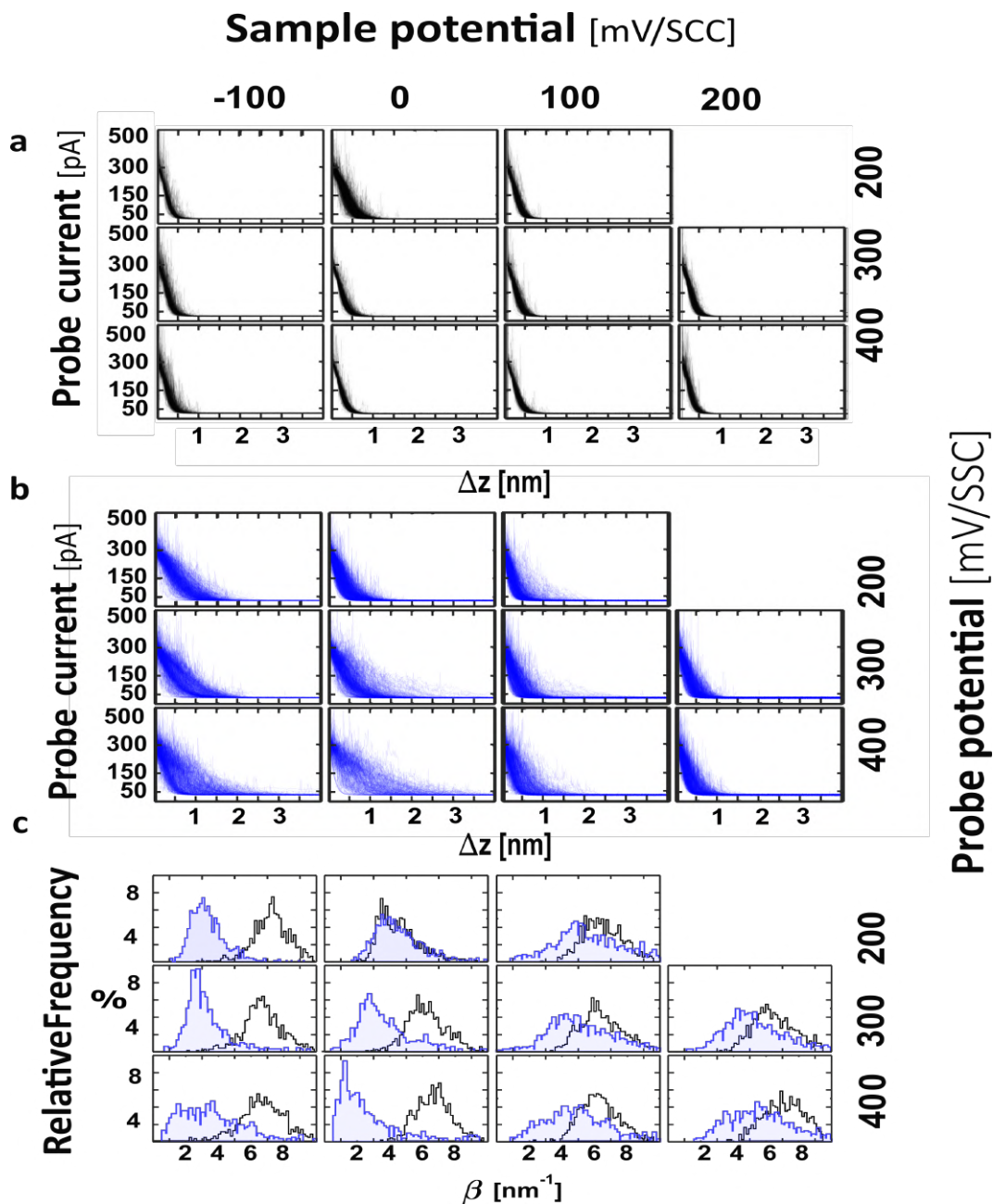


Figure 3.4: Electrochemical current–distance spectroscopy measurements with ECSTM at different sample and probe potentials: a) Semilogarithmic plots of $I(z)$ recordings of pIQA-cys-Au samples (black) and b) PSI-pIQA-cys-Au (blue) at U_{sample} potentials within the safe window for PSI activity and at U_{probe} potentials to probe charge exchange with PSI using moderate bias values. Long distance decay is observed around $U_{sample} = 0$ mV/SSC and $U_{probe} = 400$ mV/SSC. c) Normalized distribution of β distance-decay rates obtained for each condition in panels (a,b). Low values of β (≈ 1 nm⁻¹) are observed at $U_{sample} = 0$, $U_{probe} = 400$ mV/SSC

In these experiments we have focused in ETp through PSI bound to the sample electrode via pIQA-cys peptide and we have avoided ET (redox) effects like direct oxidation of P700 site by carrying out current-distance recordings in dark conditions. However, in contrast to ETp measurements, no direct molecular bond is established between the luminal side of PSI and the ECSTM probe and thus current flow depends to some extent on the aqueous solution, which may involve water molecules and protons as it occurs in ET. This partial electronic decoupling between the electrode and PSI can be seen as an advantage of ECSTM that enabled us to observe gating effects in imaging and spectroscopic experiments of PSI (Figures 3 and 4), as previously found for cytochrome c and azurin. It might allow studying the role of electronic coupling between PSI and its partners in the overall photosynthetic electron transport chain.

We reasoned that the dependence of β on U_{probe} (Figure 6) could be due to the presence of a cofactor or residue on the luminal surface whose molecular orbital could be electronically coupled to the ECSTM probe at 400 mV/SSC (low electron energies). We thus examined the residues on the luminal surface of PSI that could mediate this process, and noticed a pair of tryptophan residues (Trp625 and Trp658 in Figure 6d)³⁸ that is located in the proximity of P700 and integrates the hydrophobic recognition site of plastocyanin (Pc), an electron donor partner protein of PSI.^{51–53} Tryptophan is an oxidizable aromatic residue whose redox activity is involved in photosynthetic water splitting, nucleic acid biosynthesis, and cell signaling, acting as a hole carrier. It plays a major role in proton-coupled electron transfer,^{54,55} and it mediates photoinduced long range ET in photolyase^{56,57} and in dye-modified Az mutants.^{58,59} In plants cryptochrome, the ET constant is modified by two orders of magnitude by ATP binding and by pH modulating the electronic coupling of a Trp residue.⁶⁰ Regarding protein-electrode interfaces, it has been proposed that charge exchange is modulated by electronic coupling between electrode Fermi level and the molecular orbitals of interfacing residues.^{18,20,21,44,45,61,62} Remarkably, introducing Trp residues in 6-Alanine peptides increases their molecular conductance, lowering the effective barrier height and enhancing electronic coupling with gold electrodes.⁶³ In addition, cyclic voltammetry features of Az are abolished if the Trp residue mediating ETp with the electrode is mutated.⁶⁴ All these results suggest that aromatic Trp residues play a significant role in protein ET and in ETp. Based in our current-distance spectroscopy results, we hypothesize that surface exposed Trp625 and Trp658 may act as primary electron donors (hole acceptors) to the ECSTM probe, which would explain the gating of the apparent height and β .

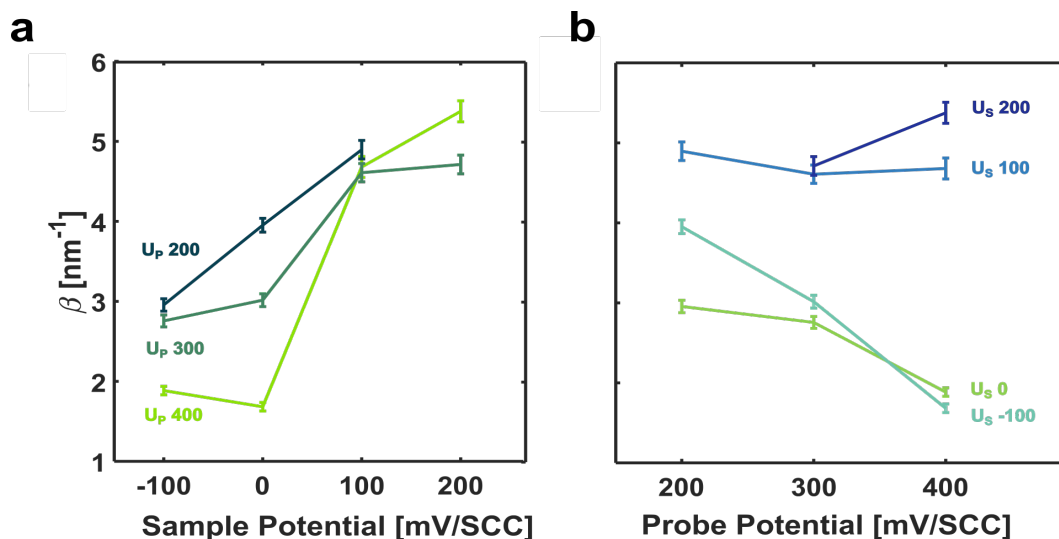


Figure 3.5: Dependence of the distance decay constant β of PSI-pIQa-cys-Au with the electrochemical potentials. The plots show the statistical representation of β values obtained from Figure 4c. a) β values vs applied sample potential. Probe potentials are indicated in color ($U_{probe} = 200, 300, 400$ mV/SSC for blue, light green, and dark green traces, respectively). b) β values vs applied probe potential with sample potential traces ($U_{sample} = 200, 100, 0,$ and -100 mV/SSC) represented in dark blue, light blue, green, and aquamarine respectively. The lowest values (corresponding to the farthest-reaching currents) are observed at $U_{sample} = 0$ mV/SSC and $U_{probe} = 400$ mV/SSC.

The physiological role of Trp residues has been studied in PSI and transient absorption experiments demonstrated that the ET kinetics of PSI with Pc are altered in *Chlamydomonas Reinhardtii* mutants Trp627Phe and Trp651Ser^{65, 66} (corresponding to Trp625 and Trp658 in *Arabidopsis Thaliana* respectively). In bulk transient absorption measurements, the kinetic contribution of the formation of a productive complex, reorganization, ET, and unbinding processes are indirectly inferred from the different time components of the transient absorption signal. In contrast, distance- and potential-dependent ECSTM experiments allow evaluating the independent contribution of the ET process to the overall charge transport process. Our results suggest that these Trp residues play an additional role as hole exchange mediators in PSI, possibly regulating ET through electronic coupling, in line with findings in other protein systems.

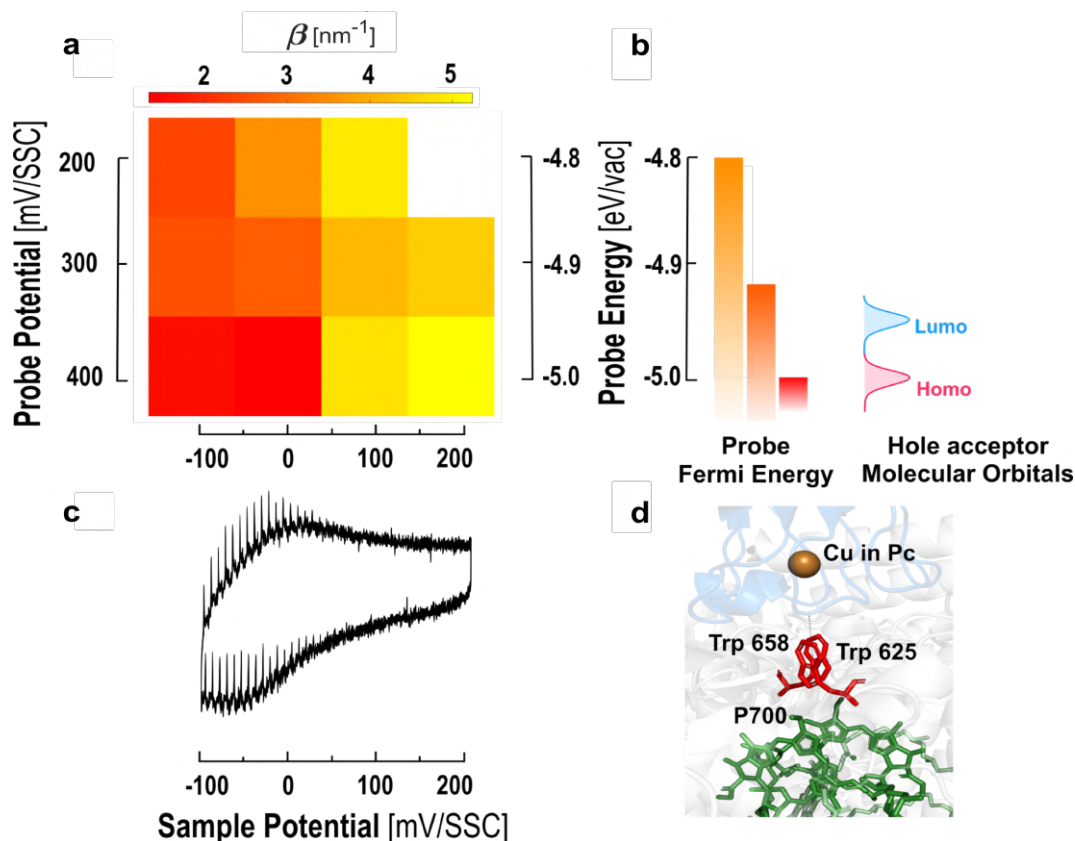


Figure 3.6: Diagram of distance-decay rates of PSI-pIQa-cys-Au showing electrochemically gated long distance current between the ECSTM probe and the P700 site of PSI in the dark. a) Distance decay rate β average values are plotted in color scale (red corresponding to 2 nm⁻¹ and yellow to 5 nm⁻¹) as a function of the probe and sample potentials and using the same layout as Figure 4. b) The correspondence of the vertical axis with the electron energy of the probe is shown in the scale on the right, together with a diagram depicting hole injection from the probe at $U_{probe} = 400$ mV/SSC into a hypothetical electron donor state of PSI in the dark. c) A chopped light voltammogram (Figure 3) is indicated under the horizontal axis to show the sample potential range of PSI photo-responses. d) Candidate electron donor sites that could mediate this current include a pair of oxidizable tryptophan residues (Trp625, Trp658, shown in red) located between P700 (green) and the copper active site of the PSI redox partner plastocyanin (Pc, orange).

4 Conclusions

In summary, we have developed a strategy to functionalize gold electrodes with plant PSI complexes that orients and exposes their luminal side to the electrolyte, in order to investigate charge exchange processes mediated by their P700 site. Sample preparation is based on a peptide sequence that binds specifically to the stromal side of PSI from cyanobacteria and plants and it should be applicable to a variety of complexes and substrates. Bulk photoelectrochemical measurements demonstrate that

PSI complexes remain fully functional in a wide window around 0 mV/SSC sample potential. Nanoscale imaging of individual complexes shows lateral sizes in agreement with the dimensions of PSI and an apparent height that is electrochemically gated for ECSTM probe potentials around 400 mV/SSC. This experimental setup enables for the first time spectroscopic measurements with ECSTM (current-distance decay at different electrochemical potentials) that unequivocally correspond to the P700 side of PSI exposed to the aqueous medium. In these conditions, we observe that the spatial span of the current is enhanced (the distance-decay constant β is reduced) through the solution at sample potential 0 mV/SSC and probe potential 400 mV/SSC. This process corresponds to hole injection into an electronic state that is available in the absence of illumination. We propose that a pair of tryptophan residues (Trp625, Trp658) located near P700 and known to integrate the hydrophobic recognition site for Pc may have an additional role as hole exchange mediator involved in the charge transport process through PSI.

5 Acknowledgements

This research received funding from the European Union Research and Innovation Programme Horizon 2020 - HBP SG3 (945539), DEEPER (ICT-36-2020-101016787), Agency for Management of University and Research Grants/Generalitat de Catalunya (CERCA Programme, 2017-SGR-1442), Fonds Européen de Développement Economique et Régional (FEDER) funds, Ministry of Science and Innovation (Grant PID2019-111493RB- I00, CTQ2015-66194-R). The project CECH, 001-P-001682 is co-financed by the European Union Regional Development Fund within the framework of the ERDF Operational Program of Catalonia 2014-2020 with a grant of 50% of total eligible cost. R.Z. was supported by Becas Chile fellowship 74190117 from the government of Chile.

6 Bibliography

1. K. Brettel, *Biochim. Biophys. Acta, Bioenerg.* **1997**, 1318, 322.
2. A. H. Teodor, B. D. Bruce, *Trends Biotechnol.* **2020**, 38, 1329.
3. J. H. Golbeck, *Photosystem I: The Light-Driven Plastocyanin:Ferredoxin Oxidoreductase*, Advances in Photosynthesis and Respiration , Vol. 24, **2010**.
4. R. Croce, H. van Amerongen, *Science* **2020**, 369, eaay2058.
5. P. R. Chitnis, *Annu. Rev. Plant Physiol. Plant Mol. Biol.* **2001**, 52, 593.

6. X. Qiu, O. Castaneda, E. Ocampo, H. W. de Vries, M. van Putten, M. Loznik, A. Herrmann, R. C. Chiechi, *ACS Appl. Mater. Interfaces* **2018**, *10*, 37625.
7. N. Nelson, *J. Nanosci. Nanotechnol.* **2009**, *9*, 1709.
8. A. Nakamura, T. Suzawa, Y. Kato, T. Watanabe, *Plant Cell Physiol.* **2011**, *52*, 815.
9. P. Salvatore, D. Zeng, K. K. Karlsen, Q. Chi, J. Wengel, J. Ulstrup, *ChemPhysChem* **2013**, *14*, 2101.
10. J. Zhang, A. M. Kuznetsov, J. Ulstrup, *J. Electroanal. Chem.* **2003**, *541*, 133.
11. J. Zhang, Q. Chi, A. M. Kuznetsov, A. G. Hansen, H. Wackerbarth, H. E. M. Christensen, J. E. T. Andersen, J. Ulstrup, *J. Phys. Chem. B* **2002**, *106*, 1131.
12. A. Alessandrini, S. Corni, P. Facci, *Phys. Chem. Chem. Phys.* **2006**, *8*, 4383.
13. Q. Chi, O. Farver, J. Ulstrup, *Proc. Natl. Acad. Sci. USA* **2005**, *102*, 16203.
14. J. M. Artés, M. López-Martínez, I. Díez-Pérez, F. Sanz, P. Gorostiza, *Small* **2014**, *10*, 2537.
15. M. López-Martínez, J. M. Artés, V. Sarasso, M. Carminati, I. Díez-Pérez, F. Sanz, P. Gorostiza, *Small* **2017**, *13*, 1700958.
16. C. D. Bostick, S. Mukhopadhyay, M. Sheves, D. Cahen, D. Lederman, *Rep. Prog. Phys.* **2018**, *81*, 026601.
17. J. M. Artés, I. Díez-Pérez, P. Gorostiza, *Nano Lett.* **2012**, *12*, 2679.
18. B. Zhang, W. Song, J. Brown, R. Nemanich, S. Lindsay, *J. Am. Chem. Soc.* **2020**, *142*, 6432.
19. B. Zhang, W. Song, P. Pang, H. Lai, Q. Chen, P. Zhang, S. Lindsay, *Proc. Natl. Acad. Sci. U.S.A.* **2019**, *116*, 5886.

20. I. Ron, L. Sepunaru, S. Ltzhakov, T. Belenkova, N. Friedman, I. Pecht, M. Sheves, D. Cahen, *J. Am. Chem. Soc.* **2010**, *132*, 4131.
21. S. Lindsay, *Life* **2020**, *10*, 72.
22. O. E. Castaneda Ocampo, P. Gordiichuk, S. Catarci, D. A. Gautier, A. Herrmann, R. C. Chiechi, *J. Am. Chem. Soc.* **2015**, *137*, 8419.
23. P. Gordiichuk, D. Pesce, O. E. C. Ocampo, A. Marcozzi, G.-J. A. H. Wetzelaer, A. Paul, M. Loznik, E. Gloukhikh, S. Richter, R. C. Chiechi, A. Herrmann, *Adv. Sci.* **2017**, *4*, 1600393.
24. B. van Haeringen, J. P. Dekker, M. Bloemendal, M. Rögner, R. van Grondelle, H. van Amerongen, *Biophys. J.* **1994**, *67*, 411.
25. R. Langen, I. J. Chang, J. P. Germanas, J. H. Richards, J. R. Winkler, H. B. Gray, *Science* **1995**, *268*, 1733.
26. J. R. Winkler, H. B. Gray, *Chem. Rev.* **2014**, *114*, 3369.
27. Q. Chi, J. Zhang, J. E. T. Andersen, J. Ulstrup, *J. Phys. Chem. B* **2001**, *105*, 4669.
28. J. M. Artés, I. Díez-Pérez, F. Sanz, P. Gorostiza, *ACS Nano* **2011**, *5*, 2060.
29. J. He, L. Lin, P. Zhang, S. Lindsay, *Nano Lett.* **2007**, *7*, 3854.
30. M. López-Martínez, M. López-Ortiz, M. E. Antinori, E. Wientjes, A. Nin-Hill, C. Rovira, R. Croce, I. Díez-Pérez, P. Gorostiza, *Angew. Chem., Int. Ed.* **2019**, *58*, 13280.
31. A. Lagunas, A. Guerra-Castellano, A. Nin-Hill, I. Díaz-Moreno, M. A. de la Rosa, J. Samitier, C. Rovira, P. Gorostiza, *Nat. Commun.* **2018**, *9*, 3.
32. D. I. Gittins, D. Bethell, D. J. Schiffrin, R. J. Nichols, *Nature* **2000**, *408*, 67.
33. G. Leblanc, E. Gizzie, S. Yang, D. E. Cliffl, G. K. Jennings, *Langmuir* **2014**, *30*, 10990.

34. I. Lee, J. W. Lee, E. Greenbaum, *Phys. Rev. Lett.* **1997**, *79*, 3294.
35. D. Mukherjee, M. May, M. Vaughn, B. D. Bruce, B. Khomami, *Langmuir* **2010**, *26*, 16048.
36. A. K. Manocchi, D. R. Baker, S. S. Pendley, K. Nguyen, M. M. Hurley, B. D. Bruce, J. J. Sumner, C. A. Lundgren, *Langmuir* **2013**, *29*, 2412.
37. X. Qin, M. Suga, T. Kuang, J. R. Shen, *Science* **2015**, *348*, 989.
38. D. Alliata, L. Andolfi, S. Cannistraro, *Ultramicroscopy* **2004**, *101*, 231.
39. L. Andolfi, G. W. Canters, M. P. Verbeet, S. Cannistraro, *Biophys. Chem.* **2004**, *107*, 107.
40. L. Andolfi, B. Bonanni, G. W. Canters, M. P. Verbeet, S. Cannistraro, *Surf. Sci.* **2003**, *530*, 181.
41. J. Zhang, Q. Chi, J. U. Nielsen, E. P. Friis, J. E. T. Andersen, J. Ulstrup, *Langmuir* **2000**, *16*, 7229.
42. J. Zhang, H. E. M. Christensen, B. L. Ooi, J. Ulstrup, *Langmuir* **2004**, *20*, 10200.
43. K. Garg, M. Ghosh, T. Eliash, J. H. van Wonderen, J. N. Butt, L. Shi, X. Jiang, F. Zdenek, J. Blumberger, I. Pecht, M. Sheves, D. Cahen, *Chem. Sci.* **2018**, *9*, 7304.
44. Z. Futera, I. Ide, B. Kayser, K. Garg, X. Jiang, J. H. van Wonderen, J. N. Butt, H. Ishii, I. Pecht, M. Sheves, D. Cahen, J. Blumberger, *J. Phys. Chem. Lett.* **2020**, *11*, 9766.
45. C. Baldacchini, A. R. Bizzarri, S. Cannistraro, *Eur. Polym. J.* **2016**, *83*, 407.
46. J. Yan, E. E. Frokjar, C. Engelbrekt, S. Leimkühler, J. Ulstrup, U. Wollenberger, X. Xiao, J. Zhang, *ChemElectroChem* **2021**, *8*, 164.
47. J. Yan, E. E. Frokjar, C. Engelbrekt, S. Leimkühler, J. Ulstrup,

- U. Wollenberger, X. Xiao, J Zhang, *ChemElectroChem* **2021**, *8*, 164.
48. F. Zhao, A. Ruff, M. Rögner, W. Schuhmann, F. Conzuelo, *J. Am. Chem. Soc.* **2019**, *141*, 5102.
49. T. Bennett, H. Niroomand, R. Pamu, I. Ivanov, D. Mukherjee, B. Khomami, *Phys. Chem. Chem. Phys.* **2016**, *18*, 8512.
50. M. Hervás, J. A. Navarro, B. de La Cerda, A. Díaz, M. A. de La Rosa, *Bioelectrochem. Bioenerg.* **1997**, *42*, 249.
51. T. Ueda, N. Nomoto, M. Koga, H. Ogasa, Y. Ogawa, M. Matsumoto, P. Stampoulis, K. Sode, H. Terasawa, I. Shimadaa, *Plant Cell* **2012**, *24*, 4173.
52. A. B. Hope, *Biochim. Biophys. Acta, Bioenerg.* **2000**, *1456*, 5.
53. A. Migliore, N. F. Polizzi, M. J. Therien, D. N. Beratan, *Chem. Rev.* **2014**, *114*, 3381.
54. E. F. Yee, B. Dzikovski, B. R. Crane, *J. Am. Chem. Soc.* **2019**, *141*, 17571.
55. F. Cailliez, P. Müller, T. Firmino, P. Pernot, A. de La Lande, *J. Am. Chem. Soc.* **2016**, *138*, 1904.
56. R. Martin, F. Lacombar, A. Espagne, N. Dozova, P. Plaza, J. Yamamoto, P. Müller, K. Brettel, A. de La Lande, *Phys. Chem. Chem. Phys.* **2017**, *19*, 24493.
57. C. Shih, A. K. Museth, M. Abrahamsson, A. M. Blanco-Rodriguez, A. J. di Bilio, J. Sudhamsu, B. R. Crane, K. L. Ronayne, M. Towrie, A. Vlček, J. H. Richards, J. R. Winkler, H. B. Gray, *Science* **2008**, *320*, 1760.
58. K. Takematsu, H. R. Williamson, P. Nikolovski, J. T. Kaiser, Y. Sheng, P. Pospíšil, M. Towrie, J. Heyda, D. Hollas, S. Zálíš, H. B. Gray, A. Vlček, J. R. Winkler, *ACS Cent. Sci.* **2019**, *5*, 192.
59. F. Cailliez, P. Mu, M. Gallois, A. de la Lande, *J. Am. Chem. Soc.* **2014**,

136, 12974.

60. J. A. Fereiro, G. Porat, T. Bendikov, I. Pecht, M. Sheves, D. Cahen, *J. Am. Chem. Soc.* **2018**, *140*, 13317.

61. X. Yu, R. Lovrincic, L. Sepunaru, W. Li, A. Vilan, I. Pecht, M. Sheves, D. Cahen, *ACS Nano* **2015**, *9*, 9955.

62. C. Guo, X. Yu, S. Refaely-Abramson, L. Sepunaru, T. Bendikov, I. Pecht, L. Kronik, A. Vilan, M. Sheves, D. Cahen, *Proc. Natl. Acad. Sci. U.S.A.* **2016**, *113*, 10785.

63. K. Fujita, N. Nakamura, H. Ohno, B. S. Leigh, K. Niki, H. B. Gray, J. H. Richards, *J. Am. Chem. Soc.* **2004**, *126*, 13954.

64. F. Sommer, F. Drepper, M. Hippler, *J. Biol. Chem.* **2002**, *277*, 6573.

65. F. Sommer, F. Drepper, W. Haehnell, M. Hippler, *J. Biol. Chem.* **2004**, *279*, 20009.

Supporting Information

Distance and Potential Dependence of Charge Transport Through the Reaction Center of Individual Photosynthetic complexes

Manuel López-Ortiz,^{†,1,2} Ricardo A. Zamora,^{†,1,2} Marina Inés Giannotti,^{1,2,3} Chen Hu,⁴ Roberta Croce,⁴ and Pau Gorostiza^{1,2,5*}

1. Institute for Bioengineering of Catalonia (IBEC), The Barcelona Institute of Science and Technology, Baldiri Reixac 10–12, Barcelona 08028

2. Network Biomedical Research Center on Bioengineering, Biomaterials and Nanomedicine (CIBER-BBN), Madrid 28029

3. Department of Materials Science and Physical Chemistry, University of Barcelona, Martí i Franquès 1-11, Barcelona 08028

4. Biophysics of Photosynthesis. Dep. Physics and Astronomy, Faculty of Sciences, Vrije Universiteit Amsterdam, De Boelelaan 1081, 1081 HV Amsterdam

5. Catalan Institution for Research and Advanced Studies (ICREA), Barcelona 08010

* E-mail: pau@icrea.cat

[†]These authors contributed equally to this work.

TABLE OF CONTENTS:

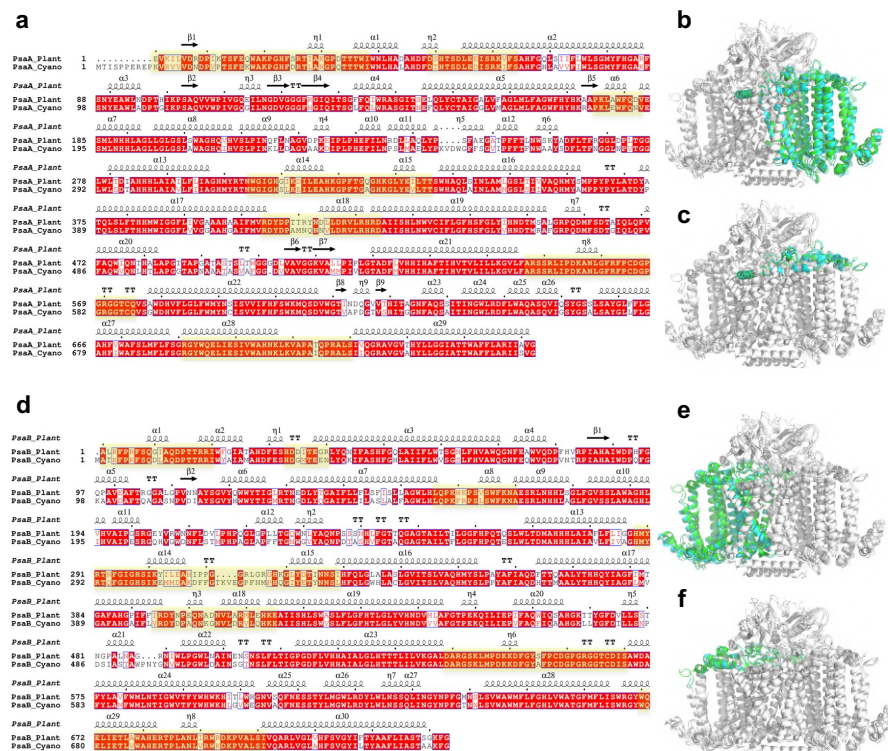
SUPPLEMENTARY FIGURES:

Supplementary Figure 1: Sequence alignment of PsaA and PsaB subunits from Plant PSI and Cyanobacteria PSI	3
Supplementary Figure 2: Sequence alignment of PsaC subunit from Plant PSI and Cyanobacteria PSI	4
Supplementary Figure 3: Sequence alignment of PsaD subunit from Plant PSI and Cyanobacteria PSI	4
Supplementary Figure 4: Sequence alignment of PsaE subunit from Plant PSI and Cyanobacteria PSI	5
Supplementary Figure 5: AFM Set-point calibration	5
Supplementary Figure 6: EC-STM Scan protein complex size fitting	6
Supplementary Figure 7: Defining a safe electrochemical window by cyclic voltammetry	7
Supplementary Figure 8: <i>Defining a safe electrochemical window by PSI photocurrent</i>	8
Supplementary Figure 9: <i>Defining a safe electrochemical window by photocurrent loss</i>	9
Supplementary Figure 10: <i>Bulk photocurrent recording of Au-adsorbed PSI molecules</i>	9

Supplementary Figure 11: <i>Double exponential model</i>	10
Supplementary Figure 12: <i>Double exponential fit parameters</i>	11
Supplementary Figure 13: <i>Fit of β distribution</i>	12
Supplementary Figure 14: <i>EC-STM Z-axis Piezo Calibration</i>	12
 <u>METHODS:</u>	
PSI-LHCI complexes purification	13
Structure-based sequence alignment of the PSI	13
PSI-plQA-cys-Au[111] Sample preparation	13
Atomic force microscopy imaging	14
ECSTM-Scans	14
ECSTM-Scan blob fitting model	14
Electrochemical characterization methods: chopped light cyclic voltammetry and chrono-amperometry	14
ECSTM current-distance decay spectroscopy	15
Current decay spectroscopy data analysis	15
Bibliography	16

SUPPLEMENTARY FIGURES

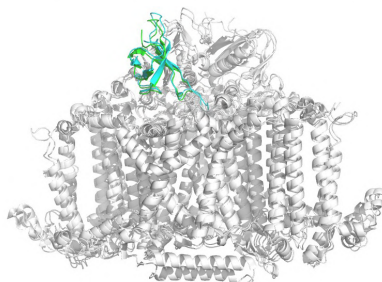
Supplementary Figure 1: Sequence alignment of PsaA and PsaB subunits from Plant PSI and Cyanobacteria PSI



Supplementary Figure S1. PsaA alignment: Length: 756, Identical residues: 620, Similar residues: 52, Percent sequence identity: 82.01, Percent sequence similarity: 88.89. The yellow boxes represent the PsaA stromal side regions exposed to the solvent. **B.** Structural representation of the alignment performed for PsaA subunits (Green: plant PSI, PDBiD: 4XK8; Cyan: cyanobacteria PSI, PDBiD: 6LU1). **C.** Structural representation showing the solvent-exposed regions of the PsaA subunits (yellow boxes). **D.** PsaB alignment. Alignment length: 741, Identical residues: 585, Similar residues: 49, Percent sequence identity: 78.95, Percent sequence similarity: 85.56. The yellow boxes represent the PsaA stromal side regions exposed to the solvent. **E.** Structural representation of the alignment performed for PsaB subunits (Green: plant PSI, PDBiD: 4XK8; Cyan: cyanobacteria PSI, PDBiD: 6LU1). **F.** Structural representation showing the solvent exposed regions of the PsaA subunits (yellow boxes).

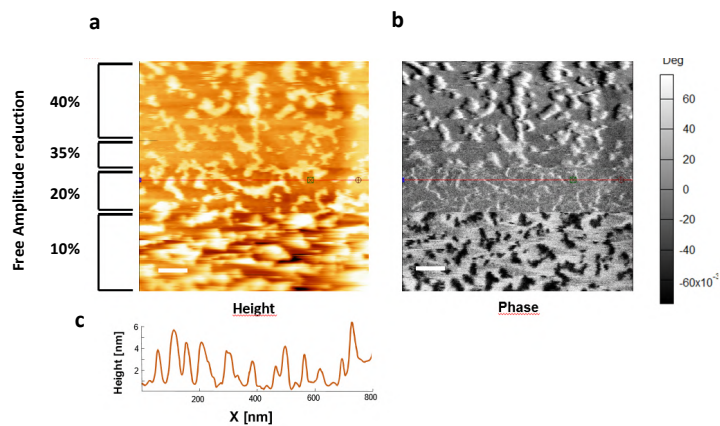
Supplementary Figure 4: Sequence alignment of PsaE subunit from Plant PSI and Cyanobacteria PSI

			TT	β1	TT		β2	TT	β3	TT		β4	η1	β5											
<i>PsaE_Plant</i>	1	IGPH	RG	KVKIL	RR	ESYHY	KGR	GSV	TV	VDC	DF	NTR	YV	VRF	KVNY	AN	VS	RNN	VAL	DF	QEV	E	
<i>PsaE_Cyano</i>	1	.MVQ	RG	KVKIL	RP	ESYHY	NEV	GV	AV	SVD	TF	GV	YV	VRF	D	KVNY	TGYS	GSAS	GV	RNN	VAL	DF	QEV	APP	KKKG



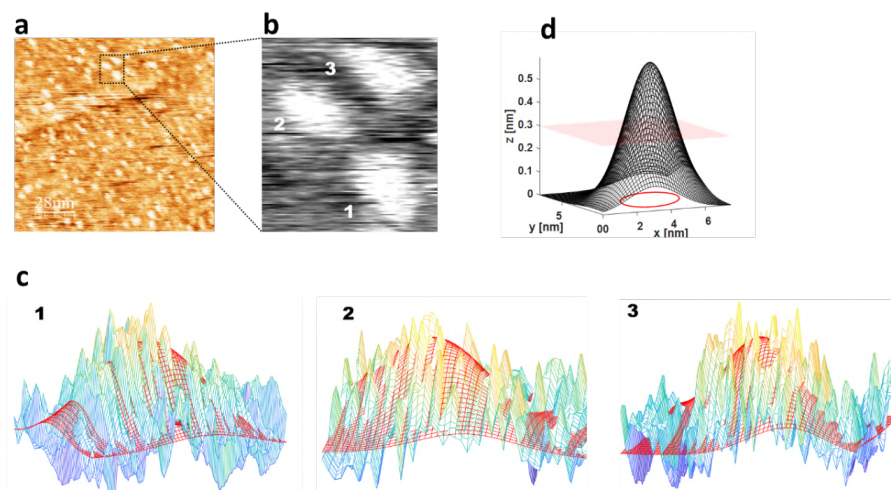
Supplementary Figure S4. PsaE alignment: Length: 77, Identical residues: 39, Similar residues: 7, Percent sequence identity: 50.65, Percent sequence similarity: 59.74. The cartoon shows the structural representation of the alignment performed for PsaE subunits (Green: Plant PSI, PDBiD: 4XK8; Cyan: Cyanobacteria PSI, PDBiD: 6LU1).

Supplementary Figure 5: AFM Set-point calibration



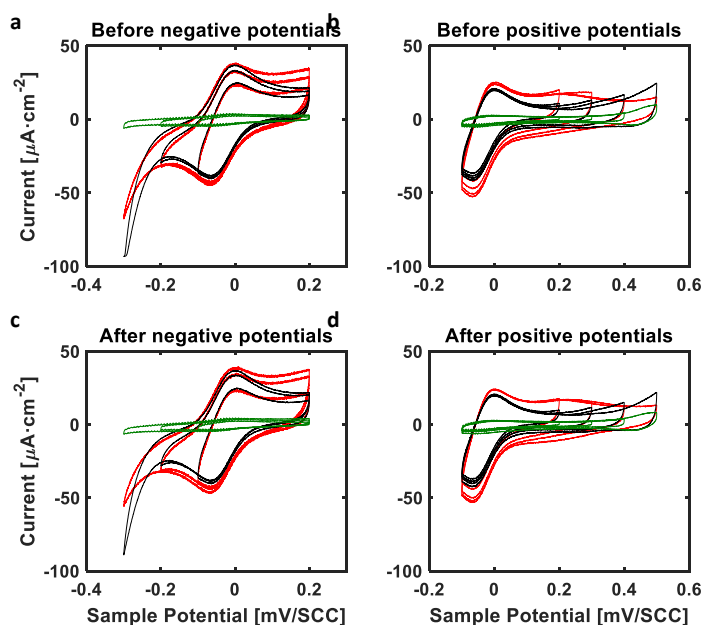
Supplementary Figure S5. AFM PSI-pIQa-cys-Au[111] scan in tapping mode: a Topography scan (color scale 6 nm, scale bar 100 nm) and b Phase image for 800x800 nm scan area. In AFM tapping mode, cantilever oscillation set-point amplitude was modulated with respect to free amplitude during scan. Set-point ratio percentage is indicated in Suppl. Figure S1a. Optimal scanning conditions preventing protein monolayer squeezing are found for 80 % ratio, where phase image contrast is minimized. c. Height profile of the scan line highlighted in red in Suppl. Figure 1a and Suppl. Figure 1b where set-point ratio is optimized.

Supplementary Figure 6: EC-STM Scan protein complex size fitting



Supplementary Figure S6. EC-STM Scan Molecule Fitting. a. PSI-pIQa-cys-Au[111] scan shown in figure 2e and b 10x10 nm zoom displaying three example molecules (1,2,3) fitted in with a 2D-gaussian model shown in red in c. d.Lateral size of PSI-pIQa-cys molecules is taken as the full width at the half-maximum of the gaussian fit (2.36σ).

Supplementary Figure 7: Defining a safe electrochemical window by cyclic voltammetry

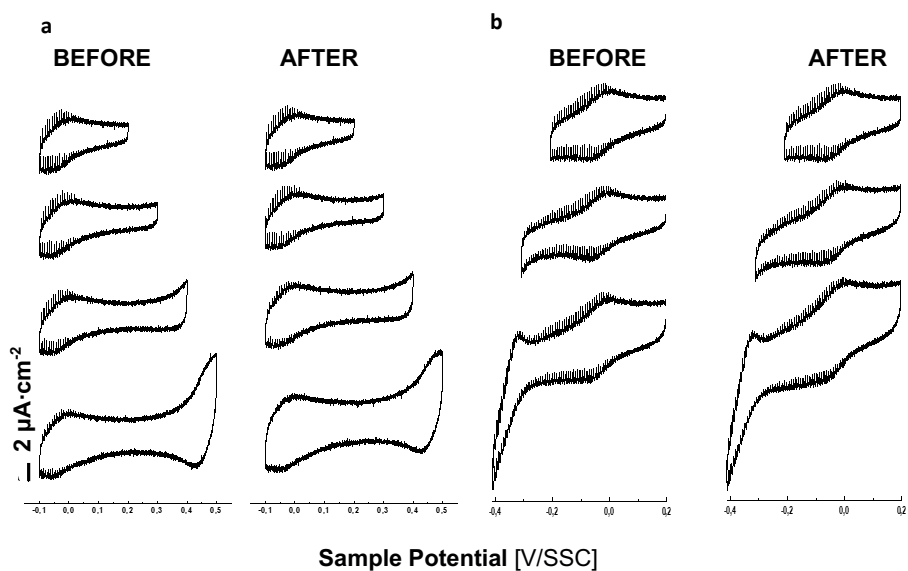


Supplementary Figure 7. Effect of pIQa-cys functionalization and sample electrode potential on cyclic voltammetry response. CV of PSI-pIQa-cys-Au[111] (green), pIQa-cys-Au[111] (red) and Au[111] (black). Upper panels A and B show CVs before applying a test (vertex) potential for 5 min. After this treatment, CVs are repeated and shown in lower panel (C and D, respectively). Negative vertex potential $U_s = -100, -200, -300$ mV/SSC are shown on the left side of the panel (A and C, respectively) and positive vertex potential $U_s = 200, 300, 400, \text{ and } 500$ mV/SSC are represented on the right side (B and D, respectively). Redox mediators methyl viologen (MV, 125 μM) and osmium bipyridine di-chloride (10 μM) were added to the PBS buffer solution. The scan rate is 80 mV/s and the LED irradiation period is 125 ms.

Cyclic Voltammetry Characterization of Au[111], pIQa-cys-Au[111] and PSI-pIQa-cys-Au[111] electrodes

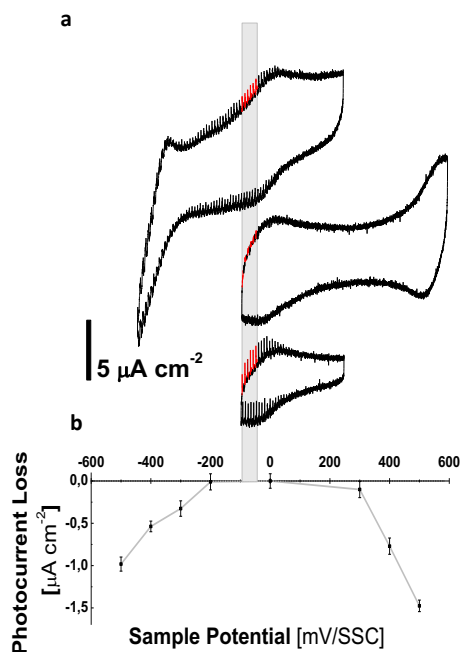
We observe a decrease in cathodic current (Supplementary Figure S7a) and an increase in anodic current (Supplementary Figure S7b) in pIQa-cys incubated samples (red traces) compared to bare gold samples (black traces), that we associate with cysteine modified peptide functionalization of gold electrodes. To evaluate sample stability, CV are repeated after applying voltammogram vertex potential for 5 minutes. In pIQa-cys-Au[111] and Au[111] samples, CV are similar before (Supplementary Figure S7a and S7b) and after (Supplementary Figure S7c and S7d) this treatment. In PSI-pIQa-cys-Au[111] electrodes (green traces in Supplementary Figure S7 and Supplementary Figure S8), currents are diminished a tenfold compared with pIQa-cys-Au[111] electrodes.

Supplementary Figure 8: *Defining a safe electrochemical window by PSI photocurrent*



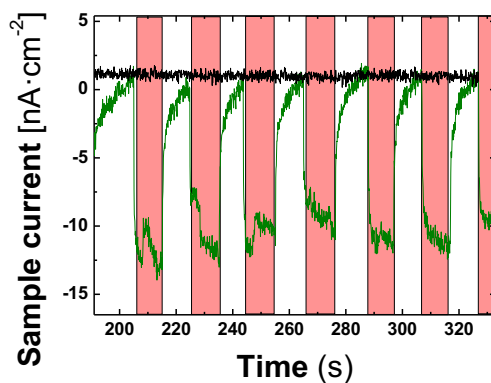
Supplementary Figure S8 : Effect of sample electrode potential on cyclic voltammetry response, zoom for PSI sample in figure Supplementary Figure S7 . CV of PSI-pIQA-cis-Au[111] sample before (left) and after (right) applying CV vertex potential for 5 min. a. Vertex potential $U_s < 300, 400, \text{ and } 500 \text{ mV/SSC}$ b. Vertex potential $U_s > 200, -300, -400 \text{ mV/SSC}$. Experimental conditions are identical to supplementary figures S7 and S9.

Supplementary Figure 9: Defining a safe electrochemical window by photocurrent loss



Supplementary Figure S9 a. Chopped light cyclic voltammetry of PSI-pIQA-cis-Au[111] samples. Redox mediators methyl viologen (MV, 125 μM) and osmium bipyridine di-chloride (10 μM) are added to buffer solution. Scan rate is set to 80 mV/s and LED irradiation period to 125 ms. Sample potential is swept between $-700 < U_s < 200$ mV (top), $-200 < U_s < 500$ (middle) and $-200 < U_s < 200$ (bottom). In the range $-150 < U_s < -100$ mV (grey shaded area) LED irradiation is indicated in red. **b. Photocurrent Loss:** Decrease of photocurrent in the range $-150 < U_s < -100$ mV (grey shaded area in Suppl. Figure 5a after applying sample potential indicated in x-axis for 5 minutes.

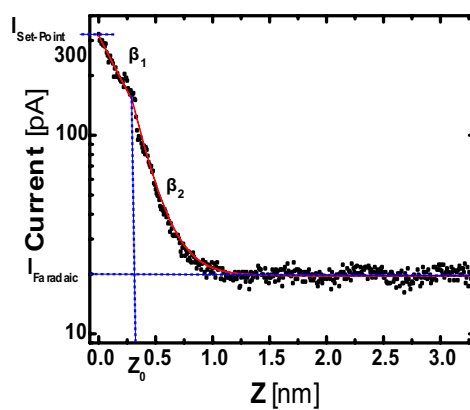
Supplementary Figure 10: Bulk photocurrent recording of Au-adsorbed PSI molecules



Supplementary Figure S10. Photo-chrono-amperometry: Prior to ECSTM experiments, the photocurrent of PSI-pIQA-cys-Au[111] (green trace) samples was evaluated. pIQA-cys-Au[111] control is shown for comparison (black trace). Working electrode potential is held constant at -100 mV/SSC while sample is illuminated with a LED of 690 nm wavelength and 20 mW cm^{-2} in cycles of 10 s, marked in red. Buffer solution is the same as ECSTM experiments, PBS buffer 50 mM, pH 7.4.

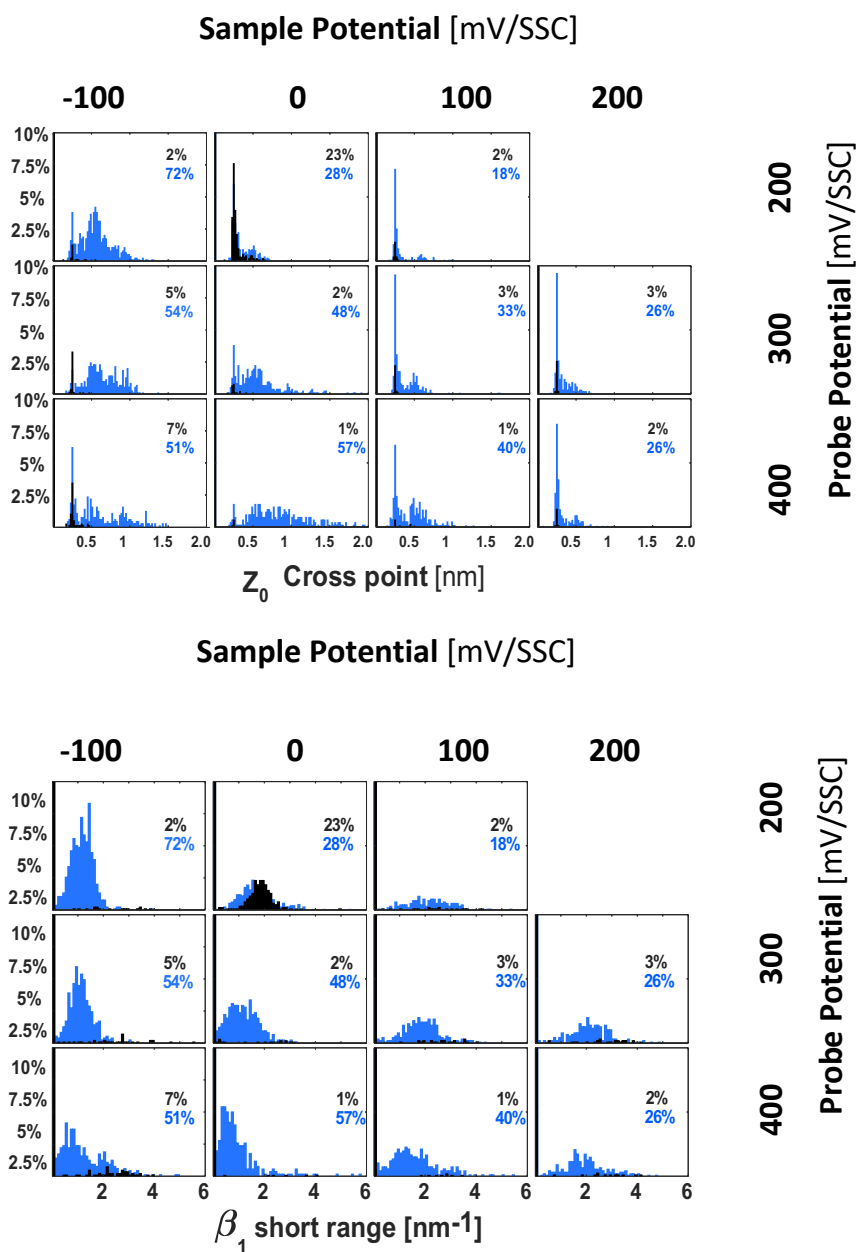
Supplementary Figure 11: Double exponential model

$$I(z) = I_{Faradaic} + I_{Set-point} \begin{cases} e^{-\beta_1 z} & \text{for } z < z_0 \\ e^{-\beta_2 z} e^{z_0(\beta_1 - \beta_2)} & \text{for } z > z_0 \end{cases}$$



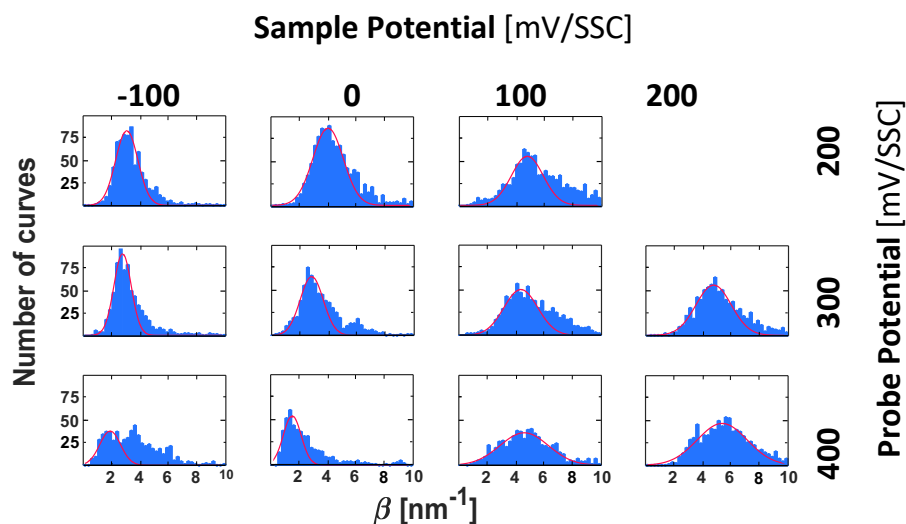
Supplementary Figure S11. Fit model. Current decay model (red trace) for ECSTM current decay data (black dots) data is fit with Golub Pereyra algorithm¹ that minimizes linear least squares for $I_{Faradaic}$ and $I_{Set-point}$ and non-linear least squares for β_1 , β_2 and z_0 . Single exponential decaying curves are fit excluding the second term $z > z_0$.

Supplementary Figure 12: Double exponential fit parameters



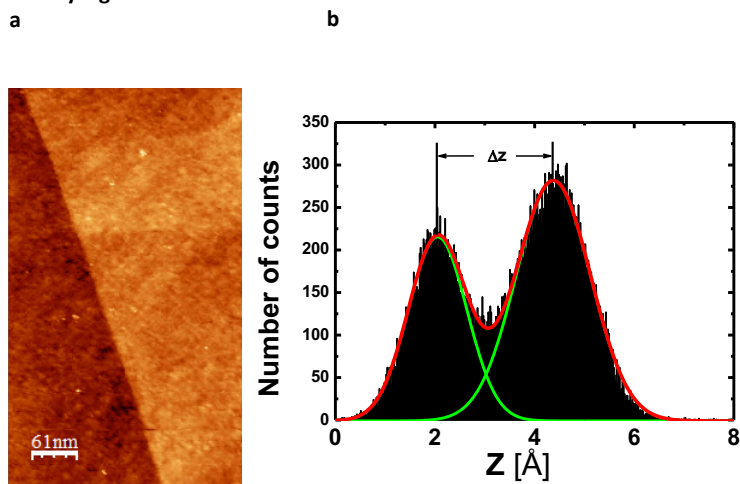
Supplementary Figure 12. Distribution of β_1 and z_0 parameters obtained from $I(z)$ data shown in Figure 4. PSI-pIQa-cis-Au[111] sample is marked in blue and pIQa-cis-Au[111] control in black. The percentage indicated the ratio of curves exhibiting double exponential decay of PSI-pIQa-cis-Au [111] (blue) and pIQa-cis-Au[111] (black) respectively. a. Histogram of z_0 cross-point between short range (β_1) and long range (β_2) regimes. b. Histogram for short range current decay constant β_1 .

Supplementary Figure 13: Fit of β distribution



Supplementary Figure 13. Fit of β distribution: Distribution of β values obtained fitting $I(z)$ curves shown in figure 4b to exponential model (blue) and fit to a normal distribution (red). The center of fit distribution was used in figures 5 and 6. In case of double exponential decay ($z_0 \neq 0$), long distance decay constant β_2 is used.

Supplementary Figure 14: EC-STM Z-axis Piezo Calibration



Supplementary Figure S14. EC-STM Z-axis Piezo Calibration. A. EC-STM topography scan displaying two Au[111] mono-atomic terraces performed under current decay spectroscopy experimental conditions: current set-point 0.3 nA and 300 mV bias in PBS buffer 50 mM. B. Histogram of height distribution in Suppl. Figure 2a. Au[111] mono-atomic terrace height ($\Delta z = 2.33 \pm 0.01 \text{ \AA}$) is compared to the reported value² 2.36 \AA to validate EC-STM z-piezo calibration.

METHODS:

PSI-LHCI complexes purification

Arabidopsis thaliana plants (Arabidopsis Col-0) were grown under white light at 120 $\mu\text{mol photons}\cdot\text{m}^{-2}\cdot\text{s}^{-1}$, 12 hr/12hr day/night cycle at 23 °C, for 5 weeks. Thylakoid membranes were isolated from Arabidopsis leaves according to Xu *et al.*³

PSI-LHCI complexes were purified from thylakoid membranes with sucrose density gradients as previously described.⁴ In brief: 350 μg Chl thylakoid were diluted to 0.5 mg Chl $\cdot\text{ml}^{-1}$ in 5 mM EDTA, 10 mM Hepes pH 7.5 and solubilized with an equal amount of detergent solution (1% *n*-decylmaltoside (DM) in 10 mM Hepes 7.5) for 10 min. After solubilization, the sample was centrifuged at 12,000 \times g, 10 min centrifugation to eliminate the insolubilized material. The supernatant was loaded onto the sucrose gradients prepared by freezing and thawing a sucrose solution (500 mM sucrose, 20 mM Hepes pH 7.5, 0.06% *n*-DM). The gradients were centrifuged for 16 hr at 4 °C at 160,000 \times g. PSI-LHCI complexes were collected with a syringe.

Structure-based sequence alignment of the PSI

Starting from structural works published by Jordan *et al.*⁵ and Quin *et al.*⁶ on the PSI structure from Cyanobacterium *Synechococcus elongatus* and the PSI structure from *Arabidopsis thaliana*, respectively, we performed a structure-based sequence alignment of the PSI subunit exposed toward the stromal side. We compared the structural homology, sequence identity, and sequence similarity between PSI stromal side regions from Cyanobacteria PSI and Higher Plant PSI. The structural alignment was performed by using PROMALS3D server.⁷ ESPript 3.0 server was used to depict similarity sequence coloring scheme.⁸ The calculation of the identity and similarity percentages was performed by using Sequence Manipulation Suite server (SMS).⁹ The alignments performed for each pair of subunits studied are shown in the supplementary Figures S1-S4. For the analyses, we only consider the PSI subunits A, B, C, D and E because these subunits are the ones that are mostly exposed to the solvent in both the stromal side of Cyanobacteria PSI and Plant PSI.¹⁰

PSI-pIQa-cys-Au[111] Sample preparation

Au[111] monocrystals (Mateck GmbH, Germany) were electropolished in H₂SO₄ and flame annealed as previously reported⁹. After annealing, samples were cooled in Ar atmosphere prior to pIQa-cys 0.1 mM incubation in CH₃COONa buffer 50 mM pH 4.5 for 30 min at room temperature. After peptide incubation, samples were gently rinsed with working buffer, Phosphate Buffer Saline (PBS) 50 mM, pH 7.4. Aliquots of 5 μl of PSI samples PSI from WT *Arabidopsis Thaliana*, Chlorophyll concentration 0.28 $\mu\text{g}/\mu\text{l}$ with 0.1% w/w DDM surfactant, isolated from sucrose gradient were incubated with 45 μl of PBS working buffer overnight in dark conditions overnight. After incubation, buffer was gently exchanged with phosphate buffered saline (PBS) PSI-free buffer to elute unbound complexes. Prior to scanning probe experiments, PSI-pIQa-cys-Au samples were mounted in the ECSTM electrochemical cell and photo-activity was evaluated. To do so, photo-chronoamperometric recordings (more details in electrochemical characterization methods) were performed at sample potential $U_s = -100$ mV/SSC in PBS buffer without adding redox mediators (Supplementary Figure S10).

Atomic force microscopy (AFM) imaging

AFM scans were performed using an MFP-3D atomic force microscope (Asylum Research, Santa Barbara, CA) using V-shaped Si_3N_4 cantilevers with sharp silicon tips and having a nominal spring constant of $0.12 \text{ N}\cdot\text{m}^{-1}$ (SNL, Bruker AFM Probes, Camarillo, CA). The AFM was operated in tapping mode in liquid, covering the sample with PBS 50 mM, pH 7.4. Set point was adjusted to minimize phase contrast to avoid compressing pIQAC-PSI- monolayer with AFM probe (Supplementary Figure S5).

ECSTM-Scans

PSI-pIQA-cys-Au[111] samples were prepared as described above. For ECSTM imaging, PSI buffer solution containing DM surfactant 0.1 % w/w was exchanged with DDM free PBS buffer (50 mM, pH 7.4) to complexes with silica beads Zeba spin desalting columns 7kDa (ThermoFischer), since excess of DDM surfactant absorbs on electrode surface hindering protein identification in ECSTM scans.¹² ECSTM probes were prepared cutting Pt-Ir wire with diameter 0.025 mm (GoodFellow, UK) and coated with Apiezon wax to prevent faradaic currents from masking tunnel current. A perfectly probe exhibits a flat cyclic voltammetry response with an offset current value of * pA in our set-up

Experiments were performed with a PicoSPM microscope head and a PicoStat bipotentiostat (Molecular Imaging) controlled by Dulcinea electronics (Nanotec Electronica) using WSxM 4.0 software.¹³ The applied bias for scans was $U_{\text{bias}} = +300 \text{ mV}$ and set point current 0.3 nA, corresponding to a point conductance of ($10^9 \Omega$). These parameters have been chosen to position probe electrode at set-point distances avoiding protein squeezing with probe.¹⁴ Sample and probe potentials were set to $U_s = -100, -50, 0, 100, 150, 200 \text{ mV/SSC}$ and $U_p = 200, 250, 300, 400, 450 \text{ mV/SSC}$, respectively. The applied bias is calculated as $U_{\text{bias}} = U_p - U_s$. Scan rate was set to 8 Hz acquiring 512 points per line.

ECSTM-Scan blob fitting model

Scans were analyzed with WsxM 4.0 Software¹³ and with a home written program to identify and measure the proteins. The program is based on Adam Ginsburg's gaussfitter (<http://github.com/keflavich/gaussfitter>) and available at (<http://github.com/Mlopeorti/Blob-2D-fitter>). The algorithm fits a 2-dimensional function to scan regions identified manually by the user as molecules. Examples of fit molecules are shown on Suppl. Figure 3. Protein lateral size is taken as the full-width-at-half maximum (2.35σ) of the fitted gaussian. Protein apparent height is obtained as the maximum of the raw data z-piezo position in the selected area. See Supplementary Figure S6 for an example.

Electrochemical characterization methods: chopped light cyclic voltammetry and chronoamperometry

A homemade electrochemical cell was used in three-electrode configuration for electrochemical characterization and four-electrode configuration for ECSTM. We used a miniaturized ultralow leakage membrane Ag/AgCl (SSC) reference electrode filled with 3 M KCl and a Pt:Ir (80:20) wire

as counter electrode. Cell and all glass material used for preparation of solutions were cleaned with piranha solution (7:3 H₂SO₄/H₂O₂ (30%) by volume). **Caution: Piranha solution should be handled with extreme caution.** Electrochemical measurements were carried out with a potentiostat PGSTAT 302N (Metrohm Autolab, Netherlands). In chopped-light cyclic voltammetry experiments, a LED of 690 nm radiating a power of 30 mW·cm⁻² in the plane of the sample was used. CV was performed at 80 mV·s⁻¹ with an illumination period of 125 ms (Supplementary Figures S7-S9). For photo-chrono-amperometric recordings (Supplementary Figure S10), the potential was held at U_s = -100 mV/SSC. The sample was illuminated in 10 s cycles.

ECSTM current-distance decay spectroscopy

The piezoelectric nanoprobe positioner was calibrated under experimental conditions taking as reference the Au[111] single atom thick terraces (0.236 nm¹⁵, Suppl. Fig. S14). Current-distance (I-z) recordings are obtained by departing from a set point fixed at 0.3 nA. The current feedback-loop is switched off and the probe electrode is retracted 10 nm at 40 nm/s. Afterwards, probe is approached again and current-distance feedback loop is reestablished for 400 ms before retracting again. 1000 I(z) curves were recorded for each sample/probe potential pair. To minimize drift artifacts, I-z plots that started with a current deviation higher than 10% of the initial setpoint were discarded.

Current decay spectroscopy data analysis

Current-distance curves showing a double exponential behavior¹⁶⁻¹⁸ were fit with a two-regime exponential function described by the following equation:

$$I(z) = I_{Faradaic} + I_{Set-point} \begin{cases} e^{-\beta_1 z} & \text{for } z < z_0 \\ e^{-\beta_2 z} e^{z_0(\beta_1 - \beta_2)} & \text{for } z > z_0 \end{cases}$$

In the model, $I_{Faradaic}$ describe faradaic current term issued from leakage currents due to probe coating defects, this term is obtained as the average of the last 200 points of the I(z) curve.

$I_{Setpoint}$ is the fixed set point starting current. The fit parameters are β_1 and β_2 , the distance decay currents for short and long distance respectively and z_0 is the point. A fit example is shown in Supplementary Figure S11.

The code to analyze I(z) data, written with R software, is available in GitHub repository. https://github.com/Mlopeorti/Tunnel_current_2exponential_fitter/blob/master/2_exp_fit_au_to_iz_ECSTM

Bibliography

- (1) Walen, H.; Liu, D. J.; Oh, J.; Lim, H.; Evans, J. W.; Kim, Y.; Thiel, P. A. Self-Organization of S Adatoms on Au(111): $\sqrt{3}R30^\circ$ rows at Low Coverage. *Journal of Chemical Physics* **2015**, *143* (1).
- (2) Golub, G. H.; Pereyra, V. The Differentiation of Pseudo-Inverses and Nonlinear Least Squares Problems Whose Variables Separate. *SIAM Journal on Numerical Analysis* **1973**, *10* (2).
- (3) Xu, P.; Tian, L.; Kloz, M.; Croce, R. Molecular Insights into Zeaxanthin-Dependent Quenching in Higher Plants. *Scientific Reports* **2015**, *5* (1), 1–10.
- (4) Caffarri, S.; Kouřil, R.; Kereïche, S.; Boekema, E. J.; Croce, R. Functional Architecture of Higher Plant Photosystem II Supercomplexes. *EMBO Journal* **2009**, *28* (19), 3052–3063.
- (5) Jordan, P.; Fromme, P.; Witt, H. T.; Klukas, O.; Saenger, W.; & Krauß, N. Three-dimensional structure of cyanobacterial photosystem I at 2.5 Å resolution. *Nature* **2001**, *411*(6840), 909-917.
- (6) Qin, X.; Suga, M.; Kuang, T.; Shen, J. R.. Photosynthesis. Structural basis for energy transfer pathways in the plant PSI-LHCI supercomplex. *Science* **2015**, *348*(6238), 989–995).
- (7) Pei, J.; Kim, B. H.; Grishin, N. V.. PROMALS3D: a tool for multiple protein sequence and structure alignments. *Nucleic acids research* **2008**, *36*(7), 2295–2300)
- (8) Robert, X.; Gouet, P. Deciphering key features in protein structures with the new ENDscript server". *Nucl. Acids Res*, **2014**, *42*(W1), W320-W324
- (9) Stothard, P. The sequence manipulation suite: JavaScript programs for analyzing and formatting protein and DNA sequences. *BioTechniques*, **2000**, *28*(6), 1102–1104).
- (10) Scheller, H. V.; Jensen, P. E.; Haldrup, A.; Lunde, C.; Knoetzel, J. Role of subunits in eukaryotic Photosystem I. *Biochimica et biophysica acta*, **2001**, *1507*(1-3), 41–60)
- (11) Nagy, G.; Wandlowski, T. Double Layer Properties of Au(111)/H₂SO₄(Cl) + Cu²⁺ from Distance Tunneling Spectroscopy. *Langmuir*, **2003**, *19*(24), 10271-10280 .
- (12) López Martínez, M. Electrochemical Tunneling Microscopy and Spectroscopy of Electron Transfer Proteins. *TDX (Tesis Doctorals en Xarxa)* **2017**.
- (13) Horcas, I.; Fernández, R.; Gómez-Rodríguez, J. M.; Colchero, J.; Gómez-Herrero, J.; Baro, A. M. WSXM: A Software for Scanning Probe Microscopy and a Tool for Nanotechnology. *Review of Scientific Instruments* **2007**, *78* (1), 013705..
- (14) Alllata, D.; Andolfi, L.; Cannistraro, S. Tip to Substrate Distances in STM Imaging of Biomolecules. *Ultramicroscopy* **2004**, *101* (2–4), 231–240.

- (15) Spurgeon, P. M.; Lai, K. C.; Han, Y.; Evans, J. W.; Thiel, P. A. Fundamentals of Au(111) Surface Dynamics: Coarsening of Two-Dimensional Au Islands. *Journal of Physical Chemistry C* **2020**, *124* (13), 7492–7499.
- (16) He, J.; Lin, L.; Zhang, P.; Lindsay, S. Identification of DNA Basepairing via Tunnel-Current Decay. *NANO LETTERS* **2007**, *7* (12).
- (17) Artés, J. M.; Díez-Pérez, I.; Sanz, F.; Gorostiza, P. Direct Measurement of Electron Transfer Distance Decay Constants of Single Redox Proteins by Electrochemical Tunneling Spectroscopy. *ACS Nano* **2011**, *5* (3), 2060–2066.
- (18) Lagunas, A.; Guerra-Castellano, A.; Nin-Hill, A.; Díaz-Moreno, I.; de la Rosa, M. A.; Samitier, J.; Rovira, C.; Gorostiza, P. Long Distance Electron Transfer through the Aqueous Solution between Redox Partner Proteins. *Nature Communications* **2018**, *9* (1).

Chapter 4

The protein matrix of plastocyanin supports long-distance charge transport with photosystem I and the copper ion regulates its spatial span and conductance

Manuel López-Ortiz,^{† 1,2} Ricardo A. Zamora,^{† 1,2} Marina I. Giannotti,^{1,2,3} Chen Hu,⁴ Roberta Croce,⁴ and Pau Gorostiza^{1,2,5*}

1. *Institute for Bioengineering of Catalonia (IBEC), The Barcelona Institute of Science and Technology, Baldori Reixac 10-12, Barcelona 08028, Spain*

2. *CIBER-BBN, ISCIII, Barcelona, Spain*

3. *Department of Materials Science and Physical Chemistry, University of Barcelona, Martí i Franquès 1-11, Barcelona 08028, Spain*

4. *Biophysics of Photosynthesis. Dep. Physics and Astronomy, Faculty of Sciences, Vrije Universiteit Amsterdam, De Boelelaan 1081, 1081 HV Amsterdam, the Netherlands*

5. *Catalan Institution for Research and Advanced Studies (ICREA), Barcelona 08010, Spain*

* *E-mail: pau@icrea.cat*

[†] *These authors contributed equally to this work.*

1 Abstract

In cellular respiration and photosynthesis electrons are shuttled in a cascade of electron transfer (ET) steps between redox cofactors. Proteins constrained between electrodes however support electron transport (ETp) through protein matrices even in absence of redox cofactors. It is unknown whether protein ETp mechanisms apply to the interprotein medium. Here, we study interprotein ETp between plant photosystem I (PSI) and its soluble redox partner plastocyanin (Pc) and address the role of Pc's copper redox center. Using electrochemical scanning tunnelling spectroscopy (ECSTS) we quantify the remote charge exchange distance and the conductance of bound PSI/Pc complexes. Pc devoid of copper exchanges charge with PSI at longer distances than copper Pc and the conductance of the complex is higher in absence of the metal. Our results suggest that Pc's copper is not essential in interprotein ETp through the aqueous solution and question the canonical view of tight complex binding between redox protein partners.

2 Introduction

Interprotein charge exchange is a fundamental process in cellular respiration and photosynthesis that includes three canonical steps:¹ diffusion of the charge-exchanging proteins, transient complex formation, and electron transfer (ET). Tunnelling mechanisms predict efficient ET between the cognate protein pair in the complex at distances below 15 Å between the donor and acceptor redox cofactors.² However, tunnelling mechanisms cannot account for experimental results of protein electron transport (ETp),^{3,4} that is, charge exchange through proteins placed in between an electrode pair that provide an electron source and drain. ETp does not require the presence of redox cofactors to transport charge⁵⁻⁷ whereas such molecular electronic states are ineluctable steppingstones in ET. The observation of ETp through non-redox proteins⁵⁻⁷ challenges the view of the polypeptide chain as a mere scaffold for redox cofactors and passive "protein matrix" akin to a low conductance dielectric medium. In addition, temperature independent ETp has been reported for protein junctions wider than 5 nm,⁷⁻⁹ a distance that largely exceeds the tunnelling range.⁵⁻⁷ All these ETp studies are reported at the level of single^{5,10-12} (or few)^{7,13-15} proteins and protein monolayers^{8,16,17}.

In the photosynthetic electron transport chain, charge between membrane bound complexes cytochrome *b₆f* (Cyt *b₆f*) and photosynthetic complex I (PSI) is carried by the Cu⁺²⁺ redox center of Plastocyanin (Pc),¹⁸ which is located in the thylakoid lumen (Figure 1a).¹⁹ In the co-crystal structure of the PSI/Pc complex,²⁰ the interacting residues lie at the luminal side of PsaA and PsaB subunits, near the P700 chlorophyll special dimer that photogenerates the electron-hole pair, and in the soluble domain of PsaF subunit (Figure 1b). Magnetic resonance cross-saturation experiments²¹ revealed

The protein matrix of plastocyanin supports long-distance charge transport with photosystem I and the copper ion regulates its spatial span and conductance

an acidic patch in Pc lying near its PSI- and Cyt *b₆f*-binding surface regions. Transient spectroscopic measurements²²⁻²⁹ showed that PSI/Pc ET kinetics features a fast μ s phase associated with the ET of preformed complexes and a slower ms phase, dependent on Pc concentration and related to the PSI/Pc complex formation. We have recently studied the binding of single PSI/Pc pairs using force spectroscopy.³⁰ Controlling the redox state of PSI and Pc, we quantified the binding probability as the number of adhesion events. For PSI/Pc, the binding probability depends on the proteins' redox state and is higher when at least one of the partners is in an ET-ready state.³⁰ Those results pave the way for disentangling the contribution of binding from the overall charge exchange process between PSI and Pc. However, characterization of the ET step between PSI/Pc pairs is lacking.

An ET-like situation can be reproduced in an electrochemical scanning tunnelling microscope (ECSTM) set-up, positioning protein partners facing each other in upon binding them to electrodes located at nanometer proximity.^{31,32} Electrochemical scanning tunnelling spectroscopy (ECSTS) has proven an advantageous technique to study single redox proteins.^{33,34} Bipotentiostatic control allows setting the electrochemical potential of the probe and sample electrodes (and thus the bias potential, $U_{\text{bias}} = U_{\text{probe}} - U_{\text{sample}}$) in aqueous solutions mimicking physiological conditions. Interprotein charge exchange is then characterized by the current flowing between the probe and sample electrodes which is mediated by the proteins bound to them. In this way, the ETp configuration reproduces an interprotein ET-like situation. For a redox cognate pair of the respiratory chain, the interprotein current is measurable at distances as long as 12 nm^{31,32} which requires a different mechanism than ET in the bound complex.³⁵ It is unclear whether the ETp mechanisms operating in the polypeptide structures can also support charge transport between proteins through the solution. The spatial span of the interprotein current in cytochrome *c* is regulated by phosphorylation,³² which highlights the biological relevance of this observation. It is yet unknown whether long-distance ET only occurs in these partner proteins, or it is a general phenomenon and it is also not known whether protein recognition, which is essential for interprotein ET^{22,25-28} plays a role in ETp.^{6,8,9}

The protein matrix of plastocyanin supports long-distance charge transport with photosystem I and the copper ion regulates its spatial span and conductance

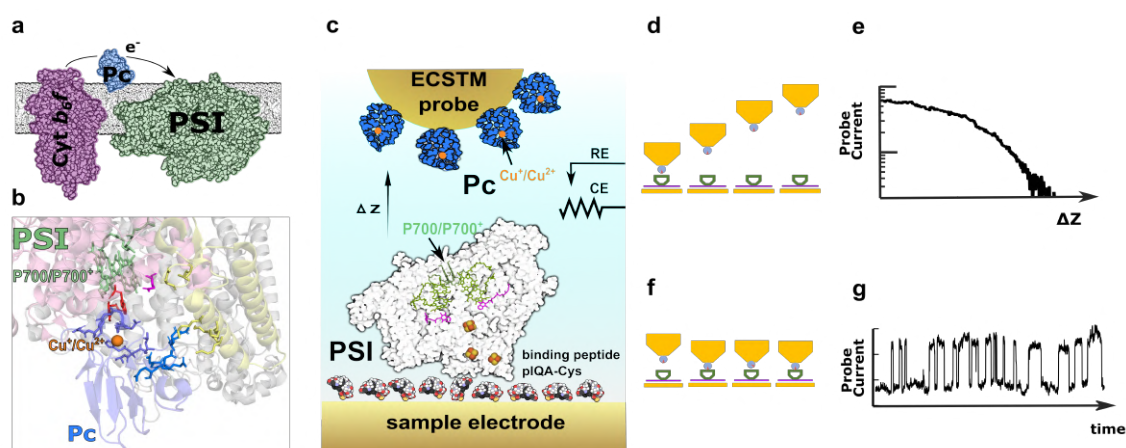


Figure 4.1: PSI-LHCI-Pc charge exchange: (a) Schematic representation of charge exchange between Cyt b6f (purple) and PSI-LHCI (green) mediated by Pc (blue) in the luminal side of thylakoid membrane. (b) PSI-Pc transient complex structure (6YEZ) in cartoon representation of Pc (blue) and PsaA (pink) and PsaB (white) and PsaF (yellow) subunits. Redox cofactors are highlighted in green for P700 pair and in orange for Cu atom in Pc. Residues with a reported role on PSI-Pc ET are also highlighted: PsaA Trp625 PsaB and Trp658 (red), PsaB Glu613 (pink) and PsaF lysines Lys93,96,100,101 (yellow). Pc Residues interacting with PsaA and PsaB are shown in purple and those interacting with PsaF lysines are shown in blue. (c) Experimental set-up for ECSTM distance current decay spectroscopy. PSI-LHCI (white) is functionalized via pIQA-cys linker peptide to Au sample electrode. Pc (blue) functionalize Au probe electrode that is retracted perpendicularly to the sample electrode plane (z axis). Arrows indicate the redox cofactors, P700/P700⁺ and Cu^{+2/+} of PSI-LHCI and Pc respectively. RE and CE represent counter electrode (Pt wire) and reference electrode (low leakage SSC) respectively. (d) Scheme depicting distance-current decay spectroscopy experiment and (e) example of current vs distance trace I(z). (f) Scheme of blinking experiment and (g) example trace of blinking events displaying a telegraphic noise signal.

Here, we address these questions by studying charge transport between protein partners of the photosynthetic electron transport chain. We measure the distance dependence and conductance of interprotein charge exchange between photosystem I light harvesting complex I (PSI-LHCI noted PSI throughout the manuscript for simplicity) and the soluble electron carrier Pc. Making use of ECSTM based techniques and suitable binding strategies for PSI and Pc on the electrodes, we aim to tell apart the contributions of diffusion, complex formation, re-arrangement, and charge exchange between cognate proteins by controlling their relative orientation and separation in current-distance spectroscopy experiments. With this configuration we aim to extend ETp measurements to the electrolyte medium.³¹ We also characterize ETp of the bound complex by measuring the conductance in transient Au-PSI/Pc-Au junctions.³⁶

^{33,34}We use ECSTS to study ET between suitably oriented PSI and Pc. This is achieved with cysteine-modified Pc mutants^{36,37} to functionalize respectively the ECSTS probe electrode and a PSI-specific recognition peptide that binds to the stromal side of PSI

The protein matrix of plastocyanin supports long-distance charge transport with photosystem I and the copper ion regulates its spatial span and conductance

(pIQAcys)^{38,39} to functionalize sample electrode, exposing their interacting surfaces facing each other (Figure 1c). The spatial span of the protein charge exchange is assessed by recording the probe current during retraction (Figure 1d) yielding a double-exponential current decay^{40,41} (current-distance $I(z)$ traces, Figure 1e). The current-distance decay rate (β , nm⁻¹) obtained by fitting current-distance plots (see experimental Methods) is a proxy indicator of the interprotein charge exchange distance.^{31,32,39-43} In previous works, we measured current-distance rates between a metal probe and PSI^{39,43} at different probe/sample potential pairs, concluding that the current is gated by the probe potential with a minimal β value (longest charge exchange distance) of 2 nm⁻¹. Although β for Pc has not been reported, the gating of β was observed in azurin,⁴¹ which is a similar Cu-coordinating electron carrier protein. Interestingly, the electrochemical gating effect vanished in redox inactive azurin, in which the Cu atom was substituted by Zn.⁴¹ The Cu ion in azurin was also shown to have a structural function, as experiments of single-molecule mechanical unfolding and computer simulations revealed that the metal-binding region is mechanically flexible in apo-azurin and high mechanical stability is imparted by copper binding.⁴⁴ We further investigate the intriguing nature of ETp in non-redox proteins using Pc_{apo} (devoid of Cu atom) and Pc_{holo} (with Cu in its binding site), to tell apart the contributions of the redox cofactor and of the protein structure, which is similar for Pc_{holo} and Pc_{apo}.⁴⁵

In addition to current-distance measurements, we investigate ET in the Pc/PSI bound complex with the "blinking" technique, which records the formation of spontaneous, transient protein junctions between sample and probe electrode^{12,46-50} (Figure 1f). As the junction is formed, a sharp increase in the current (blink) is observed resulting in a telegraphic noise like signal (Figure 1g). The junction conductance (which is proportional to the current for a fixed bias potential) provides valuable information on the intra-protein complex ETp mechanism. For instance, comparing the conductance of wildtype and mutant azurin allowed to distinguish Cu-mediated and non-Cu mediated charge transport mechanisms.⁴⁸ Additionally, the duration of blinks allows quantifying the time span of the transient complex. These complementary techniques, current distance spectroscopy and blinking, allow characterizing charge exchange at long distances and in bound complexes respectively, and provide a comprehensive view of charge exchange between PSI and Pc.

3 Results and Discussion

3.1 Current-distance spectroscopy: spatial span of the charge exchange.

Prior to study the charge exchange between PSI and Pc, we first evaluated separately the current -distance dependence of PSI and Pc individually, as well as the behavior of the PSI recognition peptide (pIQAcys). ECSTS current-distance curves and their associated β values at negative bias (-100 mV, with $U_{\text{probe}} = 100$ mV/SSC and $U_{\text{sample}} = 200$ mV/SSC, imposing electron flow from probe to sample electrode) are shown in Figure 2. For the PSI recognition peptide, pIQAcys (Figure 2, magenta) the current measured with a bare Au probe reduces abruptly beyond 2 nm, which corresponds to an average β value of 6 ± 1 nm⁻¹ (average \pm standard deviation). Compared with the current-distance rate of bare Au electrodes, ~ 9 nm⁻¹,⁴³ the pIQAcys peptide bound to the electrode increases the charge exchange distance. Upon incubation of PSI complexes on the pIQAcys sample (Figure 2, green), the charge exchange distance is further extended, lowering β to 1.5 ± 0.1 nm⁻¹. Positive bias (+100 mV, $U_{\text{probe}} = 100$ mV/SSC and $U_{\text{sample}} = 0$ mV/SSC, corresponding to hole injection from the probe electrode into the PSI decorated sample electrode) yields $\beta = 2.2 \pm 0.3$ nm⁻¹ (Supplementary Figure 1, green), in line with reported results.³⁹ Differences in β with bias sign indicate that injecting electrons to PSI as it occurs in the photosynthetic electron transport chain, facilitates charge exchange compared to hole injection. Regarding Pc functionalized probes facing the pIQAcys binding peptide on the sample, β is 1.1 ± 0.3 nm⁻¹ (Figure 2, red). In this case, no significant differences are observed between positive and negative bias (Supplementary Figure 1, red).

We then performed ECSTS current-distance measurements with the physiological partners Pc/PSI facing each other on the probe/sample electrodes (Figure 2, pale red). Interestingly, the interaction of the protein partners, with $\beta = 1.5 \pm 0.3$ nm⁻¹, yields similar charge exchange distance compared to PSI or Pc separately. This observation holds for negative bias (physiological sign) and for positive bias (Supplementary Figure 2).

In order to isolate the contribution of the protein matrix (as purified without the copper ion) to the charge exchange process, we carried out current-distance spectroscopy experiments with Cu-less Pc_{apo}¹³ (Figure 3a). Cyclic voltammetry (CV) recordings of Au electrodes incubated with Pc_{apo} (Figure 3b, blue) showed no oxidation or reduction peaks distinctive of redox protein absorbed on an electrode. Upon addition of CuSO₄ 50 mM to the buffer solution (for 1 hour) and washout, the CV of Pc_{holo} shows characteristic oxidation and reduction peaks (Figure 3a, pale red) that confirm the ability of the Au-attached protein to bind Cu ions, thereby acquiring redox functionality. Note that

following this method, as-prepared Pc_{holo} is in the oxidized form, and during the ECSTS experiments it is kept at the redox midpoint by the applied probe potential $U_{\text{probe}} = 100$ mV/SSC.

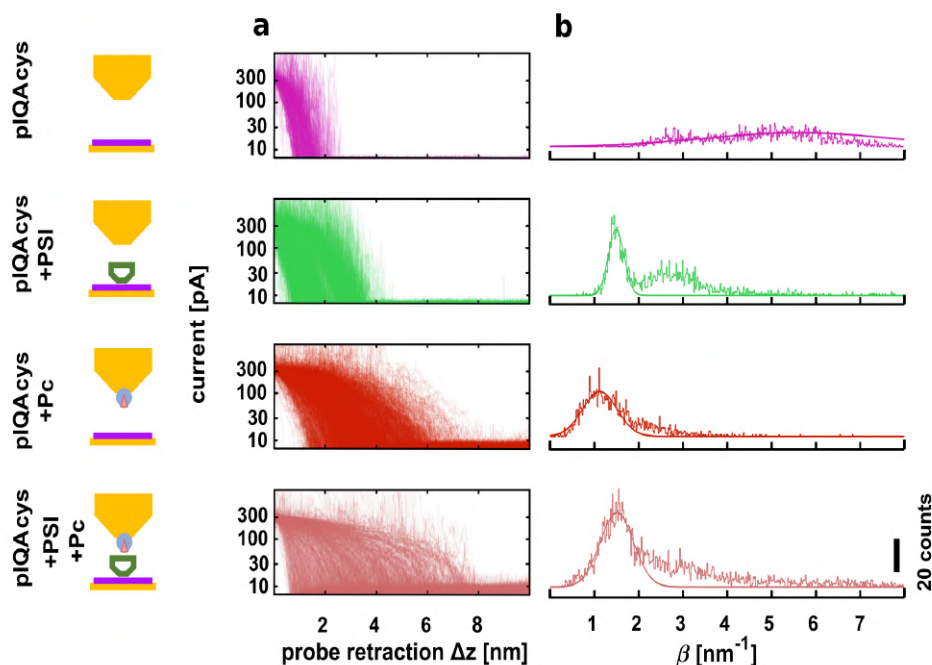


Figure 4.2: Current distance spectroscopy of pIQAcys, PSI, Pc and Pc/PSI electrodes. (a) Raw current-distance $I(z)$ curves for pIQAcys-Au (magenta) and PSI-pIQAcys-Au (green) samples using a bare Au probe; pIQAcys-Au (red) and PSI-pIQAcys-Au (pale red) samples using a Pc-Au probe. Each condition is depicted schematically on the left. In all cases, $n=1000$ curves were recorded in two independent experiments except for PSI/Pc samples that counts three independent experiments. (b) Current distance rate (β) histograms obtained using values from $I(z)$ curves in panel (a) and fit by a normal distribution (solid curve). $U_{\text{bias}} = -100$ mV; $U_{\text{probe}} = 100$ mV/SSC; $U_{\text{sample}} = 200$ mV/SSC.

Current-distance spectroscopy of Pc_{holo} probes facing pIQAcys-Au electrodes (red, Supplementary Figure 2) yield longer charge exchange distances (lower β values) compared to Pc_{apo} for both positive and negative bias (black, Supplementary Figure 2). This result indicates that charge exchange between Pc and the gold sample electrode functionalized with pIQAcys peptide (which is not a cognate partner of Pc) is facilitated in the presence of the redox center in Pc, that is, the Cu ion enlarges the spatial span of the interaction. Remarkably, facing Pc_{apo} to its cognate partner PSI, increases the charge exchange distances, yielding an average β rate of $0.8 \pm 0.2 \text{ nm}^{-1}$ for negative bias (Figure 3c, pale red) and giving rise to current-distance curves extending up to 8 nm. Strikingly,

The protein matrix of plastocyanin supports long-distance charge transport with photosystem I and the copper ion regulates its spatial span and conductance

at negative (physiological) bias, β values between Pc_{holo} and PSI ($1.5 \pm 0.3 \text{ nm}^{-1}$) are significantly higher than between Pc_{apo} and PSI, indicating that the presence of copper in Pc reduces the charge exchange distance between the partners (Figure 3d). Such decrease in the charge exchange distance between PSI/ Pc_{holo} compared to PSI/ Pc_{apo} is not observed at positive bias, which drives electrons from PSI on the sample to Pc on the probe (Supplementary Figure S3). The β values obtained in all the conditions described above are summarized in the Supplementary Information (Supplementary Table ST1).

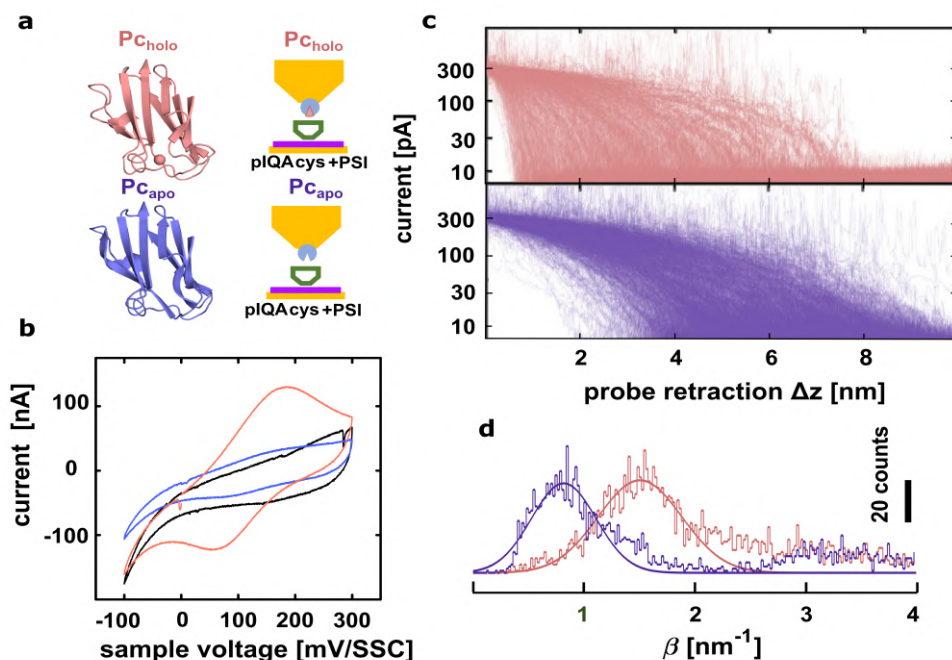


Figure 4.3: Preparation of Pc_{holo} and Pc_{apo} , C and ECSTS current-distance spectroscopy of probe-attached Pc_{holo} and Pc_{apo} facing PSI complexes bound to the sample electrode. (a) Crystallographic structure of poplar Pc_{holo} in pale red (PDB 1PLC) and Pc_{apo} in blue (PDB 2PCY) and schematic representation of PSI/ Pc_{holo} (top) and PSI/ Pc_{apo} (bottom) samples. **(b)** Cyclic voltammetry of bare Au[111] electrode (black), after incubation with as-purified Pc_{apo} for 2 hours (blue) and after incubation of Au+ Pc_{apo} sample with CuSO_4 (Pc_{holo} , pale red). **(c)** Raw ECTS $I(z)$ data plots for PSI/ Pc_{apo} (blue) and PSI/ Pc_{holo} (pale red) and PSI/ Pc_{apo} (blue) as shown in Figure 2a. **(d)** Current-distance constant rate (β) histograms for β values obtained from $n=3000$ $I(z)$ curves issued from three independent experiments of 1000 curves each shown in Figure 3c and fit by normal distribution (solid curve). $U_{\text{bias}} = -100 \text{ mV}$; $U_{\text{probe}} = 100 \text{ mV/SSC}$; $U_{\text{sample}} = 200 \text{ mV/SSC}$.

3.2 Blinking: formation of spontaneous PSI/Pc junctions

In ECSTS blinking experiments,⁵¹ the probe positioning feedback loop is transiently turned off at a desired current stpoint (typically during a few seconds) and the probe current is monitored as molecular junctions are randomly formed in the gap between probe and sample electrodes (functionalized respectively with Pc and PSI in our case). Intermittently switching events described as plateaux, telegraphic noise or “blinks” are observed in the current signal (Figure 4a), indicating the transient formation of a junction. Blinks typically last from a fraction of a ms to tens of ms and display a current increase of 0.2 - 2 nA corresponding to $2.5 - 25 \cdot 10^{-5} G_0$ for a fixed bias potential of 100 mV, where the conductance jump $\Delta G = \Delta I / U_{bias}$ is expressed as a multiple of the conductance quantum G_0 . Collections of blinking events ($N = 4110$ for PSI/Pc_{apo} and $N = 4216$ for PSI/Pc_{holo}, see example traces in Figure 4a) were analyzed to quantify their duration Δt and associated conductance change ΔG . They are represented in a ‘heat map’ two-dimensional histogram of ΔG as a function of Δt (Figure 4b). Side and bottom panels show accumulated histograms of ΔG and Δt to ease the interpretation.

Two conductance maxima are observed in $\Delta G - \Delta t$ maps a low conductance peak of $1.6 \pm 0.1 \cdot 10^{-5} G_0$ (average \pm standard error of the mean) for PSI/Pc_{holo} and $3.0 \pm 0.1 \cdot 10^{-5} G_0$ for PSI/Pc_{apo} (indicated respectively with a red and a blue circle in the side panels of Figure 4b) and a high conductance peak of $7.1 \pm 0.1 \cdot 10^{-5} G_0$ for PSI/Pc_{holo} and $10.6 \pm 0.2 \cdot 10^{-5} G_0$ for PSI/Pc_{apo} (indicated respectively with a red and a blue star in side panels of Figure 4b). In addition, the high ΔG peak has a wider distribution for PSI/Pc_{apo} than for PSI/Pc_{holo} the standard deviations of the normal fit of the peaks are $4.2 \cdot 10^{-5} G_0$ and $2.5 \cdot 10^{-5} G_0$, respectively).

The higher ΔG observed in the absence of the metal ion (PSI/Pc_{apo} in Figure 4b, side panels) are consistent with the lower β values obtained in current-distance measurements (Figures 2-3). Although Pc_{apo} cannot undergo redox reactions (see Figure 3b), non-redox proteins sandwiched between electrodes have been recently reported to sustain electron transport up to several nm⁹ and exhibit conductance resonance features.⁵ Those intriguing results have prompted the proposal of a general mechanism for electron transport in proteins⁶ that should also be applicable to apo proteins, as discussed below.

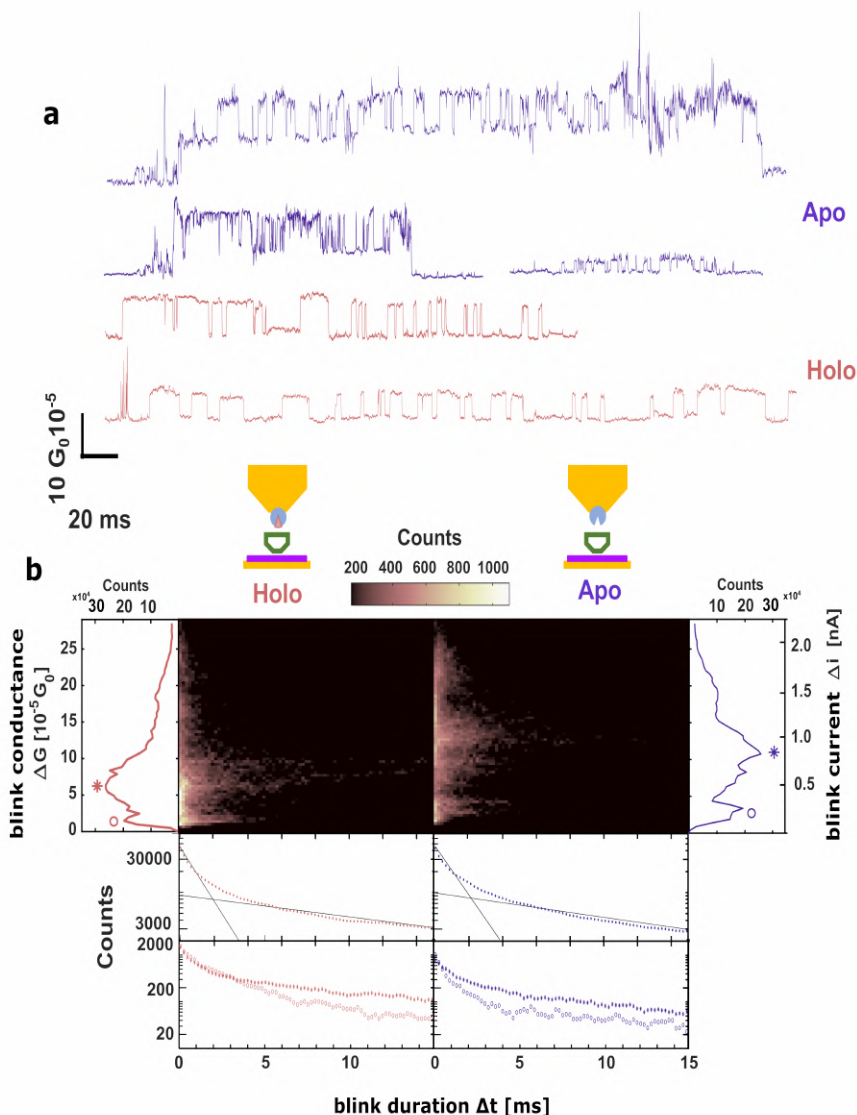


Figure 4.4: Blinking recordings in an ECSTM junction with probe-attached Pc_{holo} and Pc_{apo} facing PSI complexes on the sample electrode. (a) Examples of time course of ECSTM probe current at a fixed position in the absence of feedback control. Traces with telegraphic noise features (“blinks”) indicate a transient changes in conductivity of the junction corresponding to PSI- Pc_{holo} samples (pale red traces) and bottom to PSI- Pc_{apo} (blue traces). Set potentials are similar to blinking experiment, namely $U_{probe} = 100$ mV/SSC, $U_{sample} = 200$ mV/SSC which yields $U_{bias} = -100$ mV. (b) Blink events ($N=4110$ for PSI- Pc_{apo} and $N= 4216$ for PSI- Pc_{holo}) are pooled together to form a two-dimensional histogram representing the conductivity increase of the blink (G , left y-axis and i , right y-axis), and the duration of the blinking event (t , x-axis). Histograms on the side panels shown the conductance counts integrated during the time intervals for PSI/ Pc_{holo} in pale red (left) and PSI/ Pc_{apo} in blue (right). Two conductance peaks are present in the histograms, marked with an open circle (O) and an asterisk (*). The time course of the blinking events is shown at the middle panels under each map after integrating all conductance values. The blinking duration probability, $P(t)$, which is proportional to the number of counts, displays a bi-phasic exponential dependence (thin black lines). For conductance peaks (O and *), horizontal sections of the ΔG - Δt map are shown in the bottom panel.

The protein matrix of plastocyanin supports long-distance charge transport with photosystem I and the copper ion regulates its spatial span and conductance

Regarding the kinetics of the blinking events (Figure 4b lower panels), pooling all ΔG values yields a similar bi-phasic exponential decay for both PSI/Pc_{holo} ($\tau_{\text{fast}} = 1.4 \pm 0.2$ ms, $\tau_{\text{slow}} = 18.4 \pm 0.4$ ms) and PSI/Pc_{apo} ($\tau_{\text{fast}} = 1.6 \pm 0.2$ ms, $\tau_{\text{slow}} = 16.5 \pm 0.6$ ms). τ_{fast} and τ_{slow} and their associated uncertainties, have been obtained by linear fit (black traces in Figure 4b) of the natural logarithm of the number of counts vs Δt for short and long times regimes respectively. In addition, the time course of the blinks associated to high (*) and low (o) conductance peaks is displayed at the bottom panel of Figure 4b (red and blue symbols for PSI/Pc_{apo} and PSI/Pc_{holo}, respectively). The fast phase of blinks can be associated with high frequency switching events that are recognizable in individual traces (Supplementary Figure 4). The conductance of these characteristic features, $\Delta G \sim 2 \cdot 10^{-5} G_0$ is compatible with low conductance peaks in PSI/Pc_{holo} and PSI/Pc_{apo} experiments and a lifetime of ~ 1 ms. Similar ΔG and Δt of blinking events observed in electrochemical tunnelling junctions have been attributed to trapping/detrapping of charges at localized electronic states associated to water molecules^{52,53} Which lowers the electron energy barrier thus increasing conductance. On the other hand, the slow phase of blinks corresponds to the total duration of the blinking event (Figure 4a) which is compatible with the formation of PSI/Pc transient complexes. Direct comparison of our single molecule experiments with bulk measurements is not straightforward, as the reported ms phase²⁹ associated with PSI/Pc complex formation exhibits pseudo-first order kinetics and therefore depends on Pc concentration. Still, rates ranging from 100 to 3000 s⁻¹ in transient absorption measurements²⁹ and 50 to 400 s⁻¹ in transient photovoltage measurements²³ match the lifetime of our blinking events ($1/\tau \sim 60$ s⁻¹).

Complementarily to figure 4, we display in Supplementary Figure 5, ΔG - Δt histograms for blinking traces recorded at positive bias $U_{\text{bias}} = 100$ mV that sets the electron flow from PSI-functionalized sample electrode to Pc-functionalized probes, that is against physiological charge exchange between PSI-Pc. Comparative of conductance histograms for positive and negative bias (Supplementary figure 6) shows that low conductance peaks (marked with circles in side panels of Figure 4b) channels around $\sim 2 \cdot 10^{-5} G_0$ are also present in positive bias conditions. On the other hand, the high conductance peak of PSI/Pc_{holo} at $\sim 7 \cdot 10^{-5} G_0$ (marked with a star in side panel of Figure 4b) splits in two peaks at $\sim 5 \cdot 10^{-5} G_0$ and $\sim 11 \cdot 10^{-5} G_0$ for positive bias. Interestingly, this latter peak $\sim 11 \cdot 10^{-5} G_0$ in PSI/Pc_{apo} coincides with the high conductance peak of PSI/Pc_{apo} samples at negative bias that disappears for positive bias.

We interpret that high conductance peak of PSI/Pc_{holo} at $\sim 7 \cdot 10^{-5} G_0$ is associated to conductance pathways through Cu atom. Under this view, we associate the $\sim 5 \cdot 10^{-5} G_0$ peak observed for anti-physiological bias, as a decrease of the conductance pathways through Cu. Complementarily, we associate the $\sim 11 \cdot 10^{-5} G_0$ present in both anti-physiological bias of PSI/Pc_{holo} and notably in PSI/Pc_{apo} to conductance channels related to the protein structure that by-pass the redox center. In PSI/Pc_{apo} the decrease

The protein matrix of plastocyanin supports long-distance charge transport with photosystem I and the copper ion regulates its spatial span and conductance

conductance of peak at $\sim 11 \cdot 10^{-5} G_0$ for positive bias with respect to negative bias might indicate that electrostatic interactions are involved in the structure based conductance channels.

4 Discussion

We carried out high-resolution charge transport measurements between individual partners of the photosynthetic chain (Pc and PSI) and we quantified the contribution of the different components including the redox metal cofactor to the conductance of the junction, its spatial span and time course of interactions. The obtained values in the different experimental conditions are discussed in detail below. Yet, the most striking results are (1) the observation of charge exchange between Pc and PSI at long distances through the aqueous solution, and (2) the ability of copper-less Pc_{apo} to sustain interprotein ETp with PSI at the single protein level despite the complete absence of redox activity. Our results extend the ETp of non-redox single and monolayer proteins sandwiched between electrodes⁵⁻¹⁷ to interprotein charge exchange, providing evidence of ETp between a redox inactivated protein and its physiological ET cognate.

From a general perspective, the observation of Pc/PSI interprotein long distance charge exchange through the solution is akin to results reported previously between protein partners in the respiratory chain^{31,32} (cytochrome *c* and complex III, cytochrome *bc*₁, studied experimentally by means of hCc and pCc₁). Long distance currents between hCc and pCc₁ are electrochemically gated³¹ and regulated by phosphorylation,³² which indicate the physiological relevance of the process. Together, these studies show that physical (sub nanometric) contact between redox partners is not a prerequisite for ETp and suggests that it might not be necessary for physiological ET.³⁵ This interpretation raises many physicochemical and biological questions about the underlying mechanism of long distance interprotein charge exchange and its compatibility with published results demonstrating the formation of PSI/Pc transient complexes.^{20,21}

To answer the former, it seems reasonable to involve the aqueous solution region confined between the proteins, and to avoid explanations based on conventional quantum tunneling since reported charge exchange distances^{31,32,39,43} exceed the range accessible by one- and two-step electron tunneling. Longer charge exchange distances are described by thermally activated multi-step mechanisms, however they are incompatible with the available data of temperature independent ETp.^{3,4} It has been suggested that electrostatic potential driving ET induces a partial delocalization of the bridge electronic states able to promote long range electron transfer without thermal activation.⁵⁴ For the pair hCc/pCc₁, molecular dynamics calculations reveal a cation depletion region between the interacting partners that hinders charge screening, extending the electric field between redox partners across the electrolyte interface.^{31,32} In other words, the cognate partners

The protein matrix of plastocyanin supports long-distance charge transport with photosystem I and the copper ion regulates its spatial span and conductance

establish a Gouy-Chapman conduit between them.^{31,32} The results presented here support this view, as long distance charge transport (low β) observed for Pc_{apo} interacting with PSI is absent when Pc_{apo} faces a non-cognate sequence like that of the pIQAcys peptide. Remarkably, this extended charge exchange range of $\text{PSI}/\text{Pc}_{\text{apo}}$ with respect to $\text{PSI}/\text{Pc}_{\text{holo}}$ is favoured for positive bias driving electrons from Pc to PSI as it occurs in nature. For the reverse bias, β for $\text{PSI}/\text{Pc}_{\text{apo}}$ is similar to $\text{PSI}/\text{Pc}_{\text{holo}}$ which is not affected by the bias sign. However, extending the long-distance charge exchange mechanism to the interprotein domain brings up a question: are there intermediate molecular ‘bridge’ states outside the polypeptide chain and, if so, what is their nature? One possibility is that the localized electronic states identified with charge trapping, associated to low ΔG and fast conductance switching features in Figure 4 and Supplementary Figure 4, constitute these intermediate states. Transient configuration of water molecules leading to localized electronic states⁵³ could mediate interprotein ET as it has been previously suggested.⁵⁵⁻⁵⁸ Additionally, in *ab initio* electronic structure calculations modelling azurin proteins embedded in a tunnelling junction, it was observed an increase in conductance induced by water molecules enhancing azurin electronic coupling with the electrode.⁵⁹

Regarding the role of the redox center, as Pc_{apo} is devoid of its metal co-factor it is unable to undergo redox reactions accepting or donating electrons, and thus cannot carry and exchange them with PSI. However, in our ECSTS experiments, the probe and sample electrodes provide an electron source and drain,³ and therefore we observe that the copper redox center of Pc is not indispensable for ETp through the junction. Recently available DFT based calculations in multi-heme cytochrome⁶⁰ stuffed between electrodes show that high valence band states associated to the metal contribute poorly to the current.⁶⁰ Similar calculations performed with azurin^{59,61,62} incorporating different metal centers and an apo form, reveal that within the coherent transport approach followed by the authors, metal ions do not play a significant role in the conductance.⁶² The quantification of conductance, blinking and distance-dependence rates of $\text{PSI}/\text{Pc}_{\text{apo}}$ and $\text{PSI}/\text{Pc}_{\text{holo}}$ as well as the different controls presented here, allow dissecting the contribution of the redox center and the surrounding protein scaffold to the interprotein charge exchange, and provide insights into the mechanism of interprotein ETp and ET. In particular, we associate the lower ΔG of $\text{PSI}/\text{Pc}_{\text{holo}}$ compared to $\text{PSI}/\text{Pc}_{\text{apo}}$ to charge localization induced by the redox center. In multi-heme cytochrome and azurin trapped DFT calculations, spatial confinement of high valence band states of the Fe orbitals is responsible for its low electronic coupling and thus poor contribution to the current.⁶⁰ Also, the conductance histogram of $\text{PSI}/\text{Pc}_{\text{holo}}$ displays a narrower distribution than $\text{PSI}/\text{Pc}_{\text{apo}}$, suggesting that interprotein ET pathways of the complex are dominated or “funneled” by specific through-Cu pathways, whereas in $\text{PSI}/\text{Pc}_{\text{apo}}$ multiple and non-preferential ETp pathways through the protein matrix are available, leading to more spread conductance values. In any case, such pathways are built in the protein structure prior to metal binding,

which appears to fine-tune them. These adjustments include the small but significant increase in β upon copper binding, corresponding to a decrease in the spatial span of the current between PSI and Pc (Figure 3). We tentatively associate these three differences in PSI/Pc_{apo} with respect to PSI/Pc_{holo} (lower β , higher ΔG , and wider ΔG distribution) to the metal-induced charge localization⁶⁰ and its effects on electronic coupling between electron acceptor and donor. The physiological advantages of this adjustment are currently unknown.

Nevertheless, charge exchange distance measured in the ECSTS set-up must be interpreted cautiously. Long-range charge exchange could be promoted by the electric field applied between the sample and probe electrodes.⁹ A bias potential is necessary to elicit a probe current in order to interrogate interprotein charge exchange and, to our knowledge is the only experimental approach to dynamically study it as a function of the interprotein distance. To overcome this technical issue, we are developing a set-up that exploits PSI photo-catalytic activity using photo-generated charges as current drivers, and that should allow working in a null bias potential configuration.

From a biomolecular perspective, charge exchange between the PSI/Pc_{holo} pair spanning several nm suggests that complex formation is not essential for charge exchange in our experimental conditions. A similar conclusion was drawn from pathway model calculations of the ET rate between the bacterial reaction center and cytochrome c_2 (Pc homologue).⁵⁷ In that case, ET from the encounter complex configuration is possible, yet with a slower ET rate than in the bound complex.⁵⁷ Previous work with cytochrome partners³¹ and the results presented here with PSI/Pc question the necessity of physical contact to exchange charge between proteins in the ECSTM setup. Regarding the role of the redox center in this process, we suggest that, in addition to the widely acknowledged ability to physically host the charge (electron and hole in the reduced and oxidized forms of Pc_{holo}, respectively), the copper ion restricts the charge exchange range with respect to the “unregulated” range of the apo form. In this way, Pc might bypass charge exchange with non-cognate donors or acceptors, and/or regulate the process of interaction with its cognate partners (Cyt b_6f and PSI). Indeed, the binding affinity of PSI/Pc complexes is regulated by their redox state as shown in bulk transient spectroscopy²⁶ and single molecule force spectroscopy³⁰ measurements. In a broader context, it has been shown that binding regulates the overall ET rate in the PSI-Pc-Cyt f chain of *Chlamydomonas reinhardtii*.⁶³ In particular, the low binding affinity of Pc to PsaA-W651S mutant of PSI observed *in vitro* does not affect the overall charge exchange process *in vivo* whereas the mutation PsaB-E631N affecting Pc release, significantly reduces the overall charge exchange rate. Thus, the release of oxidized Pc from PSI regulates the rate of electron transport in the photosynthetic chain and methods to study these processes with spatiotemporal resolution and electrochemical control make unique contributions to understand its mechanism at the molecular scale.

5 Conclusions

In summary, we have characterized the remote and complex bound ETp between single protein pair complexes of the photosynthetic electron transport chain. We measure the distance dependence and conductance of interprotein charge exchange between suitably oriented PSI and Pc using current-distance and blinking techniques in electrochemical scanning tunneling spectroscopy (ECSTS), to assess the spatial span of the protein charge exchange as well as the formation of spontaneous protein junctions, respectively. We evaluated charge exchange distances for individual proteins and between the cognate protein pairs. Current-distance measurements reveal that in ECSTS configuration, PSI and Pc proteins are capable of exchanging charge over several nm through the aqueous solution, either individually against a gold electrode, or at the PSI/Pc configuration. The Cu ion in Pc enlarged the spatial span distance between Pc and a peptide functionalized electrode when compared to the non-redox Pc_{apo} . Interestingly, the presence of the Cu ion in Pc diminished the charge exchange distance with the cognate PSI for a bias that favors the electrons flow from Pc to PSI, as it occurs in the photosynthetic electron transport chain. We therefore demonstrate that charge exchange between Pc and PSI can occur at long distances through the aqueous solution, and that Cu-less Pc_{apo} can sustain interprotein ETp with PSI at the single protein level despite the absence of redox activity.

Additionally, as probe and sample electrodes are functionalized with Pc and PSI respectively, we detect conductance “*blinks*” associated with the spontaneous formation of a molecular junction with a typical duration of 6 ms. This time scale is consistent with the PSI/Pc transient complex formation reported by bulk measurements. The conductance change ΔG , measured for PSI/ Pc_{holo} shows a lower value and a narrower distribution with respect to PSI/ Pc_{apo} . In addition, a lower conductance blinking feature with a typical time decay of 1 ms was also observed, regardless the presence of the Cu ion in the Pc. The conductance and duration of these blinking events suggest that they are related to transient configuration of water molecules leading to localized electronic states⁵¹ that could mediate interprotein ET. ⁵³⁻⁵⁶ Besides, PSI/ Pc_{holo} displays a narrower conductance distribution than PSI/ Pc_{apo} , supporting the idea of multiple and non-preferential ETp pathways through the protein matrix that are “funneled” to specific pathways through the Cu center in the natural redox active protein. This suggests a role of the redox center in fine tuning the interprotein ETp.

Our results extend the inquiry of the protein ETp to the interprotein domain and allows to dissect the contribution of the redox center in Pc by direct comparison of PSI/ Pc_{apo} and PSI/ Pc_{holo} . In particular, lower β , higher ΔG , and wider ΔG distribution are measured for Cu-less PSI/ Pc_{apo} samples. We conclude that the protein matrix is sufficient to sustain long distance charge transport through the aqueous solution between Pc_{apo} and PSI as well as through the PSI/Pc transition complex, and we identify an additional role of the

The protein matrix of plastocyanin supports long-distance charge transport with photosystem I and the copper ion regulates its spatial span and conductance

redox ion as regulator of the conductance, energetic distribution, and spatial span of the current.

6 Methods

PSI-LHCI complexes purification

Whole PSI-LHCI complexes (referred simply as PSI throughout the manuscript) were extracted from *Arabidopsis thaliana* plants (*Arabidopsis* Col-0) grown under white light at 120 $\mu\text{mol photons}\cdot\text{m}^{-2}\cdot\text{s}^{-1}$, 12 hr/12 hr day/night cycles, for 5 weeks at 23 °C. Sucrose gradients were employed to purify PSI-LHCI complexes from thylakoid membranes isolated from *Arabidopsis* leaves as it has been previously described.^{64,65} In particular, 350 μg Chl thylakoid were diluted to 0.5 mg Chl $\cdot\text{ml}^{-1}$ in EDTA 5 mM, HEPES 10 mM, pH 7.5 and solubilized with detergent solution (1% α -decylmaltoside (α -DM) in HEPES 10 mM, pH 7.5) for 10 min. Following solubilization, the sample was centrifuged at 12,000 \times g for 10 min discarding insolubilized material. Resulting solution was loaded in sucrose gradients prepared by freeze and thaw method (sucrose 500 mM, HEPES 20 mM, pH 7.5, 0.06% α -DM) centrifuged for 16 h at 4 °C at 160000 \times g. PSI-LHCI complexes were collected with a syringe.

Plastocyanin mutant expression and purification

The mutant Pc-SH gene cloned into a pET-3a plasmid (pET-3a-PcSH) was used to transform *E. coli* BL21. The Pc-SH mutant (A121C) has three extra residues at its C-terminal (Thr-Cys-Gly). *E. coli* BL21 transformed with plasmid pET-3a-PcSH were grown in 2xYT medium supplemented with 100 gml^{-1} of ampicillin at 37 °C until OD600 of approximately 0.8 was reached. The expression of Pc-SH was induced by adding isopropyl thio- β -D-galactoside (IPTG) 0.3 mM for 4 h, shaking at 220 rpm and 28 °C. Cells were harvested by centrifugation (7000 rpm), suspended in MES buffer 10 mM, pH 6.5, and disrupted by sonication. The suspension was centrifuged for 1 hour at 20000 rpm. The soluble fraction was loaded onto an anion exchange column (HiTrap® Q, Cytiva). A linear NaCl gradient (0-300 mM) in MES buffer 10 mM, pH 6.5, was used to elute Pc-SH. Subsequently, the protein-containing fractions were pooled and loaded onto a size exclusion column (Superdex® 75 10/300, Cytiva). Pc-SH purity was analyzed by SDS-PAGE stained with one-step blue® protein gel stain. The pure protein-containing fractions were pooled, and glycerol was added to 40% v/v. The Pc-SH was stored at 20 °C until the experiments were performed. Pc-SH mutant was purified in a Cu-free form (Apo). To avoid the oxidation reaction between a cysteine residue of the Pc mutant and Cu^{2+} , apo Pc-SH (Pc_{apo}) was directly bound to the Au STM probe or electrode. For the experiments with Pc_{holo}, the Pc_{apo} bound to the probe was incubated with fresh Cu^{2+} solution for 1 h (CuSO_4 , 50 mM) to bind Cu^{2+} (see below).

The protein matrix of plastocyanin supports long-distance charge transport with photosystem I and the copper ion regulates its spatial span and conductance

Sample Preparation: PSI-pIQAcys-Au electrodes

Prior to peptide incubation, Au[111] single-crystal electrodes of 10 mm diameter and 1 mm thickness (MaTecK) were electrochemically polished in H₂SO₄, flame annealed and cooled in Ar atmosphere. 100 μ L of PSI linker peptide pIQAcys solution 0.1 mM in CH₃COONa buffer 50 mM pH 4.5 was incubated for 30 min at room temperature. After peptide incubation, samples were gently rinsed with Phosphate Buffer Saline (PBS) 50 mM, pH 7.4 (working buffer). 5 μ L of PSI samples (OD~20) were diluted in 45 μ L of PBS buffer for overnight incubation at 4 °C. After incubation, buffer was gently exchanged with PBS PSI-free buffer to elute unbound complexes. In a previous work, PSI-pIQAcys-Au functionalization was characterized with ECSTM and AFM and with cyclic voltammetry (CV) to define a working electrochemical window [-200, +300] mV/SSC where PSI complexes are photo-active³⁹. Prior to ECSTM experiments, PSI activity was tested measuring its photocurrent response to 690 nm irradiation in photo-chronoamperometry experiments at -100 mV/SSC.

Sample Preparation: P_c_{apo/holo}-Au electrodes and P_c_{apo/holo}-Au ECSTM probes

Pc incubation for Au electrodes and ECSTM is similar: in the former 50 μ L of Pc-SH sample 1mg·mL⁻¹ in ammonium acetate buffer 50 mM pH 4.5 were incubated in freshly annealed Au[111] electrodes (see above). For probes, six ECSTM Au probes (see preparation method below) were placed in a polydimethylsiloxane (PDMS) coated petri dish around a 100 μ L drop of P_c_{apo}-SH 1mg·mL⁻¹ in ammonium acetate buffer allowing to soak all probe tips. After 1 h incubation at 4°C, probes or electrodes were rinsed with MES buffer to remove unbound proteins. After rinsing, P_c_{apo}-SH samples were ready to use. P_c_{holo}-SH were further incubated for 1 h at 4°C in 2-(N-morpholino)ethanesulfonic acid solution (MES) buffer 5 mM pH 4.5, containing 100 mM of CuSO₄. After rinsing with MES buffer, Au electrodes or probes are ready for cyclic voltammetry or ECSTS spectroscopy experiments respectively.

ECSTM probes

ECSTM probes were fabricated from 0.5 mm Au 99% wire (Mateck), mechanically cut with sharp handheld steel wire cutter. Probe holder was modified with a 0.6 mm hypodermic needle MicrolanceTM (BD) steel tube to accommodate thicker probes for enhanced mechanical and thermal stability. Probes were coated twice with ApiezonTM wax heated up to ~120 °C in a home-built heat-coating applicator.

Cyclic voltammetry

Electrochemical measurements were carried out with a potentiostat PGSTAT 302N (Metrohm Autolab). Cyclic voltammetry (CV) experiments were performed in three-electrode cell used for ECSTM experiments. Cell counts with: i) Reference electrode, miniaturized ultralow leakage membrane Ag/AgCl (SSC) reference electrode

The protein matrix of plastocyanin supports long-distance charge transport with photosystem I and the copper ion regulates its spatial span and conductance

filled with 3M KCl (World Precision Instruments) ii) counter electrode, 0.25 mm diameter Pt80/Ir20 wire (Advent) iii) working electrode $\text{Pc}_{\text{apo/holo}}\text{-SH}$ coated Au[111] monocrystalline electrodes (see preparation above). CV were run between -100 and 300 mV/SSC at a scan rate of $5 \text{ mV}\cdot\text{s}^{-1}$. Experiments were carried out in working buffer (PBS 50 mM, pH 4.5) at room temperature. Pc_{holo} CV was performed on the same Pc_{apo} after CuSO_4 incubation and thorough rinsing. Cell and all glass material used for preparation of solutions were cleaned with piranha solution (7:3 $\text{H}_2\text{SO}_4/\text{H}_2\text{O}_2$ (30%) by volume). **Caution: Piranha solution should be handled with extreme caution.**

Electrochemical scanning tunneling spectroscopy (ECSTS) measurements

All experiments were performed with a PicoSPM microscope head and a PicoStat bipotentiostat (Agilent, USA) controlled by Dulcinea electronics (Nanotec Electronica, Spain) using the WSxM 4 software.⁶⁶ Bipotentiostat allows adjusting sample and probe potentials, U_S and U_P , independently. A homemade electrochemical cell described above was used for CV and ECSTM experiments.

The ECSTM head was placed on a passive mechanical vibration isolation system (900 kg block suspended by 3 metal springs of 4 m length) with a 0.4 Hz cut-off frequency. Damping rate was reduced to $\sim 1 \text{ min}^{-1}$ by inserting/stuffing iron/steel wool in the springs. A cylindrical cover made of 1 cm thick neoprene provided acoustic damping.

The current-distance $-I(z)$ - curves were acquired by departing from a set-point current fixed at 0.3 nA. For these experiments, probes with displaying leakages currents above 8 pA were discarded. The current feedback-loop is switched off and the probe electrode is retracted 10 nm at $40 \text{ nm}\cdot\text{s}^{-1}$. Afterwards, the probe is approached again and the current-distance feedback loop is reestablished for 100 ms before retracting again. 1000 $I(z)$ curves were recorded for each sample and two independent samples were prepared and measured for each condition. To minimize drift artifacts, $I(z)$ curves departing with a current deviation higher than 10% of the initial sETpoint were discarded. For all current-distance experiments, the probe potential was fixed to 100 mV/SSC, near the Pc redox mid-point. The sample potential was set to 0 mV/SCC and 200 mV/SSC yielding +100 and -100 mV of bias voltage, forcing the electron transfer from sample to probe and *vice versa*. The spatial span of the interprotein charge exchange process was quantified fitting $I(z)$ curves with a double exponential model described previously, fitting the current-distance rate for short and long distance separately.³⁹ $I(z)$ curve double-exponential fitting routine was implemented in R software and is available at: https://github.com/Mlopeorti/Tunnel_current_2exponential_fitter. The close distance regime has been reported to be affected by the electric double layer deployed in the vicinity of the electrode interface.^{40,41} Thus, to avoid artifacts protein charge-exchange distance results and discussion is based on the long distance regime. β -values in the close

The protein matrix of plastocyanin supports long-distance charge transport with photosystem I and the copper ion regulates its spatial span and conductance

distance regime (β_0) and the distance for regime change (Z_0) for all the experimental conditions are shown in Supplementary Figure 7 and 8 respectively.

β -values distribution histograms were analyzed and represented with Matlab 2021 (The MathWorks Inc.). β -values distribution is fit around the maximum frequency with a normal distribution, reporting the value as the mean value \pm the standard deviation of the distribution, that is $\langle \beta \rangle \pm (\beta)$.

For blinking experiments, a NI-DAQmx and BNC-2110 acquisition card controlled by Labview (National Instruments) was used. After a period of mechanical stabilization, the STM probe is placed to achieve a set-point current of 1 nA, until the feedback is turned off. Current versus time traces are then recorded in packets of three seconds during a total time of several hours. Current blinks are observed in the current transient in the form of telegraphic noise (Fig. 2a). The current increment of the blink ΔI , is transformed to conductance values using $G = \Delta I_{\text{blink}}/U_{\text{bias}}$.

At least two independent experiments were conducted in each case, adding up to $N=4110$ for PSI-Pc_{apo} and $N= 4216$ for PSI-Pc_{holo} blinking events, automatically recognized using a customized current threshold strategy (see supplementary figure 4) implemented in Matlab 2021 (The MathWorks Inc.). Data was analyzed, pooling blinking events in a common time and conductance origin to build a two-dimensional histogram with ΔG in y-axis Δt in x-axis. Conductance peaks, marked with stars and open circles in the side panel of figure 4b, were fit with a normal distribution. The reported values correspond to the mean value \pm the standard error of the mean. For the time decay of the blinking duration, we estimate the time constant and their associated error by linear regression of the natural logarithm of the number of counts for short time regime ($\Delta t < 2$ ms) and long time regime ($\Delta t > 5$ ms).

Acknowledgements

This research received funding from the European Union Research and Innovation Programme Horizon 2020 - HBP SG3 (grant agreement No. 945539), DEEPER (ICT-36-2020, grant agreement No. 101016787), European Research ERANet SynBio programme (Modulightor project), and financial support from Agency for Management of University and Research Grants (CERCA Programme; 2017-SGR-1442project), Ministry of Economy and Competitiveness (MINECO)/ FEDER (grants No. CTQ2015-66194-R and CTQ2016- 80066-R), Ministry of Science and Innovation DEEP RED grant No. PID2019-111493RB-I00 funded by MCIN/AEI/10.13039/501100011033, the Fundaluce foundation, the Commission for Universities and Research of the Department of Innovation, Universities, and Enterprise of the Generalitat de Catalunya -AGAUR- (IU16-011508) and cofinanced by the European Union Regional Development Fund within the framework of the ERDF/FEDER Operational Program of Catalonia 20142020 with a grant of 50% of total eligible cost. This research was supported by CIBER

(Consortio Centro de Investigación Biomédica en Red, CB06/01/0081), Instituto de Salud Carlos III, Ministerio de Ciencia e Innovación. R.Z. was supported by National Agency for Research and Development (ANID)/Scholarship Program POSTDOCTORADO BECAS CHILE/2018-74190117. We thank G. W. Canters, S. Cannistraro, and L. Andolfi for the kind gift of Pc clones. We would like to thank everybody involved in the development and set-up of the anti-vibratory system: Iñaki Bahamonde (HierroK), Lourdes Sanchez (Piedra Artificial), David Izquierdo (Core Facilities IBEC), Ana Mezquita (Parc Científic de Barcelona), Jaume Clapes (Applied Geophysics Service of Universitat Politècnica de Catalunya).

7 Bibliography

1. Derek Bendall. Protein Electron Transfer. *Garland Science* (1996).
2. Winkler, J. R. & Gray, H. B. Electron flow through metalloproteins. *Chem Rev* 114, 3369–3380 (2014).
3. Cahen, D., Pecht, I. & Sheves, M. What Can We Learn from Protein-Based Electron Transport Junctions? *Journal of Physical Chemistry Letters* 12, 11598–11603 (2021).
4. Bostick, C. D., Mukhopadhyay, S., Sheves, M., Cahen, D. & Lederman, D. Protein bioelectronics: a review of what we do and do not know. *Reports on Progress in Physics* 81(2), 1–150 (2018).
5. Zhang, B., Song, W., Brown, J., Nemanich, R. & Lindsay, S. Electronic Conductance Resonance in Non-Redox-Active Proteins. *J Am Chem Soc* 142, 6432–6438 (2020).
6. Lindsay, S. Ubiquitous electron transport in non-electron transfer proteins. *Life* 10, 72, (2020).
7. Garg, K. et al. Direct evidence for heme-assisted solid-state electronic conduction in multi-heme: C -type cytochromes. *Chem Sci* 9, 7304–7310 (2018).
8. Ron, I. et al. Proteins as electronic materials: Electron transport through solid-state protein monolayer junctions. *J Am Chem Soc* 132, 4131–4140 (2010).
9. Zhang, B., Ryan, E., Wang, X., Song, W. & Lindsay, S. Electronic Transport in Molecular Wires of Precisely Controlled Length Built from Modular Proteins. *ACS Nano* 16, 1671–1680 (2022).
10. Zhang, B. et al. Engineering an Enzyme for Direct Electrical Monitoring of Activity. *ACS Nano* 14, 1360–1368 (2020).
11. Zhang, B. et al. Role of contacts in long-range protein conductance. *Proc Natl Acad Sci USA* 116, 5886–5891 (2019).

The protein matrix of plastocyanin supports long-distance charge transport with photosystem I and the copper ion regulates its spatial span and conductance

12. Zhang, B. et al. Observation of giant conductance fluctuations in a protein. *Nano Futures* 1(3), 035002 (2017).
13. Kayser, B. et al. Solid-State Electron Transport via the Protein Azurin is Temperature-Independent Down to 4 K. *J Phys Chem Lett* 11, 144–151 (2020).
14. Guo, C. et al. Tuning electronic transport via hepta-alanine peptides junction by tryptophan doping. *Proc Natl Acad Sci USA* 113, 10785–10790 (2016).
15. Yu, X. et al. Insights into Solid-State Electron Transport through Proteins from Inelastic Tunneling Spectroscopy: The Case of Azurin. *ACS Nano* 9, 9955–9963 (2015).
16. Amdursky, N. et al. Electronic Transport via Proteins. *Advanced Materials* 26, 7142–7161 (2014).
17. Mukhopadhyay, S. et al. Solid-State Protein Junctions: Cross-Laboratory Study Shows Preservation of Mechanism at Varying Electronic Coupling. *iScience* 23, 101099 (2020).
18. Ricarda Höhnera et al. Plastocyanin is the long-range electron carrier between photosystem II and photosystem I in plants. *PNAS* 117, (2020).
19. Golbeck, J. H. Advances in Photosynthesis and Respiration Photosystem I The Light-Driven Plastocyanin Ferredoxin Oxidoreductase. 24, *Springer Science & Business Media*. (2007)
20. Caspy, I., Borovikova-Sheinker, A., Klaiman, D., Shkolnisky, Y. & Nelson, N. The structure of a triple complex of plant photosystem I with ferredoxin and plastocyanin. *Nat Plants* 6, 1300–1305 (2020).
21. Ueda, T. et al. Structural basis of efficient electron transport between photosynthetic membrane proteins and plastocyanin in Spinach revealed using nuclear magnetic resonance. *Plant Cell* 24, 4173–4186 (2012).
22. Hope, A. B. Electron transfers amongst cytochrome f, plastocyanin and photosystem I: Kinetics and mechanisms. *Biochim Biophys Acta Bioenerg* 1456, 5–26 (2000).
23. Mamedov, M. D., Mamedova, A. A., Chamorovsky, S. K. & Semenov, A. Y. Electrogenic reduction of the primary electron donor P700 by plastocyanin in photosystem I complexes. *FEBS Lett* 500, 172–176 (2001).
24. Hervás, M., Navarro, J. A., Díaz, A., & De la Rosa, M. A. A comparative thermodynamic analysis by laser-flash absorption spectroscopy of photosystem I reduction by plastocyanin and cytochrome c 6 in *Anabaena* PCC 7119, *Synechocystis* PCC 6803, and spinach. *Biochemistry*, 35(8), 2693- 2698 (1996).

The protein matrix of plastocyanin supports long-distance charge transport with photosystem I and the copper ion regulates its spatial span and conductance

25. Sommer, F., Drepper, F., Haehnell, W. & Hippler, M. The Hydrophobic Recognition Site Formed by Residues PsaA-Trp651 and PsaB-Trp627 of Photosystem I in *Chlamydomonas reinhardtii* Confers Distinct Selectivity for Binding of Plastocyanin and Cytochrome *c* 6. *Journal of Biological Chemistry* 279, 20009–20017 (2004).
26. Drepper, F., Hippler, M., Nitschke, W. & Haehnel, W. Binding dynamics and electron transfer between plastocyanin and photosystem I. *Biochemistry* 35, 1282–1295 (1996).
27. Sommer, F., Drepper, F. & Hippler, M. The luminal helix I of PsaB is essential for recognition of plastocyanin or cytochrome *c*6 and fast electron transfer to photosystem I in *Chlamydomonas reinhardtii*. *Journal of Biological Chemistry* 277, 6573–6581 (2002).
28. Kuhlert, S., Drepper, F., Fufezan, C., Sommer, F. & Hippler, M. Residues PsaB Asp612 and PsaB Glu613 of photosystem I confer pH-dependent binding of plastocyanin and cytochrome *c* 6. *Biochemistry* 51, 7297–7303 (2012).
29. Haehnel, W. et al. Electron transfer from plastocyanin to photosystem I. *EMBO Journal* 13, 1028–1038 (1994).
30. Zamora, R. A. et al. Light- and Redox-Dependent Force Spectroscopy Reveals that the Interaction between Plastocyanin and Plant Photosystem I Is Favored when One Partner Is Ready for Electron Transfer. *ACS nano*, 16(9), 15155–15164 (2022)
31. Lagunas, A. et al. Long distance electron transfer through the aqueous solution between redox partner proteins. *Nat Commun* 9(1), 5157 (2018).
32. Alexandre Gomila et al. Phosphorylation disrupts long-distance electron transport in cytochrome *c*. *Nat Commun* 13(1), 7100 (2022).
33. Ha, T. Q., Planje, I. J., White, J. R. G., Aragonès, A. C. & Díez-Pérez, I. Charge transport at the protein–electrode interface in the emerging field of biomolecular electronics. *Curr Opin Electrochem* 28, 100734 (2021).
34. Salvatore, P. et al. Electrochemistry of single metalloprotein and DNA-based molecules at Au(111) electrode surfaces. *ChemPhysChem* 14, 2101–2111 (2013).
35. Pérez-Mejías, G., Díaz-Quintana, A., Guerra-Castellano, A., Díaz-Moreno, I. & de la Rosa, M. A. Novel insights into the mechanism of electron transfer in mitochondrial cytochrome *c*. *Coord Chem Rev* 450, (2022).
36. Andolfi, L., Canters, G. W., Verbeet, M. P. & Cannistraro, S. Scanning tunneling spectroscopy investigation of self-assembled plastocyanin mutants onto gold substrates under controlled environment. *Biophys Chem* 107, 107–116 (2004).

The protein matrix of plastocyanin supports long-distance charge transport with photosystem I and the copper ion regulates its spatial span and conductance

37. Andolfi, L., Bonanni, B., Canters, G. W., Verbeet, M. P. & Cannistraro, S. Scanning probe microscopy characterization of gold-chemisorbed poplar plastocyanin mutants. *Surf Sci* 530, 181–194 (2003).
38. Gordiichuk, P. et al. Orientation and Incorporation of Photosystem I in Bioelectronics Devices Enabled by Phage Display. *Advanced Science* 4(5), 1600393., (2017).
39. López-Ortiz, M. et al. Distance and Potential Dependence of Charge Transport Through the Reaction Center of Individual Photosynthetic Complexes. *Small* 18(7), 2104366 (2022).
40. Wigginton, N. S., Rosso, K. M., Stack, A. G. & Hochella, M. F. Long-range electron transfer across cytochrome-hematite (-fe 2o 3) interfaces. *Journal of Physical Chemistry C* 113, 2096–2103 (2009).
41. Artés, J. M., Díez-Pérez, I., Sanz, F. & Gorostiza, P. Direct measurement of electron transfer distance decay constants of single redox proteins by electrochemical tunneling spectroscopy. *ACS Nano* 5, 2060–2066 (2011).
42. He, J., Lin, L., Zhang, P. & Lindsay, S. Identification of DNA Basepairing via Tunnel-Current Decay. *Nano Lett* 7, 3854–3858 (2007).
43. López-Martínez, M. et al. Electrochemically Gated Long-Distance Charge Transport in Photosystem I. *Angewandte Chemie - International Edition* 58, 13280–13284 (2019).
44. Giannotti, M. I. et al. Direct Measurement of the Nanomechanical Stability of a Redox Protein Active Site and Its Dependence upon Metal Binding. *J Phys Chem B* 119, 12050–12058 (2015).
45. Garrett, T. P. J., Clingleffer, D. J., Guss, J. M., Rogers, S. J. & Freeman, H. C. The Crystal Structure of Poplar Apoplastocyanin at 1.8-Å Resolution. *The American Society of Biological Chemists* 259(5), 2822--2825 (1984).
46. Díez-Pérez, I. et al. Rectification and stability of a single molecular diode with controlled orientation. *Nat Chem* 1, 635–641 (2009).
47. Artés, J. M., López-Martínez, M., Díez-Pérez, I., Sanz, F. & Gorostiza, P. Conductance switching in single wired redox proteins. *Small* 10, 2537–2541 (2014).
48. Ruiz, M. P. et al. Bioengineering a Single-Protein Junction. *J Am Chem Soc* 139, 15337–15346 (2017).
49. Aragonès, A. C. et al. Single-molecule electrical contacts on silicon electrodes under ambient conditions. *Nat Commun* 8, 1–8 (2017).
50. Tang, L. et al. Measuring conductance switching in single proteins using quantum tunneling. *Sci. Adv* 8 (2022).

The protein matrix of plastocyanin supports long-distance charge transport with photosystem I and the copper ion regulates its spatial span and conductance

51. Artés, J. M., Díez-Pérez, I. & Gorostiza, P. Transistor-like behavior of single metalloprotein junctions. *Nano Lett* 12, 2679–2684 (2012).
52. Xiang, L. et al. Conductance and Configuration of Molecular Gold-Water-Gold Junctions under Electric Fields. *Matter* 3, 166–179 (2020).
53. Boussaad, S. et al. Discrete tunneling current fluctuations in metal-water-metal tunnel junctions. *J Chem Phys* 118, 8891–8897 (2003).
54. Michaeli, K., Beratan, D. N., Waldeck, D. H. & Naaman, R. Voltage-induced long-range coherent electron transfer through organic molecules. *Proc Natl Acad Sci USA* 116, 5931–5936 (2019).
55. de La Lande, A., Babcock, N. S., Řezáč, J., Sanders, B. C. & Salahub, D. R. Surface residues dynamically organize water bridges to enhance electron transfer between proteins. *Proc Natl Acad Sci USA* 107, 11799–11804 (2010).
56. Lin, J., Balabin, I. A. & Beratan, D. N. The nature of aqueous tunneling pathways between electron-transfer proteins. *Science* 310, 1311–1313 (2005).
57. Miyashita, O., Okamura, M. Y. & Onuchic, J. N. Interprotein electron transfer from cytochrome c 2 to photosynthetic reaction center: Tunneling across an aqueous interface. *Proceedings of the National Academy of Sciences* 102, 3558–3563 (2005).
58. Halbritter, J., Repphun, G., Vinzelberg, S., Staikov, G & Lorenz, W. J. Tunneling mechanisms in electrochemical short-distance and voltage tunneling spectroscopy. *Pergamon Electrochimica Acta* 40, 1995 (1994).
59. Romero-Muñiz, C. et al. Can Electron Transport through a Blue-Copper Azurin Be Coherent? An Ab Initio Study. *J Phys Chem C* 125, 1693–1702 (2021).
60. Futera, Z. et al. Coherent Electron Transport across a 3 nm Bioelectronic Junction Made of Multi-Heme Proteins. *J Phys Chem Lett* 11, 9766–9774 (2020).
61. Kayser, B. et al. Transistor configuration yields energy level control in protein-based junctions. *Nanoscale* 10, 21712–21720 (2018).
62. Romero-Muñiz, C. et al. The Role of Metal Ions in the Electron Transport through Azurin-Based Junctions. *Applied Sciences* 11, 3732 (2021).
63. Finazzi, G., Sommer, F. & Hippler, M. Release of oxidized plastocyanin from photosystem I limits electron transfer between photosystem I and cytochrome b 6 f complex in vivo. *PNAS* 102(19), 7031-7036 (2005).
64. Xu, P., Tian, L., Kloz, M. & Croce, R. Molecular insights into Zeaxanthin-dependent quenching in higher plants. *Sci Rep* 5, 1–10 (2015).

The protein matrix of plastocyanin supports long-distance charge transport with photosystem I and the copper ion regulates its spatial span and conductance

65. Caffarri, S., Kouřil, R., Kereiche, S., Boekema, E. J. & Croce, R. Functional architecture of higher plant photosystem II supercomplexes. *EMBO Journal* 28, 3052–3063 (2009).

66. Horcas, I. et al. WSXM: A software for scanning probe microscopy and a tool for nanotechnology. *Review of Scientific Instruments* 78, 013705 (2007).

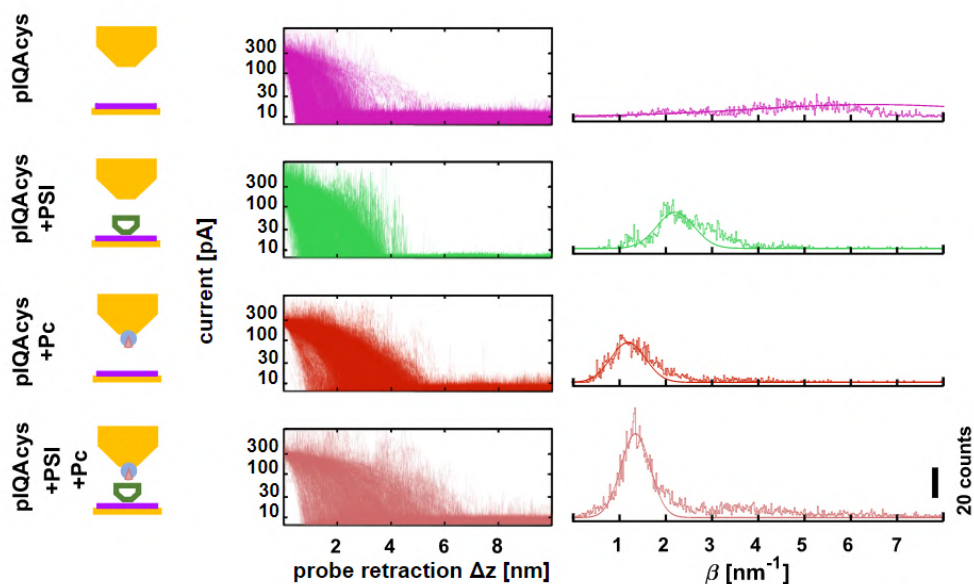
Supplementary Information

S1: β -values table

Probe electrode	Sample electrode	Diagram	 $U_{\text{Bias}} -100 \text{ mV}$	 $U_{\text{Bias}} +100 \text{ mV}$
Au	Au plQAcys		6 ± 1	6 ± 1
Au	Au plQAcys PSI		1.5 ± 0.1	2.2 ± 0.3
Au Pc-Holo	Au plQAcys		1.1 ± 0.3	1.2 ± 0.3
Au Pc-Apo	Au plQAcys		1.8 ± 0.4	1.5 ± 0.2
Au Pc-Holo	Au plQAcys PSI		1.5 ± 0.3	1.4 ± 0.2
Au Pc-Apo	Au plQAcys PSI		0.8 ± 0.2	1.2 ± 0.3

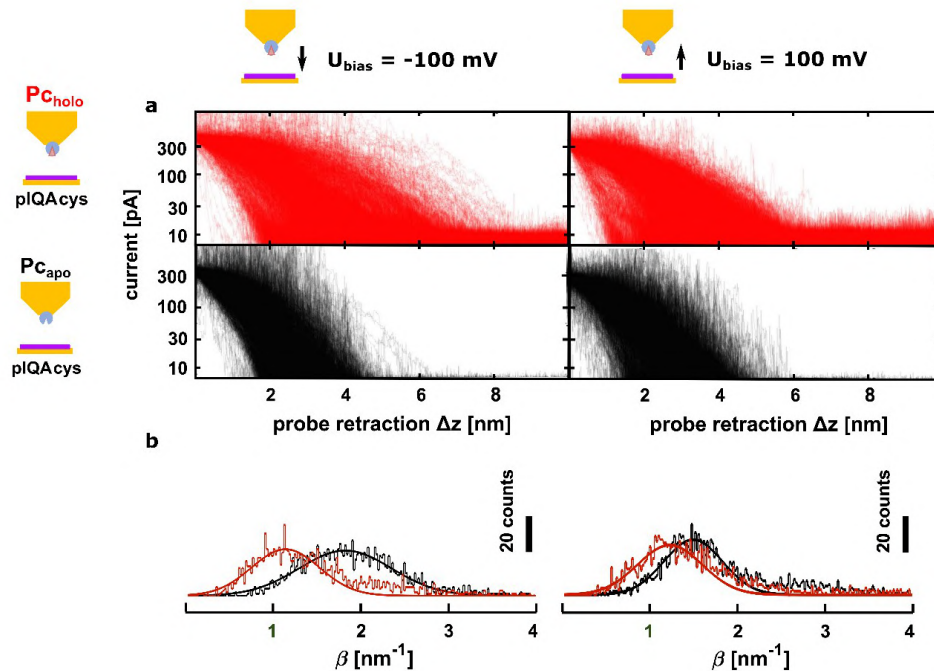
Supplementary Table 1: Current-distance rate β (nm^{-1}) values obtained from current-distance spectroscopy experiments, see methods for details of $I(z)$ traces fit. The β values were fit from 2000 curves from 2 independent experiments are pooled together. The table displays the mean \pm standard deviation of a normal distribution fitting beta-value distribution shown in Figures 2, 3, and Supplementary Figures 1, 2, and 3.

Supplementary Figure 1



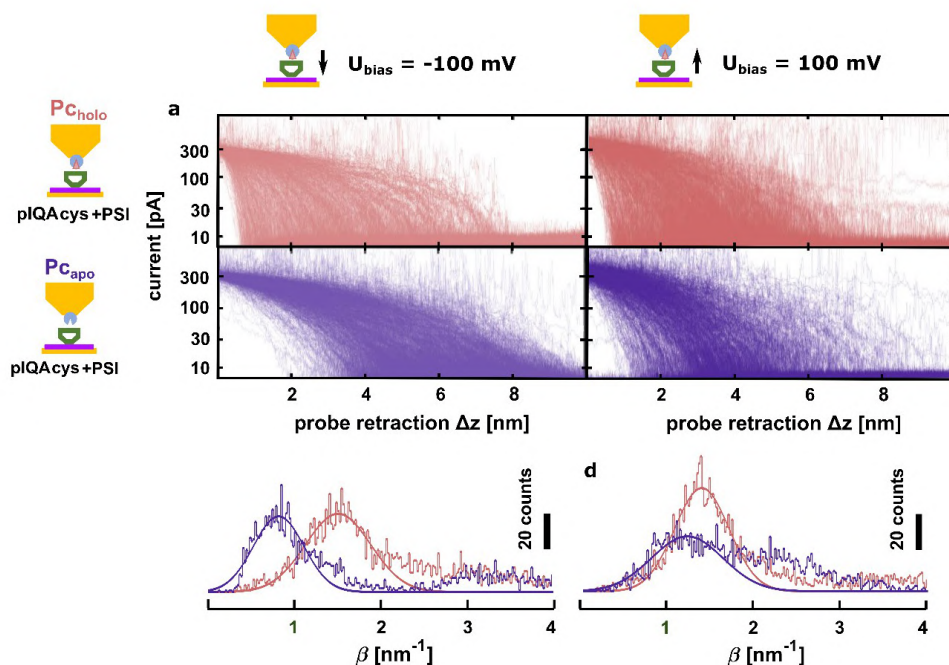
Supplementary Figure 1. Current distance spectroscopy of piQA-cys, PSI, Pc and PSI/Pc electrodes for positive bias. For positive bias, electrons flow from the sample electrode towards the probe electrode, $U_{\text{bias}} = +100$ mV; $U_{\text{probe}} = 100$ mV/SSC; $U_{\text{sample}} = 0$ mV/SSC. **(a)** Raw current-distance $I(z)$ curves for piQA-cys-Au (magenta) and PSI-piQA-cys-Au (green) samples using a bare Au probe; piQA-cys-Au (red) and PSI-piQA-cys-Au (pale red) samples using a Pc-Au probe. Each condition is depicted schematically on the left. In all cases, $n=1000$ curves were recorded in two independent experiments except for PSI/Pc samples that counts with three independent experiments. **(b)** Current distance rate (β) histograms obtained using values from $I(z)$ curves in panel (a) and fit by a normal distribution (solid curve).

Supplementary Figure 2:



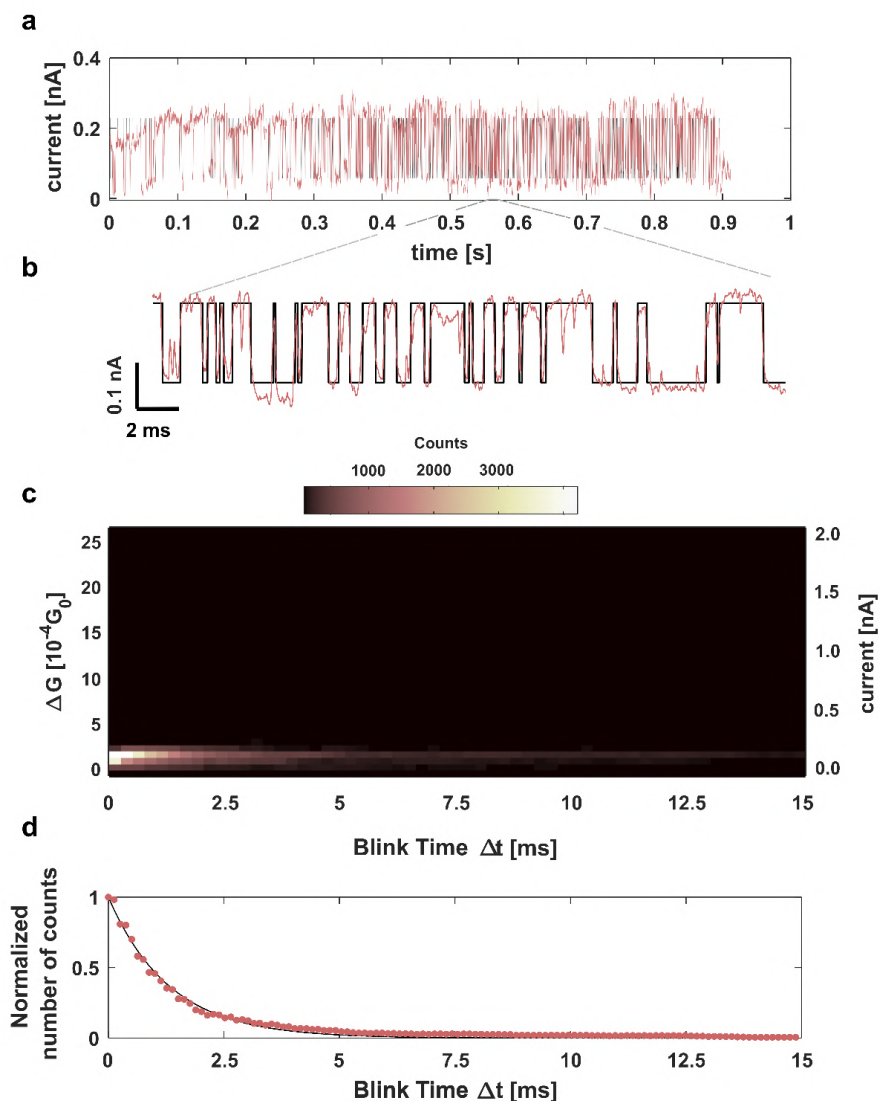
Supplementary Figure 2: $\text{Pc}_{\text{apo/holo}}$ current decay spectroscopy facing piQA_{cys} peptide sample electrode. (a) Raw current-distance $I(z)$ curves for piQA_{cys} -Au samples facing Pc_{holo} (red) and Pc_{apo} (black) probes. Negative bias (-100 mV; $U_{\text{probe}} = 100$ mV/SSC; $U_{\text{sample}} = 200$ mV/SSC electron injection from probe to sample) is shown in left side and positive bias (+100 mV; $U_{\text{probe}} = 100$ mV/SSC; $U_{\text{sample}} = 0$ mV/SSC, hole injection) is shown in right side. Each sample condition is depicted schematically on the left and electron exchange is depicted on top. In all cases, $n=1000$ curves were recorded in two independent experiments. **(b)** Current distance rate (β) histograms obtained using values from $I(z)$ curves in panel (a) and fit by a normal distribution (solid curve).

Supplementary figure 3:



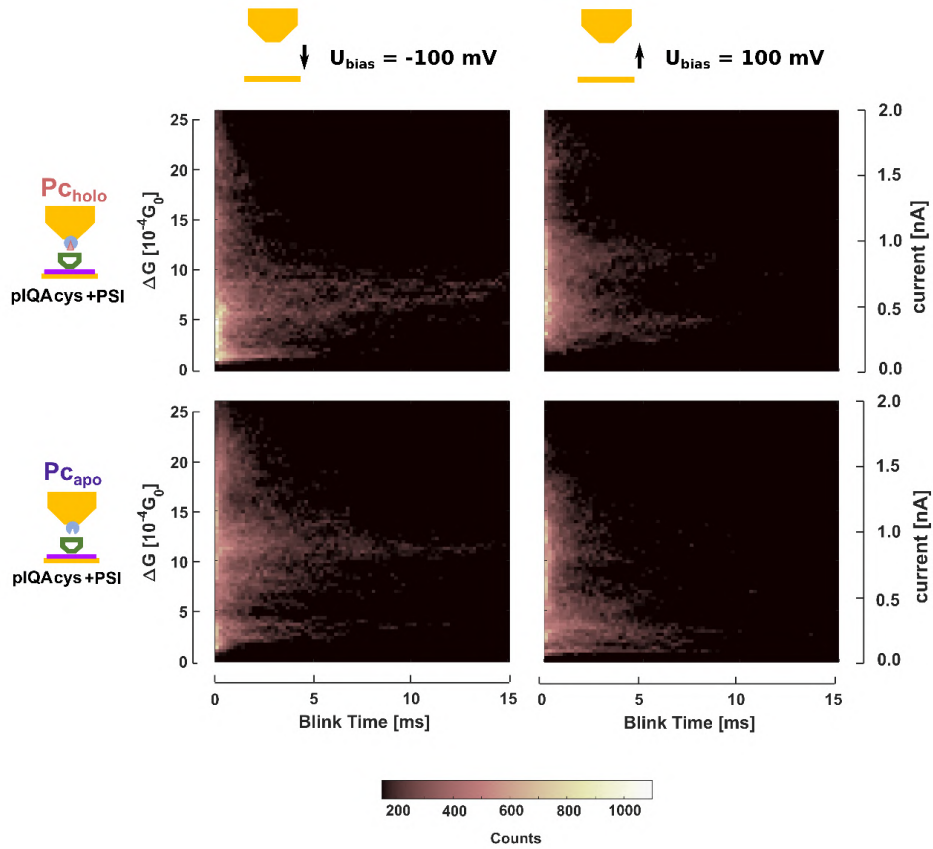
Supplementary Figure 3: $PC_{apo/holo}$ current decay spectroscopy facing PSI-pIQAcys sample electrode. (a) Raw current-distance $I(z)$ curves for PSI-pIQAcys-Au samples facing PC_{holo} (pale red) and PC_{apo} (blue) probes. Negative bias (-100 mV; $U_{probe} = 100$ mV/SSC; $U_{sample} = 200$ mV/SSC electron injection from probe to sample) is shown in left side and positive bias (+100 mV; $U_{probe} = 100$ mV/SSC; $U_{sample} = 0$ mV/SSC, hole injection) is shown in right side. Each sample condition is depicted schematically on the left and electron exchange is depicted on top. In all cases, $n=1000$ curves were recorded in three independent experiments. (b) Current distance rate (β) histograms obtained using values from $I(z)$ curves in panel (a) and fit by a normal distribution (solid curve).

Supplementary figure 4:



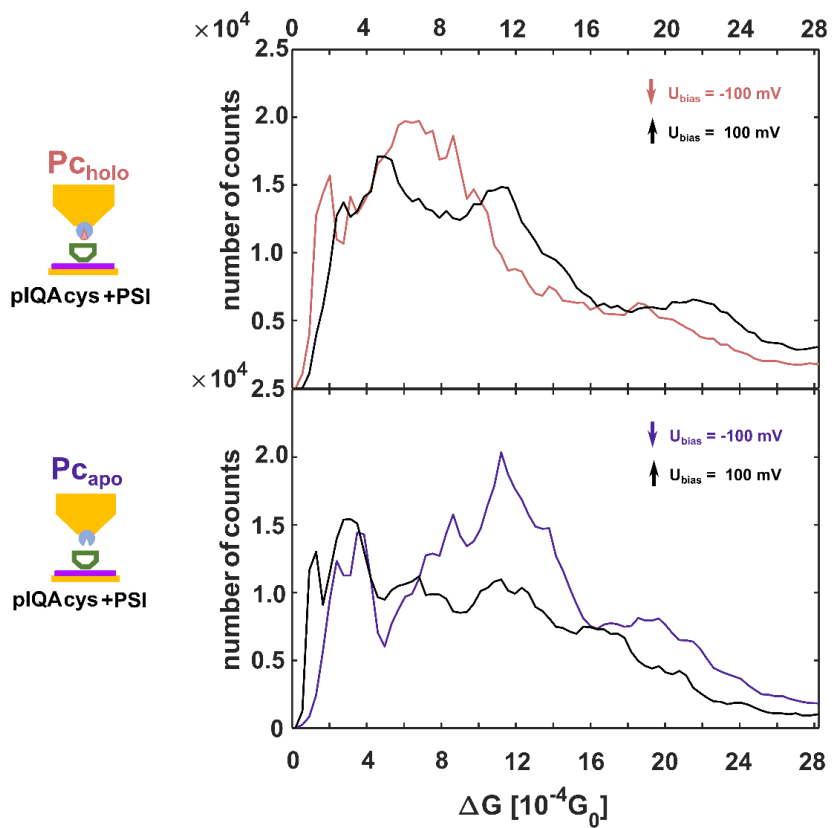
Supplementary Figure 4: Example of single trace blink raw data and analysis. (a) Example blink trace for PSI/PC_{hole} sample with $U_{\text{probe}} = 100$ mV/SCC and $U_{\text{sample}} = 200$ mV/SCC. A 1 s snapshot displaying high frequency and low conductance blinking ($\sim 2 \cdot 10^{-4} G_0$). (b) Inset displaying 25 ms of the current trace (pale red) and the two-level blinking fit (black trace) employed for analysis. (c) 2-d histogram for ΔG (y-axis) and Δt (x-axis) associated to trace in (a). For each detected blink (black trace in (b)), the initial time of blink event is subtracted to the raw data current-time trace, pooling together all the blinking events at the same time origin. The current increase (and associated ΔG) is computed with respect to the low-level state fit. The traces displaying these ΔG and Δt features are responsible for the low conductance peaks (marked with open circles) in figure 4 (see main text). (d) Normalized number of counts vs Δt . The decay constant τ for an exponential decay ($e^{-\Delta t/\tau}$) yields $\tau = 1.21 \pm 0.05$ ms.

Supplementary Figure 5:



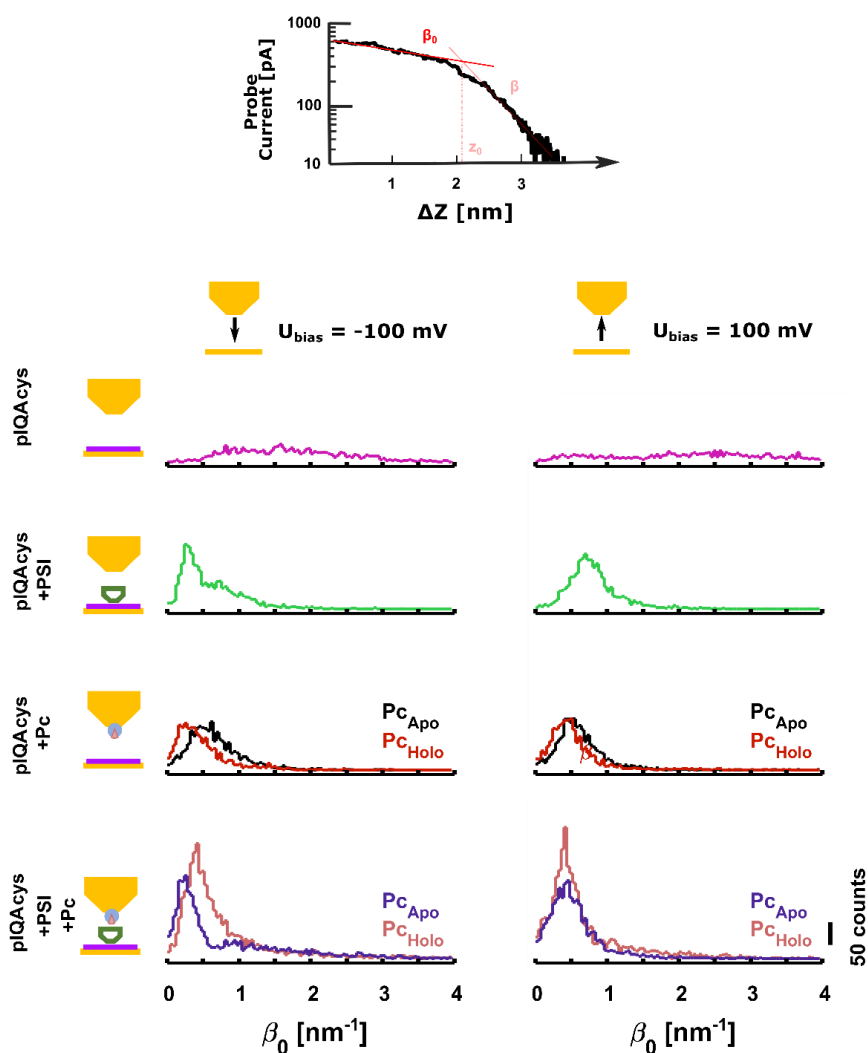
Supplementary Figure 5: two dimensional histogram of blinking ΔG and Δt for negative and positive bias. Blink events pooled together to form a two-dimensional histogram representing the conductivity increase of the blink (ΔG , left y-axis and Δi , right y-axis), and the duration of the blinking event (Δt , x-axis). Upper row corresponds to PSI/PC_{holo} samples and lower row to PSI/PC_{apo} as indicated in the diagram on the left. Left column represents $U_{\text{bias}} = -100$ mV as shown in figure 4b. This data has been included for comparison with data in the right column corresponding $U_{\text{bias}} = 100$ mV.

Supplementary Figure 6:



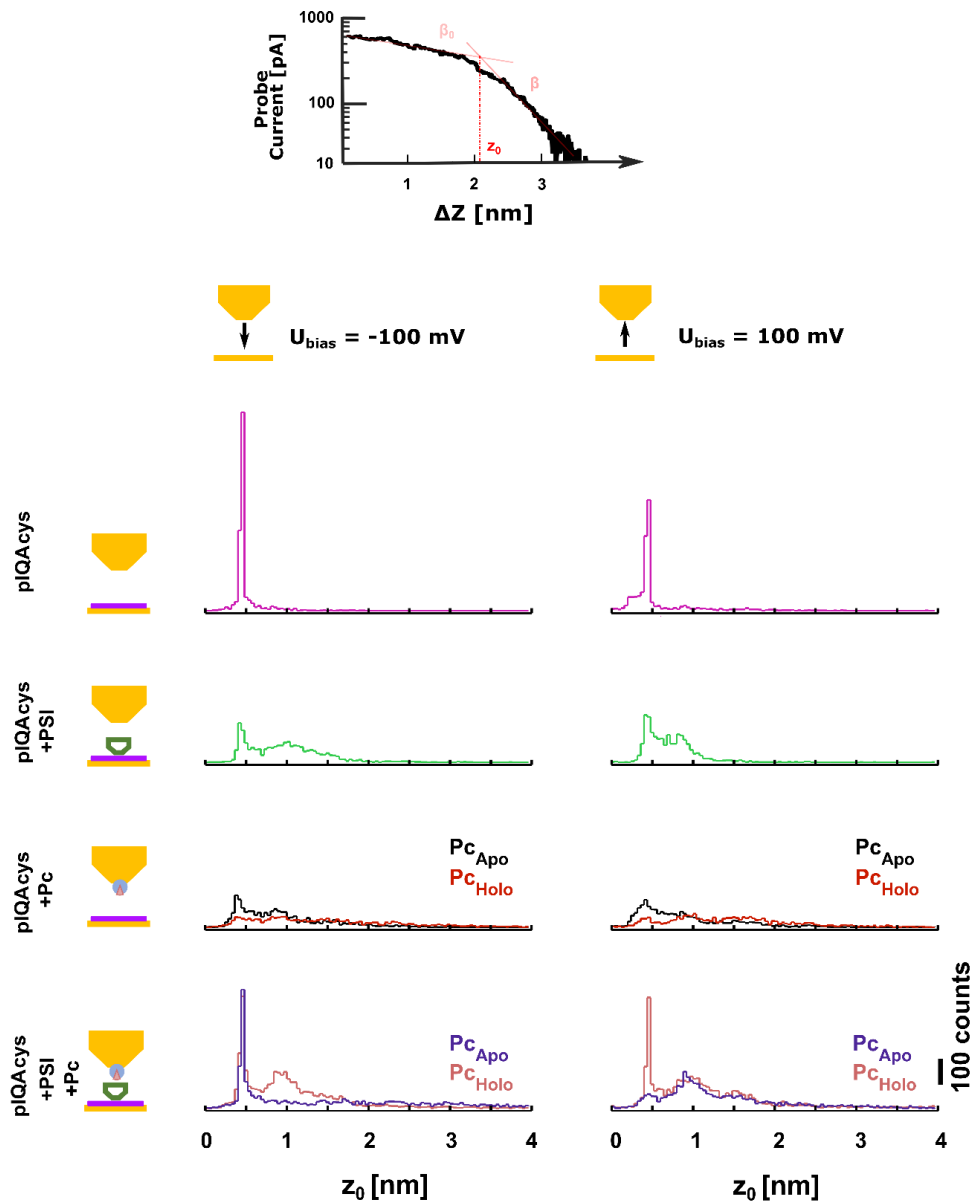
Supplementary Figure 6: Conductance histograms from blinking data for positive and negative bias. ΔG histograms issued from blinking traces for Pc_{holo} (upper panel, pale red) and Pc_{apo} (lower panel, blue) shown in figure 4b recorded at negative bias (electron flow from Pc to PSI) are compared with positive bias conditions (electron flow from PSI to Pc) shown in black traces.

Supplementary figure 7:



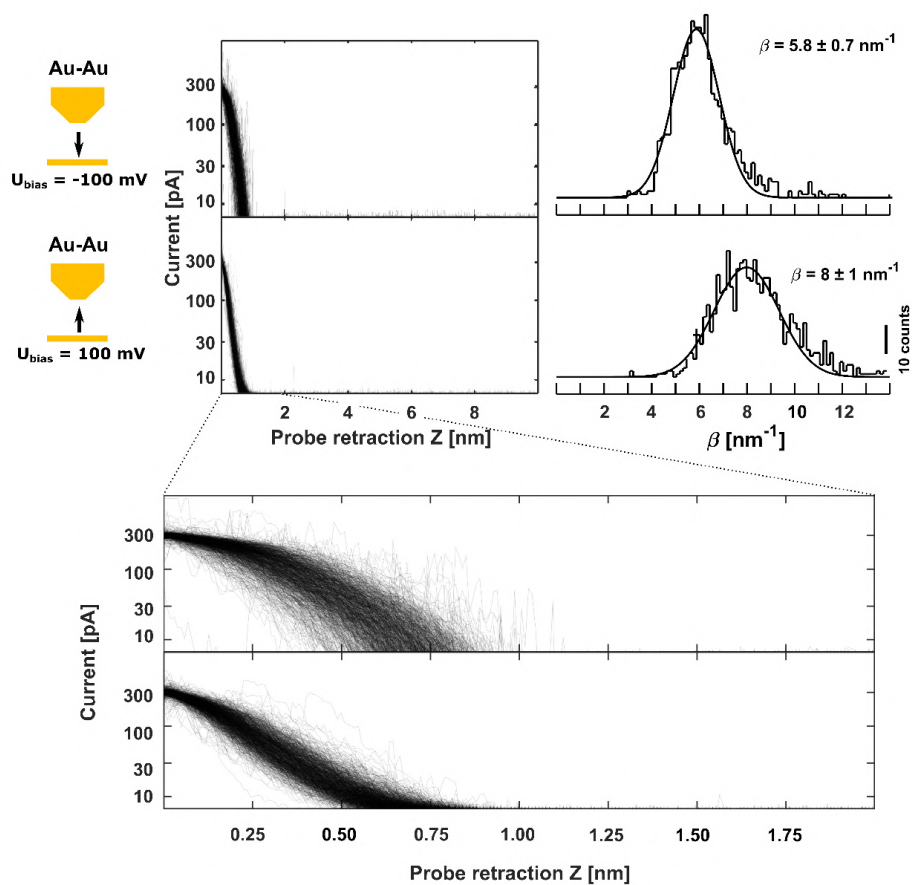
Supplementary Figure 7: Short distance regime Current-distance constant rate β_0 . Fit for the short distance current-distance rate β_0 from analysis of $I(z)$ curves recorded at negative bias $U_{\text{bias}} = -100$ mV; $U_{\text{probe}} = 100$ mV/SSC; $U_{\text{sample}} = 200$ mV/SSC displayed in figure 2 on left panel and positive bias on the right side for $I(z)$ traces shown in supplementary figure 1, $U_{\text{bias}} = +100$ mV; $U_{\text{probe}} = 100$ mV/SSC; $U_{\text{sample}} = 0$ mV/SSC. Bias value and electron flow is indicated with a black arrow. Diagrams and the color traces indicate the samples used, piQAcyS-Au (magenta) and PSI-piQAcyS-Au (green) for samples using a bare Au probe. For Pc functionalized probes, piQAcyS-Au/PC_{Holo}(red) PC_{Apo}(black). For the PSI/Pc pair, the color code is pale red PSI-piQAcyS/PC_{Holo} and blue for PSI-piQAcyS/PC_{Apo}. In all cases, $n=1000$ curves were recorded in two independent experiments.

Supplementary Figure 8:



Supplementary Figure 8: Short distance regime distance Z_0 . Fit for the short distance current-distance rate Z_0 from analysis of $I(z)$ curves recorded at negative bias $U_{bias} = -100$ mV; $U_{probe} = 100$ mV/SSC; $U_{sample} = 200$ mV/SSC displayed in figure 2 on left panel and positive bias on the right side for $I(z)$ traces shown in supplementary figure 1, $U_{bias} = +100$ mV; $U_{probe} = 100$ mV/SSC; $U_{sample} = 0$ mV/SSC. Bias value and electron flow is indicated with a black arrow. Diagrams and the color traces indicate the samples used, pIQAcys-Au (magenta) and PSI-pIQAcys-Au (green) for samples using a bare Au probe. For Pc functionalized probes, pIQAcys-Au/ Pc_{Holo} (red) Pc_{Apo} (black). For the PSI/Pc pair, the color code is pale red PSI-pIQAcys/ Pc_{Holo} and blue for PSI-pIQAcys/ Pc_{Apo} . In all cases, $n=1000$ curves were recorded in two independent experiments.

Supplementary Figure 7:



Chapter 5

Light- and redox-dependent force spectroscopy reveals that the interaction between plastocyanin and plant photosystem I is favored when one partner is ready for electron transfer

Ricardo A. Zamora,^{a,b,°} Manuel López-Ortiz,^{a,b,†} Chen Hu,^c Roberta Croce,^c Rinu Maniyara,^d Valerio Pruneri,^{d,e} Marina I. Giannotti,^{a,b,f,*} and Pau Gorostiza^{a,b,e,*}

^aInstitute for Bioengineering of Catalonia (IBEC), The Barcelona Institute of Science and Technology

^bCIBER-BBN, ISCIII

^cBiophysics of Photosynthesis. Dep. Physics and Astronomy, Faculty of Sciences, Vrije Universiteit Amsterdam ^dThe Institute of Photonic Sciences (ICFO), The Barcelona Institute of Science and Technology

^eCatalan Institution for Research and Advanced Studies (ICREA)

^fDepartment of Materials Science and Physical Chemistry, University of Barcelona * Corresponding authors: migiannotti@ibecbarcelona.eu (M.I.G.), pau@icrea.cat (P.G.)

† These authors contributed equally to this work.

1 Abstract

Photosynthesis is a fundamental process that converts photons into chemical energy, driven by large protein complexes at the thylakoid membranes of plants, cyanobacteria, and algae. In plants, water-soluble plastocyanin (Pc) is responsible for shuttling electrons between cytochrome *b6f* complex and the photosystem I (PSI) complex in the photosynthetic electron transport chain (PETC). For an efficient turnover, a transient complex must form between PSI and Pc in the PETC, which implies a balance between specificity and binding strength. Here, we studied the binding frequency and the unbinding force between suitably oriented plant PSI and Pc under redox control using single molecule force spectroscopy (SMFS). The binding frequency (observation of binding-unbinding events) between PSI and Pc depends on their respective redox states. The interaction between PSI and Pc is independent of the redox state of PSI when Pc is reduced, and it is disfavoured in the dark (reduced P700) when Pc is oxidized. The frequency of interaction between PSI and Pc is higher when at least one of the partners is in a redox state ready for electron transfer (ET), and the post-ET situation (PSI_{Red}-Pc_{Ox}) leads to lower binding. In addition, we show that the binding of ET-ready Pc_{Red} to PSI can be regulated externally by Mg²⁺ ions in solution.

Key words: single molecule measurements, photosystem I, plastocyanin, light-dependent interaction, force spectroscopy, inter-protein electron transfer.

2 Introduction

Oxygenic photosynthesis requires a high turnover electron transfer (ET) between membrane protein complexes forming the photosynthetic electron transport chain (PETC). Soluble redox proteins mediate ET through the aqueous solution between these integral membrane complexes in plants, cyanobacteria, and algae. In plants, plastocyanin (Pc) is the small water-soluble copper-containing redox protein responsible for shuttling electrons between cytochrome *b6f* complex (*Cytb6f*) and the photosystem I (PSI). The effective encounter of Pc with PSI and *Cytb6f* is determined by transient and specific interactions.¹ The transient nature of the complex formed between PSI and Pc in the PETC implies a balance between specificity and binding strength. In photosynthetic eukaryotic organisms (plants and green algae), the PSI-Pc complex is formed at least in two steps: i) recognition of Pc by PSI and correct orientation of the copper-binding site of Pc towards PSI driven by long-range electrostatic attraction interactions (PSI-Pc encounter complex), and ii) formation of the transient PSI-Pc complex mainly by hydrophobic contacts.² All these interactions together command the formation of the PSI-Pc complex similarly to the *Cytb6f*-Pc complex³ and other redox transient complexes.⁴

Light- and redox-dependent force spectroscopy reveals that the interaction between plastocyanin and plant photosystem I is favored when one partner is ready for electron transfer

There is evidence that the redox state of Pc modulates its interaction with PSI. Drepper et al. determined by laser flash absorption spectroscopy the dissociation constants for the PSI-Pc complex under different redox and illumination conditions. They found that the dissociation constant of oxidized Pc (Pc_{Ox}) from PSI is about six times larger than that of reduced Pc (Pc_{Red})⁵ corresponding to a stronger interaction for Pc_{Red} . In agreement with those results, Danielsen et al. determined a 24-fold larger dissociation constant of Cd-Pc versus Ag-Pc (as a mimic of Pc_{Ox} and Pc_{Red} , respectively), through rotational correlation time measurements.⁶ They observed a stabilization of Ag-Pc upon PSI binding which showed that the oxidation state of the metal center is involved in the complex dissociation. In addition, using X-ray absorption spectroscopy Díaz-Moreno et al. showed that although the binding of Pc to PSI does not generate significant changes in the Cu coordination sphere, differential charge distribution in the metal center of Pc is found between unbound Pc_{Red} and PSI-bound Pc_{Ox} .⁷ The electronic structure of the metal centre of Pc is modulated by the protein matrix to which Pc binds transiently (PSI or *Cytb6f* partner). This is a clear example of how the redox state can regulate transient interactions.⁷ Recently, thermodynamic and structural studies performed by Caspy et al. indicated that a strong hydrophobic interaction sustains the PSI-Pc complex formation.⁸ Upon Pc binding to PSI, water molecules are excluded from the contact interface without altering the conformation of PSI. Once the electron has been transferred from Pc_{Red} to photo-oxidized PSI (PSI_{Ox}), the Pc_{Ox} tilts at the binding site allowing the re-entry of water molecules at the PSI-Pc contact interface. This subtle structural change facilitates and initiates the dissociation process of Pc_{Ox} from re-reduced PSI (PSI_{Red}). It also explains the differences between the dissociation constants of the PSI- Pc_{Red} and PSI- Pc_{Ox} observed in solution. However, the time-resolved recordings and structural methods used so far display several drawbacks: (i) they provide an indirect measurement of the interaction based on the optical absorption changes of P700 after ET, (ii) they employ photo-stimulation for both probing and photo-oxidation, preventing probing PSI in dark conditions, and (iii) the contributions of the underlying forces responsible for the association and dissociation processes can be only obtained indirectly. To solve those problems, we have used force spectroscopy to directly follow the interaction between individual PSI-Pc partners and its dependence on the redox state and illumination. Our approach allows probing all the $PSI_{Red/Ox}$ - $Pc_{Red/Ox}$ pairs, including those not leading to ET, and reveals the binding/unbinding requirements at each stage of the interaction sequence leading to PSI-Pc charge exchange.

Single-molecule techniques provide information free from averaging over inhomogeneities, in contrast to bulk experiments in molecular ensembles. Atomic force microscopy (AFM)-based single-molecule force spectroscopy (SMFS) allows directly measuring unbinding forces to assess protein interactions at the molecular level.⁹ AFM-SMFS has been used to study redox proteins participating in the PETC. Marcuello et al. assessed the interaction of cyanobacterial ferredoxin-NADP⁺ oxidoreductase

Light- and redox-dependent force spectroscopy reveals that the interaction between plastocyanin and plant photosystem I is favored when one partner is ready for electron transfer

with its redox protein partners ferredoxin and flavodoxin, but without control on the redox states.¹⁰ Mayneord et al. characterized the binding frequencies and unbinding forces in the transient *Cytb6f*-Pc complex, controlling the redox states for both proteins. They observed an occurrence of *Cytb6f*-Pc binding interactions (binding frequency) that was five-fold higher when the redox states of the proteins were opposite (*e.g.*, oxidized/reduced), compared to the same redox states (*e.g.*, oxidized/oxidized or reduced/reduced). However, they did not observe significant differences in force.^{11,12} Vasilev et al. studied the interaction between cytochrome c_2 (Cc_2) and the photo-oxidized reaction center (RC) from purple photosynthetic bacteria.^{12,13} In those studies, RC photo-oxidation was induced using nonspecific illumination (white light) with low intensity (between 1-5% of the intensity of sunlight). They found that the dissociation of the RC- Cc_2 complex was not spontaneous after the ET process and required the application of an external force. Additionally, the authors indicated the importance of the redox states of both Cc_2 and RC redox prosthetic groups (*haem* cofactor for Cc_2 and special pair bacteriochlorophyll dimer for RC, respectively). In particular, they observed higher binding frequency when the proteins were in a redox state ready for physiological ET (reduced Cc_2 and oxidized RC).^{12,13}

Despite this progress, the interaction between plant PSI and Pc at the single-molecule level under redox control of both partners has never been studied. Here, we carried it out by orienting both redox proteins such that the active sites face each other, thereby minimizing non-native associations. Therefore, the AFM probe was functionalized with unidirectionally immobilized Pc, *via* an introduced cysteine in the C-terminal region, to expose the ET active site to the solution.¹⁴ PSI was unidirectionally immobilized to the sample surface, *via* a cysteine-modified peptide that recognizes the stromal side and exposes the Pc binding site of PSI to the solution.¹⁵ Secondly, since the activity of PSI is photo-regulated, sufficient photon flux per PSI complex must be provided in its absorption band to ensure that PSI is oxidized before complex formation. To this end, we employed an optically transparent thin gold electrode to anchor PSI and allow the passage of light through the substrate. We illuminated with monochromatic light ($\lambda = 690$) solely to photo-oxidize plant PSI *in situ* and to evaluate the influence of the photo-oxidation on the interaction between PSI and Pc_{Red} or Pc_{Ox} . In these conditions, we measured the binding frequency and the unbinding force between suitably oriented plant PSI and Pc under redox-control using AFM-SMFS. In particular, we evaluated the PSI-Pc interaction by recording force-distance curves in different redox and illumination conditions. Namely, Pc is oxidized in ambient conditions, it can be reduced with sodium ascorbate in the solution, and PSI is reduced in the dark and is oxidized under illumination. Our results show that the binding frequency between PSI and Pc depends on their respective redox states. The binding frequency between PSI and Pc is higher when at least one of the partners is in an ET-ready redox state. Accordingly, low binding frequency (*i.e.* facilitated Pc unbinding) was observed when PSI is reduced

Light- and redox-dependent force spectroscopy reveals that the interaction between plastocyanin and plant photosystem I is favored when one partner is ready for electron transfer

and Pc is oxidized. We took further advantage of this method to evaluate the effect of divalent cations (in different illumination and redox conditions) on the binding frequency and unbinding force of PSI-Pc. We found that Mg^{2+} decreases the binding frequency for Pc_{Red} and photo-oxidized PSI conditions, suggesting an intriguing regulatory role *in vivo*.

3 Results and Discussion

Plant PSI was immobilized on a thin transparent gold surface via interaction with the synthetic peptide pIQA-Cys designed recently.¹⁵ As mentioned above, pIQA-Cys allows to orient the plant PSI unidirectionally, exposing the Pc binding site toward the solution. Pc-cysteine mutant (Pc-SH)¹⁴ was immobilized onto the AFM probe via a heterobifunctional PEG₂₇ linker with a length of approximately 8 nm (monomer length 0.3 nm) (Fig. 1A),^{16,17} thereby exposing the PSI-binding site toward the sample surface (Fig. 1A). The redox states of PSI and Pc were respectively controlled by illuminating PSI ($\lambda = 690$ nm, power = $60 \text{ mW}\cdot\text{cm}^{-2}$)¹⁵ and using a reducing agent for Pc (sodium ascorbate, 5 mM)^{11,18} (Fig. 1B). Note that sodium ascorbate can also reduce P700⁺ but it does so in ~ 30 s,^{19–21} which is orders of magnitude longer than the typical times for Pc_{Ox} reduction (~ 3 ms)²², for P700 photo-oxidation (200 μs , see below), for PSI-Pc ET (10 μs)²³, and also longer than the PSI-Pc (sample-probe) contact time our experiments (~ 25 ms). Combining these conditions, we characterized the binding event frequency and the unbinding force of the interaction between PSI and Pc in all physiological and non-physiological redox states. In our AFM-SMFS experiments, the proteins onto the AFM probe and the sample surface were approached and forced into contact to a maximum force of 200 pN. Then, the AFM probe was retracted from the sample surface at constant velocity of $1 \mu\text{m}\cdot\text{s}^{-1}$. Several force-distance curves displayed unbinding events like those in Figure 1C. These curves allow quantifying the binding event frequency and the unbinding force and distance at which the contact is ruptured. As an unbinding event can be observed only after binding has taken place, the unbinding event frequency can directly be associated to the binding probability.^{24–27} The mean rupture distance between PSI and Pc was around 15 nm in all experiments, independently of the redox and illumination conditions (Fig. 2C, Fig. 3C, Fig. 4C, and Supplementary Fig. S1). We analyzed the binding event frequency and unbinding forces between PSI and Pc in all redox and illumination conditions shown in the Figure 1B. Our setup allowed measuring unbinding events frequency in ON-OFF illumination cycles for each sample while maintaining the other variables unaltered.

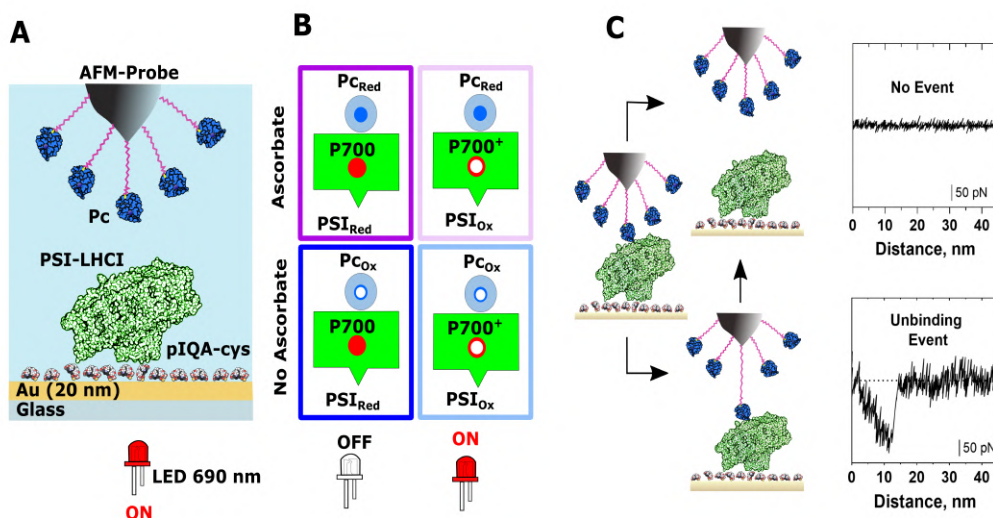


Figure 5.1: AFM-SMFS setup to evaluate PSI-Pc interactions under illumination and redox control. **A.** Schematic representation of the experimental setup. Pc is linked to the AFM probe via a heterobifunctional PEG₂₇ linker. PSI complexes were immobilized on the sample surface (thin Au-layer substrate pre-functionalized with the peptide pIQA-Cys). **B.** Redox conditions (Pc_{Ox} and Pc_{Red}, in the absence and presence of 5 mM sodium ascorbate, respectively) and dark/illumination conditions (PSI_{Red} and PSI_{Ox}, in the absence and presence of 690 nm light, respectively) that were evaluated in this work. **C.** Schematic representation of the PSI-Pc interaction process. When the force-distance retraction curve did not show a quantifiable event (upper panels), we interpreted it as the absence of interaction. When the force-distance retraction curve displayed an unbinding event (bottom panels), it was quantified and interpreted as the formation of a PSI-Pc complex.

3.1 The interaction between PSI and Pc is independent of the redox state of P700 when Pc is reduced.

We first evaluated the interaction of Pc_{Red} with PSI in either dark (PSI_{Red}, purple) or illumination (PSI_{Ox}, pink) conditions (Fig. 2A), which correspond to PSI_{Red}-Pc_{Red} and PSI_{Ox}-Pc_{Red} respectively.³ PSI_{Red}-Pc_{Red} (purple plots) corresponds to Pc_{Red} binding to PSI before photo-excitation. PSI_{Ox}-Pc_{Red} (pink plots) corresponds to an interaction in which the Pc_{Red} forms a complex with PSI after photo-excitation. We associate these binding modes with the fast and slow phases of the PSI-Pc ET process, respectively, reported from transient absorption experiments.^{5,8,28–30} The fast ET phase is due to a preformed PSI-Pc complex before PSI photo-excitation (PSI_{Red}-Pc_{Red})^{8,31} and corresponds to the OFF condition in Figure 2A (purple).

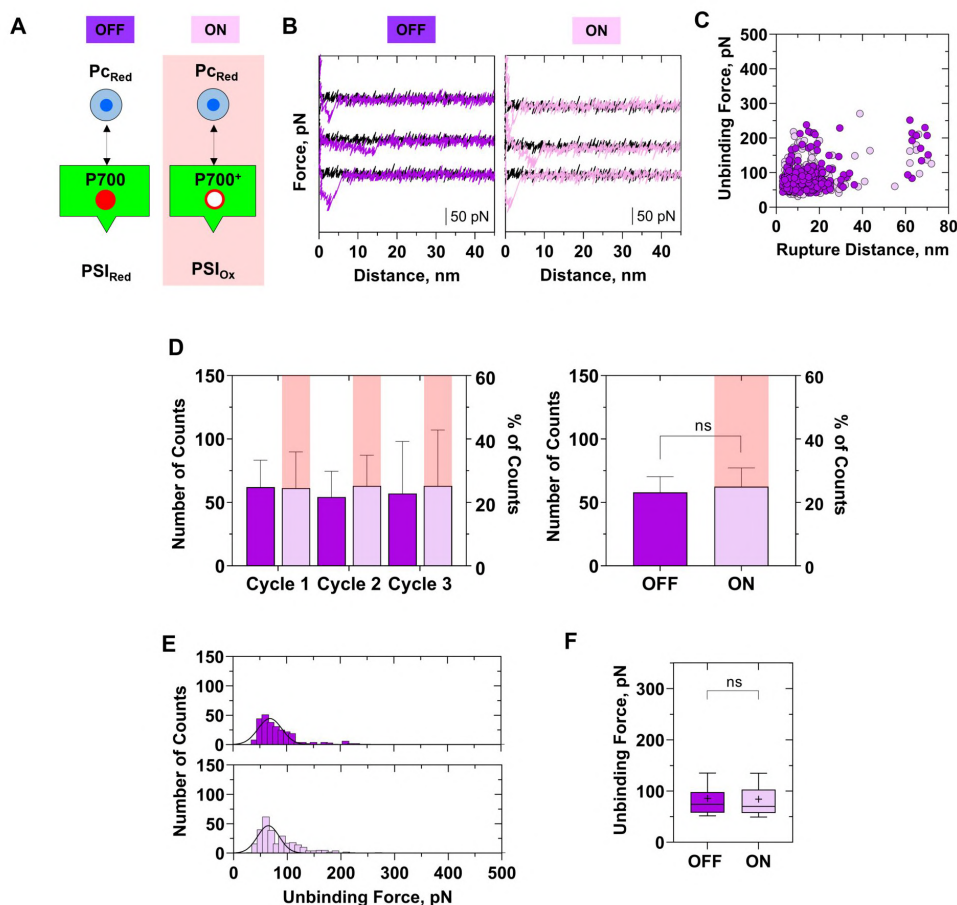


Figure 5.2: Evaluation by AFM-SMFS of the interaction between Pc_{Red} and dark/illuminated PSI. **A.** Scheme of the AFM-SMFS experimental setup. OFF condition (purple) represents the interaction between Pc_{Red} (in the presence of sodium ascorbate, 5 mM) and non-illuminated PSI (PSI_{Red}). ON condition (pink) represents the interaction between Pc_{Red} (in the presence of sodium ascorbate, 5 mM) and the PSI under 690 nm illumination (PSI_{Ox} , red box). The two-way arrow represents the movement of approach and *retraction* of Pc_{Red} (AFM probe) to PSI (sample surface). **B.** Representative force-distance retraction curves for positives event (colored traces) and in absence of interaction (black traces) in OFF (left panel) and ON (right panel) conditions. **C.** Distribution of unbinding forces and rupture distances extracted from individual unbinding events between PSI and Pc_{Red} . **D.** Quantification of the number of binding events between PSI and Pc_{Red} out of 3 consecutive cycles OFF-ON averaged from 3 independent experiments (768 force-distance curves per independent experiment). The left panel shows the average number of binding events recorded in 3 alternating ON-OFF illumination cycles. The right panel shows the mean \pm standard error of the mean (SEM) of the total number of ON-OFF cycles measured. **E.** Histogram of the unbinding forces frequency in OFF (top panel) and ON (bottom panel) conditions. The gaussian fits show in both conditions a single distribution. **F.** Box plot for unbinding force recorded in OFF and ON conditions. All measurements were done in PBS, 50 mM pH 7.4 at room temperature.

Light- and redox-dependent force spectroscopy reveals that the interaction between plastocyanin and plant photosystem I is favored when one partner is ready for electron transfer

In the slow ET phase, the complex between PSI and Pc_{Red} is formed after PSI photo-excitation, then Pc_{Red} must diffuse to interact with the photo-excited PSI and form the PSI-Pc complex ($\text{PSI}_{\text{Ox}}\text{-Pc}_{\text{Red}}$)^{8,31} and corresponds to the ON condition in Figure 2A (pink).

Figure 2 shows the binding event frequency and the unbinding force for $\text{PSI}_{\text{Red}}\text{-Pc}_{\text{Red}}$ (purple) and $\text{PSI}_{\text{Ox}}\text{-Pc}_{\text{Red}}$ (pink). The experiments were recorded in alternating ON-OFF illumination cycles (Fig. 2D). The binding event frequency and the unbinding force of interaction of Pc_{Red} are similar with either photo-excited PSI or non-photo-excited PSI, with force around 85 pN. These values are not significantly different between these conditions (Fig. 2D-2F). Thus, the interaction between Pc_{Red} and PSI is independent of the redox state of P700. The event binding frequency accounts for the probability of effective encounters between the redox partner proteins. The low unbinding forces may ensure a fast turnover for an efficient overall ET process. These results provide the first biophysical characterization of the binding of Pc_{Red} to PSI_{Ox} and yield the binding event frequency and unbinding force of Pc_{Red} to the different physiological redox forms of plant PSI. We assume that during the binding-unbinding process, the interaction analysed under illumination is between PSI_{Ox} and Pc_{Red} because i) the ET time between PSI-Pc is 10 μs ,²³ ii) the $\text{PSI}_{\text{Ox}}\text{-Pc}_{\text{Red}}$ contact time in our experimental conditions is 25 ms, iii) the time for Pc_{Ox} re-reduction by ascorbate is 3 ms,²² iv) the time for PSI reduction by ascorbate is 20-30 s¹⁹⁻²¹ and v) under our continuous illumination conditions, the photocurrent signal proportional to photo-oxidation saturates above 200 μs of pulsed illumination (see Supplementary Fig. 2). Therefore, the probability that PSI remains oxidized during the next approach/retract cycle to acquire a force curve (which lasts 400 ms) is greater than that PSI is reduced.

3.2 Reduced PSI in the dark displays a weaker interaction with oxidized Pc.

Figure 3 shows the interaction between oxidized Pc (Pc_{Ox}) and PSI under illumination (PSI_{Ox}) or darkness (PSI_{Red}) conditions (cyan and blue plots, respectively). $\text{PSI}_{\text{Red}}\text{-Pc}_{\text{Ox}}$ (blue) corresponds to the post-ET interaction step that ends with Pc_{Ox} release from PSI_{Red} . Under illumination, we observe a binding event frequency of $\text{PSI}_{\text{Ox}}\text{-Pc}_{\text{Ox}}$ (cyan) like that of $\text{PSI}\text{-Pc}_{\text{Red}}$ around 23 % (right axis of Fig. 2D-2E, purple and pink, respectively) that is strikingly lowered in the dark (Figure 3D-3E, blue). To our knowledge, these results provide the first biophysical evidence at the single-molecule level that the PSI-Pc interaction can be controlled directly by the photo-excitation of PSI. A control experiment with 520 nm irradiation, poorly absorbed by PSI, yields a similar number of binding events to dark conditions revealing the specificity of PSI photo-oxidation (Supplementary Fig. S3).

Light- and redox-dependent force spectroscopy reveals that the interaction between plastocyanin and plant photosystem I is favored when one partner is ready for electron transfer

In the histogram of unbinding force for $\text{PSI}_{\text{Red}}\text{-Pc}_{\text{Ox}}$ (Fig. 3E, blue) we observe a reduction in the main peak near 85 pN and the emergence of a small and broad secondary peak around 125 pN. Interestingly, both distributions in $\text{PSI}_{\text{Red}}\text{-Pc}_{\text{Ox}}$ present a lower frequency than the distributions obtained in Figure 2 (when Pc is reduced, purple and pink). The similar force values observed in all conditions (Fig. 2 and 3) suggest that the established contacts are equivalent. However, the lower frequency of the main peak in $\text{PSI}_{\text{Red}}\text{-Pc}_{\text{Ox}}$ (blue) suggests that this interaction is not favored. The average unbinding force between Pc_{Ox} and PSI is lower and less dispersed under illumination (Fig. 3F).

When we compared the four PSI-Pc interaction conditions (Fig. 2, 3, and Fig. 4E-F), we observed that the interaction events of $\text{PSI}_{\text{Red}}\text{-Pc}_{\text{Ox}}$ (blue) are less probable (lower binding event frequency), but when binding takes place, the unbinding force is similar (~100 pN) yet more disperse, yielding higher average than in the other conditions. The unbinding force values between PSI and Pc agree with the values reported for other redox partner proteins.³² To summarize, we observe that in our experimental conditions (1) the binding event frequency of Pc_{Red} is high and independent of the oxidation state of PSI, which agrees with the idea that Pc is primed or ready to transfer an electron to PSI; (2) the binding frequency of Pc_{Ox} is low in the dark (PSI_{Red}), as could be expected from a post-ET interaction; and (3) the Pc_{Ox} binding frequency is higher with photo-oxidized PSI, which is unable to exchange charge ($\text{PSI}_{\text{Ox}}\text{-Pc}_{\text{Ox}}$). High binding frequencies are observed when PSI is photo-oxidized, or Pc is in a reduced state. Either of the two conditions separately or together increases the binding event frequency in an equivalent way and leads to similar, narrowly distributed unbinding forces. From a physiological perspective, all conditions evaluated in Fig. 1 and Fig. 2 (except $\text{PSI}_{\text{Ox}}\text{-Pc}_{\text{Ox}}$ system) correspond to binding modes of the ET complex formation before or after PSI photo-oxidation. The interaction between individual Pc and plant PSI is favoured when at least one partner is ready for electron transfer.

Several molecular mechanisms can support these interactions and photo-redox effects. Light-induced structural changes that occur in plant PSI and in photosynthetic reaction centers are due to the oxidation of the special pair of chlorophyll molecules.^{33–36} Specifically in plants, chemical oxidation or photo-oxidation of P700 can alter the strength of hydrogen-bonding of Chla P_A/P_B in $\text{P700}/\text{P700}^+$ and shift the vibrational frequency of tryptophan residues located in the vicinity of P700.^{33,37} This spectral shift is associated to a higher dielectric constant and a change in the ability to form hydrogen bonds in a hydrophobic environment.³⁷ Residues W625 and W658 in plant PSI (W631 and W655 in cyanobacteria PSI) are associated with the hydrophobic recognition/interaction interface between PSI and Pc. Our measurements with and without illumination suggest that such photo-induced structural changes in PSI could alter the binding frequency and the unbinding force between Pc and PSI.

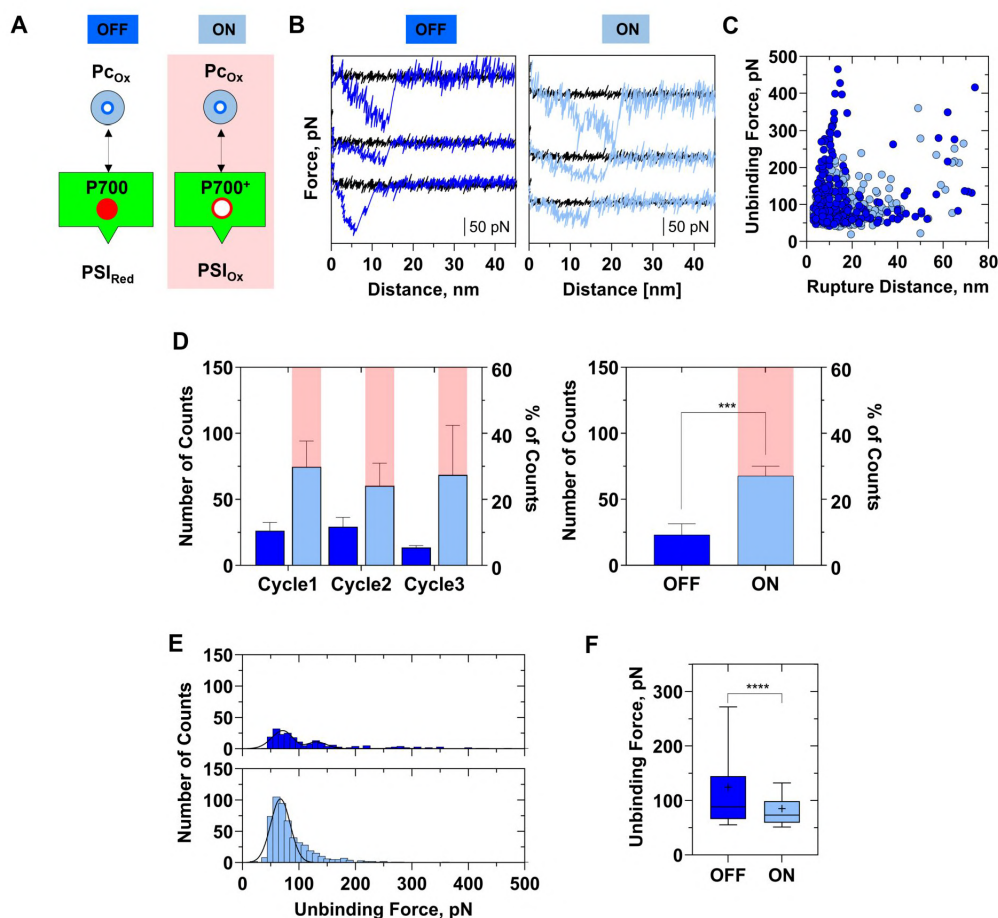


Figure 5.3: Evaluation by AFM-SMFS of the interaction between Pc_{Ox} and dark/illuminated PSI. **A.** Scheme of the AFM-SMFS experimental setup. OFF condition (blue) represents the interaction between Pc_{Ox} and non-illuminated PSI (PSI_{Red}). ON condition (cyan) represents the interaction between Pc_{Ox} and the PSI under illumination with $\lambda = 690$ nm (PSI_{Ox} , red box). The two-way arrow represents the movement of approach and *retraction* of Pc_{Ox} (AFM probe) to PSI (sample surface). **B.** Representative force-distance retraction curves for positives event (colored traces) and in absence of interaction (black traces). **C.** Distribution of unbinding forces and rupture distance extracted from individual unbinding events between PSI and Pc_{Ox} . **D.** Quantification of the number of binding events between PSI and Pc_{Ox} out of 3 consecutive cycles OFF-ON averaged from 3 independent experiments (768 force-distance curves per independent experiment). The left panel shows the average number of binding events recorded in alternating ON-OFF illumination cycles. The right panel shows the mean \pm SEM of the total number of ON-OFF cycles measured. PSI_{Red} binds Pc_{Ox} in significantly fewer events than PSI_{Ox} . **E.** Histograms of the unbinding force frequency in OFF condition (top panel) and ON (bottom panel) conditions. The gaussian fits show in both conditions a distribution with a main peak. **F.** Box plot for unbinding force recorded in OFF and ON conditions. All measurements were done in PBS, 50 mM pH 7.4 at room temperature.

3.3 Mg²⁺ ions decrease the frequency of PSI-Pc binding.

To study whether the binding of ET-ready Pc_{Red} (Fig. 2) can be regulated externally, we measured the effect of illumination on the PSI-Pc interaction in the presence of Mg²⁺ ions. *Physiologically*, the Mg²⁺ concentration in the dark is higher on the luminal side of the chloroplast than on the stromal side, whereas it decreases under illumination (Fig. 4A).^{38–42} We used 5 mM Mg²⁺^{11,18} in the dark and also measured the interaction under illumination for comparison. Mg²⁺ binds specifically to Pc leading to a conformational change³⁹ that is hypothesized to inhibit Pc binding to the PsaF subunit of PSI, thereby regulating the PSI-Pc interaction.

Figure 4 shows the AFM-SMFS results obtained for ET-ready Pc_{Red} interacting with illuminated and dark PSI samples in the presence of Mg²⁺ in solution. In comparison to Figure 2 (no Mg²⁺), 5 mM Mg²⁺ decreases the binding frequency of PSI_{Red}-Pc_{Red} and PSI_{Ox}-Pc_{Red} from 23% to 10% approximately (compare respectively purple-green and pink-yellow plots in Figure 2D and Figure 4F). This low frequency of events is like that of PSI_{Red}-Pc_{Ox} (blue, Figure 3D and Figure 4F). Interestingly, the unbinding force distributions in the presence of Mg²⁺ show a single peak near 85 pN (Figure 4D-4E).

The decrease in binding frequency indicates that Mg²⁺ inhibits the interaction between PSI and Pc. We observe this reduction both in the dark and under illumination, even though the later condition (PSI_{Ox}-Pc_{Red} under illumination and Mg²⁺, green) does not correspond to a physiologically well-defined state because PSI photo-oxidation is concomitant with Mg²⁺ depletion from the luminal side. This control condition can also be interpreted as a transient state at the onset of Mg²⁺ translocation. It suggests that Mg²⁺ binding to Pc lowers the binding frequency even when both partners are in a physiologically ET-ready redox state, *i.e.* overriding their ability to transfer an electron. If we interpret the decrease in binding frequency between PSI_{Red}-Pc_{Red} in the presence of Mg²⁺ (purple *vs* yellow, Figure 4F) as the effect of the ion accumulating in the lumen under dark physiological conditions, our results confirm *in vitro* the hypothesis of PSI-Pc binding regulation *in vivo* by Mg²⁺.³⁹ Interestingly, this regulation is achieved without altering the unbinding force (Figure 4E), *i.e.* the type of contacts between PSI and Pc. Thus, we hypothesize that Mg²⁺ screens specific electrostatic interactions involved in binding (complex formation), water interactions,⁴³ and/or the establishment of a Gouy-Chapman conduit,^{1,44,45} and that this effect is independent of illumination. Unfortunately, binding forces cannot be directly measured with SMFS, and although association constants k_{on} have been reported from AFM-SMFS measurements, these calculations are challenging and require multiple assumptions.⁴⁶

Our results indicate that the binding frequency between PSI and Pc depends on their respective redox states. In our study, the frequency of interaction between PSI and Pc was higher when at least one of the partners was in an ET-ready redox state. The

Light- and redox-dependent force spectroscopy reveals that the interaction between plastocyanin and plant photosystem I is favored when one partner is ready for electron transfer

lowest binding event frequency was found when both PSI and Pc were in a post-ET redox state. Although the association rate between redox partner proteins is reported to be higher for opposite redox states (*e.g.* $Cytb6f_{Red}-Pc_{Ox}$ compared to $Cytb6f_{Ox}-Pc_{Ox}$ or $Cytb6f_{Red}-Pc_{Red}$),¹¹ during PSI-Pc interaction, partners with the same redox states presented a higher number of binding events (*e.g.*, $PSI_{Ox}-Pc_{Ox}$ and $PSI_{Red}-Pc_{Red}$).

To aid the interpretation, in Supplementary Figure S4 we outline the situations imposed experimentally in this work to probe PSI-Pc complexes by means of photo-oxidation and reducing agents. $PSI_{Red}-Pc_{Red}$ (purple) and $PSI_{Ox}-Pc_{Red}$ (pink) represents the initial situations of Pc_{Red} binding to PSI before and after photo-excitation respectively, and prior to ET. $PSI_{Red}-Pc_{Ox}$ (blue) represents a post-ET situation. Replacement of Pc_{Ox} by Pc_{Red} leads again to $PSI_{Red}-Pc_{Red}$ (purple) and completes the cycle. $PSI_{Ox}-Pc_{Ox}$ (cyan) corresponds to the situation in which PSI is photo-oxidized before Pc_{Ox} is released. Our SMFS experiments show high (~25%) binding frequency in all situations except post-ET (~10%), in agreement with the higher dissociation rates reported for PC_{Ox} with respect to PC_{Red} .⁵ Based on cryo-EM data,⁸ Caspy et al. suggested that upon Pc oxidation, a slight tilt of bound Pc allows water molecules to accommodate in the space between Pc and PSI and drive Pc dissociation. Our results can be interpreted as disfavouring the binding of PSI_{Red} to Pc_{Ox} (blue) over fresh Pc_{Red} (purple) from the lumen, thus favouring electron carrier turnover. In other words, the low binding frequency of PSI-Pc upon ET ($PSI_{Red}-Pc_{Ox}$, blue) suggests a ratchet-like mechanism that favours Pc release (purple).

In addition, our results show that Mg^{2+} alters the PSI-Pc interaction and suggest a mechanism of regulation *in vivo*. An increase in Mg^{2+} concentration hinders the PSI-Pc interaction, independently of the PSI redox state. Interestingly, this result is related to the Mg^{2+} -enhanced binding between PSI and its stromal redox partner ferredoxin.^{47,48}

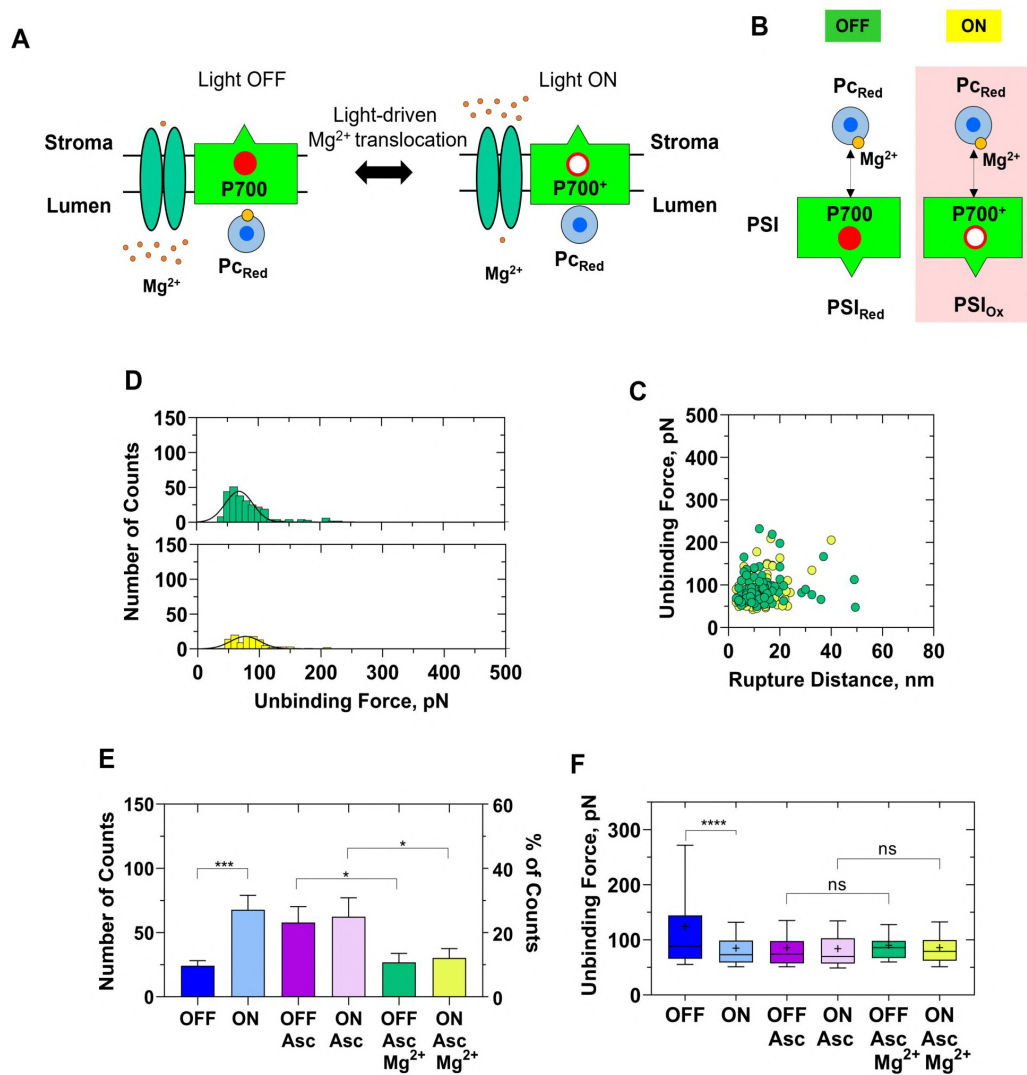


Figure 5.4: AFM-SMFS study of the interaction between Pc_{Red} and dark/illuminated PSI in the presence of Mg^{2+} . **A.** Schematic representation of the light-induced physiological changes in Mg^{2+} concentration on the luminal and stromal side of chloroplasts, which result in Mg^{2+} -mediated PSI- Pc interaction inhibition in the dark. **B.** Scheme of the AFM-SMFS binding interaction experiments: OFF condition (green) represents the interaction between Pc_{Red} (with 5 mM sodium ascorbate) and non-illuminated PSI (PSI_{Red}) in 5 mM Mg^{2+} ($MgSO_4$). ON condition (yellow) represents the interaction between Pc_{Red} (with 5 mM sodium ascorbate) and illuminated PSI (PSI_{Ox} , red box) in 5 mM Mg^{2+} . The two-way arrow represents the movement of approach and *retraction* between Pc_{Red} bound to the AFM probe and PSI bound to the sample surface. **C.** Distribution of unbinding forces and rupture distances extracted from individual PSI- Pc_{Red} unbinding events in 5 mM Mg^{2+} . **D.** Histograms of the unbinding force frequency in OFF (top panel) and ON conditions (bottom panel) in 5 mM Mg^{2+} . **E-F.** Mean \pm SEM of the total number of binding events (**E**) and box plot for unbinding force (**F**) for PSI- Pc : PSI_{Red} - Pc_{Ox} (blue), PSI_{Ox} - Pc_{Ox} (cyan), PSI_{Red} - Pc_{Red} (purple), PSI_{Ox} - Pc_{Red} (pink), PSI_{Red} - Pc_{Red} in 5 mM Mg^{2+} (green), PSI_{Ox} - Pc_{Red} in 5 mM Mg^{2+} (yellow). All measurements were done in PBS, 50 mM pH 7.4 at room temperature.

4 Conclusions

We have studied the interaction between well-oriented plant PSI and Pc at the single-molecule level, under redox control of both partners by means of photo-oxidation (for PSI) in ON-OFF illumination cycles, and using reducing agents (for Pc). We have quantified the binding event frequency, the unbinding force, and the distance at which the contact is ruptured in AFM-SMFS experiments. Our results indicate that the binding frequency between PSI and Pc is related to their respective redox states. For PSI-Pc_{Red}, the binding event frequency does not change with the redox state of P700 and the unbinding force stays around 85 pN. When Pc is oxidized, these values are maintained under illumination (PSI_{Ox}-Pc_{Ox}) but the binding frequency is strikingly lowered in the dark (PSI_{Red}-Pc_{Ox}). Hence, the interaction between PSI and Pc is independent of the redox state of PSI when Pc is reduced, but it is disfavoured by reduced P700 in the dark when Pc is oxidized. We further evaluated the effect of the presence of Mg²⁺ and observed a decrease in the binding frequency of PSI-Pc_{Red} both in the dark and under illumination, without altering the unbinding force values.

The frequency of interaction between PSI and Pc is higher when at least one of the partners is in an ET-ready redox state, and the post-ET situation (PSI_{Red}-Pc_{Ox}) leads to disfavoured binding. This suggests a ratchet-like mechanism that facilitates electron carrier turnover. In addition, we show that the binding of ET-ready Pc_{Red} to PSI can be regulated externally by Mg²⁺ ions in solution.

5 Methods

PSI-LHCI complexes purification. Arabidopsis thaliana plants (Arabidopsis Col-0) were grown under white light at 120 $\mu\text{mol photons}\cdot\text{m}^{-2}\cdot\text{s}^{-1}$, 12 hr/12 hr day/night cycles, for 5 weeks at 23 °C. Thylakoid membranes were isolated from Arabidopsis leaves according to Xu et al.⁴⁹ PSI-LHCI complexes were purified from thylakoid membranes with sucrose density gradients as previously described.⁵⁰ 350 μg Chl thylakoid were diluted to 0.5 mg Chl $\cdot\text{ml}^{-1}$ in EDTA 5 mM, HEPES 10 mM, pH 7.5 and solubilized with an equal amount of detergent solution (1% α -decylmaltoside (α -DM) in HEPES 10 mM, pH 7.5) for 10 min. After solubilization, the sample was centrifuged at 12,000 x g for 10 min to eliminate the insolubilized material. The soluble fraction was loaded onto the sucrose gradients prepared by freezing and thawing a sucrose solution (sucrose 500 mM, HEPES 20 mM, pH 7.5, 0.06% α -DM). The gradients were centrifuged for 16 h at 4 °C at 160000 x g. PSI-LHCI complexes were collected with a syringe.

Plastocyanin mutant expression and purification. The mutant Pc-SH gene cloned into a pET-3a plasmid (pET-3a-PcSH) was used to transform *E. coli* BL21. The Pc-SH mutant has three extra residues at its C-terminal (Thr-Cys-Gly). *E. coli* BL21 transformed

Light- and redox-dependent force spectroscopy reveals that the interaction between plastocyanin and plant photosystem I is favored when one partner is ready for electron transfer

with plasmid pET-3a-PcSH were grown in 2xYT medium supplemented with 100 gml⁻¹ of ampicillin at 37 °C until OD₆₀₀ of approximately 0.8 was reached. The expression of Pc-SH was induced by adding isopropyl thio-β-D-galactoside (IPTG) 0.3 mM for 4 h, shaking at 220 rpm and 28 °C. Cells were harvested by centrifugation (7000 rpm), suspended in MES buffer 10 mM, pH 6.5, and disrupted by sonication. The suspension was centrifuged for 1 hour at 20000 rpm. The soluble fraction was loaded onto an anion exchange column (HiTrap® Q, Cytiva). A linear NaCl gradient (0-300 mM) in MES buffer 10 mM, pH 6.5, was used to elute Pc-SH. Subsequently, the protein-containing fractions were pooled and loaded onto a size exclusion column (Superdex® 75 10/300, Cytiva). Pc-SH purity was analyzed by SDS-PAGE stained with one-step blue® protein gel stain. The pure protein-containing fractions were pooled, and glycerol was added to 40% v/v. The Pc-SH was stored at 20 °C until the experiments were performed. Pc-SH mutant was purified in a Cu-free form (Apo). To avoid the oxidation reaction between a cysteine residue of the Pc mutant and Cu²⁺, apo Pc-SH was first bound to the AFM probe (see AFM probes preparation). Then, apo Pc-SH was incubated with fresh Cu²⁺ solution for 1 h (CuSO₄, 50 mM) to bind Cu²⁺ in the apo Pc-SH structure.

Sample preparation. An adhesion layer of 1 nm of Cu was evaporated on fused silica substrates prior to the evaporation of 10 to 40 nm of Au at 0.2 nms⁻¹. The Cu seed layer was exposed to the ambient atmosphere prior to the gold deposition. The Au surfaces of 10 nm to 40 nm thickness allowed the sample to illuminate from below. Au surfaces were incubated with pIQA-cys peptide 0.1 mM in sodium acetate buffer 50 mM, pH 4.5, for 30 min. at room temperature. After peptide incubation, samples were gently rinsed with working buffer, Phosphate Buffer Saline (PBS) 50 mM, pH 7.4. Aliquots of 5 l of PSI-LHCI (Chl concentration: 0.28 g l⁻¹) and 45 l of PBS working buffer 50 mM, pH 7.4, were incubated overnight in dark conditions in a humid environment. After overnight incubation, buffer was gently exchanged with fresh PBS working buffer to remove unbound PSI-LHCI complexes.

AFM probes preparation. We used V-shaped Si₃N₄ probes (DNP, Bruker AFM Probes, Camarillo, CA) having a nominal spring constant of 0.06 Nm⁻¹. The probes were pre-treated for 15 minutes in a UV/Ozone ProCleaner™ (BioForce Nanosciences). Then, the probes were amino-functionalized in atmosphere of 3-aminopropyl-triethoxysilane (APTES) and triethylamine (TEA). The probes were placed inside the desiccator previously flooded with N₂ gas to remove air and moisture. Two small plastic containers with 45 l of APTES and 15 l of TEA, separately, were placed close to the probes (on a clean inert surface) and vacuum was on for 5 min. After 1.5 h, the APTES and TEA containers were removed, and vacuum was restored. The probes were left in the desiccator overnight at room temperature, and afterwards rinsed with chloroform (2x) and ethanol (2x) and dried under a gentle N₂ flow. When the tips were not used immediately, they were stored in a desiccator under

Light- and redox-dependent force spectroscopy reveals that the interaction between plastocyanin and plant photosystem I is favored when one partner is ready for electron transfer

Ar atmosphere. Afterwards, the probes were placed in glass wells filled with 0.5 mL solution of 1 mgml⁻¹ heterobifunctional PEG (n=27) (Mal-PEG₂₇-NHS, *O*-[*N*-(3-maleimidopropionyl)aminoethyl]-*O* -[3-(*N*-succinimidylloxy)-3-oxopropyl] heptacosaeethylene glycol, Sigma-Aldrich) and 5 l TEA in chloroform, and left for 1.5 h. The probes were rinsed with chloroform (2x), ethanol (2x), and MilliQ water and dried under a gentle N₂ flow. Placed on a polydimethylsiloxane (PDMS) surface, the probes were incubated during 1 h with a 25 l of Pc 1 mgml⁻¹ in PBS working buffer. Finally, the probes were rinsed with ammonium acetate buffer 50 mM, pH 4.5, and incubated with a solution of CuSO₄ 50 mM for 1 h, to bind Cu²⁺ in the apo Pc-SH structure. The Pc-functionalized probes were subsequently rinsed with ammonium acetate buffer 50 mM, pH 4.5 and with PBS working buffer 50 mM, pH 7.4, always keeping them hydrated, and were immediately used in the experiments. Cu²⁺ incorporation to the Pc was verified by cyclic voltammetry of Au electrodes incubated with Pc-SH before and after incubation with CuSO₄.

AFM force spectroscopy measurements. Force spectroscopy was done with a NanoWizard 3 BioScience AFM (JPK Instruments, Bruker Nano GmbH), at room temperature and under liquid environment (PBS working buffer 50 mM, pH 7.4). After having measured the sensitivity (Vm¹), the cantilever spring constants were individually calibrated using the equipartition theorem (thermal noise routine).⁵¹ Force-distance curves were recorded by approaching and retracting the AFM tip at constant velocity (1 ms⁻¹) and in the force map mode of 16 x 16 force-separation curves over an area of 3 x 3 μm². The redox states of PSI and Pc were respectively controlled by illuminating PSI (= 690 nm, power = 60 mW·cm⁻² continuously during episodes of 1.7 min (acquisition time of each force map of 256 curves; 400 ms for each approach/retraction cycle), that were alternated with dark conditions acquiring a total of six force maps for each sample in three ON/OFF rounds indicated as “cycles“ in Figures 2-4). In experiments labelled as Pc_{Red}, a reducing agent for Pc (sodium ascorbate, 5 mM) was used. For the experiments in the presence of Mg²⁺, MgSO₄ was added to a concentration of 5 mM, and incubated for 10 min before force measurements. The maximum applied (contact) force in each cycle was set to 200 pN. For each condition, at least 3 force maps were acquired for each condition in different regions of the same sample (256 curves each map, 768 curves in total). Three independent experiments were conducted in each case (corresponding to different Au-pIQa-PSI samples and different AFM tips functionalized with fresh Pc). AFM data were acquired and processed using the JPK AFM software. Maximum interaction force and extension were recorded from each retract trace. Statistical analysis and representation of the data was performed with GraphPad Prism 9.1.2. Errors are indicated as standard error of the mean (SEM).

6 Associated content

Supporting information

Comparison of the rupture distance for the AFM-SMFS experiments from Figures 2 and 3 in the main text. Photo-chronoamperometric signal amplitude of Au-pIQA-PSI electrodes irradiated with 690 nm according to pulse duration. Control experiment with 520 nm illumination. Outline of the situations imposed experimentally in this work by means of photo-oxidation and reducing agents.

Acknowledgements

This research received funding from the European Union Research and Innovation Programme Horizon 2020 - HBP SG3 (945539), DEEPER (ICT-36-2020-101016787), European Research ERA-Net SynBio programme (Modulightor project), and financial support from Agency for Management of University and Research Grants (CERCA Programme; 2017-SGR-1442 project), Ministry of Economy and Competitiveness (MINECO)/FEDER (Grants CTQ2015-66194-R and CTQ2016- 80066-R), the Fundaluce foundation, the Commission for Universities and Research of the Department of Innovation, Universities, and Enterprise of the Generalitat de Catalunya -AGAUR- (IU16-011508) and co-financed by the European Union Regional Development Fund within the framework of the ERDF/FEDER Operational Program of Catalonia 2014-2020 with a grant of 50% of total eligible cost. This research was supported by CIBER -Consortio Centro de Investigación Biomédica en Red- (CB06/01/0081), Instituto de Salud Carlos III, Ministerio de Ciencia e Innovación. R.Z. was supported by National Agency for Research and Development (ANID)/Scholarship Program POSTDOCTORADO BECAS CHILE/2018 - 74190117. We thank G.W. Canters, S. Cannistraro and L. Andolfi for the kind gift of Pc clones.

Author contributions

R.A.Z. and M.L.-O. contributed equally to this work.

7 References

- (1) Pérez-Mejías, G.; Díaz-Quintana, A.; Guerra-Castellano, A.; Díaz-Moreno, I.; de la Rosa, M. A. Novel Insights into the Mechanism of Electron Transfer in Mitochondrial Cytochrome c. *Coordination Chemistry Reviews* **2022**, *450*.
- (2) Ueda, T.; Nomoto, N.; Koga, M.; Ogasa, H.; Ogawa, Y.; Matsumoto, M.; Stampoulis, P.; Sode, K.; Terasawa, H.; Shimadaa, I. Structural Basis of Efficient Electron Transport

Light- and redox-dependent force spectroscopy reveals that the interaction between plastocyanin and plant photosystem I is favored when one partner is ready for electron transfer

between Photosynthetic Membrane Proteins and Plastocyanin in Spinach Revealed Using Nuclear Magnetic Resonance. *Plant Cell* **2012**, *24* (10), 4173–4186.

(3) Bendall, D. S.; Schlarb-Ridley, B. G.; Howe, C. J. Transient Interactions Between Soluble Electron Transfer Proteins. The Case of Plastocyanin and Cytochrome f. In *Bioenergetic Processes of Cyanobacteria*; Springer Netherlands, 2011; pp 541–571.

(4) Crowley, P. B.; Carrondo, M. A. The Architecture of the Binding Site in Redox Protein Complexes: Implications for Fast Dissociation. *Proteins: Structure, Function and Genetics* **2004**, *55* (3), 603–612.

(5) Drepper, F.; Hippler, M.; Nitschke, W.; Haehnel, W. Binding Dynamics and Electron Transfer between Plastocyanin and Photosystem I. *Biochemistry* **1996**, *35* (4), 1282–1295.

(6) Danielsen, E.; Scheller, H. V.; Bauer, R.; Hemmingsen, L.; Bjerrum, M. J.; Hansson, O. Plastocyanin Binding to Photosystem I as a Function of the Charge State of the Metal Ion: Effect of Metal Site Conformation. *Biochemistry* **1999**, *38* (35), 11531–11540.

(7) Díaz-Moreno, I.; Díaz-Quintana, A.; Díaz-Moreno, S.; Subías, G.; de la Rosa, M. A. Transient Binding of Plastocyanin to Its Physiological Redox Partners Modifies the Copper Site Geometry. *FEBS Letters* **2006**, *580* (26), 6187–6194.

(8) Caspy, I.; Fadeeva, M.; Kuhlert, S.; Borovikova-Sheinker, A.; Klaiman, D.; Masrati, G.; Drepper, F.; Ben-Tal, N.; Hippler, M.; Nelson, N. Structure of Plant Photosystem I-Plastocyanin Complex Reveals Strong Hydrophobic Interactions. *Biochemical Journal* **2021**, *478* (12), 2371–2384.

(9) Bonanni, B.; Kamruzzahan, A. S. M.; Bizzarri, A. R.; Rankl, C.; Gruber, H. J.; Hinterdorfer, P.; Cannistraro, S. Single Molecule Recognition between Cytochrome C 551 and Gold-Immobilized Azurin by Force Spectroscopy. *Biophysical Journal* **2005**, *89* (4), 2783–2791.

(10) Marcuello, C.; de Miguel, R.; Martínez-Júlvez, M.; Gómez-Moreno, C.; Lostao, A. Mechanostability of the Single-Electron-Transfer Complexes of Anabaena Ferredoxin-NADP + + Reductase. *ChemPhysChem* **2015**, *16*(15), 3161–3169.

(11) Mayneord, G. E.; Vasilev, C.; Malone, L. A.; Swainsbury, D. J. K.; Hunter, C. N.; Johnson, M. P. Single-Molecule Study of Redox Control Involved in Establishing the Spinach Plastocyanin-Cytochrome B6f Electron Transfer Complex. *Biochimica et Biophysica Acta - Bioenergetics* **2019**, *1860* (7), 591–599.

(12) Johnson, M. P.; Vasilev, C.; Olsen, J. D.; Hunter, C. N. Nanodomains of Cytochrome B6f and Photosystem II Complexes in Spinach Grana Thylakoid Membranes. *Plant Cell* **2014**, *26* (7), 3051–3061.

Light- and redox-dependent force spectroscopy reveals that the interaction between plastocyanin and plant photosystem I is favored when one partner is ready for electron transfer

(13) Vasilev, C.; Mayneord, G. E.; Brindley, A. A.; Johnson, M. P.; Neil Hunter, C. Dissecting the Cytochrome C2–Reaction Centre Interaction in Bacterial Photosynthesis Using Single Molecule Force Spectroscopy. *Biochemical Journal* **2019**, *476* (15), 2173–2190.

(14) Andolfi, L.; Bonanni, B.; Canters, G. W.; Verbeet, M. P.; Cannistraro, S. Scanning Probe Microscopy Characterization of Gold-Chemisorbed Poplar Plastocyanin Mutants. *Surface Science* **2003**, *530* (3), 181–194.

(15) López-Ortiz, M.; Zamora, R. A.; Giannotti, M. I.; Hu, C.; Croce, R.; Gorostiza, P. Distance and Potential Dependence of Charge Transport Through the Reaction Center of Individual Photosynthetic Complexes. *Small* **2022**, *18* (7).

(16) Zhengyu, M.; David, N. L. B.; Sharon, M. L.; Kim, A. S.; Michael, L. K.; Dennis, E. D.; Terri, H. F. Tcr Triggering by PMHC Ligands Tethered on Surfaces via Poly(Ethylene Glycol) Depends on Polymer Length. *PLoS ONE* **2014**, *9* (11).

(17) Oesterhelt, F.; Rief, M.; Gaub, H. E. Single Molecule Force Spectroscopy by AFM Indicates Helical Structure of Poly (Ethylene-Glycol) in Water. *New Journal of Physics* **1999**, *1* (11), 6–7.

(18) Jansson, H.; Hansson, Ö. Competitive Inhibition of Electron Donation to Photosystem 1 by Metal-Substituted Plastocyanin. *Biochimica et Biophysica Acta - Bioenergetics* **2008**, *1777* (9), 1116–1121.

(19) Trubitsin, B. v.; Mamedov, M. D.; Semenov, A. Y.; Tikhonov, A. N. Interaction of Ascorbate with Photosystem i. *Photosynthesis Research* **2014**, *122* (2), 215–231.

(20) Goyal, A.; Szewczyk, S.; Burdziński, G.; Abram, M.; Kargul, J.; Gibasiewicz, K. Competition between Intra-Protein Charge Recombination and Electron Transfer Outside Photosystem I Complexes Used for Photovoltaic Applications. *Photochemical and Photobiological Sciences* **2022**, *21* (3), 319–336.

(21) Wientjes, E.; Croce, R. PMS: Photosystem i Electron Donor or Fluorescence Quencher. *Photosynthesis Research* **2012**, *111* (1–2), 185–191.

(22) Mathis, P.; Sigfridsson, K.; Hansson, O. ; Karlsson, B. G.; Baltzer, L.; Nordling, M.; Lundberg, L. G. Structural Dynamics in the Plastocyanin-Photosystem 1 Electron-Transfer Complex as Revealed by Mutant Studies. *Biochim. Biophys. Acta* **1995**, *24*, 28–36.

(23) Haehnel, W.; Pröpper, A.; Krause, H. Evidence for Complexed Plastocyanin as the Immediate Electron Donor of P-700. *Biochimica et Biophysica Acta* **1980**, *593*, 384–399.

Light- and redox-dependent force spectroscopy reveals that the interaction between plastocyanin and plant photosystem I is favored when one partner is ready for electron transfer

- (24) Baumgartner, W.; Hinterdorfer, P.; Ness, W.; Raab, A.; Vestweber, D.; Schindler, H.; Drenckhahn, D. Cadherin Interaction Probed by Atomic Force Microscopy. *Proceedings of the National Academy of Sciences* **2000**, *97*(8), 4005–4010.
- (25) Wildling, L.; Rankl, C.; Haselgrübler, T.; Gruber, H. J.; Holy, M.; Newman, A. H.; Zou, M. F.; Zhu, R.; Freissmuth, M.; Sitte, H. H.; Hinterdorfer, P. Probing Binding Pocket of Serotonin Transporter by Single Molecular Force Spectroscopy on Living Cells. *Journal of Biological Chemistry* **2012**, *287* (1), 105–113.
- (26) Le, D. T. L.; Guérardel, Y.; Loubire, P.; Mercier-Bonin, M.; Dague, E. Measuring Kinetic Dissociation/Association Constants between *Lactococcus Lactis* Bacteria and Mucins Using Living Cell Probes. *Biophysical Journal* **2011**, *101* (11), 2843–2853.
- (27) Guo, S.; Lad, N.; Ray, C.; Akhremitchev, B. B. Association Kinetics from Single Molecule Force Spectroscopy Measurements. *Biophysical Journal* **2009**, *96* (8), 3412–3422.
- (28) Hope, A. B. Electron Transfers amongst Cytochrome f, Plastocyanin and Photosystem I: Kinetics and Mechanisms. *Biochimica et Biophysica Acta - Bioenergetics* **2000**, *1456* (1), 5–26.
- (29) Sommer, F.; Drepper, F.; Haehnell, W.; Hippler, M. The Hydrophobic Recognition Site Formed by Residues PsaA-Trp651 and PsaB-Trp627 of Photosystem I in *Chlamydomonas Reinhardtii* Confers Distinct Selectivity for Binding of Plastocyanin and Cytochrome c 6. *Journal of Biological Chemistry* **2004**, *279* (19), 20009–20017.
- (30) Kuhlert, S.; Drepper, F.; Fufezan, C.; Sommer, F.; Hippler, M. Residues PsaB Asp612 and PsaB Glu613 of Photosystem i Confer PH-Dependent Binding of Plastocyanin and Cytochrome c 6. *Biochemistry* **2012**, *51* (37), 7297–7303.
- (31) de La Rosa, M. A.; Navarro, J. A.; Díaz-Quintana, A.; de La Cerda, B.; Molina-Heredia, F. P.; Balme, A.; Murdoch, P. D. S.; Díaz-Moreno, I.; Durán, R. v; Hervás, M. An Evolutionary Analysis of the Reaction Mechanisms of Photosystem I Reduction by Cytochrome c 6 and Plastocyanin. *Bioelectrochemistry* **2002**, *55*, 41–45.
- (32) Bizzarri, A. R.; Cannistraro, S. The Application of Atomic Force Spectroscopy to the Study of Biological Complexes Undergoing a Biorecognition Process. *Chemical Society Reviews* **2010**, *39* (2), 734–749.
- (33) Bender, S. L.; Barry, B. A. Light-Induced Dynamics in Photosystem I Electron Transfer. *Biophysical Journal* **2008**, *95* (8), 3927–3934.
- (34) Wöhri, A. B.; Katona, G.; Johansson, L. C.; Fritz, E.; Malmerberg, E.; Andersson, M.; Vincent, J.; Eklund, M.; Cammarata, M.; Wulff, M.; Davidsson, J.; Groenhof, G.;

Light- and redox-dependent force spectroscopy reveals that the interaction between plastocyanin and plant photosystem I is favored when one partner is ready for electron transfer

Neutze, R. Light-Induced Structural Changes in a Photosynthetic Reaction Center Caught by Laue Diffraction. *Science* **2010**, *328*(5978), 630–633.

(35) M. H. B. Stowell; T. M. McPhillips; C. Rees; S. M. Soltis; E. Abreschand; G. Feher. Light-Induced Structural Changes in Photosynthetic Reaction Center: Implications for Mechanism of Electron-Proton Transfer. *Science* **1997**, *276*, 812–816.

(36) Dods, R.; B ath, P.; Morozov, D.; Gagn er, V. A.; Arnlund, D.; Luk, H. L.; K ubel, J.; Maj, M.; Vallejos, A.; Wickstrand, C.; Bosman, R.; Beyerlein, K. R.; Nelson, G.; Liang, M.; Milathianaki, D.; Robinson, J.; Harimoorthy, R.; Berntsen, P.; Malmerberg, E.; Johansson, L.; Andersson, R.; Carbajo, S.; Claesson, E.; Conrad, C. E.; Dahl, P.; Hammarin, G.; Hunter, M. S.; Li, C.; Lisova, S.; Royant, A.; Safari, C.; Sharma, A.; Williams, G. J.; Yefanov, O.; Westenhoff, S.; Davidsson, J.; DePonte, D. P.; Boutet, S.; Barty, A.; Katona, G.; Groenhof, G.; Br and en, G.; Neutze, R. Ultrafast Structural Changes within a Photosynthetic Reaction Centre. *Nature* **2021**, *589* (7841), 310–314.

(37) Chen, J.; Bender, S. L.; Keough, J. M.; Barry, B. A. Tryptophan as a Probe of Photosystem I Electron Transfer Reactions: A UV Resonance Raman Study. *The Journal of Physical Chemistry B* **2009**, *113*, 11367–11370.

(38) Farkas, D.; Hansson,  . An NMR Study Elucidating the Binding of Mg(II) and Mn(II) to Spinach Plastocyanin. Regulation of the Binding of Plastocyanin to Subunit PsaF of Photosystem i. *Biochimica et Biophysica Acta - Bioenergetics* **2011**, *1807* (12), 1539–1548.

(39) Pottosin, I.; Shabala, S. Transport Across Chloroplast Membranes: Optimizing Photosynthesis for Adverse Environmental Conditions. *Molecular Plant*. Cell Press March 7, 2016, pp 356–370.

(40) Shaul, O. Magnesium Transport and Function in Plants: The Tip of the Iceberg. *BioMetals* **2002**, *15*, 309–323.

(41) Portis, A. R.; Heldt, H. W. Light-Dependent Changes of the Mg²⁺ Concentration in the Stroma in Relation to the Mg²⁺ Dependency of CO₂ Fixation in Intact Chloroplasts. *Biochimica et Biophysica Acta* **1976**, *449*, 434–446.

(42) Ishijima, S.; Uchibori, A.; Takagi, H.; Maki, R.; Ohnishi, M. Light-Induced Increase in Free Mg²⁺ Concentration in Spinach Chloroplasts: Measurement of Free Mg²⁺ by Using a Fluorescent Probe and Necessity of Stromal Alkalinization. *Archives of Biochemistry and Biophysics* **2003**, *412* (1), 126–132.

(43) Miyashita, O.; Okamura, M. Y.; Onuchic, J. N. Interprotein Electron Transfer from Cytochrome c 2 to Photosynthetic Reaction Center: Tunneling across an Aqueous Interface. *Proceedings of the National Academy of Sciences* **2005**, *102* (10), 3558–3563.

Light- and redox-dependent force spectroscopy reveals that the interaction between plastocyanin and plant photosystem I is favored when one partner is ready for electron transfer

(44) Lagunas, A.; Guerra-Castellano, A.; Nin-Hill, A.; Díaz-Moreno, I.; de la Rosa, M. A.; Samitier, J.; Rovira, C.; Gorostiza, P. Long Distance Electron Transfer through the Aqueous Solution between Redox Partner Proteins. *Nature Communications* **2018**, *9* (1), 3–9.

(45) López-Martínez, M.; López-Ortiz, M.; Antinori, M. E.; Wientjes, E.; Nin-Hill, A.; Rovira, C.; Croce, R.; Díez-Pérez, I.; Gorostiza, P. Electrochemically Gated Long-Distance Charge Transport in Photosystem I. *Angewandte Chemie - International Edition* **2019**, *58* (38), 13280–13284.

(46) Guo, S.; Lad, N.; Ray, C.; Akhremitchev, B. B. Association Kinetics from Single Molecule Force Spectroscopy Measurements. *Biophysical Journal* **2009**, *96* (8), 3412–3422.

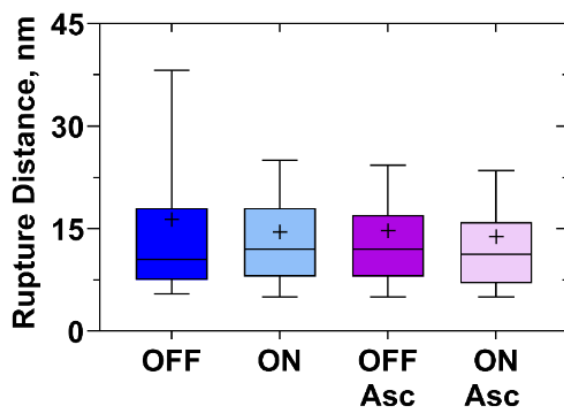
(47) Marco, P.; Kozuleva, M.; Eilenberg, H.; Mazor, Y.; Gimeson, P.; Kanygin, A.; Redding, K.; Weiner, I.; Yacoby, I. Binding of Ferredoxin to Algal Photosystem I Involves a Single Binding Site and Is Composed of Two Thermodynamically Distinct Events. *Biochimica et Biophysica Acta - Bioenergetics* **2018**, *1859* (4), 234–243.

(48) Setif, P. Q.; Bottin, H. Laser Flash Absorption Spectroscopy Study of Ferredoxin Reduction by Photosystem I in *Synechocystis* Sp. PCC 6803: Evidence for Submicrosecond and Microsecond Kinetics. *Biochemistry* **1994**, *33*, 8495–8504.

(49) Xu, P.; Tian, L.; Kloz, M.; Croce, R. Molecular Insights into Zeaxanthin-Dependent Quenching in Higher Plants. *Scientific Reports* **2015**, *5* (1), 1–10.

(50) Caffarri, S.; Kouřil, R.; Kereiče, S.; Boekema, E. J.; Croce, R. Functional Architecture of Higher Plant Photosystem II Supercomplexes. *EMBO Journal* **2009**, *28* (19), 3052–3063.

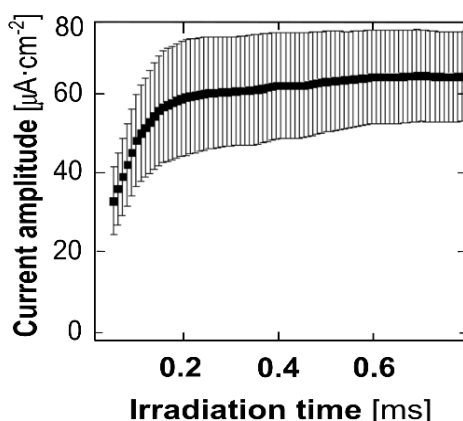
(51) Hutter, J. L.; Bechhoefer, J. Calibration of Atomic-Force Microscope Tips. *Review of Scientific Instruments* **1993**, *64* (7), 1868–1873.



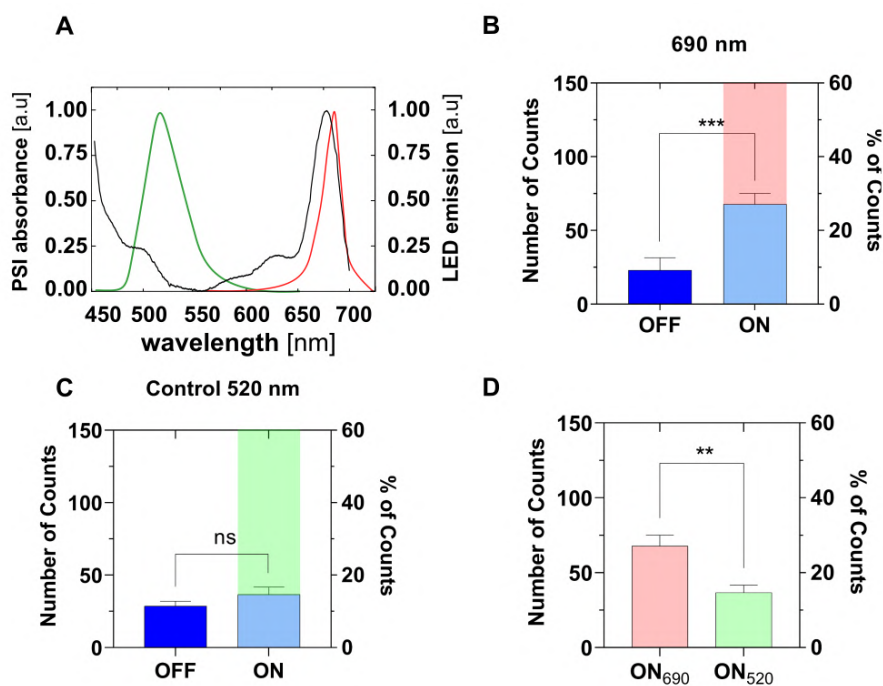
Supplementary Figure S1. AFM-SMFS of the interaction between $\text{Pc}_{\text{Red/Ox}}$ and dark/illuminated PSI. Box plot for the rupture distance for the AFM-SMFS experiments from Figures 2 and 3 in the main text. OFF condition represents the interaction between non-illuminated PSI (PSI_{Red}) and Pc_{Ox} (blue) or Pc_{Red} (purple, in presence of sodium ascorbate 5 mM). ON condition (pink) represents the interaction between the PSI under 690 nm illumination (PSI_{Ox}) and Pc_{Ox} (cyan) or Pc_{Red} (pink, in presence of sodium ascorbate 5 mM). Quantification out of 256 force-distance curves per dataset, 3 consecutive cycles OFF-ON averaged from 3 independent experiments. All measurements were done in PBS, 50 mM pH 7.4 at room temperature.

Photo-oxidation of PSI (Supplementary Figure S2)

Given the near unit photo-conversion factor (quantum yield) of PSI, to satisfy PSI_{ox} condition, photons have to be absorbed at a higher rate than P700^+ reduction. To provide a sufficient photon fluence, we make use of high-power LED SMB1N690D *Roithner Laser Technik*, with a central wavelength of 690 nm, providing an optical output $60 \text{ mW}\cdot\text{cm}^{-2}$ at the electrode plane. This optical output results in $\sim 2.4 \cdot 10^5 \text{ photons}\cdot\text{s}^{-1}$ in the surface covered by a single PSI complex, which provides a lower bound for P700 reoxidation time of $\sim 4\mu\text{s}$. However, not all incident photons result in P700 oxidation. To provide a direct estimation of the population of P700^+ in the sample, we have measured the photo-current output of Au-pIQA-PSI samples in presence of exogenous redox mediators (Methyl Viologen $125 \mu\text{M}$ and Osmium Bipyridine dichloride $40 \mu\text{M}$). Redox mediators shuttle the photogenerated charges to the Au electrode allowing to probe the P700^+ population, that is, the number of photogenerated charges. Upon pulsed irradiation, the current exhibits a sudden increase with an amplitude proportional to the population of photo-excited P700^+ in the sample. Increasing the pulse duration saturates photocurrent amplitude for pulses $> 200 \mu\text{s}$, indicating that after this exposure time, photons are in excess. This provides a higher bound for P700 re-photo-oxidation time in the reported experimental conditions.

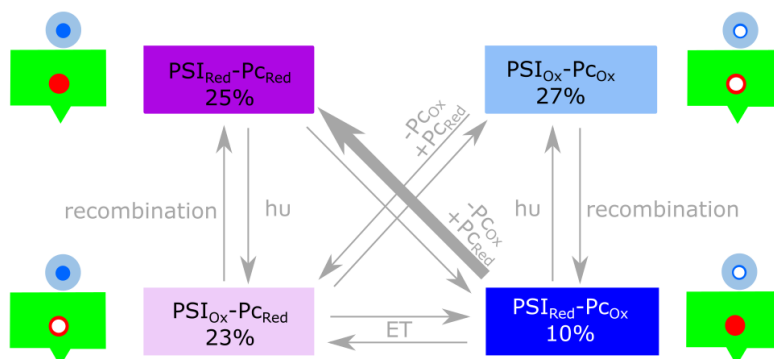


Supplementary Figure S2. Photo-chronoamperometric signal amplitude of Au-pIQA-PSI electrodes irradiated with 690 nm LED with an optical power of $60 \text{ mW}\cdot\text{cm}^{-2}$ in the sample plane. Redox mediators (Methyl Viologen $125 \mu\text{M}$ and Osmium Bipyridine dichloride $40 \mu\text{M}$) are added to PBS 50 mM pH 7.4 buffer solution to facilitate charge exchange with the sample electrode. Applied sample potential is -50 mV w.r.t silver/silver chloride (SSC) reference electrode. Average \pm standard error of the mean (SEM) for three independent experiments.



Supplementary Figure S3. Control experiment with 520 nm illumination. **A.** PSI sample absorption spectra, normalized to 680 nm peak (black trace) and normalized emission for green LED, 520 nm (green trace) and red LED, 690 nm (red trace). Relative emission spectra are adapted from provider specification sheet (Roithner Laser Technik). **B.** Quantification of the number of binding events between PSI and Pc_{Ox} from 3 independent experiments (768 force-distance curves per independent experiment). ON indicates irradiation with red LED (690 nm) and OFF indicates dark conditions. PSI_{Red} (OFF) binds Pc_{Ox} in significantly fewer events than PSI_{Ox} (ON). **C.** Control with green LED irradiation (520 nm). **D.** Comparison of number of binding events for Pc_{Ox} with PSI samples irradiated with 690 nm (red) and 520 nm (green) showing a significant difference in the number of events.

Light- and redox-dependent force spectroscopy reveals that the interaction between plastocyanin and plant photosystem I is favored when one partner is ready for electron transfer



Supplementary Figure S4. Outline the situations imposed experimentally in this work by means of photo-oxidation and reducing agents, to probe PSI-Pc complexes interaction by AFM-SMFS, including the binding frequency obtained in the experiments. The arrows represent the physiological equilibria to which every redox pair could be associated.

Chapter 6

Photoelectrochemical two-dimensional electronic spectroscopy (PEC2DES) of photosystem I to study charge separation dynamics in photosynthesis

Manuel López-Ortiz,^{a†} Luca Bolzonello,^{b†}, Matteo Bruschi^c, Elisa Fresch^c, Elisabetta Collini^c, Chen Hu,^d Roberta Croce,^d Niek F. van Hulst^{*b,e} and Pau Gorostiza^{*a,e}

^aInstitute for Bioengineering of Catalonia (IBEC), The Barcelona Institute of Science and Technology

^bThe Institute of Photonic Sciences (ICFO), The Barcelona Institute of Science and Technology

^c Dipartimento di Scienze Chimiche, Università degli Studi di Padova

^dBiophysics of Photosynthesis. Dep. Physics and Astronomy, Faculty of Sciences, Vrije Universiteit Amsterdam

^eCatalan Institution for Research and Advanced Studies (ICREA)

* Corresponding authors: niek.vanhulst@icfo.eu (N. F. van H.), pau@icrea.cat (P.G.)

† These authors contributed equally to this work.

1 Abstract

We present a non-linear spectro-electrochemical technique to investigate photosynthetic protein complexes. The PEC2DES set-up combines photo-electrochemical detection (PEC) that selectively probes the protein photogenerated charges output, with two-dimensional electronic spectroscopy excitation (2DES) that spreads in an excitation-detection map the non-linear optical response of the system. PEC allows to distinguish the contribution of charge separation (CS) from other de-excitation pathways, while 2DES allows to disentangle congested spectral bands and evaluate the exciton dynamics (decays and coherences) of the photosynthetic complex. We have developed *operando* phase-modulated 2DES by measuring the photoelectrochemical reaction rate in a biohybrid electrode functionalized with plants photosynthetic complex I- light harvesting complex-I (PSI-LHCI) layer. Optimizing the photoelectrochemical current signal yields reliable linear spectra unequivocally associated with PSI-LHCI. The 2DES signal is validated by non-linear features like the characteristic vibrational coherence at 750 cm^{-1} . No other dynamics are observed within 450 fs of population time. These intriguing results are discussed in the framework of previous reports and models. The PEC2DES method overcomes previous experimental limitations and opens the way to probe the physiological channel of CS under linear conditions.

2 Introduction

The photosynthesis is the process that underlies the conversion of light energy into chemical one in subsequent steps with timescales that span for ten orders of magnitude. The first is photon absorption followed by excitonic energy transfer (EET) in the femto-/picosecond timescale. The excitons migrate to the reaction center (RC), where charge separation (CS) takes also in the picosecond timescale¹. Then electrons are transferred in a cascade of electron transfer (ET) steps ranging from tenths of picosecond to hundreds of nanoseconds to opposite side of its embedding membrane², fostering the photosynthetic electron transport chain that promotes chemical synthesis in the millisecond scale.

To study such process as a whole, it is crucial to combine different approaches such as protein crystallization and mutations, theoretical simulations, magnetic and optical spectroscopies³. A step further could be made when more characterizations techniques can be applied simultaneously, so when chemical, electronic, or optical signatures, can be detected at the same time. Such approach has been successfully applied with many techniques. For example, combinations of electrochemical and optical spectroscopy methods have been developed, like Raman^{4,5} including surface- and tip-enhanced, transient absorption⁶, X-ray⁷, FTIR⁸, and confocal fluorescence⁹⁻¹¹. Each

spectro-electrochemical technique poses specific challenges and offers unique advantages to study reactions in static and dynamic conditions (*in situ* and *operando*, respectively).
12–15

A deeper knowledge of the secrets of photosynthesis has paved the way for artificial¹⁶, de-novo designed proteins.¹⁷ The spectral absorption of photosynthetic complexes has been engineered with the addition of synthetic dyes,^{18,19} or the assembly chimeras of photosynthetic and light harvesting complexes from different organism.²⁰ In natural and artificial systems, an increase in the absorption band is translated into an efficiency increase only if the photosynthetic excitons are eventually trapped by the reaction center and CS takes place. To decipher photosynthetic complexes and engineer novel photosynthetic strategies, it is thus key to probe the EET pathways leading to CS. The aim of this work is indeed to detach the non-linear spectroscopy features of only the “CS” excitons. To do so, we have optimized a photoelectrochemical current detection method to perform spectroscopic measurements of photosynthetic complexes.

Because of the multichromophoric structure of photosynthetic complexes and the ultrafast processes involved^{21,22} tracking the photosynthetic exciton dynamics in time, space and energy is challenging, and usually experimental results need support from computational chemistry to be interpreted. In this sense, the advent of two-dimensional electronic spectroscopy (2DES) helped to disentangle congested spectral bands, as it spreads in an excitation-detection map the non-linear optical signal. Indeed, 2DES can give a detailed picture of homogeneous and inhomogeneous broadening, spectral diffusion, transfers, and correlations between excited states, vibrational and electronic coherences, thus the entire excited state dynamics²³. Nevertheless, even the results of 2DES on the dynamics of photosynthetic systems can be inconclusive and controversial²⁴. As such, a more function-oriented spectroscopical methods are needed.

To develop photoelectrochemical current 2-dimensional electronic spectroscopy (PEC2DES), we have optimized the kinetics and the amplitude of the photoelectrochemical current of a photosynthetic protein complex tethered to an electrode under potentiostatic control. This action spectroscopy technique offers to probe the CS functionality of photosynthetic complexes and the distinct ET processes leading to CS. To validate this method, we have employed plant photosynthetic complex I and its light harvesting antenna (PSI-LHCI) as model system. In PSI-LHCI, light harvesting by the antenna chlorophylls is used to drive CS in the RC.

The conventional 2DES observable is the non-linear optical polarization^{25–27}, i.e. a coherent electric field generated by the sample interacting with laser pulses. Instead, collinear 2DES^{28–31} readout does not rely on the detection of such electric field, but on any observable proportional to the populations of the excited states after the interaction with excitation pulses. For example, if the system is luminescent, the readout can be

fluorescence. The fluorescence signal is conveniently exploited to quantify excited states population within ultrafast spectroscopy^{32–37}. However, fluorescence relaxation in photosynthesis is a loss channel, thus not a primary observable. Indeed, excitons reaching the RC and undergoing CS do not fluoresce by definition. On the other hand, CS initiates an ET cascade from the chlorophyll special pair (P700) to the terminal electron donor, the iron sulfur cluster (F_B) at the stromal side of the membrane. The excited PSI-LHCI redox cofactors, $P700^+$ and F_B^- transfer charge to their soluble redox protein partners, plastocyanin and ferredoxin respectively, thereby coupling PSI-LHCI to the photosynthetic electron transport chain. Thus, draining charges from PSI-LHCI redox cofactors yields an electrochemical current that can be exploited as a 2DES readout *in vitro*. In the experimental approach presented here, the photoelectrochemical current directly measures the ultimate physiological outcome of PSI-LHCI light harvesting, i.e. electrical charges mobilized in the photosynthetic electron transport chain. Using the higher plant *Arabidopsis Thaliana* PSI-LHCI, we have recorded for the first time PEC2DES in photosynthetic complexes.

3 Experiment

3.1 Photo electrochemical current readout of PSI-LHCI samples

In optical measurements, exogenous electron donors are introduced to boost ET kinetics of the photo-oxidized state ($F_B/P700^+$) and closed state ($F_B^-/P700$) towards the open state ($F_B/P700$), thus allowing the RC to separate new charge pairs upon successive excitations and preventing $P700^+$ from quenching excitation without CS³⁸. However, an estimation based on $P700^+$ reduction kinetics (~ 2 ms) and the fluence reported in literature found that most P700 are in the closed state³⁹. Nevertheless, due to the effective quenching of excitations by $P700^+$, absorption and fluorescence measurements are possible since they are only marginally affected by $P700/F_B$ oxidation state. In contrast, in the photo-electrochemical readout the signal is proportional to PSI-LHCI photogenerated charges, therefore $P700^+$ and F_B^- must be reduced and oxidized respectively to the open state before the next photo-excitation pulse, in order to preserve the photoelectrochemical yield⁴⁰. Efficient ET with the charge exchange cofactors is thus a requisite to restore $P700^+$ and F_B^- back to the open state at a higher rate than excitation pulse-train repetition. High ET rates with the electrode are also needed to achieve high photoelectrochemical current outputs with a signal-to-noise ratio sensitive to non-linear effects in ET leading to CS.

To maximize photoelectrochemical current output, soluble redox mediators that can exchange charge with $P700^+$ and F_B^- have been employed. We used osmium bis 2,2-bipyridine chloride (osbipy) to take advantage of the lower formal potential (higher

energy) of osbipy compared to P700⁺. The use of osbipy as redox mediator for PSI based bio-hybrid electrodes crosslinked to redox polymers^{41–44}, or diluted into electrolyte⁴² has been previously reported. Regarding the electron donor side, we have chosen methyl viologen (MV) as electron acceptor of the high energy electrons of F_B⁻. MV is a redox active heterocyclic molecule used as herbicide due to its ability to oxidize F_B⁻ and donate electrons to O₂, thus disrupting the photosynthetic electron transport chain and facilitating the formation of reactive oxygen species (ROS)^{45,46}. In an electrochemical cell however, electrodes readily oxidize the MV⁺ radical formed upon F_B⁻ oxidation, thus enhancing ET rates and limiting the formation of ROS⁴⁷. Simultaneous reduction of osbipy and oxidation of MV in the sample electrode, result in partially cancelling currents giving rise to a transient photoelectrochemical current^{48,49}. Although this configuration leads to low stationary currents, we took advantage of submillisecond electrochemical transient responses to perform spectroscopic recordings at kHz laser repetition rates.

The photoelectrochemical current was recorded under potentiostatic control (Metrohm–Autolab) making use of Au transparent screen-printed electrodes (Metrohm-Dropsens) (Figure 1a) harbored in a customized electrochemical cell adapted for spectroscopic experiments (Supplementary Figure SF1). Purified PSI-LHCI complexes (see Supplementary Information S1) were functionalized using pIQAcys linker peptide^{50,51} exposing the P700 luminal side to the electrolyte (Figure 1b and Supplementary Information 2). PSI-LHCI functionalization, orientation, working electrochemical window and scanning probe characterization has been reported in a previous work⁵².

3.2 Phase modulation and 2DES parameters

For effective and rapid photoelectrochemical current detected 2DES we exploit our recently developed pulse-by-pulse shaping with collinear laser set-up³¹. Briefly, a 3 kHz amplified Ti:sapphire laser (Coherent Libra) generates a continuous pulse train centered at 800 nm, which is converted and broadened (green area in Figure 2d) through a commercial but home-modified NOPA (Light Conversion TOPAS White). A prism compressor is used to roughly precompensate the phase dispersion and finally, an acousto-optical pulse shaper (Dazzler) finely adjusts the phase for reaching transform-limited pulse (~10 fs, see Supplementary Figure SF2) and generates 4 pulse replicas with control on their mutual time delay and phase (Supplementary Information S5). The time delay between the first and second pair of pulses (t₁ and t₃) set the excitation and detection frequencies (ω₁ and ω₃) respectively (Figure 1a), while t₂ fixes the time interval between excitation and detection pairs. In this so called “action” 2DES, phases of individual pulses (φ_{1–4}) are modulated in time and to separate the different components of the spectroscopic response of the system. In particular, rephasing and

non-rephasing responses fall into distinct peaks in the frequency domain⁵³. Additional technical details of the experiment are presented in the Supplementary Information S4,S5.

4 Results

4.1 Photo-electrochemical and AFM characterization of Au-pIQAcys-PSI-LHCI samples

Prior to the integration of electrochemical and 2DES set-ups (Figure 1a), photoelectrochemical current transient signal of Au-pIQAcys-PSI-LHCI samples was characterized with LED pulses. An example of photoelectrochemical current trace upon illumination with 125 μs pulses is shown in Figure 1c. Control experiments in absence of PSI-LHCI, and denaturated PSI-LHCI samples, heated to 60° for 1 h, exhibit negligible photoelectrochemical current. In addition, linear component of PEC2DES (*vide infra*), that is, electrochemical current linear spectra shown in Figure 2d, overlaps with PSI-LHCI absorption peak, supporting that photoelectrochemical current is due to PSI-LHCI photocatalytic activity.

Addition of 20 μM osbipy mediator to the working buffer (phosphate buffer saline, PBS, 50 mM, pH 7.4) was sufficient to observe transient photoelectrochemical currents upon pulsed illumination with $28 \pm 4 \mu\text{A}\cdot\text{cm}^{-2}$ amplitude (Figure 1d). On the other hand, buffer solution containing MV exclusively (200 mM) exhibits a four-fold lower photoelectrochemical current amplitude of $7 \pm 1 \mu\text{A}\cdot\text{cm}^{-2}$. In presence of both mediators, the photoelectrochemical current amplitude rises to $67 \pm 1 \mu\text{A}\cdot\text{cm}^{-2}$ (Figure 1c,1d) exhibiting a time decay constant of 0.27 ± 0.02 ms. To optimize osbipy concentration, the photoelectrochemical current amplitude was evaluated for increasing osbipy concentration in excess of MV (200 mM), (Figure 1e) saturating above 20 μM . Sample stability was evaluated measuring the photoelectrochemical current under pulsed illumination for several hours. Figure 1e shows the sample stability, which allows measuring several 2DES maps without significant degradation of the sample (i.e. photoelectrochemical current reduction).

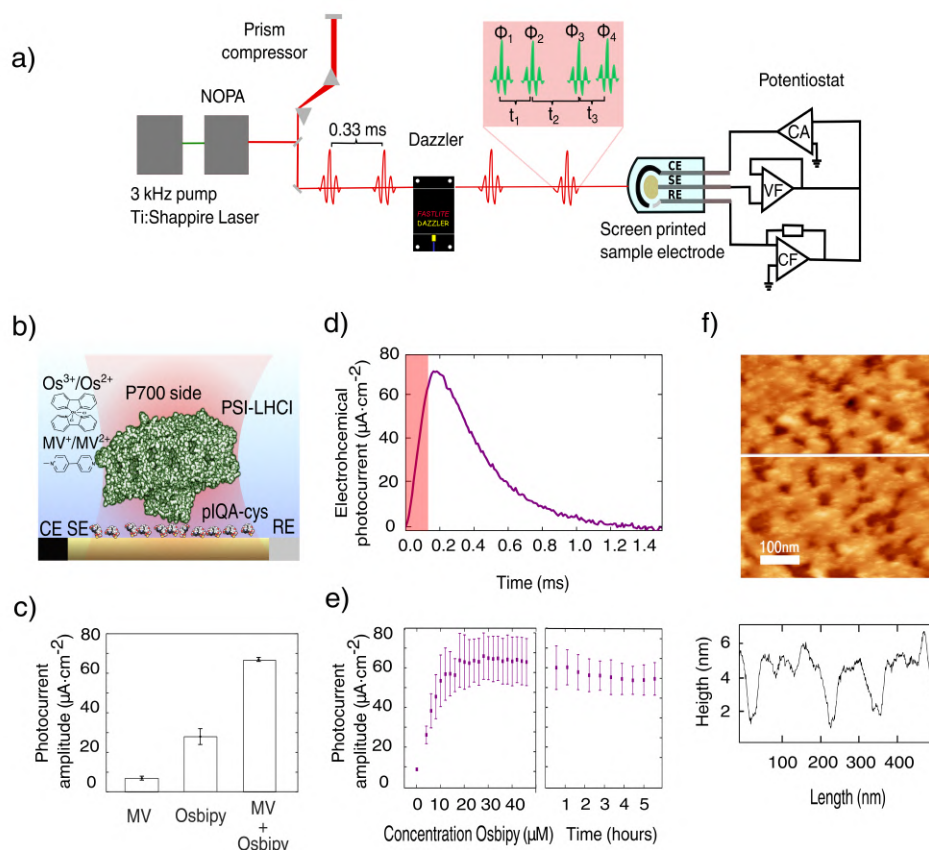


Figure 6.1: Photoelectrochemical current response of Au-pIQa-cys-PSI-LHCI electrodes. 1a) Experimental set-up for photoelectrochemical current detected 2DES. Pulse generation and shaping performed by pump laser, NOPA and acousto-optic modulator (DAZZLER) is shown on the left. 4-Pulse excitation scheme with phases ϕ_{1-4} and relative pulse delay t_{1-3} are shown in red inset. Electrochemical photoelectrochemical current detection system is depicted in the left-side including potentiostat scheme (CF: current follower, VF: voltage follower and CA: current amplifier) and sample miniaturized screen-printed electrode (CE: counter electrode, SE: sample electrode and RE: reference electrode). 1b) Cartoon representation of transparent Au electrode functionalized with pIQa-cys peptide linker orienting PSI-LHCI complexes that expose P700 luminal side to the electrolyte. 1c) Photo-chrono-amperometry of Au-pIQa-cys-PSI-LHCI electrodes at -50 mV w.r.t to silver pseudo-reference electrode. Electrolyte solution contains PBS 50 mM pH 7.4, MV 200 mM, and osbipy 20 μ M. The red shaded area represents an irradiation pulse of 125 μ s with a power of 35.7 $\text{mW}\cdot\text{cm}^{-1}$ and wavelength centered at 690 nm. Trace represents the average of 8 consecutive pulses. 1d) Photoelectrochemical current transient amplitude for Au-pIQa-cys-PSI-LHCI with MV (200 mM), osbipy (20 μ M) and MV+osbipy. 1e) Photoelectrochemical current transient amplitude versus osbipy concentration and time evolution of transient photoelectrochemical current amplitude under constant pulsed irradiation. Error bars in panels 1d and 1e represent the standard error for n=3 independent experiments. 1f) AFM characterization of PSI-pIQa-cys-Au films attached to Au electrodes. Scan size 500 \times 500 nm and a vertical axis color scale set to 10 nm amplitude. Height profile corresponding to white line in the scan. Scan image threshold results in an approximate surface coverage of \sim 75 %.

AFM scans of Au-pIQA-cys-PSI-LHCI electrodes (Figure 1f and Supplementary Information S3) reveal a sub-monolayer deposition with ~ 5 nm height, matching PSI crystallographic size as previously reported heights of PSI samples absorbed on gold electrodes^{54,55}. Scans reveal an approximate surface coverage of ~ 75 %, this approximation is employed to correct the estimation of the number of complexes in the surface of the electrode. This estimation is useful to compute the fraction of the total charge exchanged with the electrode in one pulse over the number of PSI-LHCI complexes on the electrode. The total charge is computed by integrating the photoelectrochemical current signal over time. This calculation reveals that the current output is near the maximal value for a PSI-LHCI monolayer, with ~ 40 % of PSI-LHCI complexes providing a charge pair for every pulse.

4.2 PEC2DES results

Photoelectrochemical current pulses amplitude upon illumination with laser phase-modulated four-pulse trains is shown in Figure 2a. Linear, rephasing and non-rephasing peaks in the frequency domain are shaded in yellow, red and blue respectively. It is then possible to reconstruct the linear (Figure 2c) and non-linear signals (Figure 2b, 2e) as a function of the delays between pulses t_1 - t_3 , and, through Fourier transform along the delays, obtain linear (Figure 2d) and 2DES spectra (Figure 2f, 2g), that is, the response-map of the sample excited at frequency ω_1 and detected at frequency ω_3 .

The linear spectrum obtained with this method overlaps with the optical absorption spectrum of PSI (Figure 2d), thus validating our approach. The absorptive map (Figure 2h) obtained with the sum of rephasing and non-rephasing signals, shows a main peak centered at 14750 cm^{-1} (678 nm), which corresponds to the main absorption transition of the PSI.

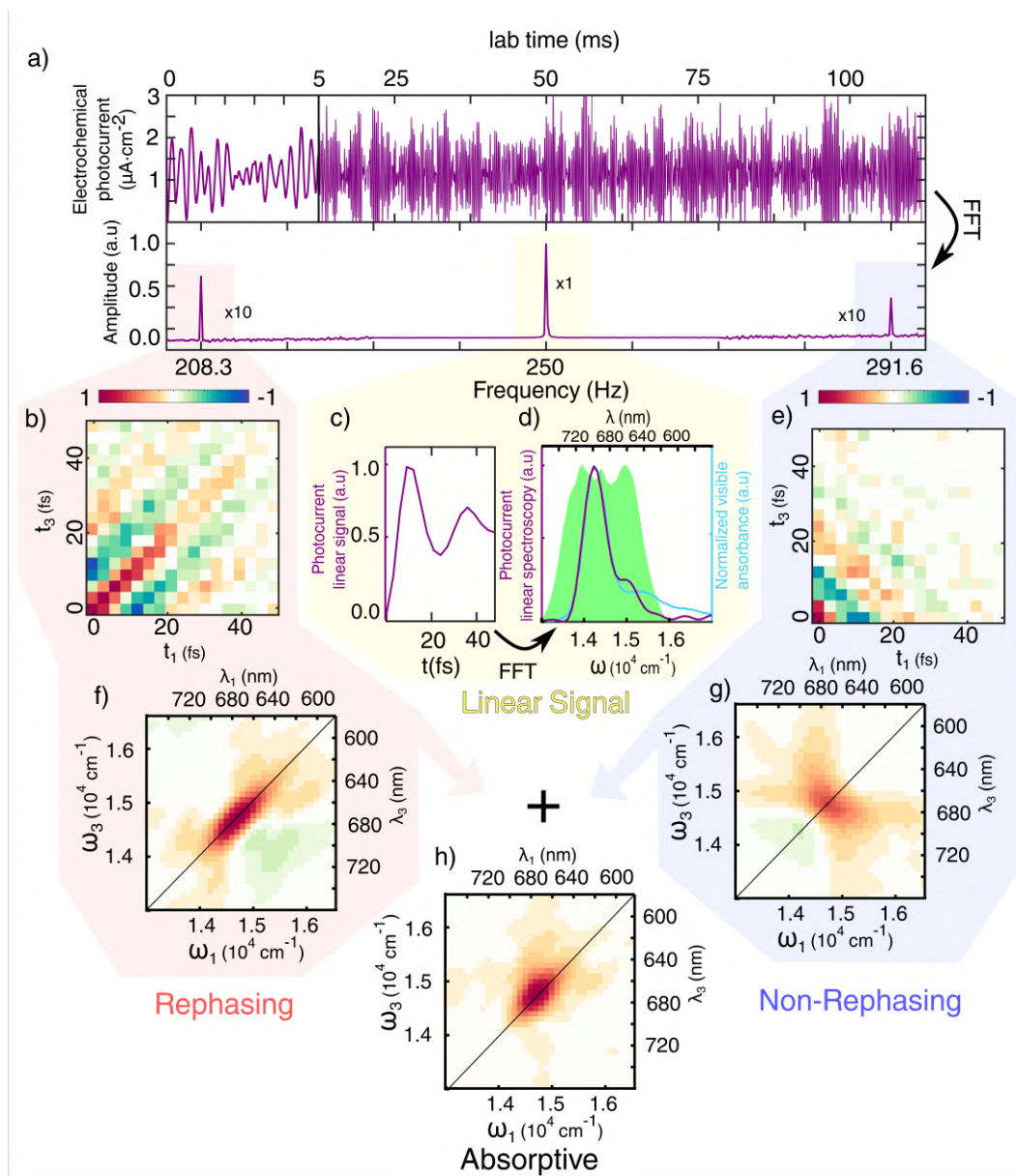


Figure 6.2: a) Top: Photoelectrochemical current readout from potentiostat (first 5 ms magnified) with periodic modulation of the phase, at fixed delay times between pulses. Bottom: Fourier Transform revealing linear, rephasing, and non-rephasing signals at different frequency combinations. c) Linear signal extracted from the first pulse pair along delay time t_1 and averaged over the other times. d) Comparison of the Fourier Transform of this signal (red) with the absorption spectrum of the PSI and the laser spectrum used for the experiment. b) and e) Time reconstruction of rephasing and non-rephasing signal into t_1 - t_3 maps (shown at $t_2=100$ fs). Their Fourier transforms produce the ω_1 - ω_3 maps f) and g) used for data interpretation. The sum of these maps leads to the absorptive map h).

4.3 Global analysis of PEC2DES data

2DES spectra are recorded for increasing excitation-detection delays (t_2), allowing to track the population of the excitonic states. The analysis of the signal evolution as a function of the population time t_2 has been performed using global analysis⁵⁶ to identify their main temporal components. The amplitudes associated to real (decays) and complex (oscillations) exponential functions that globally fit the data are retrieved to generate decay associated spectroscopy maps (2D-DAS) and coherence associated spectroscopy maps (2D-CAS) respectively. For every temporal component, a map depicting its amplitude on the excitation-detection axis is generated to ease the visualization of the map evolution. The global fit, using only real exponentials, returns two 2D-DAS components with time constants of 10 fs and $\gg 450$ fs. The fastest 2D-DAS component is generated by the overlap of all pulses around $t_2 = 0$, which gives rise to a spurious signal⁵⁷, and is not considered for the analysis. Instead, the second 2D-DAS, shown in Figure 3b (right), associated with $\gg 450$ fs component, is similar to any map along t_2 , indicating that during the first 450 fs the 2DES maps do not significantly change shape or intensity. An example of the signal evolution along t_2 is displayed in figure 3b(left), with signal extracted at peak's maximum.

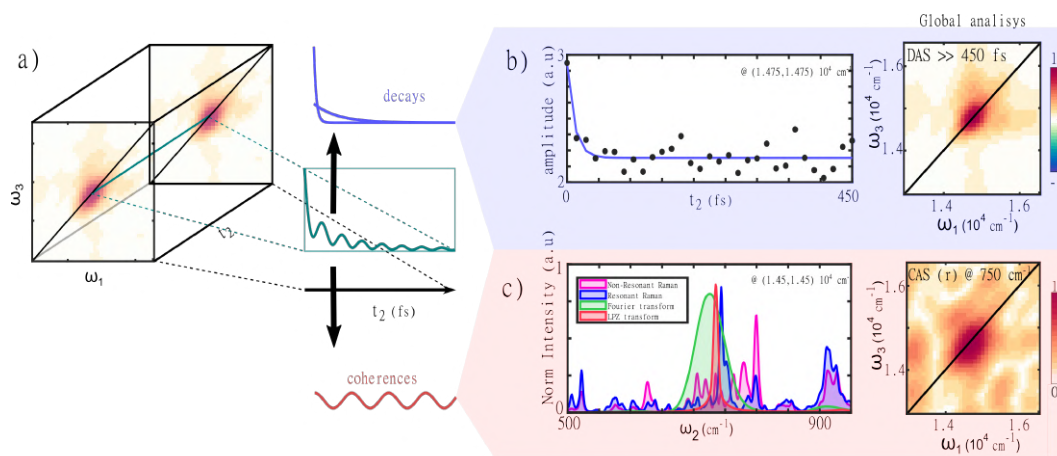


Figure 6.3: a) Schematic illustration of 2DES data. The non-linear signal along t_2 is a sum of different decaying or oscillating contributions. In b) it is shown a trace along t_2 extracted at peak's maximum, $\omega_1 = \omega_3 = 14750 \text{ cm}^{-1}$ (dots) and its global fit (blue line). Beyond the initial decay, the signal evolution is flat. The lack of signal evolution is confirmed at every coordinate with the unique DAS coming from the global fitting with a characteristic time much longer than experiment's range. An analysis on the residuals of the global fitting shows the presence of structured oscillations in the signal(c). The FFT (green) and LPZ (red) transforms²⁷ applied to residuals highlight the presence of an oscillation at 750 cm^{-1} . The same frequency component appears in the resonant (blue) raman spectrum, while it is less evident in the non-resonant (pink) one (633 and 514 nm laser excitation, respectively) of chlorophyll a in ethanol, suggesting this component comes from vibrational coherences of the molecule. The 750 cm^{-1} components is retrieved also from the global fitting with oscillating functions, returning a CAS map (on the right) with intensity distributed similarly to the DAS one.

Analysis of the oscillatory behavior of rephasing and non-rephasing signals individually, reveals signatures of coherent dynamics. Applying Fourier transform to the residuals of the fittings along t_2 , reveals a prominent peak with a frequency around 750 cm^{-1} (Figure 3c, left), suggesting the presence of coherent behavior. To verify it, the global fit has been applied, also including an oscillating component, and the same frequency component is retrieved. The amplitudes associated to this coherence component are represented by the 2D-CAS depicted in Figure 3d, and its distribution is similar to the peak intensity, slightly redshifted. It is then centered at the chlorophyll transition energy and does not show the typical off-diagonal pattern expected for vibrational coherences⁵⁸. However, we noted the overlap of a 750 cm^{-1} mode between the FFT or LPZ transform⁵⁹ on residuals (picked at $\omega_1 = \omega_3 = 14500\text{ cm}^{-1}$) with resonant Raman spectra (Figure 3b) of chlorophyll *a* (the main chromophore in PSI-LHCI complex). The resonant condition of Raman reveals an enhancement of Raman scattering at 750 cm^{-1} , suggesting the coupling of a vibrational mode with such energy to the visible transition. It is thus likely that the oscillation we detect in the 2DES is the same nuclear mode enhanced in resonant Raman.

5 Discussion

The overlap between the photoelectrochemical detected linear spectrum and the absorption spectrum (Figure 2d) demonstrates that the detected electrons are photogenerated by PSI-LHCI complexes. Moreover, the vibrational coherence found in the PEC2DES counterpart is a typical feature of time-resolved spectra of chlorophyll *a* and, in addition to our resonant Raman spectra, it was found in 2DES experiments of PSII²² and free chlorophyll⁶⁰ samples. These observations confirm that the photoelectrochemical current detected 2DES is sensitive to both linear and non-linear spectroscopic features of PSI-LHCI samples and provide experimental access to a physiologically meaningful observable that was not available previously. This has been achieved by maximizing the photoelectrochemical current output of PSI-LHCI complexes specifically bound to the electrode with a peptide, and by the choice of redox mediators' and their concentrations.

The PEC2DES results obtained exhibit neither population dynamics nor spectral diffusion between within our experimental range, as no evolution of PEC2DES maps has been detected. This behavior is in contrast to the sub-picosecond kinetics obtained from the non-linear optical response of plant PSI-LHCI samples reported without photoelectrochemical readout. Global analysis of 2DES revealed a $\sim 250\text{ fs}$ component associated with excited state equilibration and transfer to the bulk chlorophylls⁶¹ in PSI-LHCI extracted from spinach leaves while *Akthar et al.* reported an exciton relaxation time in the core antenna of 500 fs ⁶². Similar 2DES experiments (non

photoelectrochemical) in algae⁶³ and cyanobacteria⁶⁴ reveal sub-picosecond exciton equilibration and trapping kinetics ranging from 1 to 20 ps.

The absence of ultrafast dynamics in our measurements is indeed surprising. However, the different nature of the excitation and detection of PEC2DES with respect to standard 2DES may explain these observations. In particular, the differences of 4-pulses compared to 3-pulses excitation, and electrochemical photocurrent with respect to optical detection are discussed below and illustrated in figure 4.

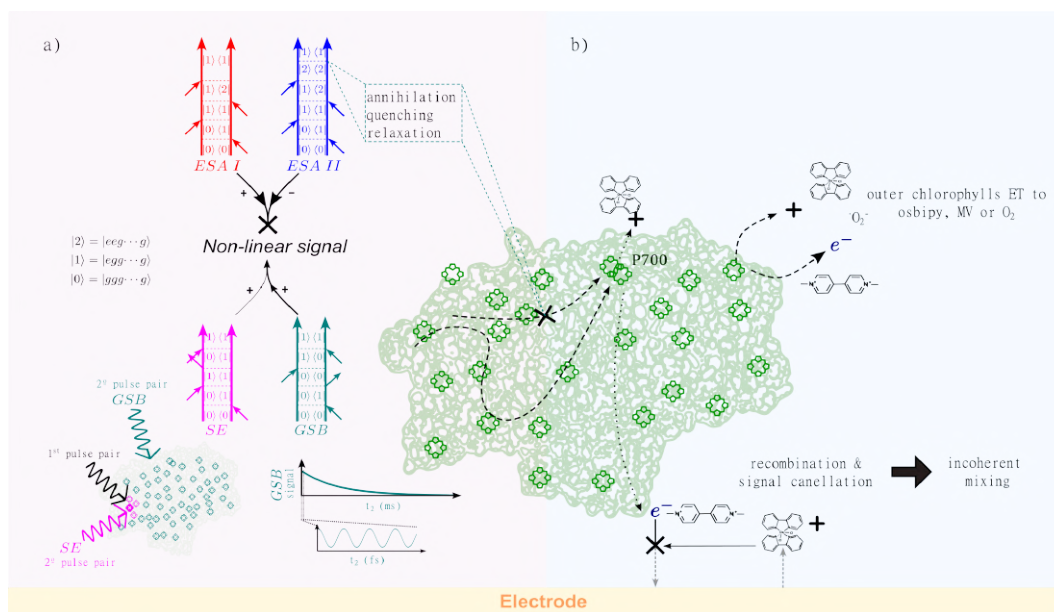


Figure 6.4: A pictorial view of the possible interpretation for the lack of dynamics in PEC2DES due to differences in excitation scheme (a) in left side and electrochemical detection (b) in right side of the panel . a) 4-pulses excitation. Feynman paths describing 4-pulses excitation are ESA I (red),ESA II (blue), SE (magenta) and GSB (aquamarine). Even if ESA II would generate 2 excitons in the same protein after the 4-pulses interaction, annihilations or quenching will reduce the detection to one CS, as much as ESA I. Having the opposite sign, the two contributions will cancel out, and the non-linear signal will be generated only by SE and GSB contributions. SE signal signal is associated to chlorophylls that are excited by both first pulse pair (black) and second pulse pair (magenta) while GSB signal is associated to non-previously excited chlorophylls (aquamarine). GSB signal decays in ms time scale, in experimental window (zoom for ~500 fs) only coherences are expected from GSB contribution. b) Electrochemical detection. CS might take place in outer chlorophylls other than P700 transferring charge to MV,Oosbipy or O₂ resulting in ultrafast dynamics of single or few chlorophylls instead of PSI-LHCI complex. Recombination of charges in the electrochemical solution before the detection and signal cancellation in the electrode could give rise to the so called “incoherent mixing” where part of the linear signal will leak into the non-linear counterpart.

Population detected 2DES observables are known to differ from optical detected ones. The differences are related to the 3rd and 4th order feynman pathways (figure 4a) and their mutual weighth^{65,66}. The generation of a second exciton in one single PSI-LHCI leads

to its annihilation, decay or quenching because the lifetime of an exciton in the protein is much shorter than the protein turnover. Therefore, only one CS per protein per pulse quartet is possible. To estimate the experimental observables, the sample wavefunction is represented as the product of the wavefunctions of the chlorophylls in a single PSI-LHCI complex. In this product, the excited state absorption (ESA) is cancelled out, limiting the non linear signal to the sum of stimulated emission (SE) and ground state bleaching (GSB) components. GSB signal decays with the turnover cycle of the protein in ms time scale, and therefore is likely constant in our experimental window. The weight of SE, the only non-linear component exhibiting population evolution along t_2 , is expected to be significantly smaller than GSB because SE path is simply less probable than GSB at experimental excitation density. In these conditions and assuming all chlorophylls in a protein equivalents, the average number of excitations per PSI-LHCI is ~ 1 after the first pair of pulses. The second pair will more likely interact with a chlorophyll in the ground state (~ 160 chlorophylls) rather than exciting the single or few chlorophylls excited by the first pulse pair. The ratio of this probabilities is related to the ratio between GSB and SE signals. This hypothesis is further supported by the presence of the 750 cm^{-1} oscillation as ground state vibrational coherences are present in the GSB pathways.

Regarding detection there are at least other two processes that may distinct electrochemical from optical detection. Population detected 2DES assume that the detected observable has to be proportional to the population of the excited state after the pulse quartet. This is not always the case, especially in an electrochemical detection technique that exploit free charges concentration in solution. Indeed the charge recombination of mediators in the solution and the cancelation leading to transient signal (figure 4b), are non-linear by definition. How this non-linearity interferes in the 2DES is actually matter of debate, but recent papers suggest that it foster the so-called incoherent mixing^{67,68}, where part of the linear signal, which is more intense and does not evolve along t_2 , ends in the non-linear counterpart. On the other hand, redox mediators employed to drain charges from the terminal electron donor/acceptor cofactors could partially penetrate in the PSI-LHCI protein matrix and directly drain charges from outer chlorophylls charge transfer states, preventing migration to RC (figure 4b). This would provide an alternative pathway wherein exciton transfer to the RC does not occur. Indeed, the Rao group has suggested that such charge scavenging can occur between outer chlorophylls and a quinone mediator for the cyanobacterial photosystem⁶⁹. Furthermore, both denaturated PSI complexes and chlorophyll molecules reduce O_2 producing H_2O_2 upon irradiation⁷⁰. However, despite inactivated PSI or chlorophyll molecules being embedded in an osbipy polymer with MV in solution, they yield no photocurrent.⁷⁰ These results^{69, 70} and ours, suggest alternative CS paths from outer chlorophylls could lead to a dynamic that does not follow the usual relaxation and trapping in the RC and thus may have different timescales.

To exclude or confirm the cited hypothesis, future developments in the photoelectrochemical setup are necessary. These include the use of larger, physiologically relevant redox carriers of PSI like its cognate proteins (plastocyanin, cytochromes, ferredoxin) that exchange charges selectively with PSI redox cofactors and thus exclude the possibility of unspecific charge draining. Moreover, to further investigate the SE and GSB ratio, it would be reasonable the use of light harvesting proteins with different amount of chlorophylls per unit. Furthermore, simultaneous PEC2DES and fluorescence detections would allow quantifying both the productive and loss exciton signals, offering direct access to their distinct relaxation pathways in a wide diversity of quasi-physiological conditions (e.g. light fluence, presence of biochemical regulators, different PSI subunits, and cofactors). This could be particularly relevant for studying uphill excitonic paths of the red forms present in PSI-LHCI complexes. Finally, measuring longer population time (t_2) would allow to have a more comprehensive picture and help to unravel the exciton dynamics from the overall non-linear signal.

6 Conclusions

We demonstrated that photoelectrochemical current can be used as readout signal of 2DES. The combination of 2DES and electrochemical detection in PEC2DES is suitable to study the non-linear response of PSI-LHCI from higher plants, and its non-linear output differs from optical detection methods. The requirements of PEC2DES (high turnover rate to open state and high signal-to-noise ratio) have been fulfilled by optimizing the photoelectrochemical current output. In particular, the unidirectional orientation of a PSI-LHCI monolayer on a transparent metal electrode, the choice of redox mediators, and their concentration yield sub-millisecond transient photoelectrochemical currents of magnitude in the range of $100 \mu\text{A}\cdot\text{cm}^{-2}$ that are stable for hours and allow the long-term signal integration required by 2DES experiments.

The overlap between the linear component of PEC2DES data and the visible absorption spectra of the sample manifests that PSI-LHCI complexes are responsible for PEC2DES results. In addition, global analysis yields an oscillatory component along delay time (t_2) depicted in the 2D-CAS map. We associate this coherence around 750 cm^{-1} with a vibrational mode coupled to the optical transition of chlorophyll *a* chromophores. Population dynamics is not observed within a delay time of 450 fs, in contrast to previous 2DES experiments of plant PSI-LHCI complexes solely based on optical detection.

We have validated the proof of concept of a novel photoelectrochemical technique (PEC2DES) with a biological multichromophoric system, PSI-LHCI protein complex of plants. This *operando* technique provides direct access to the physiological charge separation and can capture linear and notably non-linear features in the excitation-detection axis.

7 Acknowledgments

E.C. acknowledges the financial support of the MIUR PRIN2017, grant number 2017A4XRCA. This research received funding from the European Union Research and Innovation Programme Horizon 2020 HBP SG3 (grant agreement No. 945539), DEEPER (ICT-36-2020, grant agreement No. 101016787), and financial support from Agency for Management of University and Research Grants (CERCA Programme; 2017-SGR-1442 project), Ministry of Science and Innovation DEEP RED grant No. PID2019-111493RB-I00 funded by MCIN/AEI/10.13039/501100011033, the Commission for Universities and Research of the Department of Innovation, Universities, and Enterprise of the Government of Catalonia -AGAUR- (IU16-011508) and cofinanced by the European Union Regional Development Fund within the framework of the ERDF/FEDER Operational Program of Catalonia 20142020 with a grant of 50% of total eligible cost.

8 References

- (1) Croce, R.; van Amerongen, H. Light-Harvesting in Photosystem i. *Photosynth Res* 2013, *116* (2–3), 153–166. <https://doi.org/10.1007/s11120-013-9838-x>.
- (2) Chitnis, P. R. PHOTOSYSTEM I: Function and Physiology. <https://doi.org/10.1146/annurev.arplant.52.1.593> 2003, *52*, 593–626. <https://doi.org/10.1146/ANNUREV.ARPLANT.52.1.593>.
- (3) Croce, R.; van Amerongen, H. Light Harvesting in Oxygenic Photosynthesis: Structural Biology Meets Spectroscopy. *Science (1979)* 2020, *369* (6506). <https://doi.org/10.1126/science.aay2058>.
- (4) Wu, D. Y.; Li, J. F.; Ren, B.; Tian, Z. Q. Electrochemical Surface-Enhanced Raman Spectroscopy of Nanostructures. *Chem Soc Rev* 2008, *37* (5), 1025–1041. <https://doi.org/10.1039/b707872m>.
- (5) Lynk, T. P.; Sit, C. S.; Brosseau, C. L. Electrochemical Surface-Enhanced Raman Spectroscopy as a Platform for Bacterial Detection and Identification. *Anal Chem* 2018, *90* (21), 12639–12646. <https://doi.org/10.1021/acs.analchem.8b02806>.
- (6) Griffin, P. J.; Charette, B. J.; Gurke, J.; Malme, J.; Schaller, R. D.; Gosztola, D. J.; Vura-Weis, J.; Olshansky, L. Improved Charge Separation Through Conformational Control. *J Am Chem Soc* 2022, *In Prep.* (27), 12116–12126. <https://doi.org/10.1021/jacs.2c02580>.
- (7) Hung, S. F.; Wu, F. Y.; Lu, Y. H.; Lee, T. J.; Tsai, H. J.; Chen, P. H.; Lin, Z. Y.; Chen, G. L.; Huang, W. Y.; Zeng, W. J. Operando X-Ray Absorption Spectroscopic Studies

Photoelectrochemical two-dimensional electronic spectroscopy (PEC2DES) of photosystem I to study charge separation dynamics in photosynthesis

of the Carbon Dioxide Reduction Reaction in a Modified Flow Cell. *Catal Sci Technol* 2022, 12 (9), 2739–2743. <https://doi.org/10.1039/D2CY00220E>.

(8) Iwasita, T.; Nart, F. C. In Situ Infrared Spectroscopy at Electrochemical Interfaces. *Prog Surf Sci* 1997, 55 (4), 271–340. [https://doi.org/10.1016/S0079-6816\(97\)00032-4](https://doi.org/10.1016/S0079-6816(97)00032-4).

(9) Pande, N.; Chandrasekar, S. K.; Lohse, D.; Mul, G.; Wood, J. A.; Mei, B. T.; Krug, D. Electrochemically Induced PH Change: Time-Resolved Confocal Fluorescence Microscopy Measurements and Comparison with Numerical Model. *Journal of Physical Chemistry Letters* 2020, 11 (17), 7042–7048. <https://doi.org/10.1021/acs.jpcclett.0c01575>.

(10) Tassy, B.; Dauphin, A. L.; Man, H. M.; Le Guenno, H.; Lojou, E.; Bouffier, L.; De Poulpiquet, A. In Situ Fluorescence Tomography Enables a 3D Mapping of Enzymatic O₂Reduction at the Electrochemical Interface. *Anal Chem* 2020, 92 (10), 7249–7256. <https://doi.org/10.1021/acs.analchem.0c00844>.

(11) Bouffier, L.; Doneux, T. Coupling Electrochemistry with in Situ Fluorescence (Confocal) Microscopy. *Curr Opin Electrochem* 2017, 6 (1), 31–37. <https://doi.org/10.1016/j.coelec.2017.06.015>.

(12) Timoshenko, J.; Roldan Cuenya, B. In Situ/ Operando Electrocatalyst Characterization by X-Ray Absorption Spectroscopy. *Chemical Reviews*. 2021, pp 882–961. <https://doi.org/10.1021/acs.chemrev.0c00396>.

(13) Petersen, H.; Weidenthaler, C. A Review of Recent Developments for the in Situ/Operando Characterization of Nanoporous Materials. *Inorg Chem Front* 2022, 9 (16), 4244–4271. <https://doi.org/10.1039/d2qi00977c>.

(14) Liu, D.; Shadike, Z.; Lin, R.; Qian, K.; Li, H.; Li, K.; Wang, S.; Yu, Q.; Liu, M.; Ganapathy, S.; Qin, X.; Yang, Q. H.; Wagemaker, M.; Kang, F.; Yang, X. Q.; Li, B. Review of Recent Development of In Situ/Operando Characterization Techniques for Lithium Battery Research. *Advanced Materials* 2019, 31 (28), 1806620. <https://doi.org/10.1002/adma.201806620>.

(15) Heitmüller, J.; Eckstein, K.; Renner, R.; Stolte, M.; Hertel, T.; Würthner, F.; Brixner, T. Coherent Two-Dimensional Electronic Spectroelectrochemistry. *Spectrochim Acta A Mol Biomol Spectrosc* 2021, 253, 119567. <https://doi.org/10.1016/J.SAA.2021.119567>.

(16) Zhang, B.; Sun, L. Artificial Photosynthesis: Opportunities and Challenges of Molecular Catalysts. *Chem Soc Rev* 2019, 48 (7), 2216–2264. <https://doi.org/10.1039/C8CS00897C>.

(17) Ennist, N. M.; Zhao, Z.; Stayrook, S. E.; Discher, B. M.; Dutton, P. L.; Moser, C. C. De Novo Protein Design of Photochemical Reaction Centers. *Nature Communications* 2022 13:1 2022, 13 (1), 1–10. <https://doi.org/10.1038/s41467-022-32710-5>.

- (18) Hancock, A. M.; Swainsbury, D. J. K.; Meredith, S. A.; Morigaki, K.; Hunter, C. N.; Adams, P. G. Enhancing the Spectral Range of Plant and Bacterial Light-Harvesting Pigment-Protein Complexes with Various Synthetic Chromophores Incorporated into Lipid Vesicles. *J Photochem Photobiol B* 2022, 237, 112585. <https://doi.org/10.1016/J.JPHOTOBIOB.2022.112585>.
- (19) Hancock, A. M.; Son, M.; Nairat, M.; Wei, T.; Jeuken, L. J. C.; Duffy, C. D. P.; Schlau-Cohen, G. S.; Adams, P. G. Ultrafast Energy Transfer between Lipid-Linked Chromophores and Plant Light-Harvesting Complex II. *Physical Chemistry Chemical Physics* 2021, 23 (35), 19511–19524. <https://doi.org/10.1039/D1CP01628H>.
- (20) Liu, J.; Friebe, V. M.; Frese, R. N.; Jones, M. R. Polychromatic Solar Energy Conversion in Pigment-Protein Chimeras That Unite the Two Kingdoms of (Bacterio)Chlorophyll-Based Photosynthesis. *Nature Communications* 2020 11:1 2020, 11 (1), 1–12. <https://doi.org/10.1038/s41467-020-15321-w>.
- (21) S. Sardjan, A.; P. Westerman, F.; P. Ogilvie, J.; L. C. Jansen, T. Observation of Ultrafast Coherence Transfer and Degenerate States with Polarization-Controlled Two-Dimensional Electronic Spectroscopy. *J Phys Chem B* 2020, 124 (42), 9420–9427. <https://doi.org/10.1021/acs.jpcc.0c08126>.
- (22) Romero, E.; Prior, J.; Chin, A. W.; Morgan, S. E.; Novoderezhkin, V. I.; Plenio, M. B.; Van Grondelle, R. Quantum - Coherent Dynamics in Photosynthetic Charge Separation Revealed by Wavelet Analysis. *Sci Rep* 2017, 7 (1), 1–8. <https://doi.org/10.1038/s41598-017-02906-7>.
- (23) Gelzinis, A.; Augulis, R.; Butkus, V.; Robert, B.; Valkunas, L. Two-Dimensional Spectroscopy for Non-Specialists. *Biochim Biophys Acta Bioenerg* 2019, 1860 (4), 271–285. <https://doi.org/10.1016/j.bbabi.2018.12.006>.
- (24) Cao, J.; Cogdell, R. J.; Coker, D. F.; Duan, H. G.; Hauer, J.; Kleinekathöfer, U.; Jansen, T. L. C.; Mančal, T.; Dwayne Miller, R. J.; Ogilvie, J. P.; Prokhorenko, V. I.; Renger, T.; Tan, H. S.; Tempelaar, R.; Thorwart, M.; Thyryhaug, E.; Westenhoff, S.; Zigmantas, D. Quantum Biology Revisited. *Sci Adv* 2020, 6 (14), 1–12. <https://doi.org/10.1126/sciadv.aaz4888>.
- (25) Bolzonello, L.; Volpato, A.; Meneghin, E.; Collini, E. Versatile Setup for High-Quality Rephasing, Non-Rephasing, and Double Quantum 2D Electronic Spectroscopy. *Journal of the Optical Society of America B* 2017, 34 (6), 1223. <https://doi.org/10.1364/josab.34.001223>.
- (26) Brixner, T.; Mancal, T.; Stiopkin, I. V.; Fleming, G. R. Phase-Stabilized Two-Dimensional Electronic Spectroscopy. *J Chem Phys* 2004, 121 (9), 4221–4236. <https://doi.org/10.1063/1.1776112>.

- (27) Tekavec, P. F.; Myers, J. A.; Lewis, K. L. M.; Ogilvie, J. P. Two-Dimensional Electronic Spectroscopy with a Continuum Probe. *Opt Lett* 2009, *34* (9), 1390. <https://doi.org/10.1364/OL.34.001390>.
- (28) Tekavec, P. F.; Lott, G. A.; Marcus, A. H. Fluorescence-Detected Two-Dimensional Electronic Coherence Spectroscopy by Acousto-Optic Phase Modulation. *Journal of Chemical Physics* 2007, *127* (21), 214307. <https://doi.org/10.1063/1.2800560>.
- (29) Damtie, F. A.; Wacker, A.; Pullerits, T.; Karki, K. J. Two-Dimensional Action Spectroscopy of Excitonic Systems: Explicit Simulation Using a Phase-Modulation Technique. *Phys Rev A (Coll Park)* 2017, *96* (5), 053830. <https://doi.org/10.1103/PhysRevA.96.053830>.
- (30) Karki, K. J.; Widom, J. R.; Seibt, J.; Moody, I.; Lonergan, M. C.; Pullerits, T.; Marcus, A. H. Coherent Two-Dimensional Photocurrent Spectroscopy in a PbS Quantum Dot Photocell. *Nat Commun* 2014, *5* (1), 5869. <https://doi.org/10.1038/ncomms6869>.
- (31) Bolzonello, L.; Bernal-Texca, F.; Gerling, L. G.; Ockova, J.; Collini, E.; Martorell, J.; Van Hulst, N. F. Photocurrent-Detected 2D Electronic Spectroscopy Reveals Ultrafast Hole Transfer in Operating PM6/Y6 Organic Solar Cells. *Journal of Physical Chemistry Letters* 2021, *12* (16), 3983–3988. <https://doi.org/10.1021/acs.jpcllett.1c00822>.
- (32) Goetz, S.; Li, D.; Kolb, V.; Pflaum, J.; Brixner, T. Coherent Two-Dimensional Fluorescence Micro-Spectroscopy. *Opt Express* 2018, *26* (4), 3915. <https://doi.org/10.1364/oe.26.003915>.
- (33) Tiwari, V.; Matutes, Y. A.; Gardiner, A. T.; Jansen, T. L. C.; Cogdell, R. J.; Ogilvie, J. P. Spatially-Resolved Fluorescence-Detected Two-Dimensional Electronic Spectroscopy Probes Varying Excitonic Structure in Photosynthetic Bacteria. *Nat Commun* 2018, *9* (1), 4219. <https://doi.org/10.1038/s41467-018-06619-x>.
- (34) Mueller, S.; Draeger, S.; Ma, X.; Hensen, M.; Kenneweg, T.; Pfeiffer, W.; Brixner, T. Fluorescence-Detected Two-Quantum and One-Quantum-Two-Quantum 2D Electronic Spectroscopy. *Journal of Physical Chemistry Letters* 2018, *9* (8), 1964–1969. <https://doi.org/10.1021/acs.jpcllett.8b00541>.
- (35) Malý, P.; Lüttig, J.; Mueller, S.; Schreck, M. H.; Lambert, C.; Brixner, T. Coherently and Fluorescence-Detected Two-Dimensional Electronic Spectroscopy: Direct Comparison on Squaraine Dimers. *Physical Chemistry Chemical Physics* 2020, *22* (37), 21222–21237. <https://doi.org/10.1039/d0cp03218b>.
- (36) Karki, K. J.; Chen, J.; Sakurai, A.; Shi, Q.; Gardiner, A. T.; Kühn, O.; Cogdell, R. J.; Pullerits, T. Before Förster. Initial Excitation in Photosynthetic Light Harvesting. *Chem Sci* 2019, *10* (34), 7923–7928. <https://doi.org/10.1039/c9sc01888c>.

- (37) Perdomo-Ortiz, A.; R. Widom, J.; A. Lott, G.; Aspuru-Guzik, A.; H. Marcus, A. Conformation and Electronic Population Transfer in Membrane-Supported Self-Assembled Porphyrin Dimers by 2D Fluorescence Spectroscopy. *J Phys Chem B* 2012, *116* (35), 10757–10770. <https://doi.org/10.1021/jp305916x>.
- (38) John H. Golbeck. *Photosystem I*; Golbeck, J. H., Ed.; Advances in Photosynthesis and Respiration; Springer Netherlands: Dordrecht, 2006; Vol. 24. <https://doi.org/10.1007/978-1-4020-4256-0>.
- (39) Wientjes, E.; Croce, R. PMS: Photosystem i Electron Donor or Fluorescence Quencher. *Photosynth Res* 2012, *111* (1–2), 185–191. <https://doi.org/10.1007/s11120-011-9671-z>.
- (40) Nawrocki, W. J.; Jones, M. R.; Frese, R. N.; Croce, R.; Friebe, V. M. *In Situ Time-Resolved Spectroelectrochemistry Reveals Limitations of Biohybrid Photoelectrode Performance*; 2022. <https://doi.org/10.26434/CHEMRXIV-2022-1SX92>.
- (41) Baker, D. R.; Manocchi, A. K.; Lamicq, M. L.; Li, M.; Nguyen, K.; Sumner, J. J.; Bruce, B. D.; Lundgren, C. A. Comparative Photoactivity and Stability of Isolated Cyanobacterial Monomeric and Trimeric Photosystem i. *Journal of Physical Chemistry B* 2014, *118* (10), 2703–2711. <https://doi.org/10.1021/jp407948p>.
- (42) Manocchi, A. K.; Baker, D. R.; Pendley, S. S.; Nguyen, K.; Hurley, M. M.; Bruce, B. D.; Sumner, J. J.; Lundgren, C. A. Photocurrent Generation from Surface Assembled Photosystem i on Alkanethiol Modified Electrodes. *Langmuir* 2013, *29* (7), 2412–2419. <https://doi.org/10.1021/la304477u>.
- (43) Zhao, F.; Hardt, S.; Hartmann, V.; Zhang, H.; Nowaczyk, M. M.; Rögner, M.; Plumeré, N.; Schuhmann, W.; Conzuelo, F. Light-Induced Formation of Partially Reduced Oxygen Species Limits the Lifetime of Photosystem 1-Based Biocathodes. *Nat Commun* 2018, *9* (1), 1–9. <https://doi.org/10.1038/s41467-018-04433-z>.
- (44) Zhao, F.; Ruff, A.; Rögner, M.; Schuhmann, W.; Conzuelo, F. Extended Operational Lifetime of a Photosystem-Based Bioelectrode. *J Am Chem Soc* 2019, *141* (13), 5102–5106. <https://doi.org/10.1021/jacs.8b13869>.
- (45) Zhang, W.; Liu, M.; Zhang, P.; Yu, F.; Lu, S.; Li, P.; Zhou, J. Effects of Paraquat on Photosynthetic Pigments, Antioxidant Enzymes, and Gene Expression in *Chlorella Pyrenoidosa* under Mixotrophic Compared with Autotrophic Conditions. *Arch Environ Contam Toxicol* 2014, *67* (4), 593–600. <https://doi.org/10.1007/S00244-014-0067-X/FIGURES/4>.
- (46) Forouzesh, A.; Zand, E.; Soufizadeh, S.; Samadi Foroushani, S. Classification of Herbicides According to Chemical Family for Weed Resistance Management Strategies – an Update. *Weed Res* 2015, *55* (4), 334–358. <https://doi.org/10.1111/WRE.12153>.

(47) Zhao, F.; Plumeré, N.; Nowaczyk, M. M.; Ruff, A.; Schuhmann, W.; Conzuelo, F. Interrogation of a PS1-Based Photocathode by Means of Scanning Photoelectrochemical Microscopy. *Small* 2017, *13* (26), 1604093. <https://doi.org/10.1002/sml.201604093>.

(48) López-Ortiz, M.; Zamora, R. A.; Antinori, M. E.; Remesh, V.; Hu, C.; Croce, R.; Van Hulst, N. F.; Gorostiza, P. Fast Photo-Chrono-Amperometry of Photosynthetic Complexes for Biosensors and Electron Transport Studies. *ACS Sens* 2021, *6* (2), 581–587. <https://doi.org/10.1021/acssensors.1c00179>.

(49) Buesen, D.; Hofer, T.; Zhang, H.; Plumeré, N. A Kinetic Model for Redox-Active Film Based Biophotocathodes. *Faraday Discuss* 2019, *215* (0), 39–53. <https://doi.org/10.1039/c8fd00168e>.

(50) Torabi, N.; Qiu, X.; López-Ortiz, M.; Loznik, M.; Herrmann, A.; Kermanpur, A.; Ashrafi, A.; Chiechi, R. C. Fullerenes Enhance Self-Assembly and Electron Injection of Photosystem I in Biophotovoltaic Devices. *Langmuir* 2021, *37* (39), 11465–11473. <https://doi.org/10.1021/acs.langmuir.1c01542>.

(51) Gordiichuk, P.; Pesce, D.; Ocampo, O. E. C.; Marcozzi, A.; Wetzelaer, G. J. A. H.; Paul, A.; Loznik, M.; Gloukhikh, E.; Richter, S.; Chiechi, R. C.; Herrmann, A. Orientation and Incorporation of Photosystem I in Bioelectronics Devices Enabled by Phage Display. *Advanced Science* 2017, *4* (5), 1–7. <https://doi.org/10.1002/advs.201600393>.

(52) López-Ortiz, M.; Zamora, R. A.; Giannotti, M. I.; Hu, C.; Croce, R.; Gorostiza, P. Distance and Potential Dependence of Charge Transport Through the Reaction Center of Individual Photosynthetic Complexes. *Small* 2022, *18* (7), 1–9. <https://doi.org/10.1002/sml.202104366>.

(53) Tekavec, P. F.; Lott, G. A.; Marcus, A. H. Fluorescence-Detected Two-Dimensional Electronic Coherence Spectroscopy by Acousto-Optic Phase Modulation. *Journal of Chemical Physics* 2007, *127* (21), 214307. <https://doi.org/10.1063/1.2800560>.

(54) K. Manocchi, A.; R. Baker, D.; S. Pendley, S.; Nguyen, K.; M. Hurley, M.; D. Bruce, B.; J. Sumner, J.; A. Lundgren, C. Photocurrent Generation from Surface Assembled Photosystem I on Alkanethiol Modified Electrodes. *Langmuir* 2013, *29* (7), 2412–2419. <https://doi.org/10.1021/la304477u>.

(55) Mukherjee, D.; May, M.; Vaughn, M.; D. Bruce, B.; Khomami, B. Controlling the Morphology of Photosystem I Assembly on Thiol-Activated Au Substrates. *Langmuir* 2010, *26* (20), 16048–16054. <https://doi.org/10.1021/la102832x>.

(56) Volpato, A.; Bolzonello, L.; Meneghin, E.; Collini, E. Global Analysis of Coherence and Population Dynamics in 2D Electronic Spectroscopy. *Opt Express* 2016, *24* (21), 24773. <https://doi.org/10.1364/oe.24.024773>.

- (57) Paleček, D.; Edlund, P.; Gustavsson, E.; Westenhoff, S.; Zigmantas, D. Potential Pitfalls of the Early-Time Dynamics in Two-Dimensional Electronic Spectroscopy. *J Chem Phys* 2019, *151* (2), 024201. <https://doi.org/10.1063/1.5079817>.
- (58) Turner, D. B. D.; Wilk, K. E. K.; Curmi, P. M. G.; Scholes, G. D. Comparison of Electronic and Vibrational Coherence Measured by Two-Dimensional Electronic Spectroscopy. *J Phys Chem Lett* 2011, *2* (15), 1904–1911. <https://doi.org/10.1021/jz200811p>.
- (59) Tang, J.; Norrist, J. R. Linear Prediction Z-Transform (LPZ) Method, Padé Rational Approximation, and the Burg Maximum Entropy Extrapolation. *Journal of Magnetic Resonance (1969)* 1988, *78* (1), 23–30. [https://doi.org/10.1016/0022-2364\(88\)90153-9](https://doi.org/10.1016/0022-2364(88)90153-9).
- (60) Meneghin, E.; Leonardo, C.; Volpato, A.; Bolzonello, L.; Collini, E. Mechanistic Insight into Internal Conversion Process within Q-Bands of Chlorophyll a. *Sci Rep* 2017, *7* (1), 11389. <https://doi.org/10.1038/s41598-017-11621-2>.
- (61) Russo, M.; Casazza, A. P.; Cerullo, G.; Santabarbara, S.; Maiuri, M. Direct Evidence for Excitation Energy Transfer Limitations Imposed by Low-Energy Chlorophylls in Photosystem I-Light Harvesting Complex i of Land Plants. *Journal of Physical Chemistry B* 2021, *125* (14), 3566–3573. <https://doi.org/10.1021/acs.jpcc.1c01498>.
- (62) Akhtar, P.; Zhang, C.; Liu, Z.; Tan, H. S.; Lambrev, P. H. Excitation Transfer and Trapping Kinetics in Plant Photosystem I Probed by Two-Dimensional Electronic Spectroscopy. *Photosynth Res* 2018, *135* (1–3), 239–250. <https://doi.org/10.1007/s11120-017-0427-2>.
- (63) Russo, M.; Casazza, A. P.; Cerullo, G. Ultrafast Excited State Dynamics in the Monomeric and Trimeric Photosystem I Core Complex of *Spirulina Platensis* Probed by Two-Dimensional Electronic Spectroscopy COLLECTIONS. *J. Chem. Phys* 2022, *156*, 164202. <https://doi.org/10.1063/5.0078911>.
- (64) Akhtar, P.; Caspy, I.; Nowakowski, P. J.; Malavath, T.; Nelson, N.; Tan, H. S.; Lambrev, P. H. Two-Dimensional Electronic Spectroscopy of a Minimal Photosystem I Complex Reveals the Rate of Primary Charge Separation. *J Am Chem Soc* 2021, *143* (36), 14601–14612. <https://doi.org/10.1021/jacs.1c05010>.
- (65) Kühn, O.; Mančal, T.; Pullerits, T. Interpreting Fluorescence Detected Two-Dimensional Electronic Spectroscopy. *J Phys Chem Lett* 2020, *11* (3), 838–842. <https://doi.org/10.1021/acs.jpcclett.9b03851>.
- (66) Kunsel, T.; Tiwari, V.; Acosta Matutes, Y.; T. Gardiner, A.; J. Cogdell, R.; P. Ogilvie, J.; L. C. Jansen, T. Simulating Fluorescence-Detected Two-Dimensional Electronic Spectroscopy of Multichromophoric Systems. *J Phys Chem B* 2018, *123* (2), 394–406. <https://doi.org/10.1021/acs.jpcc.8b10176>.

(67) Grégoire, P.; Srimath Kandada, A. R.; Vella, E.; Tao, C.; Leonelli, R.; Silva, C. Incoherent Population Mixing Contributions to Phase-Modulation Two-Dimensional Coherent Excitation Spectra. *Journal of Chemical Physics* 2017, *147* (11). <https://doi.org/10.1063/1.4994987>.

(68) Kalaei, A. A. S.; Dامتie, F.; Karki, K. J. Differentiation of True Nonlinear and Incoherent Mixing of Linear Signals in Action-Detected 2D Spectroscopy. *Journal of Physical Chemistry A* 2019, *123* (19), 4119–4124. <https://doi.org/10.1021/acs.jpca.9b01129>.

(69) Baikie, T. K.; Wey, L. T.; Medipally, H.; Reisner, E.; Nowaczyk, M. M.; Friend, R. H.; Howe, C. J.; Schnedermann, C.; Rao, A.; Zhang, J. Z. Photosynthesis Re-Wired on the Pico-Second Timescale. 2022.

(70) Zhao, F.; Hardt, S.; Hartmann, V.; Zhang, H.; Nowaczyk, M. M.; Rögner, M.; Plumeré, N.; Schuhmann, W.; Conzuelo, F. Light-Induced Formation of Partially Reduced Oxygen Species Limits the Lifetime of Photosystem 1-Based Biocathodes. *Nat Commun* 2018, *9* (1), 1–9. <https://doi.org/10.1038/s41467-018-04433-z>.

(71) Nelson, N.; Junge, W. Structure and Energy Transfer in Photosystems of Oxygenic Photosynthesis. *Annu Rev Biochem* 2015, *84* (February), 659–683. <https://doi.org/10.1146/annurev-biochem-092914-041942>.

(72) Croce, R.; van Amerongen, H. Light Harvesting in Oxygenic Photosynthesis: Structural Biology Meets Spectroscopy. *Science* 2020, *369* (6506), eaay2058. <https://doi.org/10.1126/science.aay2058>.

The modulation is based on evolving individual phases of the 4 pulses at every laser repetition with a different step. Different combinations of modulation frequencies (f_n) are linked to different combination of phases of the response of the system, that in turn is connected to the response frequencies combinations : $\pm f_1 \pm f_2 \pm f_3 \pm f_4 \rightarrow \pm \varphi_1 \pm \varphi_2 \pm \varphi_3 \pm \varphi_4 \rightarrow \pm \omega_1 \pm \omega_2 \pm \omega_3 \pm \omega_4$. The table below summarize the different combination and frequencies.

component	divisors	Frequency (Hz)
<i>linear</i>		
f_{21}	6-0	250
f_{31}	8-0	333.33
f_{41}	9-0	375
f_{32}	8-6	83.33
f_{42}	9-6	125
f_{43}	9-8	41.66
<i>4th order</i>		
f_{reph}	-0+6+8-9	208.33
$f_{\text{non-reph}}$	-0+6-8+9	291.66
f_{2Q}	-0-6+8+9	458.33

SO, rephasing and non rephasing signals are extracted at 208.33 and 291.66 Hz respectively and the linear signal shown in the main text at 250 Hz.

SI6. Dazzler intensity artifact

It has been reported that Dazzler generates artifacts in population detected 2DES especially in the rephasing signal². This artifact affects the shape of the rephasing spectrum maps in time domain displaying a constant signal on the diagonal ($t_1=t_3$) and has shown to be constant also along the delay time t_2 . Potential artifacts have been limited comparing PEC2DES with a control signal measuring excitation intensity simultaneously acquired with a linear detector (see below). Uneven excitation is not responsible for the overall PEC2DES signal as photo-diode signal has a different shape with respect to photo-current response.

The Dazzler has limited capabilities in keeping constant intensity while changing phases of a quartet of pulse. This give rise to nonlinearities that are not dependent on the response of the sample but on the fluctuant intensity of excitation. This effect, mainly present in the rephasing signal, has already been reported in the PhD thesis of Roeding S. from the group of Brixner². They correct this effect by iteratively searching for intensity correction factor at any collection point, until a linear response sample gives no non-linear effect.

We adopted instead a a posteriori approach where we detect the linear response of a photodiode simultaneously with the experiment and making a properly normalized subtraction of the photodiode generated feature.

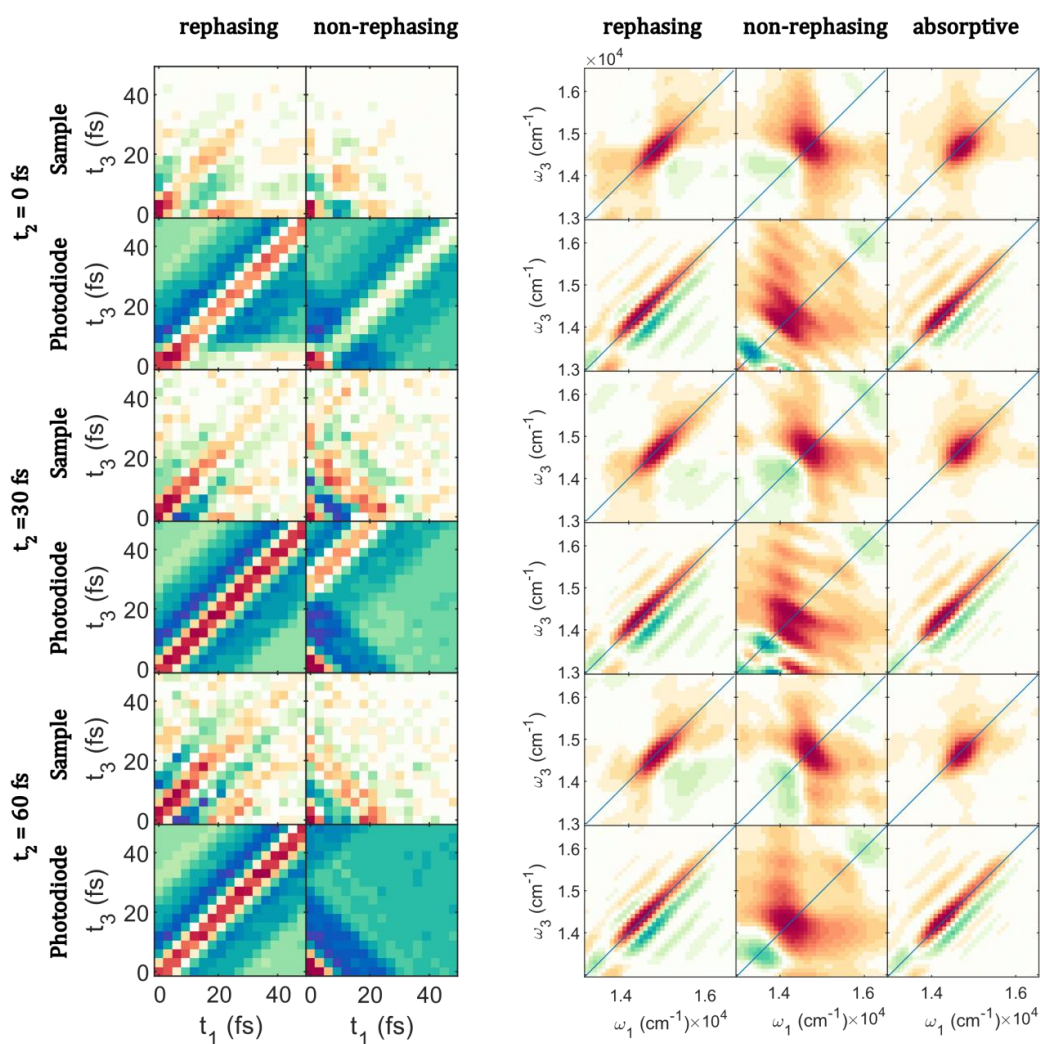


Figure S16-1 Signal coming from sample and photodiode at different t_2 . The time-dependent photodiode rephasing signal shows a constant feature along the diagonal that does not decrease increasing coherence times. This leads to a frequency dependent signal distributed along the diagonal that will depend on the coherence time range used. In the sample signal the photodiode collected artifact is removed, and the remaining signal decays showing the typical shape in the frequency domain. Moreover, note that in the time dependent non-rephasing the artifact disappears when t_2 is larger than coherence time range. In the frequency dependent non-rephasing the peak is shifted with respect to the sample confirming that the signal from the sample is not due to dazzler artifact.

S7. Incoherent mixing, linear reconstruction

Incoherent mixing is an effect that takes place when the detected signal is not proportional to the population generated by the quartet of pulses which is the first principle of population detected 2DES. This proportionality will not hold if excitons, or eventually charges, interact and annihilate between each other before being detected. In the latter case, part of the linear signal falls into the modulated detection frequencies of rephasing and non-rephasing signals. This contribution is constant along t_2 and thus would fit well our situation. The reconstructed linear signal into the 2D maps (see Supplementary below) has similar shape to rephasing and non-rephasing maps but is expected to have opposite sign. Moreover, the presence of the vibrational coherence and the different intensity of rephasing and non-rephasing signals suggest that, at least in part, non-linear signal is present in the detected frequencies. A way to evaluate the amount of coherent mixing is to compare the non-linear spectrum with the reconstructed linear on the t_1 - t_3 map using equations 28 and 29 found in Gregoire et al. paper³

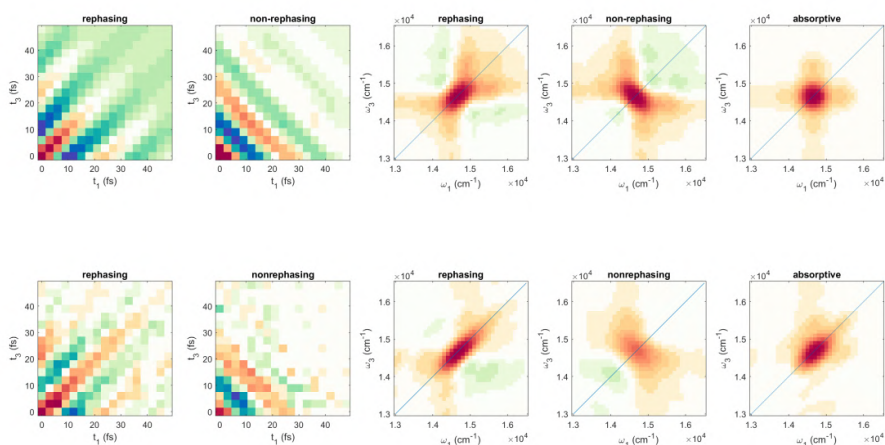


Figure S17-1 Linear signal reconstruction (top row) and actual acquired signal at $t_2 = 60$ fs (bottom row).

The comparison between the reconstructed linear signal and the acquired ones. The shapes of rephasing and non-rephasing are very similar in between each other. However, the intensity ratio between rephasing and non-rephasing is different (as expected for a non-linear response, because of the slower decay along coherence time of the rephasing signal) giving rise to different absorptive maps. The non-linear is indeed elongated along the diagonal.

Supplementary Figures

Supplementary Figure SF1: Custom electrochemical cell design

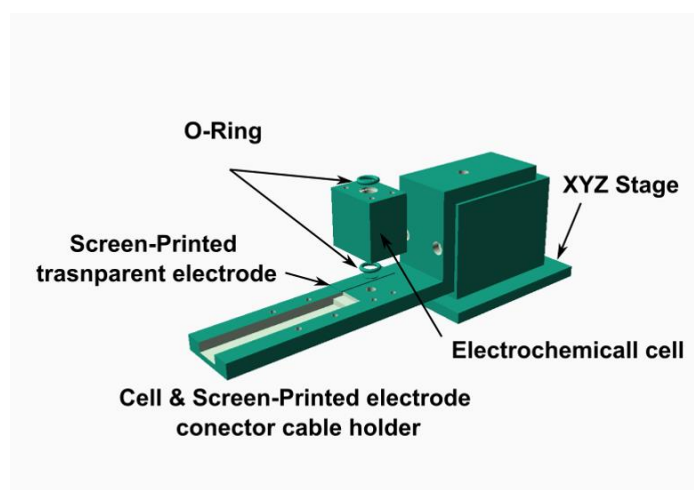


Figure SF1 Blueprint of electrochemical cell and screen-printed electrode holder adapted to spectro-electrochemical set-up.

Supplementary Figure SF2: Pulse compression

Pulse duration (~ 10 fs) was measured by exploiting standard sum frequency signal (FROG) generated on a $10 \mu\text{m}$ BBO crystal.

Chapter 7

Fast photochronoamperometry of photosynthetic complexes for biosensors and electron transport studies

Manuel López-Ortiz^a, Ricardo A. Zamora,^a Maria Elena Antinori^a, Vikas Remesh^b, Chen Hu^c, Roberta Croce^c, Niek F. van Hulst^{*c,d} and Pau Gorostiza^{*a,d}

^aInstitute for Bioengineering of Catalonia (IBEC), The Barcelona Institute of Science and Technology

^bThe Institute of Photonic Sciences (ICFO), The Barcelona Institute of Science and Technology

^cBiophysics of Photosynthesis. Dep. Physics and Astronomy, Faculty of Sciences, Vrije Universiteit Amsterdam

^dCatalan Institution for Research and Advanced Studies (ICREA)

* Corresponding author: pau@icrea.cat (P.G.)

1 Abstract

Photosynthetic reactions in plants, algae, and cyanobacteria are driven by photosystem I and photosystem II complexes, which specifically reduce or oxidize partner redox biomolecules. Photosynthetic complexes can also bind synthetic organic molecules, which inhibit their photoactivity and can be used both to study the electron transport chain and as herbicides and algicides. Thus, their development, characterization, and sensing bears fundamental and applied interest. Substantial efforts have been

devoted to developing photosensors based on photosystem II to detect compounds that bind to the plastoquinone sites of this complex. In comparison, photosystem I based sensors have received less attention and could be used to identify novel substances displaying phytotoxic effects, including those obtained from natural product extracts. We have developed a robust procedure to functionalize gold electrodes with photo- and redox-active photosystem I complexes based on transparent gold and a thiolate self-assembled monolayer, and we have obtained reproducible electrochemical photoresponses. Chronoamperometric recordings have allowed us to measure photocurrents in the presence of the viologen derivative paraquat at concentrations below 100 nM under lock-in operation and a sensor dynamic range spanning six orders of magnitude up to 100 mM. We have modeled their time course to identify the main electrochemical processes and limiting steps in the electron transport chain. Our results allow us to isolate the contributions from photosystem I and the redox mediator, and evaluate photocurrent features (spectral and power dependence, fast transient kinetics) that could be used as a sensing signal to detect other inhibitors and modulators of photosystem I activity.

2 Introduction

In nature, photosynthetic reactions are driven by two multiprotein complexes: Photosystem I (PSI) and Photosystem II (PSII). Both photosynthetic complexes have oxidoreductase functions capable of specifically reducing or oxidizing partner biomolecules. Despite their high specificity toward natural redox biomolecules like cytochromes, plastocyanin, and plastoquinone, both PSI and PSII can also bind synthetic organic molecules, which inhibit their photoactivity.¹ These compounds can be used both to dissect the photosynthetic electron transport chain and as herbicides and algicides, and thus their development, characterization, and sensing bear fundamental and applied interest. In the case of PSII, most herbicides compete for the binding sites of the plastoquinone (Q_A and Q_B). The binding of compounds such as triazine, triazinone, pyridazinone, benzothiadiazinone, nitrile, phenylpyridazine, and phenol derivatives at the Q_B site inhibits the electron transfer between primary quinone site Q_A (D_2 subunit) and Q_B site in the D_1 subunit.² Due to the affinity between PSII and this type of herbicide, many studies have been focused on developing PSII-based photosensors for the detection of these compounds. Alternatively, the structural similarity between plastoquinone binding sites of PSII and bacterial reaction center (RC)³ allows replacement of PSII with the more robust bacterial RC, in order to study herbicide performance. RC biosensor based strategies include RC absorption band bleaching⁴ and photoelectrochemical (PEC) sensing. In RC PEC biosensors, the decrease in photocurrent due to herbicide binding to RC is used to quantify analyte concentration.³ Synthetic compounds that interact with PSI have also been developed and used as herbicides. They are generally referred to as

PSI electron diverters. These molecules bind at the PsaC subunit of PSI, competing with the physiological redox partner ferredoxin (Fd) to uptake the photogenerated electrons from the F_B cluster, thereby preventing the generation of reducing power (NADPH) that is necessary to maintain normal cell function. Bipyridillium compounds of the Quat family (Paraquat, PQ; Diquat, DQ, and Ciperquat CQ) are viologen derivatives that can interact with PSI and prevent its normal oxidation via Fd.^{5,6} In particular, PQ (methyl viologen) has been extensively used in bioelectrochemical studies and in biohybrid devices as an artificial electron acceptor (redox mediator) of PSI photoactivated electrons. In contrast to PSII/ RC PEC biosensors where analyte concentration inhibits protein photoactivity, we propose a model system where PQ act as a redox mediator; therefore, in PSI based biosensor the photocurrent readout increases with analyte concentration. In PSI, the structural basis of photogeneration and separation of electron-hole pairs is relatively well understood.^{7,8} It acts as a photodiode that upon illumination shuttles electrons in one direction through its embedding membrane. Photoexcited electrons occupy high energy states at the chlorophyll special pair site (P700), where the separation from the vacancy states (holes) is initiated by means of a fast (10^{-8} - 10^{-7} s) electron transfer (ET) cascade.⁹ The process involves an electron transport chain of several protein cofactors, from P700 located at the luminal side of the complex toward the terminal iron sulfur cluster F_B at the stromal surface, which is the electron donor site to Fd and PQ (Figure 1A). Upon excitation of one of the pigments associated with PSI, the energy is quickly transferred to the reaction center, where it drives charge separation. The charge separated state, $P700^+/F_B^-$ has a recombination rate orders of magnitude smaller than charge transfer rates through the protein's electron transport chain. These two factors make PSI a very efficient photoconversion system with a quantum yield near 100%.¹⁰ As such, the PSI photoconversion capacity can be exploited as photoactive material in a PEC sensors if proper electrode functionalization can be achieved.¹¹ Increasingly efficient PSI biohybrid photoanodes have been developed by improving protein complex functionalization¹² and stability,¹³ enhancing ET between electrode and PSI with mediators, and avoiding short-circuiting recombination processes.¹⁴ These achievements have led to a 105-fold increase of photocurrent output from the first reported photocurrents¹⁵ of $0.1 \text{ nA}\cdot\text{cm}^{-2}$ and $10 \mu\text{A}\cdot\text{cm}^{-2}$.^{16,17} However, despite these achievements and notwithstanding that PSI has better protein stability, quantum yield, and more direct electronic coupling with electrodes than PSII, to our knowledge the use of PSI as a photoactive material for PEC biosensing has not been reported. In order to explore this possibility, we based our design on screen-printed gold transparent electrodes (AUTR10 MetrohmDropsens), which can be customized and coupled to a variety of measurement setups. In particular, we functionalized transparent gold electrodes with a thiolated self-assembled monolayer of 6-mercapto hexanol (MHO) prior to depositing the purified PSI protein complexes following the protocol described previously.^{18,19} The hydroxyl-terminated film interacts preferentially with the positively

charged luminal side of PSI and enables orientation of a PSI monolayer with a biased orientation with the P700 side pointing toward the electrode. This orientation facilitates direct electron transfer to P700^{15,18,20,21} and exposes the F_B site to the bulk solution.²² This arrangement allows transfer of electrons from F_B⁻ to acceptors in solution like the PQ²⁺/PQ⁺ couple, which acts as a redox mediator. Under aerobic conditions, reduced PQ⁺ rapidly transfer electrons to O₂ which plays the role of a sacrificial electron acceptor. Since the mediator does not have to be regenerated by the electrode, photocurrents can be achieved at fairly low potentials. However, the production of reactive superoxide O₂⁻ and hydrogen peroxide H₂O₂ species compromises biosensor durability due to damage by these reactive oxygen species (ROS).²³ In anaerobic systems, PQ regeneration at the electrode eventually short-circuits photogenerated charges back to the electrode, giving rise to a transient photocurrent characteristic of PSI-PQ-electrode ET processes.^{24,25} The photoelectrochemical behavior of PQ in solid PSI-based biohybrid systems has only been characterized with a temporal resolution in the range of seconds. However, recording transient photoresponses with submillisecond resolution (in well-defined PSI monolayer arrangements) and modeling the underlying photoelectrochemical processes are essential steps to understand their mechanisms, and to determine the necessary conditions for using PSI as a biophotosensor device, as well as to improve its performance. Thus, the aims of this work are (1) setting up a reproducible method to functionalize gold electrodes with photo- and redox-active PSI complexes to evaluate the feasibility of a PSI based biosensor under aerobic conditions, (2) using fast chronoamperometric recordings to measure photocurrent responses in anaerobic conditions with PQ²⁺/PQ⁺ as the only electron mediator, and (3) modeling the time course of the photoresponses as a means to identify the leading electrochemical processes and limiting steps in the ET chain. Our results allow evaluation of photocurrent features (spectral and power dependence, fast transient kinetics) that could be used as a sensing signal to detect inhibitors and modulators of PSI activity, including viologen-derived herbicides. We also modeled photocurrent transient signal to deconvolute contributions from PSI and redox mediator.

2.1 Sample Characterization: AFM and Spectral Dependence.

To evaluate our functionalization strategy, MHO-PSI gold electrodes were scanned with an atomic force microscope (AFM). AFM images were performed on an ultrathin gold substrate using an MFP-3D atomic force microscope (Asylum Research, Santa Barbara, CA) using V-shaped Si₃N₄ cantilevers with sharp silicon tips and having a nominal spring constant of 0.12 N·m⁻¹ (SNL, Bruker AFM Probes, Camarillo, CA). The AFM was operated in tapping mode in liquid, covering the sample with phosphate buffered saline (PBS, 50 mM). Scan of gold-MHO-PSI electrodes (Figure 1B) shows submonolayer substrate functionalization of approximately 6 nm thickness (Figure 1C) in agreement with previously reported gold- MHO-PSI assemblies.^{18,26} Surface coverage is estimated around 40%. Chronoamperometric measurements of PSI functionalized screenprinted

gold electrodes immersed in PBS buffer containing PQ 125 μM were performed in aerobic conditions in a Autolab (PGSTAT302N) potentiostat. Upon irradiation, PSI functionalized electrodes generate photocurrent. Photocurrent excitation spectra (Figure 1D) were recorded controlling the sample irradiation wavelength through acousto-optic tunable filtering of a broadband fiberlaser. The similarity between the photoconversion response of the sample and the PSI visible absorption spectrum measured in the bulk confirm that PSI molecules are responsible for the photoconversion ability of the electrode.

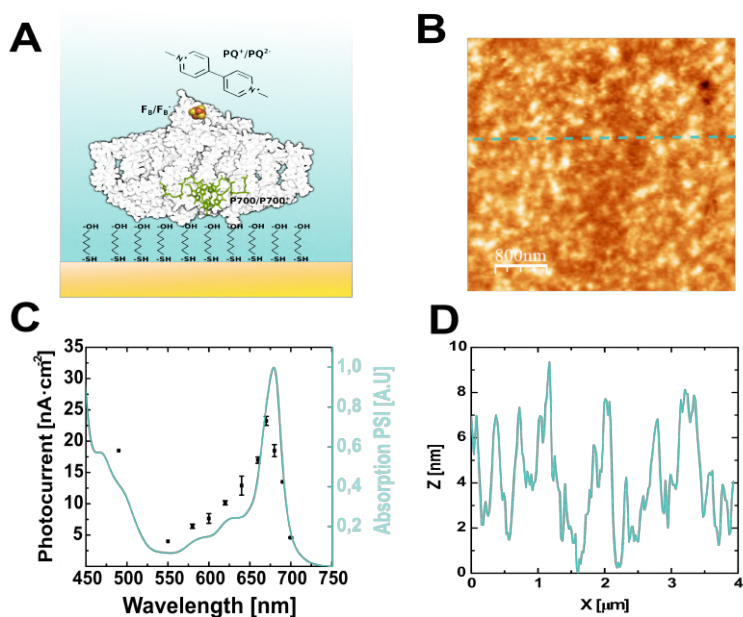


Figure 7.1: Au-MHO-PSI electrode characterization: (A) Scheme of gold functionalized with MHO-PSI protein complexes (PDB4XK8)²⁷. Redoxcofactors chlorophyll special pair, P700 and iron sulfur cluster, and F_B are shown in green wireframe and yelloworange spheres, respectively. (B) 4 μm scan of Au-6MHO-PSI samples, z-color scale 20 nm. (C) AFM profile height corresponding to the scan line marked with a dashed cyan line in (B). (D) Photocurrent-excitation (left axis, black dots) and absorption (right axis, cyan line) spectra of Au-MHO-PSI samples. Photocurrent data is issued from chronoamperometric measurements performed at a sample potential 50 mV w.r.t. the silver pseudo reference electrode.

3 results and discussion

3.1 Proof of Concept: Power Dependence and Sensing

Performance. Photocurrent features a transient response with a sharp peak of tens of $\text{nA}\cdot\text{cm}^{-2}$ followed by a steady photocurrent in the $\text{nA}\cdot\text{cm}^{-2}$ range (Figure 2A). In the investigated power range, we observe a linear photocurrent response with monochromatic

light power (Figure 2C). The maximum slope is observed at 690 nm and corresponds to a sensitivity of $0.2 \text{ nA}\cdot\text{mW}^{-1}$. Increasing PQ concentration increases the magnitude of the photocurrent, a property that can be exploited to probe the PQ concentration. To this end, in order to improve signal-to-noise ratio and simplify data analysis, the photocurrent signal was treated with a lock-in amplifier (Stanford Research instruments SR530) fed with the light source excitation frequency (Figure 2B). In the calibration curve (Figure 2C), no photocurrent saturation is observed up to 125 mM. Concentrations below the μM range are not detectable for direct chronoamperometric measurements, while lock-in detection allows one to probe PQ concentrations below $0.1 \mu\text{M}$. Concerning stability, the signal is reduced by 20% after 1 h of continuous operation in a 125 mM PQ solution in aerobic conditions.

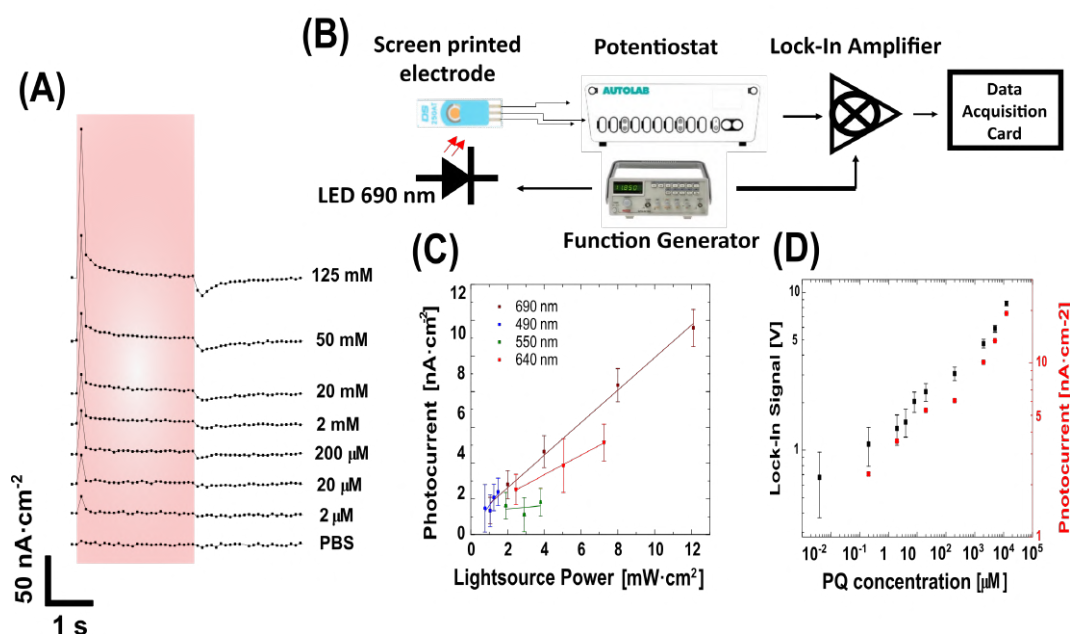


Figure 7.2: PSI-based PQ biosensor proof of concept. (A) Chronoamperometric data of Au-MHO-PSI samples at electrode potential 50 mV in PBS buffer 50 mM pH 7.4. Red background indicates irradiation with a 690 nm wavelength 375 mW LED. PQ concentration (125 mM, 50 mM, 20 mM, 2 mM, 200 μM , 20 μM , 2 μM , and PQ free) are indicated for each trace. (B) Measurement setup of lock-in detection strategy used to test biophotocathode PQ sensing performance (D). (C) Photocurrent response to light irradiated power in the sample. Broadband fiber laser is modulated to center excitation wavelength at 490 nm (blue), 550 nm (green), 640 nm (red), and 690 nm (brown). (D) PQ concentration calibration curve. Peak photocurrent (right axis, red) extracted from data in (A) and lock-in signal (left axis, black) response to LED excitation at 70 Hz.

3.2 Chopped Light Voltammetry: Transient Photocurrent

Dependence with Sample Potential. To get further insights into the photocurrent, samples were purged with Ar to remove O_2 , leaving PQ as the only electron acceptor in the system. In the cyclic voltammetry performed in the MHO functionalized electrode without PSI shown in Figure 3A (black trace), the reduction peak ($PQ^{2+} \rightarrow PQ^+$) can be observed at -900 mV/Ag and the corresponding oxidation peak ($PQ^+ \rightarrow PQ^{2+}$) at -815 mV/Ag. PSI incubation shifts the PQ's redox peaks to -765 and -700 mV/Ag, respectively, indicating an enhanced ET with the electrode (Figure 3A, blue trace). The widening of the CV for PQ in MHO-PSI compared to MHO microelectrode indicates an increased electrode capacity that can be attributed to the absorption of PSI complexes. Sample irradiation cycles give rise to photocurrent peaks. The photocurrent magnitude increases as sample potential approaches PQ redox potentials (Figure 3A, red trace). Remarkably, O_2 removal wipes out observed photocurrents at -50 mV/Ag in aerobic conditions. To recover the photocurrent signal, sample electrode must be polarized at least to -500 mV/Ag. In anaerobic conditions, observed photocurrents are significantly larger than in ambient conditions. In Figure 3B, we display chopped light linear voltammetry ranging from -450 mV/Ag to -900 mV/Ag, where sample irradiation has been indicated with red marker. A sudden increase in current is observed upon illumination accompanied by a negative peak that follows the end of the illumination cycle. Transient current amplitude and characteristic decay time are remarkably affected by sample electrode potential. Photocurrent vanish around the redox midpoint of PQ in the sample $V_{PQ} \approx -650$ mV. Below the redox midpoint the sign of the light switching current transients is inverted.

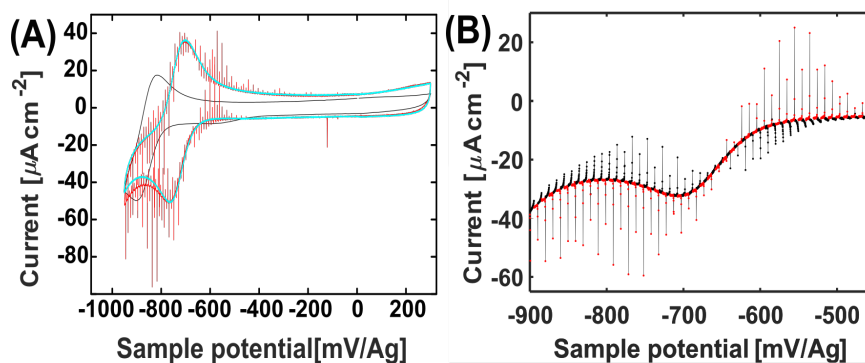


Figure 7.3: PSI photocurrent responses as a function of electrode potential. (A) Cyclic voltammetry of Au-SAM transparent electrodes prior to (gray trace) and after incubation (cyan trace) in PSI complex solution and wash (potential scan rate 50 mV/s). Au-SAM-PSI irradiated LED (690 nm, 340 mW photoswitch rate 50 ms, red trace). (B) Linear scan voltammetry of Au-SAM-PSI irradiated LED (690 nm, 340 mW photoswitch rate 300 ms). Illumination and dark conditions are indicated with red and black markers, respectively.

3.3 Fast Chronoamperometry: Empirical Characterization with Double Exponential Function.

To further quantify the PSI-PQ system's photocurrent transient behavior, we performed chrono-amperometry experiments for a set of fixed sample potentials (Figure 4A). This operation mode allowed a higher sampling rate (100 kHz) than cyclic voltammetry. As expected from chopped light CV, we observed a remarkable dependence with the applied sample potential in the magnitude, sign, and time course of the photoresponses, upon turning the LED on and off. Transient photocurrents were empirically fit using two exponential functions of opposite sign, yielding four fitted parameters for off-on (A_{ON+} , A_{ON-} , τ_{ON+} , τ_{ON-}) and four for on-off transitions (A_{OFF+} , A_{OFF-} , τ_{OFF+} , τ_{OFF-}).

$$j(t) = A_+ e^{\frac{-t}{\tau_+}} - A_- e^{\frac{-t}{\tau_-}}$$

An example fit is presented in Figure 4B, and the obtained parameters are shown in Figure 4C as a function of the electrode potential. The time constant of the positive component of the off-on transition (τ_{ON+}) shows a fast response with $1/\tau_+ 5 \text{ ms}^{-1}$ for $V < V_{PQ}$ that switches to slower process with $1/\tau_+ 1 \text{ ms}^{-1}$ as potential is increased above PQ redox midpoint. On the other hand, the negative component describes a slow process for $V < V_{PQ}$ that switches to a faster process $1/\tau_- 2 \text{ ms}^{-1}$ for $V > V_{PQ}$ (Figure 4C top, left). On- off transients display a similar behavior with opposite signs (Figure 4C top, right). Regarding A^+ and A^- amplitudes, transitions have similar magnitude ranging between 1 and $8 \mu\text{A}$ with opposite signs. We observe that on-off transition amplitudes are smaller for the on-off transition compared to the switching on transient (Figure 4C bottom).

3.4 Kinetic Model: Describe Mediator and PSI Cofactors Concentration.

The two-component fit of the photocurrent indicates that ET to and from the electrode take place simultaneously with $\text{PQ}^{2+}/\text{PQ}^+$ and PSI redox cofactors. To further elucidate the role of the PQ in the photocurrent generation, we have build a kinetic model describing the concentration of the redox actives species, namely: the redox cofactors in PSI P700/P700⁺ and F_B/F_B^- and with the mediator $\text{PQ}^{2+}/\text{PQ}^+$. The concentration of the species changes due to (i) photoexcitation, (ii) recombination, (iii) ET from F_B^- to PQ^{2+} , (iv) direct ET from the electrode to P700⁺, and (v) oxidation of PQ^+ and reduction of PQ^{2+} at the electrode. The ET rate with the electrode (iv and v) allow us to estimate the current. Modeled current is fitted to the experimental data adjusting the reaction constants of processes (i-v). The ET rate between $\text{PQ}^{2+}/\text{PQ}^+$ and the electrode depends on the electrode potential.

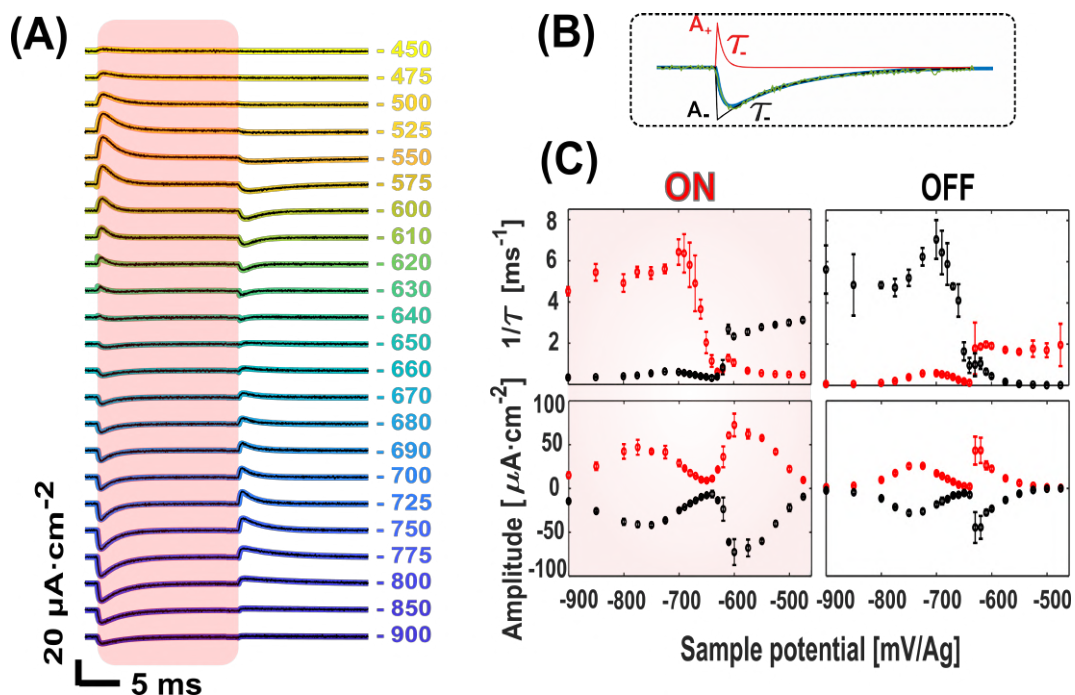


Figure 7.4: PSI photoresponse kinetics and empirical fits. (A) Fast photochronoamperometry traces of PSI-SAM-Au functionalized electrodes at different potentials (between 400 and 900 mV versus Ag electrode) and sampled at 100 kHz (or 10 μs resolution). Red box indicates the period of illumination with a 690 nm LED. (B) Each photocurrent trace could be fit (nonlinear least-squares method) with the sum of two exponential decay functions having different amplitudes and decay times ($A_{\text{ON}+}$, $A_{\text{ON}-}$, $\tau_{\text{ON}+}$, $\tau_{\text{ON}-}$, $A_{\text{OFF}+}$, $A_{\text{OFF}-}$, $\tau_{\text{OFF}+}$, $\tau_{\text{OFF}-}$). (C) Parameters obtained from fitting the traces of panel (A) as a function of the potential applied to the PSI-SAM electrode.

This behavior was modeled as a sigmoidal function of the sample potential centered at $V = V_{\text{PQ}}$, while the rest of the reaction rate parameters are potential-independent. Data sets corresponding to 14 different sample potentials ranging from -800 mV to -610 mV were simultaneously adjusted (Figure 5A). Similar kinetics models describing PSI photocurrents have been published previously.^{25,28-31} However, in our model we have not considered the mediator's diffusion. To assume this simplification, the thickness of the SAM-PSI monolayer in the system should be less than the typical diffusion length. This diffusion length can be calculated as $L = \sqrt{2DT}$, where T is a lower bound of the observed characteristic time of the PSI- PQ system (1 ms). Considering a coefficient of $10^{-6} \text{ cm}^2\cdot\text{s}^{-1}$ for PQ, the diffusion length obtained is 500 nm, which is significantly larger than the 6 nm layer thickness shown in Figure 1C and the reported Au-SAM-PSI monolayer.³² The major contribution to the current in our model is the electron exchange of the mediator with the electrode. Electrode potential determines the generation rates of oxidized/reduced PQ species. After an equilibration time, $\text{PQ}^{2+}/\text{PQ}^+$ relative concentration reaches a steady state. As the sample is irradiated,

this balance is altered by the sudden increase in PQ^+ produced by the ET from F_B^- to PQ^{2+} . For $V < V_{PQ}$ where the $PQ^{2+} + e^- \rightarrow PQ^+$ is the dominant reaction, the transient current is negative. On the other hand, for $V > V_{PQ}$, the favored process is $PQ^+ \rightarrow PQ^{2+} + e^-$ producing positive transient currents. Kinetic modeling output provides access to the relative concentrations of PQ^+/PQ^{2+} (Figure 5B, top row), excited $P700^+/P700$ and F_B^-/F_B (Figure 5B, middle row), and contributions to the current from PQ^{2+} , PQ^+ , and $P700^+$ (Figure 5B, bottom row). The PQ^+/PQ^{2+} relatively steady concentration (for $t = 0$ and $t \rightarrow \infty$) decreases as sample potential is increased. We observe that illumination (starting at $t = 0$) increases PQ^+/PQ^{2+} relative concentration for all potentials. This is due to the oxidation of F_B^- by PQ^{2+} producing PQ^+ . Notably, a light-induced PQ^+ increment with respect to steady concentration is more pronounced for $V > V_{PQ}$ with respect to $V < V_{PQ}$. We also note that F_B^-/F_B relative concentration is higher than $P700^+/P700$ for $V < V_{PQ}$, indicating that electrons are not efficiently withdrawn from the protein. This bottleneck effect is due to low PQ^{2+} concentration for $V < V_{PQ}$ where the main form of PQ is PQ^+ . On the other hand, for $V > V_{PQ}$, where PQ^{2+} is majority, $P700^+$ and F_B^- concentrations indicate that the electrons are drained from F_B^- by the PQ^{2+} forming PQ^+ as can be seen in the top right panel of Figure 5B. PQ^{2+} reduction at the electrode gives rise to a positive current (Figure 5B, red trace in bottom row) that cancels out the contribution of the current issued from the ET between the electrode and $P700^+$ (Figure 5B, green trace in bottom row).

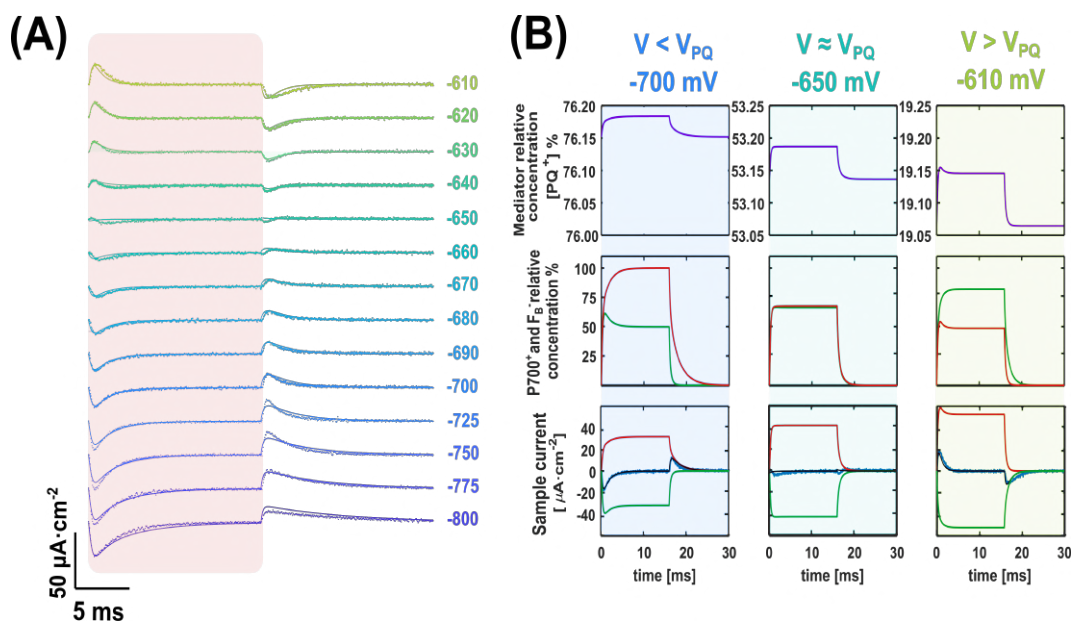


Figure 7.5: Kinetic model fit. (A) On (red shaded area) and off kinetic model fit of transient photocurrents. Applied sample potential (mV/Ag) is indicated for each trace. (B) PQ⁺ relative concentration for $V = 700$ mV/Ag (blue, left), 650 mV/Ag (aquamarine, middle), and 610 mV/Ag (light green, right) (top row). The same potentials, indicated with color boxes, are applied to the middle and bottom rows. P700⁺ (green trace) and F_B⁻ (red trace) are indicated as relative concentrations (middle row). Components of modeled transient current from PQ⁺/PQ²⁺ (red), P700⁺ (green), total modeled current (blue), and experimental data (black) (bottom row).

3.5 Considerations for Sensor Design and Optimization.

We have found several key advantages of transparent microelectrodes to sense PSI mediators like PQ: (1) they can operate with 10-100 μL of sample volume (corresponding to 1-10 nmol of analyte at 100 mM); (2) they produce faster photocurrent transients that require shorter integration time to be detected and would lead to faster responding sensors; (3) they are ready to use and help reduce variability in electrode preparation; (4) backside illumination is reproducible at the sensing surface, not subject to solution effects (absorption, scattering), and favors sensor robustness and compatibility with spectro-electrochemical measurements (UV-vis, Raman, NIR). Current efforts in the laboratory are directed at overcoming the limitations in the coupling of PSI to the electrode by improving the orientation and electrical connection of the complex.^{14,33} The direct ET functionalization strategy, employed in this work to simplify the system modelisation, can be replaced by a mediated ET strategy including redox polymers¹² or PSI partner proteins³⁴ increasing photocurrent signal and thus detection level. As can be seen in the photocurrent-power characterization (Figure 2C), photocurrent response does not saturate with light power in the explored regime, which suggests that photocurrent

signal can be further increased at higher illumination power. Enhanced detection sensitivity and faster responses can be achieved with redox polymer components and nanoscale junction geometries,³⁵ altogether these improvements may provide higher sensitivity and accuracy, and allow testing smaller analyte concentrations. This will allow screening a diversity of electron diverter analytes, including synthetic herbicides, analog compound libraries, redox protein partners and modulators, and, most interestingly, extracts of natural products to evaluate their use for sustainable weed control. Note that the use of a natural photosynthetic complex as the sensing element also avoids toxic components and potentially allows regeneration of the sensing surface, as shown in biophotovoltaic devices based also on PSI.³⁶

4 Conclusions

We have prepared electrodes functionalized with a SAM and photosystem I that allow sensing the presence of PQ in physiological conditions using photocurrent as sensing signal. We have characterized the power and spectral photocurrent response of the modified electrodes. The photocurrent spectra's correlation with the PSI absorption spectrum corroborates that in our biophotoelectrochemical sensor system, the photoconversion process is mediated by PSI. AFM characterization of the PSI incubated electrodes also suggests the functionalization of protein complexes on the gold electrode. The compact sensor setup built is based on transparent gold microelectrodes coated with fresh SAM, and PSI layers, with the built-in red LED behind a transparent electrode. Taking advantage of the widely characterized redox interaction between PSI and the herbicide PQ, our work represents the first systematic study on fast photocurrent transients in the millisecond range in this type of system. The observed transients can be fitted with a double exponential function, which indicates that both the PSI-mediated photoconversion process and the PQ recombination process can be clearly differentiated. We observe a change of behavior near the PQ redox potential. The characterization of the transients generated by PSI and PQ is relevant to design sensors with shorter integration times for electrochemical determinations. The kinetic model introduced in this work allows the identification and electrochemical evaluation of the different species involved in the detection process. This is an essential step to improve the performance of the photosystem I based sensor and to use it for the identification of other relevant inhibitors.

5 Acknowledgements

This research received funding from the Barcelona Institute of Science and Technology (Ignite program to N.F.v.H. and P.G.), from the Agency for Management of University and Research Grants (AGAUR of the Generalitat de Catalunya (CERCA

Programme; 2017-SGR-1442 and 2017-SGR-1369 grants; RIS3CAT plan), Fonds Européen de Développement Economique et Régional (FEDER) funds, MICINN (grants CTQ2016-80066-R and PID2019-111493RB-I00). R.Z. was supported by Becas Chile fellowship 74190117 from the government of Chile. N.F.v.H. acknowledges the financial support by the European Commission (ERC Advanced Grant 670949-LightNet), Spanish MICINN: PGC2018-096875-BI00 and “Severo Ochoa” program for Centers of Excellence in RD CEX2019-000910-S; Fundació Privada Cellex, and Fundació Privada Mir-Puig.

6 Bibliography

- (1) Ricardo, R.; Luiz, J.; Luiz, W. Photosynthetic Inhibitors. *Applied Photosynthesis* 2012,.
- (2) Lambrea, M. D.; Russo, D.; Polticelli, F.; Scognamiglio, V.; Antonacci, A.; Zobnina, V.; Campi, G.; Rea, G. *Curr. Protein Pept. Sci.* 2014, 15, 285295.
- (3) Swainsbury, D. J. K.; Friebe, V. M.; Frese, R. N.; Jones, M. R. Evaluation of a Biohybrid Photoelectrochemical Cell Employing the Purple Bacterial Reaction Centre as a Biosensor for Herbicides. *Biosens. Bioelectron.* 2014, 58, 172178.
- (4) Giustini, M.; Autullo, M.; Mennuni, M.; Palazzo, G.; Mallardi, A. Polymer-Photosynthetic Protein Multilayer Architectures for Herbicide Optical Detection. *Sens. Actuators, B* 2012, 163 (1), 6975.
- (5) Zhang, W.; Liu, M.; Zhang, P.; Yu, F.; Lu, S.; Li, P.; Zhou, J. Effects of Paraquat on Photosynthetic Pigments, Antioxidant Enzymes, and Gene Expression in *Chlorella Pyrenoidosa* under Mixotrophic Compared with Autotrophic Conditions. *Arch. Environ. Contam. Toxicol.* 2014, 67 (4), 593600.
- (6) Forouzesh, A.; Zand, E.; Soufizadeh, S.; Samadi Foroushani, S. Classification of Herbicides According to Chemical Family for Weed Resistance Management Strategies-an Update. *Weed Res.* 2015, 55 (4), 334358.
- (7) Croce, R.; van Amerongen, H. Light Harvesting in Oxygenic Photosynthesis: Structural Biology Meets Spectroscopy. *Science* 2020, 369 (6506).
- (8) Jumper, C. C.; Rafiq, S.; Wang, S.; Scholes, G. D. From Coherent to Vibronic Light Harvesting in Photosynthesis. *Curr. Opin. Chem. Biol.* 2018, 47, 3946.
- (9) Brettel, K.; Leibl, W. Electron Transfer in Photosystem I. *Biochim. Biophys. Acta, Bioenerg.* 2001, 1507 (13), 100114.

- (10) Nelson, N. Plant Photosystem I - The Most Efficient Nano- Photochemical Machine. *J. Nanosci. Nanotechnol.* 2009, 9 (3), 1709 1713.
- (11) Shu, J.; Tang, D. Recent Advances in Photoelectrochemical Sensing: From Engineered Photoactive Materials to Sensing Devices and Detection Modes. *Anal. Chem.* 2020, 92 (1), 363377.
- (12) Robinson, M. T.; Gizzie, E. A.; Mwambutsa, F.; Cliffel, D. E.; Jennings, G. K. Mediated Approaches to Photosystem I-Based Biophotovoltaics. *Current Opinion in Electrochemistry* 2017, 5 (1), 211217.
- (13) Zhao, F.; Ruff, A.; Rogner, M.; Schuhmann, W.; Conzuelo, F. Extended Operational Lifetime of a Photosystem-Based Bioelectrode. *J. Am. Chem. Soc.* 2019, 141 (13), 51025106.
- (14) Terasaki, N. PS-I and PS-II on Electrodes for Energy Generation and Photo-Sensor. *Lecture Notes in Energy* 2016, 32, 419449.
- (15) Ko, B. S.; Babcock, B.; Jennings, G. K.; Tilden, S. G.; Peterson, R. R.; Cliffel, D.; Greenbaum, E. Effect of Surface Composition on the Adsorption of Photosystem I onto Alkanethiolate Self-Assembled Monolayers on Gold. *Langmuir* 2004, 20 (10), 40334038.
- (16) Ciobanu, M.; Kincaid, H. A.; Lo, V.; Dukes, A. D.; Kane Jennings, G.; Cliffel, D. E. Electrochemistry and Photoelectrochemistry of Photosystem I Adsorbed on Hydroxyl-Terminated Monolayers. *J. Electroanal. Chem.* 2007, 599 (1), 7278.
- (17) Zhao, F.; Wang, P.; Ruff, A.; Hartmann, V.; Zacarias, S.; Pereira, I. A. C.; Nowaczyk, M. M.; Rogner, M.; Conzuelo, F.; Schuhmann, W. A Photosystem I Monolayer with Anisotropic Electron Flow Enables Z-Scheme like Photosynthetic Water Splitting. *Energy Environ. Sci.* 2019, 12 (10), 31333143.
- (18) Manocchi, A. K.; Baker, D. R.; Pendley, S. S.; Nguyen, K.; Hurley, M. M.; Bruce, B. D.; Sumner, J. J.; Lundgren, C. A. Photocurrent Generation from Surface Assembled Photosystem I on Alkanethiol Modified Electrodes. *Langmuir* 2013, 29 (7), 24122419.
- (19) López-Martínez, M.; López-Ortiz, M.; Antinori, M. E.; Wientjes, E.; Nin-Hill, A.; Rovira, C.; Croce, R.; Díez-Pérez, I.; Gorostiza, P. Electrochemically Gated Long-Distance Charge Transport in Photosystem I. *Angew. Chem., Int. Ed.* 2019, 58 (38), 13280 13284.
- (20) Ciobanu, M.; Kincaid, H. A.; Jennings, G. K.; Cliffel, D. E. Photosystem I Patterning Imaged by Scanning Electrochemical Microscopy. *Langmuir* 2005, 21 (2), 692698.

- (21) Leblanc, G.; Gizzie, E.; Yang, S.; Cliffel, D. E.; Jennings, G. K. Photosystem I Protein Films at Electrode Surfaces for Solar Energy Conversion. *Langmuir* 2014, 30 (37), 1099011001.
- (22) López-Martínez, M.; López-Ortiz, M.; Antinori, M. E.; Wientjes, E.; Nin-Hill, A.; Rovira, C.; Croce, R.; Díez-Pérez, I.; Gorostiza, P. Electrochemically Gated Long-Distance Charge Transport in Photosystem I. *Angew. Chem., Int. Ed.* 2019, 58 (38), 13280 13284.
- (23) Zhao, F.; Hardt, S.; Hartmann, V.; Zhang, H.; Nowaczyk, M. M.; Rogner, M.; Plumeré, N.; Schuhmann, W.; Conzuelo, F. Light- Induced Formation of Partially Reduced Oxygen Species Limits the Lifetime of Photosystem I-Based Biocathodes. *Nat. Commun.* 2018, 9 (1), 1
- (24) Zhao, F.; Plumeré, N.; Nowaczyk, M. M.; Ruff, A.; Schuhmann, W.; Conzuelo, F. Interrogation of a PS1-Based Photocathode by Means of Scanning Photoelectrochemical Microscopy. *Small* 2017, 13 (26), 18.
- (25) Buesen, D.; Hofer, T.; Zhang, H.; Plumeré, N. A Kinetic Model for Redox-Active Film Based Biophotoelectrodes. *Faraday Discuss.* 2019, 215 (i), 3953.
- (26) Mukherjee, D.; May, M.; Vaughn, M.; Bruce, B. D.; Khomami, B. Controlling the Morphology of Photosystem I Assembly on Thiol- Activated Au Substrates. *Langmuir* 2010, 26 (20), 1604816054.
- (27) Qin, X.; Suga, M.; Kuang, T.; Shen, J. R. Structural basis for energy transfer pathways in the plant PSI-LHCI supercomplex. *Science* 2015, 348 (6238), 989995.
- (28) Robinson, M. T.; Cliffel, D. E.; Jennings, G. K. An Electrochemical Reaction-Diffusion Model of the Photocatalytic Effect of Photosystem i Multilayer Films. *J. Phys. Chem. B* 2018, 122 (1), 117125.
- (29) Ciesielski, P. N.; Cliffel, D. E.; Jennings, G. K. Kinetic Model of the Photocatalytic Effect of a Photosystem i Monolayer on a Planar Electrode Surface. *J. Phys. Chem. A* 2011, 115 (15), 33263334.
- (30) Caterino, R.; Csiki, R.; Lyuleeva, A.; Pfisterer, J.; Wiesinger, M.; Janssens, S. D.; Haenen, K.; Cattani-Scholz, A.; Stutzmann, M.; Garrido, J. A. Photocurrent Generation in Diamond Electrodes Modified with Reaction Centers. *ACS Appl. Mater. Interfaces* 2015, 7 (15), 80998107.
- (31) Milano, F.; Ciriaco, F.; Trotta, M.; Chirizzi, D.; De Leo, V.; Agostiano, A.; Valli, L.; Giotta, L.; Guascito, M. R. Design and Modelling of a Photo-Electrochemical Transduction System Based on Solubilized Photosynthetic Reaction Centres. *Electrochim. Acta* 2019, 293, 105115.

- (32) Manocchi, A. K.; Baker, D. R.; Pendley, S. S.; Nguyen, K.; Hurley, M. M.; Bruce, B. D.; Sumner, J. J.; Lundgren, C. A. Photocurrent Generation from Surface Assembled Photosystem i on Alkanethiol Modified Electrodes. *Langmuir* 2013, 29 (7), 24122419.
- (33) Gordiichuk, P.; Pesce, D.; Ocampo, O. E. C.; Marcozzi, A.; Wetzelaer, G. J. A. H.; Paul, A.; Loznik, M.; Gloukhikh, E.; Richter, S.; Chiechi, R. C.; Herrmann, A. Orientation and Incorporation of Photosystem I in Bioelectronics Devices Enabled by Phage Display. *Advanced Science* 2017, 4 (5), 17.
- (34) Ciornii, D.; Kolsch, A.; Zouni, A.; Lisdat, F. A Precursor- Approach in Constructing 3D ITO Electrodes for the Improved Performance of Photosystem I-Cyt c Photobioelectrodes. *Nanoscale* 2019, 11 (34), 1586215870.
- (35) Forzani, E. S.; Zhang, H.; Nagahara, L. A.; Amlani, I.; Tsui, R.; Tao, N. A Conducting Polymer Nanojunction Sensor for Glucose Detection. *Nano Lett.* 2004, 4 (9), 17851788.
- (36) Qiu, X.; Castaneda Ocampo, O.; De Vries, H. W.; Van Putten, M.; Loznik, M.; Herrmann, A.; Chiechi, R. C. Self-Regenerating Soft Biophotovoltaic Devices. *ACS Appl. Mater. Interfaces* 2018, 10 (43), 3762537633.

SUPPLEMENTARY INFORMATION FILE

Fast photo-chrono-amperometry of photosynthetic complexes for biosensors and electron transport studies

Manuel López-Ortiz^{1,2}, Ricardo A. Zamora^{1,2}, Vikas Remesh³, Chen Hu⁴, Roberta Croce⁴, Niek van Hulst^{3,5}, Pau Gorostiza^{1,2,5,*}

1. IBEC - Institute for Bioengineering of Catalonia, the Barcelona Institute for Science and Technology, Baldiri Reixac 15-21, Barcelona 08028

2. CIBER-bbn - Network Biomedical Research Center in Biomaterials, Bioengineering and Nanomedicine.

3. ICFO - The Institute of Photonic Sciences, The Barcelona Institute of Science and Technology, 08860 Castelldefels (Barcelona), Spain.

4. Department of Physics and Astronomy and Institute for Lasers, Life and Biophotonics, Faculty of Sciences, Vrije Universiteit Amsterdam, De Boelelaan 1081, 1081 HV Amsterdam, The Netherlands.

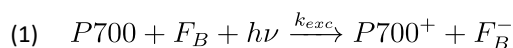
5. ICREA - Catalan Institution for Research and Advanced Studies, 08020 Barcelona Spain

(*) Correspondence to pau@icrea.cat

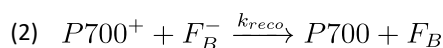
1. Kinetic Model

The model describes the concentration of the reaction kinetics of the involved species, namely PSI redox cofactors: chlorophyll special pair P700-P700⁺, iron sulfur cluster F_B-F_B⁻ and the paraquat analyte/redox mediator PQ⁺-PQ²⁺. The reactions, with rate k_x, are described below:

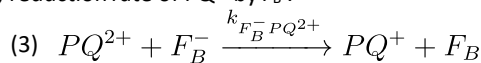
k_{exc}, photo-excitation rate of P700-F_B couple:



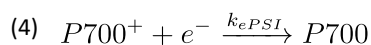
k_{reco}, recombination rate of P700⁺-F_B⁻ couple:



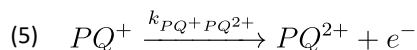
k_{FB-PQ2+}, reduction rate of PQ²⁺ by F_B⁻:



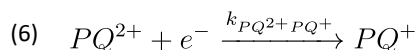
k_{ePSI}, electron transfer rate between electrode and P700⁺:



k_{PQ2+PQ+}, PQ reduction rate at the electrode:



k_{PQ+PQ2+}, PQ oxidation rate at the electrode:



For the last two rates (PQ electron transfer rate with the electrode) the dependence with the applied potential has been modeled empirically using sigmoidal functions (equations 7-8), where k_{PQ} is an effective rate; V is the applied voltage w.r.t. Ag electrode; V_{PQ} is the measured redox mid-point $V_{PQ} \sim -650$ mV/Ag; and α, β , are two fitting parameters with $1/V$ units.

$$(7) \quad k_{PQ+PQ^{2+}} = \frac{k_{PQ}}{1 + e^{\alpha(V-V_{PQ})}}$$

$$(8) \quad k_{PQ+PQ^{2+}} = \frac{k_{PQ}}{1 + e^{-\beta(V-V_{PQ})}}$$

The kinetic equations describe the rate of change in the concentrations of the species due to reactions (1-6):

$$(9) \quad \frac{d([P700])}{dt} = -k_{exc}[P700][F_B] + k_{reco}[P700^+][F_B^-] + k_{ePSI}[P700^+]$$

$$(10) \quad \frac{d([Fb])}{dt} = -k_{exc}[P700][F_B] + k_{reco}[P700^+][F_B^-] + k_{F_B^-PQ^{2+}}[F_B^-][MV^+]$$

$$(11) \quad \frac{d([P700^+])}{dt} = +k_{exc}[P700][F_B] - k_{reco}[P700^+][F_B^-] - k_{ePSI}[P700^+]$$

$$(12) \quad \frac{d([F_B^-])}{dt} = -\frac{d([F_B])}{dt}$$

$$(13) \quad \frac{d([PQ^{2+}])}{dt} = -k_{PQ^{2+}PQ^+}[PQ^{2+}] + k_{PQ+PQ^{2+}}[PQ^+] - k_{F_B^-PQ^{2+}}[F_B^-][PQ^{2+}]$$

$$(14) \quad \frac{d([PQ^+])}{dt} = -\frac{d([PQ^{2+}])}{dt}$$

In the absence of diffusion, the current flowing through the electrode is due to the charge exchange of the electrode with the redox species described by reactions (equations 4-6). To compute current density j the rates of charges flowing from (positive sign, equation 4 and 6) and to (negative sign, equation 5) are summed (equation 15) where e denotes electron charge, V cell volume, and S the electrode surface.

$$(15) \quad j = \frac{eV}{S} (k_{PQ^{2+}PQ^+}[PQ^{2+}] + k_{ePSI}[P700^+] - k_{PQ+PQ^{2+}}[PQ^+])$$

The differential equation system (7-14) is solved numerically using MATLAB© ode23tb solver, an implicit Runge-Kutta algorithm suitable for stiff problems. All the reaction rates and α, β parameters are fit to minimize the square error between modeled and experimental current density with a non-linear least square algorithm (trust region reflective).

Chapter 8

Summary of the obtained results

The core of this dissertation deals with interprotein electron transfer (ET), that is canonically described by diffusion, binding, and actual charge exchange stages. For my thesis, I have focused on the binding and charge exchange steps. I consider that the most relevant contribution within the manuscript is the study of the charge exchange stage. Interprotein ET is key for two essential cell process, cell respiration and photosynthesis. In this thesis, I have exploited photosystem I (PSI) as model system while plastocyanin (Pc) is employed as cognate redox partner for ET. For the PSI-Pc pair, I have studied the distance- and potential-dependence of the interprotein charge exchange, the conductance of the PSI-Pc complex, and their binding process. Additionally, taking advantage of the acquired know-how studying ET in PSI, I have developed a biohybrid herbicide biosensor and, in collaboration with the institute of photonic sciences (ICFO), we have developed a set-up for photo-electrochemical current (PEC) detected two-dimensional spectroscopy (2DES), that we have named PEC2DES.

In summary, throughout this thesis I have studied different facets of the PSI complex: the ET within PSI, the inter-protein ET with Pc, the binding regulation with Pc and the light absorption and EET within the photosystem. In addition, an application perspective is explored in chapter 7. In the following, I will highlight and summarize the results and achievements obtained throughout my thesis. For the sake of clarity, I have expressed them in a bullet list format indicating the experimental observations (o_i) and the interpretation of these observations (i_i).

Chapter 3: Distance and Potential Dependence of Charge Transport Through the Reaction Centre of Individual Photosynthetic Complexes

In Chapter 3, I developed a molecular strategy to functionalize gold electrodes with plant PSI complexes. Unidirectional robust functionalization of PSI complexes was the requisite for single protein experiments in chapters 3-5 and for PEC2DES experiments in chapter 6.

To test this functionalization strategy, the samples were characterized with bulk photo-electrochemistry and nanoscale imaging:

o_i PSI complexes remain fully functional in [-200, 300] mV/SSC window.

o_{ii} Individual PSI complexes show lateral sizes in agreement with the crystallographic dimensions of PSI.

o_{iii} PSI complexes are bound via their stromal side and expose the luminal side (P700, Pc binding site) to the solution.

With this set up, I evaluated the PSI apparent height and the current-distance decay constant β .

o_{iv} The apparent height is electrochemically gated for ECSTM probe potentials, with a maximum value around 400 mV/SSC.

o_v The β -values depend on the probe potential and display a minimal value at 400 mV/SSC.

o_{vi} The β dependence with the probe potential is observed only if the PSI electrode is in a potential range able to generate photocurrent in bulk experiments.

Given the bias sign, the studied process corresponds to hole injection into an electronic state that is available in the absence of illumination.

i_l I propose that a pair of tryptophan residues (Trp625, Trp658) located near P700 and known to integrate the hydrophobic recognition site for Pc may have an additional role as hole exchange mediator.

Chapter 4: The protein matrix of plastocyanin supports long-distance charge transport with photosystem I and the copper ion regulates its spatial span and conductance.

I have characterized the ETp between PSI and Pc, both forming a complex or located at a distance. I have measured the distance dependence and conductance of the interprotein charge exchange between suitably oriented PSI and Pc using current-distance and

blinking techniques. I assessed the spatial span of the protein charge exchange and the formation of spontaneous protein junctions. In particular, I consider the following observations are relevant for discussion:

o_i Charge exchange between a bare electrode and either individual PSI or Pc spans for several nm. This observation agrees with previous results of the group with Az,⁸⁷ PSI complexes,²²² and cytochrome subunits from the respiratory chain^{223,224}

o_{ii} When Pc faces a non-homologous peptide sequence, the presence of the Cu ion in Pc_{holo} increases the charge exchange distance, as it occurs with Cu-Az with respect to redox inactive Zn-Az.⁸⁷

o_{iii} For the PSI/Pc cognate pair, charge-exchange is longer for Pc_{apo} than for Pc_{holo} when the electron flow is biased in the physiological direction (from Pc to PSI). If the electrons flow from PSI to Pc, the β value is similar for Pc_{apo} and Pc_{holo}.

o_{iv} The conductance of the PSI-Pc transient complex is higher for Pc_{apo} with respect to Pc_{holo}

o_v The high conductance peak of PSI-Pc_{apo} for negative bias has the same value as PSI-Pc_{holo} for positive bias.

o_{vi} In blinking experiments, we have identified a short lifetime (ms scale) associated with low conductance value compatible with the conductance of water molecules trapped in the tunnelling junction.

Based on these observations, I suggest four interpretations (*i_i-i_{iv}*):

i_i The redox centre is not essential for remote or complex bound interprotein charge exchange provided that charges are supplied by the electrodes. (*o_{ii}-o_v*). We suggest that the lower conductance and spatial span of PSI/Pc_{holo} (*o_{iii},o_v*) is due to charge localization in Cu atom reducing extension of the electronic coupling between cognate protein structures. This implies that protein structures play an active role in the interprotein electronic coupling and would not be restricted to the redox centres. We tentatively associate the protein induced electronic coupling to the residues responsible for long-range electrostatic interactions.

i_{ii} Localized electronic states associated to water molecules (*o_{vi}*) play the role of bridge states in long-range charge exchange (*o_i*).

i_{iii} We suggest that voltage induced charge delocalization of the bridge states¹⁸⁴ (*i_{ii}*) is responsible for the observed long-range charge exchange (*o_i*).

This voltage-induced extension of the bridge-mediated electronic coupling would be facilitated by the Gouy-Chapman conduit formed upon cation depletion of the interprotein domain.

i_{iv} If the observed charge-exchange distances in the ECSTM set-up were held under physiological conditions, cognate protein binding would not be essential for ET (*o_i*). We thus envisage binding as a regulatory mechanism for ET rates rather than a necessary condition for ET. In this sense, we interpret the shorter range of PSI/Pc_{holo} charge exchange vs PSI/Pc_{apo} (*o_{iii}*) as a regulatory function of the Cu atom that favours specific and short-range interactions vs unspecific and long -range interactions, in addition to its charge carrying function.

Chapter 5: Light- and redox-dependent force spectroscopy reveals that the interaction between plastocyanin and plant photosystem I is favored when one partner is ready for electron transfer.

In Chapter 5, the binding of individual PSI/Pc complexes has been evaluated by means of SMFS. The binding probability was estimated as the ratio of SMFS curves displaying adhesion events. The redox states of PSI and Pc were orthogonally controlled by illumination and a reducing agent preferential for Pc. Our results indicate that the binding frequency between PSI and Pc is related to their respective redox states.

o_i The frequency of interaction between PSI and Pc is higher when at least one of the partners is in an ET-ready redox state, and the post-ET situation (PSI_{Red}-Pc_{Ox}) leads to disfavoured binding.

o_{ii} The binding of ET-ready Pc_{Red} to PSI can be regulated externally by Mg²⁺ ions in solution.

Chapter 6: Photoelectrochemical two-dimensional electronic spectroscopy (PEC2DES) of photosystem I to study charge separation dynamics in photosynthesis.

In this chapter, we have developed a photoelectrochemical current 2d-electronic spectroscopy set-up for photosynthetic light-harvesting proteins, using PSI as model system. Our contribution to this collaboration has been the photoelectrochemical detection and the biohybrid electrode preparation as well as photocurrent output characterization.

o_i PSI complexes tethered to gold electrodes yield transient photo-electrochemical currents with 10 $\mu\text{A}\cdot\text{cm}^{-2}$ amplitude in ms pulses making this signal suitable for kHz spectroscopic experiments.

o_{ii} Photo-electrochemical current amplitude is stable for several hours under experimental conditions.

o_{iii} We estimate that ~40 % of PSI complexes deliver charge for each pulsed irradiation.

The PEC2DES maps in the accessible experimental delay time (t_2 max = 450 fs) yield two observations.

o_{iv} Coherent associated spectra (CAS) maps reveal a coherence centered at 750 cm^{-1} .

o_v No features of decay of the signal in DAS maps are observed within 450 fs.

These results disagree with previously reported 2DES spectra of PSI complexes. However, there are two significant differences between PEC2DES and conventional 2DES. First, PEC2DES exploits 4 pulses population detection scheme while standard 2DES makes use of 3-pulses scheme detecting 3rd order polarization. Secondly, PEC2DES is exclusively sensitive to de-excitation pathways leading to effective charge separation (CS). We thus interpret:

i_i 4-pulse collinear configuration leads to signal cancelation of excited states absorption (ESA) I and ESA II pathways, leaving ground state bleaching (GSB) and stimulated emission (SE) channel as the sole non-linear effect detectable within 450 fs. However due to PSI architecture with hundreds of chlorophylls and a single CS site, the SE path is very unlikely. On the other hand, GSB signal decays with turn-over rate in ms timescale and is thus not observable in the experimental window (450 fs).

i_{ii} It has been recently suggested that charge transfer states of chlorophylls located near the PSI complex surface might quench excitations.² However, in absence of the electron transport chain draining separated charges from P700, recombination rates of outer chlorophyll CS might outcompete direct ET making this de-excitation pathway undetectable by photo-electrochemical current.

Chapter 7: Fast Photo-Chrono-Amperometry of Photosynthetic Complexes for Biosensors and Electron Transport Studies

In this chapter, I presented a proof-of-concept PSI-based herbicide biosensor that detects the concentration of the electro diverter herbicide paraquat (PQ). The detection is based on the electrochemical photocurrent output of the device. The transient photocurrent signal at different electrode potentials was characterized and modelled.

o_i PQ concentrations on the μM range are detectable in the raw photocurrent signal. Making use of the lock-in detection strategy, concentrations down to 10 nM are detected.

o_{ii} In the absence of other redox mediators (anaerobic conditions), the transient photocurrent sign is inverted for sample potentials below and above the PQ redox mid-point.

Chapter 9

Discussion

The common ground holding the experimental work presented throughout this dissertation is the PSI complex from higher plants. All experiments have been performed on PSI samples extracted from *Arabidopsis Thaliana* leaves and purified from thylakoid extracts by my colleague Chen Hu working in *Biophysics of Photosynthesis* group lead by Roberta Croce in the *Vrije Universiteit* in Amsterdam.

Throughout the dissertation, the same object of study, PSI, is addressed from different perspectives and experimental approaches. We have paid special attention to the ET between PSI and its redox cognate Pc. As I outlined previously, canonical ET is described by protein diffusion, long-range recognition, complex rearrangement, and “actual” electron transfer. I remark that, to my knowledge, there are no different terms in the scientific literature vocabulary to precisely distinguish the whole interprotein charge exchange process from the eventual charge transfer step. I interpret that this lack of nomenclature is partly due to the limited experimental tools to tell apart the contribution of the different stages (long-range interactions, encounter complex formation, reorganization, charge transfer, and unbinding) to the overall process. To fill this gap, the aim of chapters 4 and 5 was to study the charge exchange and the binding stages, respectively.

In chapters 3 and 4, I sought to understand how holes are injected into PSI by a bare ECSTM probe (chapter 3) and how electrons and holes are exchanged with PSI by a probe decorated with Pc (chapter 4). Specifically, I focused on charge exchange with the PSI luminal side harbouring the chlorophyll special pair P700/P700⁺. This orientation-specific experiment was possible thanks to the peptide pIQAcys, that links the PSI stromal side and the gold electrode. Peptide-protein assembly and functionality essays carried out in chapter 3, have been the starting point for PSI experiments throughout most of the manuscript (chapters 3-7). The hole injection was scrutinized by

sweeping the Fermi energy of the probe and sample electrodes to match the molecular energy levels of the interfacing protein cofactors. To interpret our results, I hypothesize that energy alignment with the aromatic tryptophan residues lying at the Pc-binding surface of PSI facilitate long distance charge exchange with the ECSTM probe.

Since protein–protein interactions involved in ET (including those in the photosynthetic electron transfer chain) display weak dissociation constants and are transient in nature compared to most biochemical interactions, in this Thesis I made special emphasis in time-resolved methods at the single molecule level that could capture properties of the interactions that were previously not accessible. ET proteins form highly transient complexes that are just specific enough to allow electron exchange but prioritize rapid dissociation and turnover. Thus, they are difficult to follow using bulk methods including crystallography.

In chapter 4, I have studied PSI charge-exchange with its redox cognate partner Pc at distance (current-distance spectroscopy experiments) and in bound (blinking experiments) configurations. In both cases, interprotein charge-exchange is driven by the bias potential set between the ECSTM electrodes. The charge flow between an electrode pair bridged by a single protein or a protein monolayer is referred to as Electron Transport (ETp). This situation differs from physiological interprotein electron transfer (ET) between diffusible and membrane-tethered proteins which is driven by the free energy reduction as the electron is transferred between the cognate redox centres. It is unclear whether the results in ETp configuration in ECSTM experiments can be directly correlated to the physiological ET process. However, ETp results provide valuable insights to the ET process, and to our knowledge, it is the only experimental approach allowing to control interprotein orientation, distance, and redox state while simultaneously tracking the charge exchange process. Thus, our novel single-molecule interprotein ETp setup and results have intrinsic and complementary value to bulk intraprotein ET experiments reported previously using protein film voltammetry of electrodes coated with self-assembled monolayer spacers,^{117, 195, 196} flash photolysis rate measurements in redox proteins modified site-specifically with ruthenium complexes,^{?, 154, 190–193} and single-molecule STM experiments based on imaging.^{173, 186, 187}

In addition, ETp configuration allowed to study the charge exchange between PSI and Cu-free Pc_{apo}, that is in principle impossible in ET configuration. Comparing Pc_{apo} and Pc_{holo}, I'm able to set apart the role of the redox centre in charge exchange with PSI partner.

In blinking experiments, PSI and Pc transiently form a complex that bridges the gap between the electrodes. Picturing the PSI/Pc complex as a protein “wire”, I studied the ETp process responsible for the conductance of the junction. In this configuration, I have observed that the conductance of PSI/Pc_{apo} is higher than PSI/Pc_{holo}, leading to

the conclusion that the redox centre, which is essential for ET, charge storage, and carriage, is not necessary for ETp, which can still proceed *via* the protein matrix and through the aqueous solution.^{223,224} This seemingly reasonable result had so far escaped experimental determination.

In current-distance spectroscopy, proteins are generally separated by the electrolytic aqueous medium. It is thus unclear whether the underlying mechanisms of reported ETp results (which are obtained with proteins wired to electrodes, see section 5 in the introduction) involve electrolyte-mediated charge exchange, especially regarding the long-range charge exchange observed here. If ET instead of ETp mechanisms are taking place, I consider two hypotheses that can explain the observed long-range charge exchange in our experiments. One possibility is that following a tunnelling-based mechanism (super-exchange, flickering resonance, hopping or non-perturbative models described in the introduction), electrons are transferred in a single or sequential steps along several nm through the interprotein medium. This would require the presence of bridge electronic states in the interprotein medium,^{184,185} otherwise the accessible tunnelling range for a single tunnelling step is limited (< 2.5 nm). Another possibility is that the molecules present in the solution could facilitate the charge exchange. ET assisted by protons, dissolved oxygen or reactive oxygen species, or ions in solution could be responsible for the observed long-range ET. Regarding the role of ions in solution, decreasing the ionic strength increases the observed charge exchange distances in bacterial outer membrane multiheme cytochromes,⁸⁵ and between cytochrome subunits partners of the respiratory chain.²²³ In the latter study, molecular dynamics simulations revealed a cation depletion zone in the interprotein region. The locally diminished ionic strength gives rise to a Gouy-Chapman conduit that extends the spatial span of the electric potential that would otherwise be screened by the ions in the solution.²²³ Interestingly, this cation depletion is disrupted in phosphomimetic cytochrome mutants in which the long-range charge exchange is not observed, suggesting a physiological regulation mechanism for the remote charge exchange.²²⁴

In addition, mechanisms underlying ETp could be operating in the interprotein domain. However, most of ETp models can hardly account for the experimental observations^{179,181,182,203} of temperature-independent and long-range (>2 nm) charge exchange. While this issue remains an open question in the scientific community,¹⁸⁰ we hope that the results presented in chapter 4 can contribute to the discussion and help to elucidate the common and particular mechanisms underlying interprotein ET and ETp. A recently published non-perturbative model is able to reproduce long-range temperature-independent ETp processes between electrodes.¹⁸⁵ The model describes explicitly the electron reorganization in the molecules which yields a power law dependence of the current with distance.

In vivo,⁴² and *in vitro*³⁵ experiments support the view that the redox state of Pc (inseparable from the metallic cofactor) regulates the binding with PSI. This prompted us to tell apart the contribution of protein binding to the charge exchange process. In bulk experiments, transient absorption^{14,36–38,235} or photovoltage^{39–41} is employed to monitor PSI redox state by measuring a signal proportional to the population of P700/P700⁺ after an actinic flash. Binding/unbinding process and the ET of a pre-formed complex are associated to the slow and fast phases of the transient signal, respectively.^{14,36–38,235} However, bulk measurements cannot directly probe the binding rates, and neither separate the binding contribution from the ET process, because they are proportional to the P700/P700⁺ population that depends on the ET process.

Therefore, the experimental approach I followed to separate the binding contribution is single-molecule force spectroscopy (SMFS). In chapter 5, the binding probability of the transient PSI-Pc has been calculated as the ratio of force-distance curves displaying specific adhesion events over the total number of recorded force-distance curves. In chapter 5, the impact of the redox state of the cognate partners on the binding probability was evaluated. In our setup, the redox state of PSI and Pc were orthogonally controlled by light and the reducing agent sodium ascorbate, respectively. Since Pc is not photo-active, and it doesn't absorb light of the excitation wavelength (690 nm), it can be safely assumed that red-light excitation does not modify the Pc redox state. The optical power employed yields a fluence of $2.4 \cdot 10^5$ photons·s⁻¹ through the surface of a single layer of PSI complexes. Given the ~1 quantum yield of PSI, and the recombination rate of the P700⁺/F_B⁻ state ~100 ms,¹⁶ prior to the interaction it is very likely that P700 is reduced in dark conditions and photo-oxidized (P700⁺) when are irradiated. In the absence of a reducing agent, Pc is in oxidized state. This is because the protein is expressed in the apo form (without Cu) and after immobilization it is incubated with Cu²⁺ ions to incorporate the Cu atom. Sodium ascorbate is employed to reduce Pc, with a reported reduction rate of ~3 ms,²³⁶ that is significantly shorter than the duration of the approach/retraction cycles (400 ms) in the SMFS experiments. It can be argued that sodium ascorbate might also reduce the photo-oxidized P700⁺. However, the reported reduction rate of P700⁺ by sodium ascorbate (~ 20-30 s)^{54,228,237,238} is several orders of magnitude higher than photo-oxidation rates discussed above. Therefore, P700 is very likely in the oxidized state (P700⁺) upon irradiation despite the presence of sodium ascorbate in the medium.

SMFS experiments revealed that when Pc is reduced, the binding probability with PSI is independent of the redox state of PSI. However, when Pc is oxidized, the binding probability is lower in the dark (PSI reduced) compared to irradiated samples (PSI oxidized), in which case, the binding probability is similar to the Pc reduced condition. In other words, PSI-Pc binding is favoured when at least one of the two partners is ready for ET and it is disfavoured when PSI is reduced and Pc is oxidized. I interpret that

the lower-binding of $\text{Pc}_{\text{ox}}/\text{PSI}_{\text{red}}$, that we associate to a post-ET situation, facilitates the electron carrier dissociation from PSI and overall reaction turn-over.

Additionally, we have evaluated the effect of Mg^{2+} on the PSI/Pc binding and unbinding. Mg^{2+} regulates the photosynthetic electron transport chain *in vivo*. In particular, Mg^{2+} concentration is higher on the luminal side of the thylakoid membrane with respect to the stromal side in dark conditions while it decreases under illumination.^{239–243} It has been proposed that Mg^{2+} inhibits the binding between Pc the PsaF subunit in PSI.²⁴² The SMFS experiments in this Thesis revealed that upon addition of Mg^{2+} to the buffer solution, the binding probability lowered to the level of the post-ET situation, despite the presence of sodium ascorbate and irradiation of the samples.

Regarding the unbinding forces, the post-ET situation ($\text{Pc}_{\text{ox}}/\text{PSI}_{\text{red}}$) exhibits a wider dispersion in the force values with respect to the three conditions of high binding frequency, which occur at similar forces. However, the decrease in the binding probability produced by Mg^{2+} ions does not disperse the force values as it occurs for $\text{Pc}_{\text{ox}}/\text{PSI}_{\text{red}}$. This suggests that Mg^{2+} does not alter the type of contacts between PSI and Pc. On the other hand, Mg^{2+} might disrupt long-range electrostatic interactions that favour the formation of the complex, thus diminishing the binding probability. In this view, once the complex is formed, short range hydrophobic interactions and hence the measured force distribution remain unaltered.

I propose that the long-range electrostatic interactions driving the complex formation also control the electronic coupling between cognate proteins and thus the spatial span of the charge exchange. Based on the learnt lessons from STS and SMFS complementary studies, I have designed additional STS experiments with PSI-Pc partners in the presence of Mg^{2+} to verify this hypothesis.

In chapter 7, I presented a PSI-based biosensor for methyl viologen (MV), measuring the photocurrent output of the PSI-functionalized electrode under illumination. While in research MV is employed as redox mediator, MV was originally designed and broadly employed as herbicide under the name of paraquat. Our approach exploits photocurrent lock-in detection that enhances the sensitivity with respect to unprocessed photo-current readout. The results presented are a proof-of-concept rather than an operative device optimized for field samples, which may contain mixtures of electron diverters herbicides and as well as other families of herbicide compounds that might alter the activity of PSI complexes and thus the biosensor readout. Despite being presented in the last chapter, the experiments and modelling shown in chapter 7 were carried out in the first place. The puzzling observation of current inversion with bias sign, motivated the detailed characterization of the photocurrent transients. Thus fast-photo-chrono-amperometry measurements paved the way for the development of PEC2DES technique, that we

presented in chapter 6. The results in chapter 6 describe, to our knowledge, the first characterization of PSI photocurrent with sub-ms resolution.

PEC2DES is the combination of photoelectrochemical current detection with two dimensional electronic spectroscopy. We evaluated the performance of this technique with biological samples using PSI as model system. The characterization of the photocurrent response of PSI-electrodes demonstrated that the current amplitude, transient signal duration, and sample stability, meet the requirements for non-linear spectroscopy experiments. A global analysis of PEC2DES data yielded two main results: a coherence observed at $\approx 750 \text{ cm}^{-1}$ in the coherent associated spectra, and the absence of changes in decay associated spectra signal within 450 fs. The presence of this coherence indicates that the PEC2DES technique is sensitive to non-linear phenomena. The optimization of electrochemical photocurrent signals up to a signal-to-noise ratio sensitive to non-linear features was thus achieved. However, the lack of excitation dynamics or spectral diffusion within the first 450 fs is inconsistent with previously reported experiments of PSI-LHCI complexes based on 3-pulses 2DES. We propose three hypotheses to explain this observation (discussed in detail in chapter 6):

- i) CS by outer Chlorophylls CT states leading to charge recombination.
- ii) Incoherent mixing of linear and non-linear spectroscopic signals due to the non-linear electrochemical response.
- iii) Cancellation of excited state absorption pathways (ESA I and ESA II) and low excitation probability of stimulated emission (SE) pathway. This latter scenario leaves ground state bleaching (GSB) as the only available Feynman diagram, however, the latter decays with the turn over cycle (ms time scale) and it is thus constant in the experimental window of 450 fs.

In the first two hypotheses, photocurrent detection would bring to the fore a de-excitation pathway that was previously attributed to CS in the RC. In the third scenario, our results would prove experimentally the signal cancellation of ESA I and ESA II pathways in the 4-pulse configuration.

Due to the complexity of this biological system, it would be naïve and reductionist to state that the different perspectives from which we have regarded PSI and the distinct experimental approaches that we have developed lead to a complete understanding of the system. Nevertheless, the experimental procedures developed in the different chapters from the complementary study of a single system have helped us to implement experimental set-ups of increasing complexity. In this regard, it would not have been prudent to attempt PSI-Pc single molecule experiments with both AFM and ECSTM without a proper characterization of oriented PSI complexes at the nanoscale. In the same line, we would not have embarked on the venture of developing PEC2DES without

having measured high amplitude and fast transient photocurrents before. Experiments complementarity has also helped us to avoid (some of) the narrow vision trickery often associated to high-end time-consuming techniques.

Regarding recent, ongoing and future experiments, the role of pH in the charge-exchange distance of adsorbed Pc proteins was explored in the frame of the master's thesis project of Iñigo Hierro, carried out under my supervision. His preliminary results indicate that the current-distance constant β is regulated by the pH. In the framework of another Master's thesis project, by Judit Donada and Montserrat Sales, we are currently extending this experimental data. These experiments are at an early stage of development and are out of the scope of this dissertation.

Chapter 10

Conclusions

The main conclusions obtained from this thesis are:

1. Introducing a cysteine residue in the cyanobacterial reaction centre orienting peptide allows to functionalize gold electrodes with plant PSI complexes exposing their luminal side to the liquid medium.
2. PSI immobilized onto electrodes complexes provide stable photocurrent responses in a wide sample potential window [-200,300] mV/SSC.
3. In ECSTM current-distance spectroscopy of PSI, the spatial span of the current is enhanced at sample potential 0 mV/SSC and probe potential 400 mV/SSC.
4. PSI and Pc proteins are capable of exchanging charge over several nm through the aqueous solution (β values ranging between 0.8 and 1.8 nm⁻¹), either individually against a gold electrode or facing each other.
5. The protein matrix is sufficient to sustain long distance charge transport through the aqueous solution between Pc_{apo} and PSI (β value 0.8 nm⁻¹) as well as through the PSI/Pc complex with a conductance peak at $11 \cdot 10^{-4} G_0$.
6. The Cu²⁺ in Pc diminishes the charge exchange distance with the cognate PSI in ECSTM configuration for negative bias (physiological charge exchange direction). For positive bias (current flow against physiological charge exchange) β is similar for PSI-Pc_{holo} and PSI-Pc_{apo}.
7. When PSI and Pc face each other in ECSTM experiments, conductance blinks typically lasting ≈ 6 ms are observed and associated to the spontaneous formation of PSI/Pc transient complexes. The conductance change of blinks for PSI/Pc_{holo} ($7 \cdot 10^{-4} G_0$) is lower with respect to PSI/Pc_{apo} ($11 \cdot 10^{-4} G_0$).

8. Low conductance peaks ($\approx 2 \cdot 10^{-4} G_0$) with a lifetime of ≈ 1 ms are observed in Pc_{holo} and $PSI-Pc_{\text{apo}}$ samples. According to previous results, they are attributed to the transient configuration of water molecules leading to localized electronic states that could mediate interprotein ET.
9. We suggest an additional role of the redox ion cofactor in Pc , as regulator of the protein intrinsic conductance and spatial span in ET.
10. The binding frequency between PSI and Pc depends on their respective redox states. The interaction between PSI and Pc is higher when at least one partner is in an ET-ready redox state.
11. Mg^{2+} can modulate the $PSI-Pc$ interaction in individual complexes. An increase in Mg^{2+} concentration hinders $PSI-Pc$ interaction, independently of PSI redox state.
12. We have validated a novel photoelectrochemical technique (PEC2DES) with a biological multichromophoric system, the PSI protein complex of plants.
13. Photoelectrochemical current signal exhibits sub-millisecond transients of $\approx 100 \mu A \cdot cm^{-2}$ and is stable for hours.
14. The overlap between the linear component of PEC2DES data and the visible absorption spectra of the sample manifests that PSI complexes are responsible for PEC2DES results.
15. Global analysis yields an oscillatory component coherence centered at 750 cm^{-1} with a vibrational mode coupled to the optical transition of chlorophyll a chromophores.
16. Population dynamics is not observed within a delay time of 450 fs, in contrast to previous 2DES experiments of plant $PSI-LHCI$ complexes solely based on optical detection.
17. We present a proof-of-concept PSI -based biosensor that probes the concentration of PQ using photocurrent as sensing signal.
18. Systematically studying photocurrent transients of $PSI-PQ$ system allows to identify the different contributions giving rise to the transient signal.
19. The corresponding kinetic model allows the identification and electrochemical evaluation of the different species involved in the detection process.

Bibliography

- 1 Maturana H, Varela F. *Autopoiesis and cognition: The realization of the living*, vol. 42. Springer Science & Business Media. 1972.
- 2 Svirezhev Y. Entropy and entropy flows in the biosphere. In: *Global ecology*, edited by Sven Erik J. 2010;.
- 3 Wütscher F, ed. *Sustainable Development and Innovation in the Energy Sector*. Berlin/Heidelberg: Springer-Verlag. 2005.
- 4 Hohmann-Marriott MF, Blankenship RE. Evolution of Photosynthesis. *Annual Review of Plant Biology*. 2011;62(1):515–548.
- 5 Wollman FA. State transitions reveal the dynamics and flexibility of the photosynthetic apparatus. *The EMBO Journal*. 2001;20(14):3623–3630.
- 6 Lucker B, Kramer DM. Regulation of cyclic electron flow in *Chlamydomonas reinhardtii* under fluctuating carbon availability. *Photosynthesis Research*. 2013; 117(1-3):449–459.
- 7 Blankenship RE. *Molecular Mechanisms of Photosynthesis*. Wiley. 2002.
- 8 Busch A, Hippler M. The structure and function of eukaryotic photosystem I. *Biochimica et Biophysica Acta (BBA) - Bioenergetics*. 2011;1807(8):864–877.
- 9 Pan X, Ma J, Su X, Cao P, Chang W, Liu Z, Zhang X, Li M. Structure of the maize photosystem I supercomplex with light-harvesting complexes I and II. *Science*. 2018; 360(6393):1109–1113.
- 10 Ben-Shem A, Frolow F, Nelson N. Crystal structure of plant photosystem I. *Nature*. 2003;426(6967):630–635.
- 11 Ramesh VM, Gibasiewicz K, Lin S, Bingham SE, Webber AN. Bidirectional Electron Transfer in Photosystem I: Accumulation of A0- in A-Side or B-Side Mutants of the Axial Ligand to Chlorophyll A0. *Biochemistry*. 2004;43(5):1369–1375.

BIBLIOGRAPHY

- 12 Müller MG, Slavov C, Luthra R, Redding KE, Holzwarth AR. Independent initiation of primary electron transfer in the two branches of the photosystem I reaction center. *Proceedings of the National Academy of Sciences*. 2010;107(9):4123–4128.
- 13 Hippler M, Drepper F, Haehnel W, Rochaix JD. The N-terminal domain of PsaF: Precise recognition site for binding and fast electron transfer from cytochrome c₆ and plastocyanin to photosystem I of *Chlamydomonas reinhardtii*. *Proceedings of the National Academy of Sciences*. 1998;95(13):7339–7344.
- 14 Sommer F, Drepper F, Haehnell W, Hippler M. The Hydrophobic Recognition Site Formed by Residues PsaA-Trp651 and PsaB-Trp627 of Photosystem I in *Chlamydomonas reinhardtii* Confers Distinct Selectivity for Binding of Plastocyanin and Cytochrome c₆. *Journal of Biological Chemistry*. 2004;279(19):20009–20017.
- 15 Croce R, Van Amerongen H. Light-harvesting in photosystem I. *Photosynthesis Research*. 2013;116(2-3):153–166.
- 16 Chitnis PR. Photosystem I: Function and Physiology. *Annual Review of Plant Physiology and Plant Molecular Biology*. 2001;52(1):593–626.
- 17 Brettel K. Electron transfer and arrangement of the redox cofactors in photosystem I. *Biochimica et Biophysica Acta - Bioenergetics*. 1997;1318(3):322–373.
- 18 Redinbo MR, Yeates TO, Merchant S. Plastocyanin: Structural and functional analysis. *Journal of Bioenergetics and Biomembranes*. 1994;26(1):49–66.
- 19 De La Rosa MA, Navarro JA, Díaz-Quintana A, De La Cerda B, Molina-Heredia FP, Balme A, Murdoch PDS, Díaz-Moreno I, Durán RV, Hervás M. An evolutionary analysis of the reaction mechanisms of photosystem I reduction by cytochrome c₆ and plastocyanin. *Bioelectrochemistry*. 2002;55:41–45.
- 20 Zatwarnicki P, Barciszewski J, Krzywda S, Jaskolski M, Kolesinski P, Szczepaniak A. Cytochrome c_{6B} of *Synechococcus* sp. WH 8102 – Crystal structure and basic properties of novel c₆-like family representative. *Biochemical and Biophysical Research Communications*. 2014;443:1131–1135.
- 21 Paraskevopoulos K, Sundararajan M, Surendran R, Hough MA, Eady RR, Hillier IH, Hasnain SS. Active site structures and the redox properties of blue copper proteins: atomic resolution structure of azurin II and electronic structure calculations of azurin, plastocyanin and stellacyanin. *Dalton Transactions*. 2006;(25):3067.
- 22 Chothia C, Lesk AM. Evolution of proteins formed by β -sheets. *Journal of Molecular Biology*. 1982;160(2):309–323.
- 23 Derek Bendall. *Protein Electron Transfer*. Garland Science. 1996.

BIBLIOGRAPHY

- 24 Garrett T, Clingeffer DJ, Guss JM, Rogers SJ, Freeman H. The crystal structure of poplar apoplastocyanin at 1.8-Å resolution. The geometry of the copper-binding site is created by the polypeptide. *Journal of Biological Chemistry*. 1984;259(5):2822–2825.
- 25 Guss JM, Bartunik HD, Freeman HC. Accuracy and precision in protein structure analysis: restrained least-squares refinement of the structure of poplar plastocyanin at 1.33 Å resolution. *Acta Crystallographica Section B Structural Science*. 1992; 48(6):790–811.
- 26 Bendall DS, Schlarb-Ridley BG, Howe CJ. Transient Interactions Between Soluble Electron Transfer Proteins. The Case of Plastocyanin and Cytochrome f. In: *Bioenergetic Processes of Cyanobacteria*, pp. 541–571. Springer Netherlands. 2011;.
- 27 Cruz-Gallardo I, Díaz-Moreno I, Díaz-Quintana A, De la Rosa MA. The cytochrome-f plastocyanin complex as a model to study transient interactions between redox proteins. *FEBS Letters*. 2012;586(5):646–652.
- 28 Hope AB. Electron transfers amongst cytochrome f, plastocyanin and photosystem I: Kinetics and mechanisms. *Biochimica et Biophysica Acta - Bioenergetics*. 2000; 1456(1):5–26.
- 29 Schreiber G, Haran G, Zhou HX. Fundamental Aspects of Protein-Protein Association Kinetics. *Chemical Reviews*. 2009;109(3):839–860.
- 30 Höhner R, Pribil M, Herbstová M, Lopez LS, Kunz HH, Li M, Wood M, Svoboda V, Puthiyaveetil S, Leister D, Kirchhoff H. Plastocyanin is the long-range electron carrier between photosystem II and photosystem I in plants. *Proceedings of the National Academy of Sciences*. 2020;117(26):15354–15362.
- 31 Kirchhoff H, Hall C, Wood M, Herbstová M, Tsabari O, Nevo R, Charuvi D, Shimoni E, Reich Z. Dynamic control of protein diffusion within the granal thylakoid lumen. *Proceedings of the National Academy of Sciences*. 2011;108(50):20248–20253.
- 32 Kovalenko IB, Knyazeva OS, Antal TK, Ponomarev VY, Riznichenko GY, Rubin AB. Multiparticle Brownian dynamics simulation of experimental kinetics of cytochrome b₆ oxidation and photosystem I reduction by plastocyanin. *Physiologia Plantarum*. 2017;161(1):88–96.
- 33 Ueda T, Nomoto N, Koga M, Ogasa H, Ogawa Y, Matsumoto M, Stampoulis P, Sode K, Terasawa H, Shimada I. Structural basis of efficient electron transport between photosynthetic membrane proteins and plastocyanin in Spinach revealed using nuclear magnetic resonance. *Plant Cell*. 2012;24(10):4173–4186.

BIBLIOGRAPHY

- 34 Caspy I, Borovikova-Sheinker A, Klaiman D, Shkolnisky Y, Nelson N. The structure of a triple complex of plant photosystem I with ferredoxin and plastocyanin. *Nature Plants*. 2020;6(10):1300–1305.
- 35 Caspy I, Fadeeva M, Kuhlert S, Borovikova-Sheinker A, Klaiman D, Masrati G, Drepper F, Ben-Tal N, Hippler M, Nelson N. Structure of plant photosystem I-plastocyanin complex reveals strong hydrophobic interactions. *Biochemical Journal*. 2021;478(12):2371–2384.
- 36 Drepper F, Hippler M, Nitschke W, Haehnel W. Binding dynamics and electron transfer between plastocyanin and photosystem I. *Biochemistry*. 1996;35(4):1282–1295.
- 37 Kuhlert S, Drepper F, Fufezan C, Sommer F, Hippler M. Residues PsaB Asp612 and PsaB Glu613 of photosystem I confer pH-dependent binding of plastocyanin and cytochrome c₆. *Biochemistry*. 2012;51(37):7297–7303.
- 38 Sommer F, Drepper F, Hippler M. The luminal helix I of PsaB is essential for recognition of plastocyanin or cytochrome c₆ and fast electron transfer to photosystem I in *Chlamydomonas reinhardtii*. *Journal of Biological Chemistry*. 2002;277(8):6573–6581.
- 39 Drachev LA, Kaurov BS, Mamedov MD, Mulkidjanian AY, Semenov AY, Shinkarev VP, Skulachev VP, Verkhovsky MI. Flash-induced electrogenic events in the photosynthetic reaction center and bc₁ complexes of *Rhodospira rubra* chromatophores. *BBA - Bioenergetics*. 1989;973(2):189–197.
- 40 Mamedov MD, Mamedova AA, Chamorovsky SK, Semenov AY. Electrogenic reduction of the primary electron donor P700 by plastocyanin in photosystem I complexes. *FEBS Letters*. 2001;500(3):172–176.
- 41 Semenov AY, Mamedov MD, Chamorovsky SK. Photoelectric studies of the transmembrane charge transfer reactions in photosystem I pigment-protein complexes. *FEBS Letters*. 2003;553(3):223–228.
- 42 Finazzi G, Sommer F, Hippler M. Release of oxidized plastocyanin from photosystem I limits electron transfer between photosystem I and cytochrome b₆f complex in vivo. *Proceedings of the National Academy of Sciences*. 2005;102:7031–7036.
- 43 Qin X, Suga M, Kuang T, Shen JR. Structural basis for energy transfer pathways in the plant PSI-LHCI supercomplex. *Science*. 2015;348(6238):989–995.
- 44 Amunts A, Toporik H, Borovikova A, Nelson N. Structure determination and improved model of plant photosystem I. *Journal of Biological Chemistry*. 2010;285(5):3478–3486.

BIBLIOGRAPHY

- 45 Parson WW. *Modern Optical Spectroscopy*. Berlin, Heidelberg: Springer Berlin Heidelberg. 2015.
- 46 Croce R, van Amerongen H. Light harvesting in oxygenic photosynthesis: Structural biology meets spectroscopy. *Science*. 2020;369(6506).
- 47 Meneghin E, Leonardo C, Volpato A, Bolzonello L, Collini E. Mechanistic insight into internal conversion process within Q-bands of chlorophyll a. *Scientific Reports*. 2017;7(1):11389.
- 48 Romero E, Prior J, Chin AW, Morgan SE, Novoderezhkin VI, Plenio MB, van Grondelle R. Quantum – coherent dynamics in photosynthetic charge separation revealed by wavelet analysis. *Scientific Reports*. 2017;7(1):2890.
- 49 Beddard G, Carlin S, Porter G. Concentration quenching of chlorophyll fluorescence in bilayer lipid vesicles and liposomes. *Chemical Physics Letters*. 1976;43(1):27–32.
- 50 Croce R. A close view of photosystem I. *Science*. 2015;348(6238):970–971.
- 51 Förster T. Intermolecular energy transfer and fluorescence. *Annalen der Physik*. 1948; 2:55–75.
- 52 van Amerongen H, van Grondelle R, Valkunas L. *Photosynthetic Excitons*. World Scientific. 2000.
- 53 Croce R, Zucchelli G, Garlaschi FM, Bassi R, Jennings RC. Excited State Equilibration in the Photosystem I Light-Harvesting I Complex: P700 Is Almost Isoenergetic with Its Antenna. *Biochemistry*. 1996;35(26):8572–8579.
- 54 Golbeck JH. *Photosystem I: the light-driven plastocyanin: ferredoxin oxidoreductase*, vol. 24. Springer Science & Business Media. 2007.
- 55 Zhang B, Lindsay S. Electronic Decay Length in a Protein Molecule. *Nano Letters*. 2019;19(6):4017–4022.
- 56 Ennist NM, Zhao Z, Stayrook SE, Discher BM, Dutton PL, Moser CC. De novo protein design of photochemical reaction centers. *Nature Communications*. 2022; 13(1):4937.
- 57 Ennist NM, Zhao Z, Stayrook SE, Discher BM, Dutton PL, Moser CC. De novo protein design of photochemical reaction centers. *Nature Communications*. 2022; 13(1):4937.
- 58 Hancock AM, Son M, Nairat M, Wei T, Jeuken LJC, Duffy CDP, Schlau-Cohen GS, Adams PG. Ultrafast energy transfer between lipid-linked chromophores and plant light-harvesting complex II. *Physical Chemistry Chemical Physics*. 2021; 23(35):19511–19524.

BIBLIOGRAPHY

- 59 Hancock AM, Swainsbury DJ, Meredith SA, Morigaki K, Hunter CN, Adams PG. Enhancing the spectral range of plant and bacterial light-harvesting pigment-protein complexes with various synthetic chromophores incorporated into lipid vesicles. *Journal of Photochemistry and Photobiology B: Biology*. 2022;237:112585.
- 60 Liu J, Friebe VM, Frese RN, Jones MR. Polychromatic solar energy conversion in pigment-protein chimeras that unite the two kingdoms of (bacterio)chlorophyll-based photosynthesis. *Nature Communications*. 2020;11(1):1542.
- 61 Wang HW, Wang JW. How cryo-electron microscopy and X-ray crystallography complement each other. *Protein Science*. 2017;26(1):32–39.
- 62 Bouffier L, Doneux T. Coupling electrochemistry with in situ fluorescence (confocal) microscopy. *Current Opinion in Electrochemistry*. 2017;6(1):31–37.
- 63 Pande N, Chandrasekar SK, Lohse D, Mul G, Wood JA, Mei BT, Krug D. Electrochemically Induced pH Change: Time-Resolved Confocal Fluorescence Microscopy Measurements and Comparison with Numerical Model. *The Journal of Physical Chemistry Letters*. 2020;11(17):7042–7048.
- 64 Tassy B, Dauphin AL, Man HM, Le Guenno H, Lojou E, Bouffier L, de Poulpiquet A. In Situ Fluorescence Tomography Enables a 3D Mapping of Enzymatic O₂ Reduction at the Electrochemical Interface. *Analytical Chemistry*. 2020;92(10):7249–7256.
- 65 Lynk TP, Sit CS, Brosseau CL. Electrochemical Surface-Enhanced Raman Spectroscopy as a Platform for Bacterial Detection and Identification. *Analytical Chemistry*. 2018;90(21):12639–12646.
- 66 Wu DY, Li JF, Ren B, Tian ZQ. Electrochemical surface-enhanced Raman spectroscopy of nanostructures. *Chemical Society Reviews*. 2008;37(5):1025.
- 67 Iwasita T, Nart F. In situ infrared spectroscopy at electrochemical interfaces. *Progress in Surface Science*. 1997;55(4):271–340.
- 68 Binnig G, Rohrer H. Scanning tunneling microscopy. *Surface Science*. 1983; 126(1-3):236–244.
- 69 Giannotti MI, Vancso GJ. Interrogation of single synthetic polymer chains and polysaccharides by AFM-based force spectroscopy. 2007;8(16):2290–2307.
- 70 Müller DJ, Dumitru AC, Lo Giudice C, Gaub HE, Hinterdorfer P, Hummer G, De Yoreo JJ, Dufrêne YF, Alsteens D. Atomic Force Microscopy-Based Force Spectroscopy and Multiparametric Imaging of Biomolecular and Cellular Systems. *Chemical Reviews*. 2021;121(19):11701–11725.

BIBLIOGRAPHY

- 71 Stroschio J, Kaiser W. *Scanning Tunneling Microscopy*, vol. 27. Academic Press. 1993.
- 72 Güell AG, Díez-Pérez I, Gorostiza P, Sanz F. Preparation of reliable probes for electrochemical tunneling spectroscopy. *Analytical Chemistry*. 2004; 76(17):5218–5222.
- 73 Zhu L, Claude-Montigny B, Gattrell M. Insulating method using cataphoretic paint for tungsten tips for electrochemical scanning tunnelling microscopy (ECSTM). *Applied Surface Science*. 2005;252(5):1833–1845.
- 74 Gewirth AA, Craston DH, Bard AJ. Fabrication and Characterization of microtips for in situ scanning tunnelling microscopy. *Journal of Electroanalytical Chemistry*. 1989; 261:477.
- 75 Vitus CM, Chang SC, Schardt BC, Weaver MJ. In situ scanning tunneling microscopy as a probe of adsorbate-induced reconstruction at ordered monocrystalline electrodes: carbon monoxide on platinum(100). *The Journal of Physical Chemistry*. 1991; 95(20):7559–7563.
- 76 Abadal G, Perez-Murano F, Barniol N, Aymerich X. The measurement of the tip current noise as a method to characterize the exposed area of coated ESTM tips. *IEEE Transactions on Instrumentation and Measurement*. 2003;52(3):859–864.
- 77 Chi Q, Zhang J, Nielsen JU, Friis EP, Chorkendorff I, Canters GW, Andersen JE, Ulstrup J. Molecular monolayers and interfacial electron transfer of *Pseudomonas aeruginosa* azurin on Au(111). *Journal of the American Chemical Society*. 2000; 122(17):4047–4055.
- 78 Andolfi L, Bonanni B, Canters GW, Verbeet MP, Cannistraro S. Scanning probe microscopy characterization of gold-chemisorbed poplar plastocyanin mutants. *Surface Science*. 2003;530(3):181–194.
- 79 Zhang J, Christensen HE, Ooi BL, Ulstrup J. In situ STM imaging and direct electrochemistry of *Pyrococcus furiosus* ferredoxin assembled on thiolate-modified Au(111) surfaces. *Langmuir*. 2004;20(23):10200–10207.
- 80 Alliata D, Andolfi L, Cannistraro S. Tip to substrate distances in STM imaging of biomolecules. *Ultramicroscopy*. 2004;101(2-4):231–240.
- 81 Chi Q, Farver O, Ulstrup J. Long-range protein electron transfer observed at the single-molecule level: In situ mapping of redox-gated tunneling resonance. *Proceedings of the National Academy of Sciences of the United States of America*. 2005;102(45):16203–16208.

BIBLIOGRAPHY

- 82 Halbritter J, Repphun G, Vinzelberg S, Staikov G, Lorenz W. Tunneling mechanisms in electrochemical STM—distance and voltage tunneling spectroscopy. *Electrochimica Acta*. 1995;40(10):1385–1394.
- 83 Artés JM, López-Martínez M, Díez-Pérez I, Sanz F, Gorostiza P. Conductance switching in single wired redox proteins. *Small*. 2014;10(13):2537–2541.
- 84 He J, Sankey O, Lee M, Tao N, Li X, Lindsay S. Measuring single molecule conductance with break junctions. *Faraday Discuss*. 2006;131:145–154.
- 85 Wigginton NS, Rosso KM, Stack AG, Hochella MF. Long-range electron transfer across cytochrome-hematite (α -Fe₂O₃) interfaces. *Journal of Physical Chemistry C*. 2009;113(6):2096–2103.
- 86 He J, Lin L, Zhang P, Lindsay S. Identification of DNA Basepairing via Tunnel-Current Decay. *Nano Letters*. 2007;7(12):3854–3858.
- 87 Artés JM, Díez-Pérez I, Sanz F, Gorostiza P. Direct measurement of electron transfer distance decay constants of single redox proteins by electrochemical tunneling spectroscopy. *ACS Nano*. 2011;5(3):2060–2066.
- 88 Simeone FC, Kolb DM, Venkatachalam S, Jacob T. Tunneling behavior of electrified interfaces. *Surface Science*. 2008;602(7):1401–1407.
- 89 Millonas MM, Hanck DA. Nonequilibrium Response Spectroscopy of Voltage-Sensitive Ion Channel Gating. *Biophysical Journal*. 1998;74(1):210–229.
- 90 Yuzhelevski Y, Yuzhelevski M, Jung G. Random telegraph noise analysis in time domain. *Review of Scientific Instruments*. 2000;71(4):1681–1688.
- 91 Horcas I, Fernández R, Gómez-Rodríguez JM, Colchero J, Gómez-Herrero J, Baro AM. WSXM: A software for scanning probe microscopy and a tool for nanotechnology. *Review of Scientific Instruments*. 2007;78(1):013705.
- 92 Brett C, Oliveira Brett AM. *Electrochemistry: Principles, Methods, and Applications*. Oxford University Press. 1993.
- 93 Plumeré N, Nowaczyk MM. Biophotoelectrochemistry of photosynthetic proteins. *Biophotoelectrochemistry: From Bioelectrochemistry to Biophotovoltaics*. 2016;pp. 111–136.
- 94 Bennett T, Niroomand H, Pamu R, Ivanov I, Mukherjee D, Khomami B. Elucidating the role of methyl viologen as a scavenger of photoactivated electrons from photosystem i under aerobic and anaerobic conditions. *Physical Chemistry Chemical Physics*. 2016;18(12):8512–8521.

BIBLIOGRAPHY

- 95 Zhao F, Hardt S, Hartmann V, Zhang H, Nowaczyk MM, Rögner M, Plumeré N, Schuhmann W, Conzuelo F. Light-induced formation of partially reduced oxygen species limits the lifetime of photosystem 1-based biocathodes. *Nature Communications*. 2018;9(1).
- 96 Zhang Y, Liu C, Balaeff A, Skourtis SS, Beratan DN. Biological charge transfer via flickering resonance. *Proceedings of the National Academy of Sciences*. 2014; 111(28):10049–10054.
- 97 Duke SO, Dayan FE. *Bioactivity of Herbicides*, vol. 4. Elsevier. 2011.
- 98 Zhao F, Ruff A, Rögner M, Schuhmann W, Conzuelo F. Extended Operational Lifetime of a Photosystem-Based Bioelectrode. *Journal of the American Chemical Society*. 2019;141(13):5102–5106.
- 99 Manocchi AK, Baker DR, Pendley SS, Nguyen K, Hurley MM, Bruce BD, Sumner JJ, Lundgren CA. Photocurrent generation from surface assembled photosystem i on alkanethiol modified electrodes. *Langmuir*. 2013;29(7):2412–2419.
- 100 Baker DR, Manocchi AK, Lamicq ML, Li M, Nguyen K, Sumner JJ, Bruce BD, Lundgren CA. Comparative Photoactivity and Stability of Isolated Cyanobacterial Monomeric and Trimeric Photosystem I. *The Journal of Physical Chemistry B*. 2014; 118(10):2703–2711.
- 101 Białek R, Friebe V, Ruff A, Jones MR, Frese R, Gibasiewicz K. In situ spectroelectrochemical investigation of a biophotoelectrode based on photoreaction centers embedded in a redox hydrogel. *Electrochimica Acta*. 2020;330:135190.
- 102 Kothe T, Plumeré N, Badura A, Nowaczyk MM, Guschin DA, Rögner M, Schuhmann W. Combination of A Photosystem1-Based Photocathode and a Photosystem2-Based Photoanode to a Z-Scheme Mimic for Biophotovoltaic Applications. *Angewandte Chemie International Edition*. 2013;52(52):14233–14236.
- 103 Gelzinis A, Augulis R, Butkus V, Robert B, Valkunas L. Two-dimensional spectroscopy for non-specialists. *Biochimica et Biophysica Acta - Bioenergetics*. 2019;1860(4):271–285.
- 104 Fuller FD, Ogilvie JP. Experimental Implementations of Two-Dimensional Fourier Transform Electronic Spectroscopy. *Annual Review of Physical Chemistry*. 2015; 66:667–690.
- 105 Tollerud JO, Davis JA. Coherent multi-dimensional spectroscopy: Experimental considerations, direct comparisons and new capabilities. *Progress in Quantum Electronics*. 2017;55:1–34.

BIBLIOGRAPHY

- 106 Mukamel S. *Principles of Nonlinear Optical Spectroscopy*, vol. 6. Oxford University Press. 1999.
- 107 Jonas DM. Two-Dimensional Femtosecond Spectroscopy. *Annual Review of Physical Chemistry*. 2003;54:425–463.
- 108 Volpato A, Bolzonello L, Meneghin E, Collini E. Global analysis of coherence and population dynamics in 2D electronic spectroscopy. *Optics Express*. 2016; 24(21):24773.
- 109 Goetz S, Li D, Kolb V, Pflaum J, Brixner T. Coherent two-dimensional fluorescence micro-spectroscopy. *Optics Express*. 2018;26:3915.
- 110 Bakulin AA, Silva C, Vella E. Ultrafast Spectroscopy with Photocurrent Detection: Watching Excitonic Optoelectronic Systems at Work. *The Journal of Physical Chemistry Letters*. 2016;7:250–258.
- 111 Bolzonello L, Bernal-Texca F, Gerling LG, Ockova J, Collini E, Martorell J, van Hulst NF. Photocurrent-Detected 2D Electronic Spectroscopy Reveals Ultrafast Hole Transfer in Operating PM6/Y6 Organic Solar Cells. *The Journal of Physical Chemistry Letters*. 2021;12(16):3983–3988.
- 112 Castañeda Ocampo OE, Gordiichuk P, Catarci S, Gautier DA, Herrmann A, Chiechi RC. Mechanism of Orientation-Dependent Asymmetric Charge Transport in Tunneling Junctions Comprising Photosystem i. *Journal of the American Chemical Society*. 2015;137(26):8419–8427.
- 113 Danelon C, Brando T, Winterhalter M. Probing the orientation of reconstituted maltoporin channels at the single-protein level. *Journal of Biological Chemistry*. 2003;278(37):35542–35551.
- 114 Fereiro JA, Porat G, Bendikov T, Pecht I, Sheves M, Cahen D. Protein Electronics: Chemical Modulation of Contacts Control Energy Level Alignment in Gold-Azurin-Gold Junctions. *Journal of the American Chemical Society*. 2018; 140(41):13317–13326.
- 115 Guo C, Yu X, Refaely-Abramson S, Sepunaru L, Bendikov T, Pecht I, Kronik L, Vilan A, Sheves M, Cahen D. Tuning electronic transport via hepta-alanine peptides junction by tryptophan doping. *Proceedings of the National Academy of Sciences of the United States of America*. 2016;113(39):10785–10790.
- 116 Zhang B, Song W, Pang P, Lai H, Chen Q, Zhang P, Lindsay S. Role of contacts in long-range protein conductance. *Proceedings of the National Academy of Sciences of the United States of America*. 2019;116:5886–5891.

BIBLIOGRAPHY

- 117 Jeuken LJ. *Biophotoelectrochemistry: from bioelectrochemistry to biophotovoltaics*, vol. 158. Springer. 2017.
- 118 Häkkinen H. The gold–sulfur interface at the nanoscale. *Nature Chemistry*. 2012; 4(6):443–455.
- 119 Vericat C, Vela ME, Benitez G, Carro P, Salvarezza RC. Self-assembled monolayers of thiols and dithiols on gold: New challenges for a well-known system. *Chemical Society Reviews*. 2010;39(5):1805–1834.
- 120 Arrigan DW, Le Bihan L. A study of L-cysteine adsorption on gold via electrochemical desorption and copper(II) ion complexation. *Analyst*. 1999; 124(11):1645–1649.
- 121 Zhang J, Chi Q, Nielsen JU, Friis EP, Andersen JE, Ulstrup J. Two-dimensional cysteine and cystine cluster networks on Au(111) disclosed by voltammetry and in situ scanning tunneling microscopy. *Langmuir*. 2000;16(18):7229–7237.
- 122 Yates NDJ, Fascione MA, Parkin A. Methodologies for “Wiring” Redox Proteins/Enzymes to Electrode Surfaces. *Chemistry - A European Journal*. 2018; 24(47):12164–12182.
- 123 Baldacchini C, Bizzarri AR, Cannistraro S. Electron transfer, conduction and biorecognition properties of the redox metalloprotein Azurin assembled onto inorganic substrates. *European Polymer Journal*. 2016;83:407–427.
- 124 Ruiz MP, Aragonès AC, Camarero N, Vilhena JG, Ortega M, Zotti LA, Pérez R, Cuevas JC, Gorostiza P, Díez-Pérez I. Bioengineering a Single-Protein Junction. *Journal of the American Chemical Society*. 2017;139(43):15337–15346.
- 125 Gerster D, Reichert J, Bi H, Barth JV, Kaniber SM, Holleitner AW, Visoly-Fisher I, Sergani S, Carmeli I. Photocurrent of a single photosynthetic protein. *Nature Nanotechnology*. 2012;7(10):673–676.
- 126 Gordiichuk P, Pesce D, Ocampo OE, Marcozzi A, Wetzelaer GJA, Paul A, Loznik M, Gloukhikh E, Richter S, Chiechi RC, Herrmann A. Orientation and Incorporation of Photosystem I in Bioelectronics Devices Enabled by Phage Display. *Advanced Science*. 2017;4(5).
- 127 Lee I, Lee JW, Greenbaum E. Biomolecular electronics: Vectorial arrays of photosynthetic reaction centers. *Physical Review Letters*. 1997;79(17):3294–3297.
- 128 Stieger KR, Feifel SC, Lokstein H, Lisdat F. Advanced unidirectional photocurrent generation via cytochrome c as reaction partner for directed assembly of photosystem i. *Physical Chemistry Chemical Physics*. 2014;16(29):15667–15674.

BIBLIOGRAPHY

- 129 Terasaki N, Yamamoto N, Hiraga T, Yamanoi Y, Yonezawa T, Nishihara H, Ohmori T, Sakai M, Fujii M, Tohri A, Iwai M, Inoue Y, Yoneyama S, Minakata M, Enami I. Plugging a molecular wire into photosystem I: Reconstitution of the photoelectric conversion system on a gold electrode. *Angewandte Chemie - International Edition*. 2009;48(9):1585–1587.
- 130 Torabi N, Qiu X, López-Ortiz M, Loznik M, Herrmann A, Kermanpur A, Ashrafi A, Chiechi RC. Fullerenes Enhance Self-Assembly and Electron Injection of Photosystem i in Biophotovoltaic Devices. *Langmuir*. 2021;37(39):11465–11473.
- 131 Kim Y, Shin SA, Lee J, Yang KD, Nam KT. Hybrid system of semiconductor and photosynthetic protein. *Nanotechnology*. 2014;25(34).
- 132 Mershin A, Matsumoto K, Kaiser L, Yu D, Vaughn M, Nazeeruddin MK, Bruce BD, Graetzel M, Zhang S. Self-assembled photosystem-I biophotovoltaics on nanostructured TiO₂ and ZnO. *Scientific Reports*. 2012;2:1–7.
- 133 Gunther D, LeBlanc G, Prasai D, Zhang JR, Cliffel DE, Bolotin KI, Jennings GK. Photosystem i on graphene as a highly transparent, photoactive electrode. *Langmuir*. 2013;29(13):4177–4180.
- 134 Ciornii D, Kölsch A, Zouni A, Lisdat F. A precursor-approach in constructing 3D ITO electrodes for the improved performance of photosystem I-cyt c photobioelectrodes. *Nanoscale*. 2019;11(34):15862–15870.
- 135 Leblanc G, Gizzie E, Yang S, Cliffel DE, Jennings GK. Photosystem I protein films at electrode surfaces for solar energy conversion. *Langmuir*. 2014;30(37):10990–11001.
- 136 Nguyen K, Bruce BD. Growing green electricity: Progress and strategies for use of Photosystem i for sustainable photovoltaic energy conversion. *Biochimica et Biophysica Acta - Bioenergetics*. 2014;1837(9):1553–1566.
- 137 Friebe VM, Barszcz AJ, Jones MR, Frese RN. Back Cover: Sustaining Electron Transfer Pathways Extends Biohybrid Photoelectrode Stability to Years (Angew. Chem. Int. Ed. 24/2022). *Angewandte Chemie International Edition*. 2022;61(24).
- 138 Wolfe KD, Gargye A, Mwambutsa F, Than L, Cliffel DE, Jennings GK. Layer-by-Layer Assembly of Photosystem I and PEDOT:PSS Biohybrid Films for Photocurrent Generation. *Langmuir*. 2021;37(35):10481–10489.
- 139 Zhao F, Wang P, Ruff A, Hartmann V, Zacarias S, Pereira IA, Nowaczyk MM, Rögner M, Conzuelo F, Schuhmann W. A photosystem i monolayer with anisotropic electron flow enables Z-scheme like photosynthetic water splitting. *Energy and Environmental Science*. 2019;12(10):3133–3143.

BIBLIOGRAPHY

- 140 Kaniber SM, Simmel FC, Holleitner AW, Carmeli I. The optoelectronic properties of a photosystem I-carbon nanotube hybrid system. *Nanotechnology*. 2009;20(34).
- 141 Simmerman RF, Zhu T, Baker DR, Wang L, Mishra SR, Lundgren CA, Bruce BD. Engineering Photosystem I Complexes with Metal Oxide Binding Peptides for Bioelectronic Applications. *Bioconjugate Chemistry*. 2015;26(10):2097–2105.
- 142 Jordan P, Fromme P, Witt HT, Klukas O, Saenger W, Krauß N. Three-dimensional structure of cyanobacterial photosystem I at 2.5Å resolution. *Nature*. 2001;411(6840):909–917.
- 143 Pei J, Kim BH, Grishin NV. PROMALS3D: a tool for multiple protein sequence and structure alignments. *Nucleic Acids Research*. 2008;36(7):2295–2300.
- 144 Robert X, Gouet P. Deciphering key features in protein structures with the new ENDscript server. *Nucleic Acids Research*. 2014;42(W1):W320–W324.
- 145 Stothard P. The Sequence Manipulation Suite: JavaScript Programs for Analyzing and Formatting Protein and DNA Sequences. *BioTechniques*. 2000;28(6):1102–1104.
- 146 Scheller HV, Jensen PE, Haldrup A, Lunde C, Knoetzel J. Role of subunits in eukaryotic Photosystem I. *Biochimica et Biophysica Acta (BBA) - Bioenergetics*. 2001;1507(1-3):41–60.
- 147 Andolfi L, Canters GW, Verbeet MP, Cannistraro S. Scanning tunneling spectroscopy investigation of self-assembled plastocyanin mutants onto gold substrates under controlled environment. *Biophysical Chemistry*. 2004;107(2):107–116.
- 148 Cohen-Tannoudji C, Diu B, Laloë F. *Mécanique Quantique*, vol. I-II. Collection Enseignement des sciences. 1973.
- 149 Sakurai JJ, Napolitano J. *Modern Quantum Mechanics*. 1985.
- 150 Blumberger J. Recent Advances in the Theory and Molecular Simulation of Biological Electron Transfer Reactions. *Chemical Reviews*. 2015;115(20):11191–11238.
- 151 Gray HB, Winkler JR. Electron Transfer in Proteins. *Annual Review of Biochemistry*. 1996;65:537–561.
- 152 Hopfield JJ. Electron Transfer Between Biological Molecules by Thermally Activated Tunneling. *Proceedings of the National Academy of Sciences*. 1974;71(9):3640–3644.
- 153 Jones ML, Kurnikov IV, Beratan DN. The Nature of Tunneling Pathway and Average Packing Density Models for Protein-Mediated Electron Transfer. *The Journal of Physical Chemistry A*. 2002;106(10):2002–2006.

BIBLIOGRAPHY

- 154 Winkler JR, Gray HB. Long-range electron tunneling. *Journal of the American Chemical Society*. 2014;136(8):2930–2939.
- 155 Page CC, Moser CC, Dutton PL. Mechanism for electron transfer within and between proteins. 2003.
- 156 Moser CC, Chobot SE, Page CC, Dutton PL. Distance metrics for heme protein electron tunneling. *Biochimica et Biophysica Acta (BBA) - Bioenergetics*. 2008;1777(7-8):1032–1037.
- 157 Page CC, Moser CC, Chen X, Dutton PL. Natural engineering principles of electron tunnelling in biological oxidation–reduction. *Nature*. 1999;402(6757):47–52.
- 158 Beratan DN, Betts JN, Onuchic JN. Protein Electron Transfer Rates Set by the Bridging Secondary and Tertiary Structure. *Science*. 1991;252(5010):1285–1288.
- 159 Jones ML, Kurnikov IV, Beratan DN. The Nature of Tunneling Pathway and Average Packing Density Models for Protein-Mediated Electron Transfer. *The Journal of Physical Chemistry A*. 2002;106(10):2002–2006.
- 160 Moser CC, Keske JM, Warncke K, Farid RS, Dutton PL. Nature of biological electron transfer. *Nature*. 1992;355(6363):796–802.
- 161 Ennist NM, Stayrook SE, Dutton PL, Moser CC. Rational design of photosynthetic reaction center protein maquettes. *Frontiers in Molecular Biosciences*. 2022;9.
- 162 Miyashita O, Okamura MY, Onuchic JN. Interprotein electron transfer from cytochrome *c*₂ to photosynthetic reaction center: Tunneling across an aqueous interface. *Proceedings of the National Academy of Sciences*. 2005;102(10):3558–3563.
- 163 Ubbink M. The courtship of proteins: Understanding the encounter complex. *FEBS Letters*. 2009;583(7):1060–1066.
- 164 Bostick CD, Mukhopadhyay S, Sheves M, Cahen D, Lederman D. Protein bioelectronics : a review of what we do and do not know. *Reports on Progress in Physics*. 2018;81(2):1–150.
- 165 Skourtis SS. Review probing protein electron transfer mechanisms from the molecular to the cellular length scales. *Biopolymers*. 2013;100(1):82–92.
- 166 Zhang Y, Liu C, Balaeff A, Skourtis SS, Beratan DN. Biological charge transfer via flickering resonance. *Proceedings of the National Academy of Sciences*. 2014;111:10049–10054.

BIBLIOGRAPHY

- 167 Breuer M, Rosso KM, Blumberger J, Butt JN. Multi-haem cytochromes in *Shewanella oneidensis* MR-1: structures, functions and opportunities. *Journal of The Royal Society Interface*. 2015;12(102):20141117.
- 168 El-Naggar MY, Wanger G, Leung KM, Yuzvinsky TD, Southam G, Yang J, Lau WM, Neilson KH, Gorby YA. Electrical transport along bacterial nanowires from *Shewanella oneidensis* MR-1. *Proceedings of the National Academy of Sciences*. 2010;107(42):18127–18131.
- 169 Pirbadian S, El-Naggar MY. Multistep hopping and extracellular charge transfer in microbial redox chains. *Physical Chemistry Chemical Physics*. 2012;14(40):13802.
- 170 Xu S, Barrozo A, Tender LM, Krylov AI, El-Naggar MY. Multiheme Cytochrome Mediated Redox Conduction through *Shewanella oneidensis* MR-1 Cells. *Journal of the American Chemical Society*. 2018;140(32):10085–10089.
- 171 Troisi A. The speed limit for sequential charge hopping in molecular materials. *Organic Electronics*. 2011;12(12):1988–1991.
- 172 John Goldbeck. *Photosystem I: The Light-Driven Plastocyanin: Ferredoxin Oxidoreductase*, vol. 24. Dordrecht: Springer Netherlands. 2006.
- 173 Zhang J, Kuznetsov AM, Medvedev IG, Chi Q, Albrecht T, Jensen PS, Ulstrup J. Single-molecule electron transfer in electrochemical environments. *Chemical Reviews*. 2008;108(7):2737–2791.
- 174 Futera Z, Ide I, Kayser B, Garg K, Jiang X, van Wonderen JH, Butt JN, Ishii H, Pecht I, Sheves M, Cahen D, Blumberger J. Coherent Electron Transport across a 3 nm Bioelectronic Junction Made of Multi-Heme Proteins. *The Journal of Physical Chemistry Letters*. 2020;11:9766–9774.
- 175 Romero-Muñiz C, Ortega M, Vilhena JG, Pérez R, Cuevas JC, Zotti LA. The Role of Metal Ions in the Electron Transport through Azurin-Based Junctions. *Applied Sciences*. 2021;11(9):3732.
- 176 Futera Z, Ide I, Kayser B, Garg K, Jiang X, Van Wonderen JH, Butt JN, Ishii H, Pecht I, Sheves M, Cahen D, Blumberger J. Coherent Electron Transport across a 3 nm Bioelectronic Junction Made of Multi-Heme Proteins. *Journal of Physical Chemistry Letters*. 2020;11(22):9766–9774.
- 177 Kayser B, Fereiro JA, Guo C, Cohen SR, Sheves M, Pecht I, Cahen D. Transistor configuration yields energy level control in protein-based junctions. *Nanoscale*. 2018; 10(46):21712–21720.

BIBLIOGRAPHY

- 178 Romero-Muñiz C, Ortega M, Vilhena JG, Díez-Pérez I, Pérez R, Cuevas JC, Zotti LA. Can Electron Transport through a Blue-Copper Azurin Be Coherent? An Ab Initio Study. *The Journal of Physical Chemistry C*. 2021;125(3):1693–1702.
- 179 Amdursky N, Marchak D, Sepunaru L, Pecht I, Sheves M, Cahen D. Electronic Transport via Proteins. *Advanced Materials*. 2014;26(42):7142–7161.
- 180 Cahen D, Pecht I, Sheves M. What Can We Learn from Protein-Based Electron Transport Junctions? *Journal of Physical Chemistry Letters*. 2021; 12(47):11598–11603.
- 181 Kayser B, Fereiro JA, Bhattacharyya R, Cohen SR, Vilan A, Pecht I, Sheves M, Cahen D. Solid-State Electron Transport via the Protein Azurin is Temperature-Independent Down to 4 K. *The Journal of Physical Chemistry Letters*. 2020;11(1):144–151.
- 182 Mukhopadhyay S, Karuppanan SK, Guo C, Fereiro JA, Bergren A, Mukundan V, Qiu X, Castañeda Ocampo OE, Chen X, Chiechi RC, McCreery R, Pecht I, Sheves M, Pasula RR, Lim S, Nijhuis CA, Vilan A, Cahen D. Solid-State Protein Junctions: Cross-Laboratory Study Shows Preservation of Mechanism at Varying Electronic Coupling. *iScience*. 2020;23(5):101099.
- 183 Yu X, Lovrincic R, Sepunaru L, Li W, Vilan A, Pecht I, Sheves M, Cahen D. Insights into Solid-State Electron Transport through Proteins from Inelastic Tunneling Spectroscopy: The Case of Azurin. *ACS Nano*. 2015;9(10):9955–9963.
- 184 Michaeli K, Beratan DN, Waldeck DH, Naaman R. Voltage-induced long-range coherent electron transfer through organic molecules. *Proceedings of the National Academy of Sciences of the United States of America*. 2019;116(13):5931–5936.
- 185 Naaman R, Waldeck DH, Fransson J. New Perspective on Electron Transfer through Molecules. *The Journal of Physical Chemistry Letters*. 2022;13(50):11753–11759.
- 186 Alessandrini A, Corni S, Facci P. Unravelling single metalloprotein electron transfer by scanning probe techniques. *Physical Chemistry Chemical Physics*. 2006; 8(38):4383–4397.
- 187 Zhang J, Chi Q, Hansen AG, Jensen PS, Salvatore P, Ulstrup J. Interfacial electrochemical electron transfer in biology - Towards the level of the single molecule. *FEBS Letters*. 2012;586(5):526–535.
- 188 Ha TQ, Planje IJ, White JR, Aragonès AC, Díez-Pérez I. Charge transport at the protein–electrode interface in the emerging field of biomolecular electronics. *Current Opinion in Electrochemistry*. 2021;28:100734.
- 189 Brettel K, Leibl W. Electron transfer in photosystem I. *Biochimica et Biophysica Acta - Bioenergetics*. 2001;1507(1-3):100–114.

BIBLIOGRAPHY

- 190 Gray HB, Winkler JR. Long-range electron transfer. *Proceedings of the National Academy of Sciences of the USA*. 2005;102(10):3534–3539.
- 191 Shih C, Museth AK, Abrahamsson M, Blanco-Rodriguez AM, Di Bilio AJ, Sudhamsu J, Crane BR, Ronayne KL, Towrie M, Vlček A, Richards JH, Winkler JR, Gray HB. Tryptophan-accelerated electron flow through proteins. *Science*. 2008;320(5884):1760–1762.
- 192 Takematsu K, Williamson HR, Nikolovski P, Kaiser JT, Sheng Y, Pospíšil P, Towrie M, Heyda J, Hollas D, Záliš S, Gray HB, Vlček A, Winkler JR. Two Tryptophans Are Better Than One in Accelerating Electron Flow through a Protein. *ACS Central Science*. 2019;5(1):192–200.
- 193 Winkler JR, Gray HB. Electron flow through metalloproteins. *Chemical Reviews*. 2014;114(7):3369–3380.
- 194 Chi Q, Zhang J, Jensen PS, Christensen HE, Ulstrup J. Long-range interfacial electron transfer of metalloproteins based on molecular wiring assemblies. *Faraday Discussions*. 2006;131:181–195.
- 195 Léger C, Elliott SJ, Hoke KR, Jeuken LJC, Jones AK, Armstrong FA. Enzyme Electrokinetics: Using Protein Film Voltammetry To Investigate Redox Enzymes and Their Mechanisms. *Biochemistry*. 2003;42(29):8653–8662.
- 196 Léger C, Bertrand P. Direct electrochemistry of redox enzymes as a tool for mechanistic studies. *Chemical Reviews*. 2008;108(7):2379–2438.
- 197 Melin F, Hellwig P. Redox Properties of the Membrane Proteins from the Respiratory Chain. *Chemical Reviews*. 2020;120(18):10244–10297.
- 198 Wang VCC, Ragsdale SW, Armstrong FA. Investigations of Two Bidirectional Carbon Monoxide Dehydrogenases from *Carboxydotherrnus hydrogenoformans* by Protein Film Electrochemistry. *ChemBioChem*. 2013;14(14):1845–1851.
- 199 Armstrong FA, Evans RM, Hexter SV, Murphy BJ, Roessler MM, Wulff P. Guiding Principles of Hydrogenase Catalysis Instigated and Clarified by Protein Film Electrochemistry. *Accounts of Chemical Research*. 2016;49(5):884–892.
- 200 Armstrong FA, Evans RM, Megarity CF. Protein film electrochemistry of iron–sulfur enzymes. In: *Methods in enzymology*, vol. 599, pp. 387–407. Elsevier. 2018;.
- 201 Zigah D, Lojou E, Poulpiquet A. Micro- and Nanoscopic Imaging of Enzymatic Electrodes: A Review. *ChemElectroChem*. 2019;6(22):5524–5546.
- 202 Ron I, Sepunaru L, Ltzhakov S, Belenkova T, Friedman N, Pecht I, Sheves M, Cahen D. Proteins as electronic materials: Electron transport through solid-state

BIBLIOGRAPHY

- protein monolayer junctions. *Journal of the American Chemical Society*. 2010; 132(12):4131–4140.
- 203 Garg K, Ghosh M, Eliash T, Van Wonderen JH, Butt JN, Shi L, Jiang X, Zdenek F, Blumberger J, Pecht I, Sheves M, Cahen D. Direct evidence for heme-assisted solid-state electronic conduction in multi-heme: C -type cytochromes. *Chemical Science*. 2018;9(37):7304–7310.
- 204 Nichols RJ, Higgins SJ. Single Molecular Electrochemistry within an STM. *Advances in Electrochemical Science and Engineering*. 2014;14:99–136.
- 205 Madden C, Vaughn MD, Díez-Pérez I, Brown KA, King PW, Gust D, Moore AL, Moore TA. Catalytic Turnover of [FeFe]-Hydrogenase Based on Single-Molecule Imaging. *Journal of the American Chemical Society*. 2012;134(3):1577–1582.
- 206 Wigginton NS, Rosso KM, Lower BH, Shi L, Hochella MF. Electron tunneling properties of outer-membrane decaheme cytochromes from *Shewanella oneidensis*. *Geochimica et Cosmochimica Acta*. 2007;71(3):543–555.
- 207 Yan J, Frøkjær EE, Engelbrekt C, Leimkühler S, Ulstrup J, Wollenberger U, Xiao X, Zhang J. Voltammetry and Single-Molecule In Situ Scanning Tunnelling Microscopy of the Redox Metalloenzyme Human Sulfite Oxidase. *ChemElectroChem*. 2021; 8(1):164–171.
- 208 López-Martínez M, Artés JM, Sarasso V, Carminati M, Díez-Pérez I, Sanz F, Gorostiza P. Differential Electrochemical Conductance Imaging at the Nanoscale. *Small*. 2017;13(36).
- 209 Pia EAD, Chi Q, Jones DD, Macdonald JE, Ulstrup J, Elliott M. Single-Molecule Mapping of Long-range Electron Transport for a Cytochrome *b*₅₆₂ Variant. *Nano Letters*. 2011;11(1):176–182.
- 210 Alessandrini A, Gerunda M, Canters GW, Verbeet MP, Facci P. Electron tunnelling through azurin is mediated by the active site Cu ion. *Chemical Physics Letters*. 2003; 376(5-6):625–630.
- 211 Artés JM, Díez-Pérez I, Gorostiza P. Transistor-like behavior of single metalloprotein junctions. *Nano Letters*. 2012;12(6):2679–2684.
- 212 Lindsay S. Ubiquitous electron transport in non-electron transfer proteins. *Life*. 2020; 10(5).
- 213 Nagahara LA, Thundat T, Lindsay SM. Preparation and characterization of STM tips for electrochemical studies. *Review of Scientific Instruments*. 1989;60(10):3128–3130.

BIBLIOGRAPHY

- 214 Tang L, Yi L, Jiang T, Ren R, Paulose Nadappuram B, Zhang B, Wu J, Liu X, Lindsay S, Edel JB, et al. Measuring conductance switching in single proteins using quantum tunneling. *Science Advances*. 2022;8(20):eabm8149.
- 215 Zhang B, Deng H, Mukherjee S, Song W, Wang X, Lindsay S. Engineering an Enzyme for Direct Electrical Monitoring of Activity. *ACS Nano*. 2020;14(2):1360–1368.
- 216 Zhang B, Song W, Pang P, Lai H, Chen Q, Zhang P, Lindsay S. Role of contacts in long-range protein conductance. *Proceedings of the National Academy of Sciences of the United States of America*. 2019;116(13):5886–5891.
- 217 Zhang B, Ryan E, Wang X, Lindsay S. Probing Bioelectronic Connections Using Streptavidin Molecules with Modified Valency. *Journal of the American Chemical Society*. 2021;143(37):15139–15144.
- 218 Zhang B, Ryan E, Wang X, Song W, Lindsay S. Electronic Transport in Molecular Wires of Precisely Controlled Length Built from Modular Proteins. *ACS Nano*. 2022; 16(1):1671–1680.
- 219 Zhang B, Song W, Brown J, Nemanich R, Lindsay S. Electronic Conductance Resonance in Non-Redox-Active Proteins. *Journal of the American Chemical Society*. 2020;142(13):6432–6438.
- 220 Zhang B, Sun L. Artificial photosynthesis: opportunities and challenges of molecular catalysts. *Chemical Society Reviews*. 2019;48:2216–2264.
- 221 Zhang B, Song W, Pang P, Zhao Y, Zhang P, Csabai I, Vattay G, Lindsay S. Observation of giant conductance fluctuations in a protein. *Nano Futures*. 2017; 1(3).
- 222 López-Martínez M, López-Ortiz M, Antinori ME, Wientjes E, Nin-Hill A, Rovira C, Croce R, Díez-Pérez I, Gorostiza P. Electrochemically Gated Long-Distance Charge Transport in Photosystem I. *Angewandte Chemie - International Edition*. 2019;58(38):13280–13284.
- 223 Lagunas A, Guerra-Castellano A, Nin-Hill A, Díaz-Moreno I, De la Rosa MA, Samitier J, Rovira C, Gorostiza P. Long distance electron transfer through the aqueous solution between redox partner proteins. *Nature Communications*. 2018; 9(1):3–9.
- 224 Alexandre Gomila, Gonzalo Pérez-Mejías, Alba Nin Hill, Alejandra Guerra, Laura Casas-Ferrer, Sthefany Ortiz-Tescari, Antonio Díaz-Quintana, Josep Samitier, Carme Rovira, Miguel Angel de la Rosa, Irene Díaz-Moreno, Pau Gorostiza, Marina Inés Giannotti, Anna Lagunas. Phosphorylation disrupts long-distance electron transport in cytochrome c. *Nature Communications*. 2022;.

BIBLIOGRAPHY

- 225 Gehring P, Thijssen JM, van der Zant HSJ. Single-molecule quantum-transport phenomena in break junctions. *Nature Reviews Physics*. 2019;1(6):381–396.
- 226 Friebe VM, Frese RN. Photosynthetic reaction center-based biophotovoltaics. *Current Opinion in Electrochemistry*. 2017;5(1):126–134.
- 227 Kornienko N, Zhang JZ, Sakimoto KK, Yang P, Reisner E. Interfacing nature's catalytic machinery with synthetic materials for semi-artificial photosynthesis. *Nature Nanotechnology*. 2018;13(10):890–899.
- 228 Goyal A, Szewczyk S, Burdziński G, Abram M, Kargul J, Gibasiewicz K. Competition between intra-protein charge recombination and electron transfer outside photosystem I complexes used for photovoltaic applications. *Photochemical & Photobiological Sciences*. 2022;21(3):319–336.
- 229 Wolfe KD, Dervishogullari D, Passantino JM, Stachurski CD, Jennings GK, Cliffel DE. Improving the stability of photosystem I-based bioelectrodes for solar energy conversion. *Current Opinion in Electrochemistry*. 2020;19:27–34.
- 230 Qiu X, Castaneda Ocampo O, de Vries HW, van Putten M, Loznik M, Herrmann A, Chiechi RC. Self-regenerating soft biophotovoltaic devices. *ACS applied materials & interfaces*. 2018;10(43):37625–37633.
- 231 Suresh L, Vaghasiya JV, Jones MR, Tan SC. Biodegradable Protein-Based Photoelectrochemical Cells with Biopolymer Composite Electrodes That Enable Recovery of Valuable Metals. *ACS Sustainable Chemistry & Engineering*. 2019;7(9):8834–8841.
- 232 Ravi SK, Rawding P, Elshahawy AM, Huang K, Sun W, Zhao F, Wang J, Jones MR, Tan SC. Photosynthetic apparatus of *Rhodobacter sphaeroides* exhibits prolonged charge storage. *Nature Communications*. 2019;10(1):902.
- 233 Ravi SK, Wu T, Udayagiri VS, Vu XM, Wang Y, Jones MR, Tan SC. Photosynthetic Bioelectronic Sensors for Touch Perception, UV-Detection, and Nanopower Generation: Toward Self-Powered E-Skins. *Advanced Materials*. 2018;30(39):1802290.
- 234 Swainsbury DJ, Friebe VM, Frese RN, Jones MR. Evaluation of a biohybrid photoelectrochemical cell employing the purple bacterial reaction centre as a biosensor for herbicides. *Biosensors and Bioelectronics*. 2014;58:172–178.
- 235 Kuhlert S, Drepper F, Fufezan C, Sommer F, Hippler M. Residues PsaB Asp612 and PsaB Glu613 of photosystem I confer pH-dependent binding of plastocyanin and cytochrome c 6. *Biochemistry*. 2012;51(37):7297–7303.

BIBLIOGRAPHY

- 236 Mathis P, Sigfridsson K, Hansson O Karlsson BG, Baltzer L, Nordling M, Lundberg LG. Structural Dynamics in the Plastocyanin-Photosystem 1 Electron-Transfer Complex as Revealed by Mutant Studies. *Biochim Biophys Acta*. 1995;24:28–36.
- 237 Trubitsin BV, Mamedov MD, Semenov AY, Tikhonov AN. Interaction of ascorbate with photosystem i. *Photosynthesis Research*. 2014;122(2):215–231.
- 238 Wientjes E, Croce R. PMS: Photosystem i electron donor or fluorescence quencher. *Photosynthesis Research*. 2012;111(1-2):185–191.
- 239 Farkas D, Hansson Ö. An NMR study elucidating the binding of Mg(II) and Mn(II) to spinach plastocyanin. Regulation of the binding of plastocyanin to subunit PsaF of photosystem i. *Biochimica et Biophysica Acta - Bioenergetics*. 2011; 1807(12):1539–1548.
- 240 Ishijima S, Uchibori A, Takagi H, Maki R, Ohnishi M. Light-induced increase in free Mg²⁺ concentration in spinach chloroplasts: Measurement of free Mg²⁺ by using a fluorescent probe and necessity of stromal alkalinization. *Archives of Biochemistry and Biophysics*. 2003;412(1):126–132.
- 241 Portis AR, Heldt HW. Light-dependent changes of the Mg²⁺ concentration in the stroma in relation to the Mg²⁺ dependency of CO₂ fixation in intact chloroplasts. *Biochimica et Biophysica Acta*. 1976;449:434–446.
- 242 Pottosin I, Shabala S. Transport Across Chloroplast Membranes: Optimizing Photosynthesis for Adverse Environmental Conditions. 2016.
- 243 Shaul O. Magnesium transport and function in plants: the tip of the iceberg. *BioMetals*. 2002;15:309–323.